



Francois Miterand Njock Bayock

THERMAL ANALYSIS OF DISSIMILAR WELD JOINTS OF HIGH-STRENGTH AND ULTRA- HIGH-STRENGTH STEELS

Francois Miterand Njock Bayock

THERMAL ANALYSIS OF DISSIMILAR WELD JOINTS OF HIGH-STRENGTH AND ULTRA- HIGH-STRENGTH STEELS

Dissertation for the degree of Doctor of Science (Technology) to be presented with due permission for public examination and criticism in the Room 1316 at Lappeenranta-Lahti University of Technology LUT, Lappeenranta, Finland on the 30th of June, 2020, at noon.

Acta Universitatis
Lappeenrantaensis 911

Supervisors Professor Heidi Piili
LUT School of Energy Systems
Lappeenranta-Lahti University of Technology LUT
Finland

Professor Paul Kah
(Docent of Lappeenranta-Lahti University of Technology LUT)
Department of Engineering Science
University West
Sweden

Professor Antti Salminen
Faculty of Science and Engineering
University of Turku
Finland

Reviewers Professor Leif Karlsson
Department of Engineering Science
University West
Sweden

Professor Sambao Lin
Harbin Institute of Technology
China

Opponent Professor Sambao Lin
Harbin Institute of Technology
China

ISBN 978-952-335-527-9
ISBN 978-952-335-528-6 (PDF)
ISSN-L 1456-4491
ISSN 1456-4491

Lappeenranta-Lahti University of Technology LUT
LUT University Press 2020

Abstract

Francois Miterand Njock Bayock

Thermal analysis of dissimilar weld joints of high-strength and ultra-high-strength steels

Lappeenranta 2020

126 pages

Acta Universitatis Lappeenrantaensis 911

Diss. Lappeenranta-Lahti University of Technology LUT

ISBN 978-952-335-527-9, ISBN 978-952-335-528-6 (PDF), ISSN-L 1456-4491, ISSN 1456-4491

Advances in steel production processes in the last two decades have enabled the production of novel materials with improved strength, weldability and usability. Many industries are implementing these novel materials into production, primarily to benefit from the higher strength-to-weight ratio. Improved material properties are especially important for industries engaged in advanced structural engineering and applications such as construction plants, piping systems of nuclear power plants, and products in the automotive and aeronautical sectors. Another trend in modern manufacturing is increased use of dissimilar metals welding, and welding of dissimilar steel grades is becoming common in the economically critical energy sector. Dissimilar welding of high-strength steels is especially advantageous for regions with extreme weather conditions, such as sub-Saharan Africa and Arctic regions.

When dissimilar joints for high strength steel (HSS) are welded, gas metal arc welding (GMAW) is extensively used because of its adaptability and controllability (control of input and output) and well-established production quality. The most important issue in dissimilar welding of HSS is control of the thermal cycle, as these steels have rather narrow process parameter windows and are prone to softening in the heat-affected zone (HAZ). This thesis addresses the issue of improving the weld quality of dissimilar material welds through improved understanding of the relationship between the welding parameters and resulting microstructure determining the mechanical properties of the joint.

The materials used in this thesis belong to the classes of high strength steels, ultra-high-strength steels (UHSS) with a static strength of 690 to 960 MPa, steels manufactured by a thermo-mechanically controlled process (TMCP) and quenched and tempered (QT) steels. A specific objective is to define favourable heat input values that can improve the quality of dissimilar joints of S690QT-TMCP and S700MC-S960QC. The main difficulty in welding of dissimilar HSS is control of HAZ softening on both sides of the joint. Many factors have an influence on HAZ characteristics, e.g., welding parameters, filler wire composition, and groove geometry. Therefore, selecting parameters that produce the desired properties in both materials being joined is very important. An appropriate choice of parameters results in improved microstructural constitution and mechanical properties.

The research has been carried out using three methods: literature review, numerical modelling and experimental validation. The literature review formed the first part of the study and examined thermal effects on the microstructural constituents and mechanical properties of dissimilar HSS welds. A numerical model of the thermal cycle was developed in second part of the study to understand the effect of cooling rate on changes in microstructure. The third part of this thesis comprised experimental validation of the influence of cooling rate on the properties of the weld joints.

The literature analysis demonstrated the feasibility of developing a numerical model predicting the thermal cycle of dissimilar welds made with GMAW by improving understanding of thermal transfer in the HAZ. In the experimental part, the thermal cycle data obtained during numerical modelling were applied to dissimilar welds of HSS and UHSS. Based on analysis of numerical and experimental data, optimum welding conditions were proposed, and their accuracy further validated with standard mechanical testing: Vickers hardness testing, tensile testing, scanning electron microscopy (SEM), and energy dispersive spectroscopy (EDS) mapping. Microscopic analysis of the specimens was used to determine the process parameters having the most significant influence on the microstructure and mechanical properties of the welded joint.

Analytical and experimental approaches to control heat transfer in the weld joints of dissimilar HSS have been developed and experimentally validated in this thesis. The findings enable weld quality to be improved and the microstructural constituents and mechanical properties of the joints to be optimised by precise control of heat input. The proposed approach allows the number of tests needed for welding parameters definition to be reduced by providing an improved understanding of the effect of heat transfer on microstructure characteristics.

Keywords: High strength steels, ultra-high-strength steels, numerical model, thermal cycle, weld quality, microstructure characterisation, SEM, EDS, TMCP, QT, Vickers hardness, tensile strength

Acknowledgments

This doctoral thesis was carried out at the Laboratory of Laser Materials Processing and Additive Manufacturing, and the Laboratory of Welding Technology of the Department of Mechanical Engineering at LUT University, Finland, between 2016 and 2020.

My profound thanks go to Professor Paul Kah presently at University West Sweden for enabling me to gain admission to the doctoral studies program in the Laboratory of Welding Technology at LUT University. Many thanks, Professor, for your support, as you know things were not easy. You help me acquire funds from different funding association during my study. You were always by my side, giving me valuable advice and driving me forward with your enthusiasm. *“Toute ma famille vous dises grand merci”*.

I would like to thank Professor Heidi Piili, for her motivation, support during this period to finalise my thesis. I am grateful for her encouragement and financial support during the last phase of my thesis. As you always said, *“you can do it”*.

My sincere thanks go to my main supervisor Docent Paul Kah, who supported and guided me since my first day at LUT University. Since that time, for guiding me in my research journey, teach me how to write well-structured and logical academic articles among other valuable academic skills. I would also like to thank Professor Emeritus Jukka Martikainen for encouraging me to travel to Finland for my study and help me with valuable advice. You are actually our family here in Finland.

I would like to thank Professor Antti Salminen for the help in my research and for giving valuable support and comments on my topic. Dear Professor Antti Salminen, I am very grateful to you. Thank you very much for the initiative that you took for the last support I got from LUT University.

I want to thank EDUFI for the first grant I got from Finland. I want to thank The Finnish Cultural Foundation (190749) for the grant for the research funding for one year during my study. I would like to thank the Research Foundation of Lappeenranta-Lahti University for the support of accommodation in Lappeenranta during the research period.

I would like to express my gratitude to Manufacturing 4.0 (MFG4.0) project which is funded by Strategic Research Council (Which is part of Academic of Finland) and to project partners of MFG4.0 for all support to my thesis. MFG4.0 project started 1.1.2018 and ends 31.12.2020, and it has five working packages in it. Project involves four universities in Finland (University of Turku, LUT University, University of Jyväskylä and University of Helsinki) and seven research group from these universities. MFG4.0 project (number 335992) aims multidisciplinary research for strong foresight for future manufacturing in Finland, understanding what business models will work in this context and analysing and creation of education systems and social security models for a better match for the future demands. Support of this project was especially crucial when I was finalising my thesis.

My sincere thanks go to my colleagues and friends: Dr. Mvola Belinga, Dr. Anna Unt, Dr. Pavel Layus, Dr. Emmanuel Affrane Gyasi, Benoit Ndiwe, Sakari Penttilä, Esa Hiltunen, Martin Kesse, and all my family friends in Lappeenranta. I would also like to thank my English teacher Peter Jones for his help with the language and suggestions of the articles and dissertation.

I would like to thank reviewers Prof. Leif Karlsson and Prof. Sambao Lin for their willingness and their valuable comments and suggestions to improve the manuscript during the review process. Dear Prof. Karlsson, thank you very much for your detail comments and remarks help me to get a deep understanding on microstructure characterisation allowed me to make the work more complete and technical, and comment of Prof. Sambao Lin on numerical model approach and mechanical testing helped me to improve the clarity of the results. Additionally, I would like to thank Prof. Sambao Lin for acting as an opponent and to attending my public examination.

Thanks go to the administration team of the University of Douala (Cameroon): Rector Professor Magloire Ondo, for allowing me to study abroad. Director of ENSET of the University of Douala, Associate Professor Leandre Nneme Nneme, to encourage me to continue my doctoral studies and encourage the cooperation between the two universities. I would like to thank the head of the Department of Mechanical Engineering Assoc. Professor Fabien Betene Ebanda for his encouragement and support. I would like to thank my colleagues Assoc. Professor Alexandre Boum and Mr. Sadrack Timba for their motivations.

I express my profound gratitude to my grandfather, Ndjock Sadrack (deceased), my father, Bayock Ndjock Theodore, and my mother, Ngo Mabong Jeanne. They encouraged me and I am thankful for all that they have contributed to my life. I would like to thank all my brothers and sisters, for their support and love.

My heartfelt thanks to my wife, Onana Nwaha Francine epse Njock Bayock, who supported me throughout this study and helped me to carry on no matter what. I love you! My adorable kids, Bayock Cathy Isis, Bayock Jade Iris, Bayock Nwaha Francine Patricia, and Bayock Njock Frank Mylan, they have given me the strength to finish this thesis.

A special thanks go to my sister in Finland mummy Clotilde Kah for her support, encouragement, and laughter during my entire stay in Finland, thanks for being part of my family during difficult moments.



Francois Miterand Njock Bayock

June 2020

Lappeenranta, Finland

Dedication

*To my wife and children, Onana Nwaha epse Njock Bayock,
Bayock Cathy Isis, Bayock Jade Iris, Bayock Nwaha Francine
Patricia, and Bayock Njock Frank Mylan.*

Contents

Abstract

Acknowledgments

Contents

List of publications	11
Nomenclature	13
1 Introduction	19
1.1 Research background	19
1.1.1 Weldability of dissimilar welds of high strength steel.....	20
1.1.2 Effect of heat input on dissimilar weld joints	20
1.1.3 Microstructure characterisation of dissimilar weld joints	21
1.1.4 Mechanical tests of welded joints	21
1.2 Motivation and objective of the research	22
1.3 Research questions	23
1.4 Scope and limitations of the thesis	25
1.5 Scientific contribution to material and welding technology	28
1.6 Structure of the thesis	29
1.7 Social and environmental impact	31
2 State of the art of dissimilar welding of HSS-UHSS	33
2.1 Classification	33
2.2 Influence of heat input on weldability of dissimilar HSS joints	34
2.2.1 Numerical formulations of the heat cycle in the HAZ.....	43
2.2.2 Cooling rate after the welding process.....	44
2.3 Microstructure characterisation of dissimilar HSS welds	45
2.4 Mechanical properties of dissimilar HSS welds.....	49
3 Materials and Methods	54
3.1 Numerical simulation procedure of GMAW process.....	54
3.1.1 Geometry design and materials.....	55
3.1.2 Model and algorithm.....	57
3.2 Experimental setup	60
3.2.1 Experimental set-up	61
3.2.2 Measurement of thermal cycles	62
3.2.3 Microstructure analysis	63
3.2.4 Vickers-hardness and tensile strength test set-up	63
3.3 Schematic cross-section of the weld, materials, and filler wire	64
3.3.1 Schematic cross-section of the weld	64
3.3.2 Materials and filler wire	65

4	Test results	68
4.1	Thermal cycle analysis	68
4.2	Microstructure characterisation	73
4.2.1	Microstructure of dissimilar S690QT-TMCP steels	73
4.2.2	Microstructure of S700MC-S960QC weld sub-zones using undermatched filler wire	78
4.2.3	Microstructure of S700MC-S960QC weld sub-zones using overmatched filler wire	83
4.3	Vickers-hardness results	87
4.3.1	Micro-hardness of dissimilar S690QT-TMCP steels	87
4.3.2	Vickers-hardness using undermatched filler wire	89
4.3.3	Vickers-hardness using overmatched filler wire	90
4.4	Tensile test results	92
5	Overview of the publications	95
6	Discussion	104
6.1	State of the art of weldability of dissimilar high strength steel	104
6.2	Thermal cycle model and mechanical properties of the weld joints	105
6.3	Microstructure and mechanical properties using undermatched WM	105
6.4	Microstructure and mechanical properties using overmatched WM	106
6.5	Welding process recommended for dissimilar welding of HSS	107
7	Conclusions	110
	References	111
	Appendix A: List of equations	118
	Appendix B: List of tables	120
	Appendix C: List of figures	122
	Publications	

List of publications

This thesis is based on the following papers published during doctoral studies. The papers are referred to in this dissertation by Roman numerals I–V.

- I. **Njock Bayock, F.**, Kah, P., Mvola, B., and Layus, P. (2019). Experimental review of thermal analysis of dissimilar welds of high-strength steel. *Reviews on Advanced Materials Science*, 58(1), pp. 38-49.
- II. **Njock Bayock, F.**, Kah, P., Layus, P., and Karkhin, V. (2019). Numerical and experimental investigation of the heat input effect on the mechanical properties and microstructures of dissimilar weld joints of 690-MPa QT and TMCP steel. *Metals*, 9(3):355, pp. 1-19.
- III. **Njock Bayock, F.**, Kah, P., Mvola, B., and Layus, P. (2019). Effect of heat input and undermatched filler wire on the microstructure and mechanical properties of dissimilar S700MC/S960QC high-strength steels. *Metals*, 9(8):883, pp. 1-20.
- IV. **Njock Bayock, F.**, Kah, P., Mvola, B., Layus, P. and Cai, X. (2019). Characterisation of bainite-ferrite structures formed on the heat-affected zone of dissimilar welds of high-strength steel (S700MC/S960QC) and their dependency on cooling time. *Proceedings of 72nd IIW Annual Assembly and International Conference*, Bratislava, Slovakia, 7-12 July, 1-10.
- V. **Njock Bayock, F.**, Kah, P., Salminen, A., Mvola, B., and Yang, X. (2020). Feasibility study of welding dissimilar Advanced and Ultra high strength steels. *Reviews on Advanced Materials Science*, 59(1), pp. 54-66.

Other scientific publication

Benoit Ndiwe, Belinga Mvola, Paul Kah, and **Francois Njock Bayock**. (2017). Effect of consumable filler wire composition to mismatches of high-Mn steels welded joints. *International Offshore and Polar Engineering Conference (ISOPE)*, San Francisco, CA, USA, June 25-30.

Author's contribution

In all of the publications presented in this thesis, the author was the principal contributor responsible for developing the numerical model of the thermal cycle, experimental investigation, and writing the final manuscript.

- I. **Njock Bayock, F.**, Kah, P., Mvola, B., and Layus, P. (2019). Experimental review of thermal analysis of dissimilar welds of high-strength steel. *Reviews on Advanced Materials Science*, 58(1), pp. 38-49.
This literature review paper was written and presented by the candidate. The paper was corrected and modified together with the candidate's supervisor, Associate Professor Paul Kah. Belinga Mvola and Pavel Layus gave advice and recommendations for improving the paper.

- II. **Njock Bayock, F.**, Kah, P., Layus, P., and Karkhin, V. (2019). Numerical and experimental investigation of the heat input effect on the mechanical properties and microstructures of dissimilar weld joints of 690-MPa QT and TMCP steel. *Metals*, 9(3):355, pp. 1-19.
The candidate wrote the literature review, performed the numerical and experimental analysis, and wrote the original draft. The paper was corrected and proofread by the candidate's supervisor, Associate Professor Paul Kah. The resources were provided by Doctor Pavel Layus and Professor Victor Karkhin.
- III. **Njock Bayock, F.**, Kah, P., Mvola, B., and Layus, P. (2019). Effect of heat input and undermatched filler wire on the microstructure and mechanical properties of dissimilar S700MC/S960QC high-strength steels. *Metals*, 9(8):883, pp. 1-20.
In this paper, the candidate performed the experimental analysis, wrote the entire manuscript, and prepared the final draft of the manuscript following discussion with the other authors. The clarity of the manuscript was improved by the candidate's supervisor, Associate Professor Paul Kah.
- IV. **Njock Bayock, F.**, Kah, P., Mvola, B., Layus, P. and Cai, X. (2019). Characterisation of bainite-ferrite structures formed on the heat-affected zone of dissimilar welds of high-strength steel (S700MC/S960QC) and their dependency on cooling time. *Proceedings of 72nd IIW Annual Assembly and International Conference*, Bratislava, Slovakia, 7-12 July, 1-10.
The candidate wrote the whole manuscript. The discussion and conclusion part of the paper was completed following discussion with the candidate's supervisor, Associate Professor Paul Kah.
- V. **Njock Bayock, F.**, Kah, P., Salminen, A., Mvola, B., and Yang, X. (2020). Feasibility study of welding dissimilar Advanced and Ultra high strength steels. *Reviews on Advanced Materials Science*, 59(1), pp. 54-66.
The candidate was the principal investigator and author for the whole thesis. Comments and suggestions from the co-authors helped to improve the clarity of the manuscript.

Nomenclature

Latin alphabet

A	area	mm^2
a_j	non-constant coefficients	
c	specific heat capacity	
I	arc current	A
U	arc voltage	V
Q	heat input	kJ/cm
k	coefficient of thermal conductivity	$\text{W/m}^\circ\text{C}$
k_x, k_y, k_z	thermal conductivity in the x, y, z directions	-
e	thickness of the work piece	mm
h	heat transfer coefficient	$\text{W}/(\text{m}^2\text{K})$
h	enthalpy	J/kg
l	length	mm
N	number of particles	-
N_l	Lagrange interpolation	
p_j	nominal base function	
q	heat flux	W/m^2
r	radius	m
T	internal temperature	$^\circ\text{C}$
T_o	ambient temperature	-
T_s	surface temperature	$^\circ\text{C}$
t	time	s
q_m	mass flow	kg/s
V	volume	m^3
v	welding speed	m/s
X	length	mm
Y	width	mm
Z	height	mm

Greek alphabet

α	alfa
β	beta
γ	gamma
δ	delta
ε	epsilon
ϵ	epsilon variant
ζ	zeta
η	eta
η_{eff}	Approximate value of arc efficiency

ϑ	theta variant
λ	lambda
μ	mu
ν	nu
ξ	xi
π	pi $\pi = 3.14159...$
ρ	rho
Σ	capital sigma
σ	sigma
τ	tau
υ	upsilon
Φ	capital phi
ϕ	phi
φ	phi
Ω	capital omega

Subscripts

p	particle
g	gas
max	maximum
min	minimum
tot	total
$t_{8/5}$	cooling time (from 800 to 500 °C)

Abbreviations

2D	Two Dimensional
3D	Three Dimensional
A	Austenite
A_{c1}	Peak temperature in lower critical point
A_{c3}	Peak temperature in upper critical point
AHSS	Advanced High Strength Steel
AM	Additive Manufacturing
Ar	Argon
ASME	American Society of Mechanical Engineering
ASTM	American Society for Testing and Materials
af	Acicular Ferrite
B	Bainite
BM	Base material
B_L	Lower Bainite
B_s	Bainite start temperature
C_2H_6O	Ethanol
C_3H_6O	Acetone
CCT	Continuous Cooling Transformation

CEV	Carbon Equivalent
CFD	Computational Fluid Dynamics
CGHAZ	Coarse Grain Heat Affected Zone
CLR	Crack Length Ratio
CMT	Cold Metal Transfer
CO ₂	Carbon dioxide
CP	Complex Phase steel
CTE	Coefficient Thermal Expansion
Cr	Chromium
Cu	Copper
DC	Direct Quenched
DIC	Digital Image Correlation
DOE	Design of Experiments
DP	Duplex Phase steel
EBSD	Electron Backscatter Diffraction
EBW	Electron Beam Welding
ECSC	European Coal and Steel Community
EDS	Energy –Dispersive X-ray spectroscopy
EFG	Element Free Galerkin
EFREA	Energy-efficient systems based on Renewable Energy for Arctic conditions
EHSS	Extra High Strength Steel
ERW	Electric Resistance Weld
Exp.	Experimental
F	Ferrite
Fe	Iron
FEM	Finite Element Model
FGHAZ	Fine Grain Heat Affected Zone
GB	Granular Bainite
GMAW	Gas Metal Arc Welding
GTAW	Gas Tungsten Arc Welding
HAZ	Heat Affected Zone
HF	Hot Formed steel
HSLA	High Strength Low Alloy steel
HSLAB	High Strength Low Alloy Bainitic Steel
HSS	High Strength Steel
HV	Vicker Hardness
ICHAZ	Inter Critical Heat Affected Zone
IIW	International Institute of Welding
IL	Illinois state (USA)
ISO	International Organisation for Standardization
ITW	Illinois Tool Works Inc
LBW	Laser Beam Welding
LUT	Lappeenranta-Lahti University of Technology
M	Martensite

MAG	Metal Active Gas
MIG	Metal Inert Gas
Mn	Manganese
Mo	Molybdenum
Ms	Martensite start temperature
MSt	Mild Steel
N	Nitrogen
Nb	Niobium
NDT	Non-Destructive Testing
Ni	Nickel
N _o .	Number
Num.	Numerical
O	Oxygen
OM	Optical Microscopy
Pr	Pearlite
PF	Polygonal Ferrite
PWHT	Post Weld Heat Treatment
pWPS	Pre Welding Procedure Specification
QT	Quenching and Tempered
RA	Retained Austenite
SAW	Submerged Arc Welding
SCHAZ	Sub-Critical Heat Affected Zone
SEM	Scanning Electron Microscopy
SFS	Finnish Standards Association
Si	Silicon
SMAW	Shielded Metal Arc Welding
TEM	Transmission Electron Microscopy
TCS	Thermal Cycle Sensor
TIG	Tungsten Inert Gas
TMA	Tempered Martensite
TMCP	Thermo-Mechanically Controlled Processing
TRIP	Transformation Induced Plasticity
TS	Tensile Strength
TTT	Time Temperature Transformation
TWIP	Twinning Induced Plasticity
UHSS	Ultra High Strength Steel
UTS	Ultimate Tensile Strength
V	Vanadium
VHSS	Very High Strength Steel
WF	Widmanstätten Ferrite
WM	Weld Metal
WP	Welding Position
WPS	Welding Procedure Specification
WS	Weld Sample

WZ	Weld Zone
YS	Yield Strength
Zn	Zinc

1 Introduction

The research presented in this thesis was completed in the research Group of Laser Materials Processing and Additive Manufacturing and Laboratory of Welding Technology of LUT University between 2016 and 2020. This thesis aims to contribute to knowledge of material science through improved characterization of dissimilar weld joints of high strength steel (HSS). This thesis focuses on thermal analysis of dissimilar weld joints of high-strength and ultra-high-strength steels used in the energy sector.

This doctoral thesis contributes to academic research and industrial practice by providing valuable comparative data acquired by both numerical modelling and experimental work. The data generated enable improvements to be made in dissimilar welding of HSS for use in regions with extreme weather conditions. Additionally, the research provides recommendations (especially for industrial use) for selecting optimum heat input and a suitable filler wire for welding dissimilar grades of HSS and UHSS by GMAW. The results presented in this thesis contribute to improved knowledge of and more accurate characterisation of the microstructural constituents in the heat-affected zone (HAZ) of dissimilar HSS/UHSS welded joints. The results were obtained by numerical analysis of thermal cycles and experimental data produced during welding of S690QT-TMCP and S700MC-S960QC steels.

The research work undertaken in this doctoral thesis is presented in three parts: a review of previous studies on the weldability of dissimilar HSS and UHSS joints and the effect of heat input on the microstructure and mechanical properties of such joints. The second part focuses on the numerical analysis of dissimilar welds of HSS. Data obtained were used to estimate the heat input which would produce reasonable strength in the HAZ. The third part of the study is based on analysis of experimental results.

1.1 Research background

Dissimilar weld joints bring many advantages and permit improvements in the strength-to-weight ratio, notably when using HSS and UHSS grade steels. One issue that needs careful consideration when welding HSS is the effect of the heat input and filler wire composition (depending on the welding process) on the weld quality. Additionally, understanding of the influence of the production processes used to manufacture high strength steels, their chemical composition and mechanical properties would be beneficial for improving the performance of the weld joint as well. HSS is considered viable for use in Nordic and Arctic regions because its ability to withstand the cold temperatures found in northern areas. As regards the sub-Saharan region, notably in Central Africa, the ambient temperature is about 28 to 30 °C. Use of HSS instead of conventional structural steel can improve the strength and durability of structures, which in turn reduces future maintenance costs.

From the research background, it becomes evident that achieving the research goal requires competence in four main areas: 1) weldability of dissimilar high strength and ultra-high-strength steel, 2) understanding of the effect of heat input on dissimilar weld joints, 3) expertise in microstructure characterisation, and 4) familiarity in the testing and analysis of the mechanical properties of welded joints.

1.1.1 Weldability of dissimilar welds of high strength steel

One of the definition of *weldability* is defined by (Lippold, 2015) as “*the capacity of a material to be welded under fabrication conditions imposed into a specific, suitable designed structure and to perform satisfactorily in the intended service*”.

The “good weldability” of steel can be justified as a welded sample without any dangerous consequences occurring is said to possess. Phenomena that determine weldability include weld imperfections and defects, crack propagation, microstructural constituents in the HAZ, and the mechanical properties of the welded joint. A definition of the weldability of high strength steel (HSS) or ultra-high-strength steel (UHSS) requires a good understanding of the properties of the base materials. The HSS and UHSS used in this study are manufactured by thermomechanical controlled (TMCP) and quenched and tempered process (QT) and the steels have yield strength in the range of 690 MPa to 960 MPa. TMCP steel has a lower carbon content than QT steel, giving the material better weldability. The base material characteristics of the studied steels are shown in chapter 3 of the thesis. The term “*dissimilar joint*” refers to a welded joint of two alloys (with or without filler materials) having different chemical composition and mechanical properties. In dissimilar welding of HSS, the most important aspects that need to be considered are groove geometry, mechanical properties of both materials, and the welding parameters (Chan, 1984). When welding dissimilar joints using filler wire, the most significant consideration is the composition of the filler wire. The composition of an appropriate filler wire depends on the base materials (BM) and their dilution rate. Selection of the welding process requires special attention because suitable values of current, voltage, welding speed, filler wire feed speed and torch position are process specific. Heat input has a direct effect on the weld joint, and changes in heat input will have a direct influence on the microstructure of the welded joint.

1.1.2 Effect of heat input on dissimilar weld joints

Studies of the HAZ of dissimilar HSS welded joints have indicated the importance of controlling the following aspects: the thermal cycle after welding, microconstituents in the different zones, and the mechanical properties of the weld joint. A numerical model for weld heat sources using a double ellipsoidal power density distribution was developed by (Goldak, 1984) (Karkhin, 2015). This model of double ellipsoidal power density is used to simulate heat distribution in the weld pool applicable to arc welding. Especially, this model is used to simulate the thermal cycle within the longitudinal and transversal direction of the weld pool. Since the early 2000’s, considerable progress has been made

in arc welding simulation by using three-dimensional heat propagation (Chattopadhyay, 2000). However, only a small number of numerical model-based studies applicable to dissimilar welds have been published. In 2014, (Chan, 1984) developed a transient temperature model for laser beam welding of butt joints of dissimilar HSS. Chan evaluated in his study stress and distortion of the welded joint using different values of heat input. However, weld geometry and resulting microconstituents were not discussed in the study of Chan (Chan 1984). The effect of heat input on the geometry of a weld joint using S960QL-steel was analysed by (Gaspar, 2019). It was found that fast cooling rate (lower heat input) caused incomplete penetration and crack propagation (cold crack) due to a lack of heat propagation. Lower cooling rate (higher heat input) increased softening in the HAZ of the weld joint, allowing a crack propagation along the weld zone (Gaspar 2019).

1.1.3 Microstructure characterisation of dissimilar weld joints

Welding of HSS, especially high strength low alloy steels (HSLA), is complicated for many reasons: their sensitivity to excessive heat input, the need to choose a filler with a suitable composition, and the effect of joint geometry specifics. The higher strength of HSLA steels originates from the manufacturing process used. These steels have low carbon content, which is good for weldability. The principal microstructural constituents defining the properties of HSLA steels are the proportion of ferrite (F), pearlite (P), bainite (B) and martensite (M) during the cooling phase. The volume fraction of the different microstructural phases depends, not only on heat input, but also on the composition of the base material (BM) and filler wire. Investigation of microstructural constituents when welding HSLA steel was performed by (Chen, 2014) for several welding processes. The authors analysed the proportion of bainite in microconstituents of HSLA steel by studying the effect of niobium (Nb) on the microstructural constituents. The Nb alloying element increased the critical transformation temperature (A_{c3}) and did not affect the strength of the joint. Weld metal microstructure with carbon content of $\geq 0.13\%$ caused a change in the proportion of martensite to upper bainite when the heat input (Q) was increased (14 kJ/cm). The results of the research were obtained using HSLA steel by (Glover, 1977), which confirmed the formation of carbides caused by residing between the ferrite laths. Evaluation of the strengthened area of the heat-affected zone caused slow cooling rate (higher heat input) was studied by (Yamamoto, 2009). The authors evaluated the dependency on the thermal cycle of the mechanical characteristics of martensite microconstituents.

1.1.4 Mechanical tests of welded joints

Several methods are used to assess the quality of weld joints. Mechanical tests include: impact, tensile, bending, hardness, and fillet weld break tests. The mechanical test methods used in this thesis were tensile testing and hardness testing. When welding dissimilar HSS and UHSS, a hardness test is required to evaluate hardenability of the joint, which allows avoidance of crack defects due to high or low heat input. Tensile

testing allows softening in the weld joint to be evaluated and stress propagation due to high or low cooling rate to be avoided.

1.2 Motivation and objective of the research

Industrial companies nowadays are increasingly using dissimilar welded joints of high-strength and ultra-high-strength steel materials in manufacturing of their products. Dissimilar welded joints improve product quality, permit benefits to be gained from different materials, enable innovative design, and provide enhanced structural stability. As an example of the use of dissimilar welded joints in modern manufacturing, Figure 1.1 shows the body-in-white of a Volvo XC90 SUV (Huetter, 2017). Joints between different steel grades are highlighted and numbered in Figure 1.1.

The HAZ of a weld of dissimilar high strength low alloy steel (HSLA) steels is particularly sensitive in the welding operation. In this area, the welded structure needs to keep structural stability. The microstructure characterisation such as austenite grain geometry, microstructural constituents and alloying element composition will have an interest in the welding of dissimilar HSS. To estimate the weldability of two different materials, understanding the relationship between microstructural changes and welding parameters is essential. In the case of HSLA steels, the alloying elements play an important role in ensuring the desired mechanical properties because of the low carbon content.

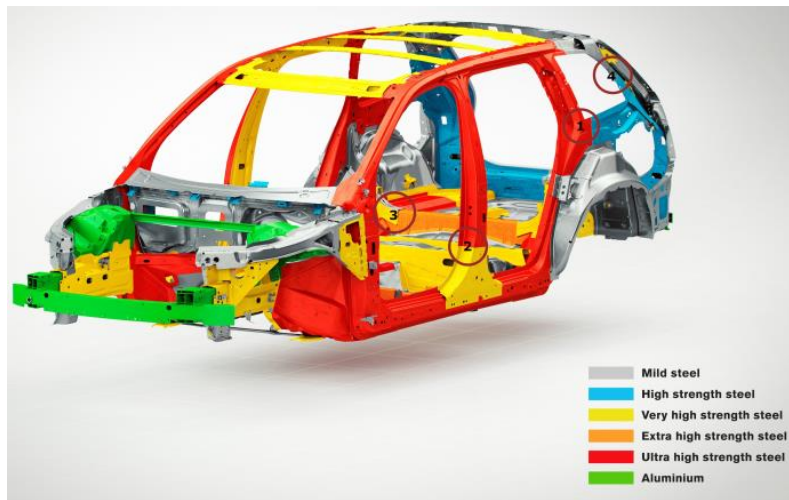


Figure 1.1: Exterior body of Volvo XC90 as an example of the use of dissimilar welds of mixed metal materials for weight reduction: (1) UHSS-HSS, (2) VHSS-UHSS, (3) EHSS-VHSS, and (4) MSt-HSS (Huetter, 2017).

The research objective in this thesis is to develop accurate data for estimation of the proper cooling rate when welding dissimilar high-strength and ultra-high-strength steel. The data will enable: (i) the thermal cycle to be correlated with the microstructural constituents in the heat-affected zone of the base materials; (ii) the phase change in the solid-state of austenite grains of the welded joint to be determined; (iii) the welding stresses in the welded dissimilar HSS joint to be minimised; and (iv) the impact of cooling rate in the alloying element forming in the weld metal area.

Welding HSS grades using fusion welding creates a number of typical short temperature cycles close to the fusion line. In the first phase, the temperature increases very fast and decreases gradually during the cooling phase. The thermally induced changes depend on the alloying element composition formed between the filler wire and the base material. The different thermal changes in the microstructure will lead to increased hardness and the development of tensile strength in the welded joint.

1.3 Research questions

Based on the research problem and the objective, this thesis will address the following research questions:

- 1) What is the state-of-the-art of knowledge and experimental investigations regarding the effect of heat input on the microstructure and mechanical properties of dissimilar HSS and UHSS welded joints?
- 2) What is the influence of the transient thermal effects on the microstructure and hardenability of dissimilar high and ultra-high-strength steels?
- 3) What is the influence of heat input and use of an undermatched filler wire on the microstructure and mechanical properties of dissimilar HSS and UHSS welded joints?
- 4) What is the effect of heat input and use of an overmatched filler wire on the microstructure and mechanical properties of dissimilar HSS/UHSS welded joints?
- 5) How can welding of dissimilar advanced and ultra-high-strength steels improve strength and microstructural constituents in the HAZ?

Figure 1.2 shows the research objective of this thesis and the research questions and illustrates the connections between the research questions and the publications included in this thesis.

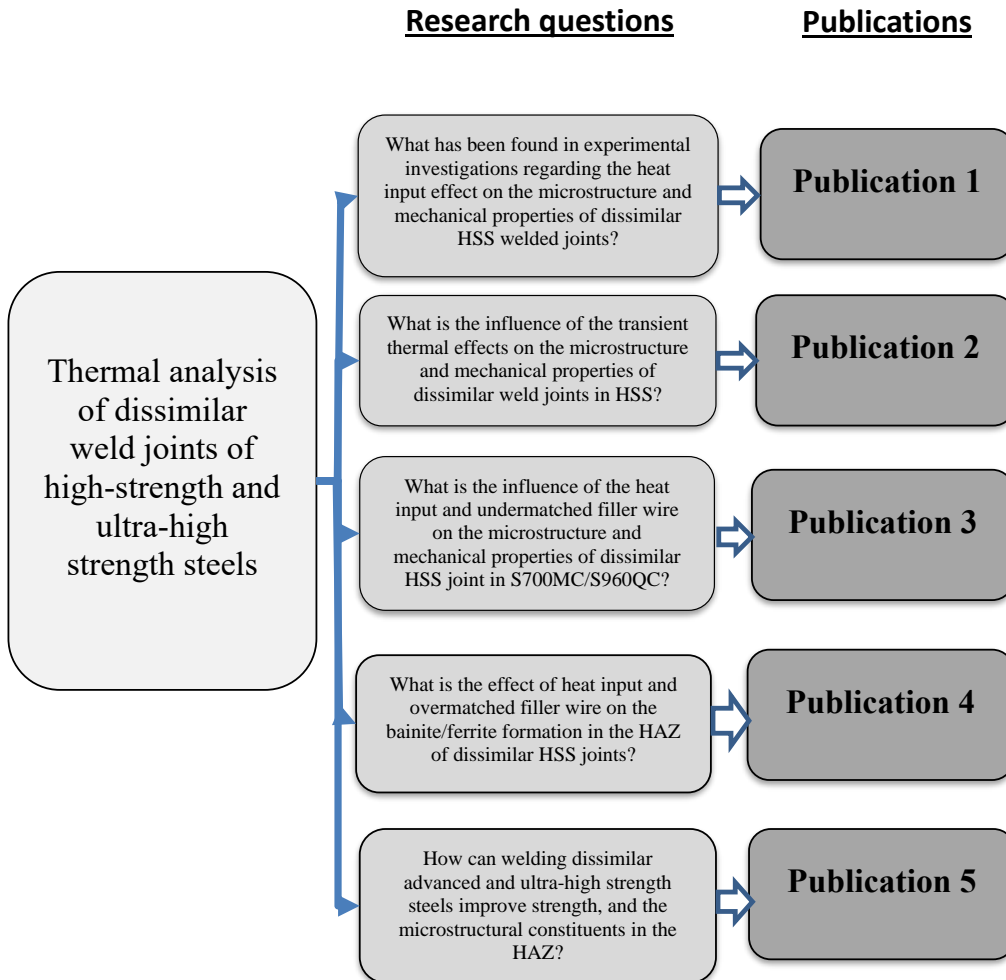


Figure 1.2: Research objective and research questions of the study and connections to the publications in this thesis.

- i. **What has been found in experimental investigations regarding the heat input effect on the microstructure and mechanical properties of dissimilar HSS welded joints?** The analysis in this thesis will focus on state-of-the-art knowledge and recent research to address this question. The findings provide an understanding of the influence of welding parameters on the microstructural composition and resulting mechanical properties of dissimilar HSS welded joints.
- ii. **What is the influence of the transient thermal effects on the microstructure and mechanical properties of dissimilar weld joints in**

- HSS?** This question focuses on the study of numerical and experimental investigation of the effect of heat input on the microstructure and mechanical properties of weld joints of 690-MPa QT and TMCP steel.
- iii. **What is the influence of the heat input and undermatched filler wire on the microstructure and mechanical properties of dissimilar HSS joint in S700MC/S960QC?** This research question addresses the issue of heat input and the use of undermatched filler wire to minimise softening in the HAZ of dissimilar S700MC/S960QC welds.
 - iv. **What is the effect of heat input and overmatched filler wire on the bainite/ferrite formation in the HAZ of dissimilar HSS joint?** This research question addresses the issue of heat input and the use of overmatched filler wire in dissimilar HSS joints. The aim is to characterise the formation of bainite/ferrite and martensite in the HAZ of dissimilar S700MC/S960QC welds and assess the composition of alloying elements in the weld.
 - v. **How can welding dissimilar Advanced and Ultra high strength steels improve strength, reduce the incomplete carbide dissolution, and improve the microstructural constituents in the HAZ?** This research question considers optimal welding processes to improve the weldability of dissimilar HSS of S700MC/S960QC welds.

1.4 Scope and limitations of the thesis

This thesis is based on the following hypotheses:

First hypothesis in this thesis is that a model based on element-free Galerkin methods in ANSYS software can be developed to calculate the thermal cycle of dissimilar HSS and UHSS welds. The cooling time can be evaluated from the thermal cycle and the cooling rate calculated as a function of the cooling time and welding parameters. The aim is to generate an appropriate cooling rate for welding a dissimilar joint of S690 and S960 QT and TMCP steels. The comparison of numerical data produced with experimental results was done.

Second hypothesis consists of the microstructural constituents in the HAZ that can be characterised after GMAW processing of the joint using SEM images, EDS X-ray spectroscopy, and ImageJ evaluation of the volume fraction. This part of this thesis provides a larger understanding of the HAZ, in particular, the microstructural constituents in the HAZ and the alloying element composition in the weld joint, which will enable improvement in the weldability of dissimilar HSS and UHSS joints.

Third hypothesis is that the results from mechanical tests in this thesis of the performance of the welded samples, for example, Vickers hardness measurements and tensile strength tests, will provide knowledge enabling improvements to be made to the resistance against crack propagations in dissimilar HSS and UHSS joints.

Fourth hypothesis includes the information gained from the above analysis of this thesis can be used for selection of optimal welding parameters that improve the mechanical properties and the weldability of dissimilar HSS welded joints.

This thesis analyses thermal cycles using numerical modelling and experimental investigation. Use of numerical modelling allows reduction in the number of samples needed for physical testing and thereby reduces welding costs. The flowchart in Figure 1.3 shows the steps taken to reach the goal of the study.

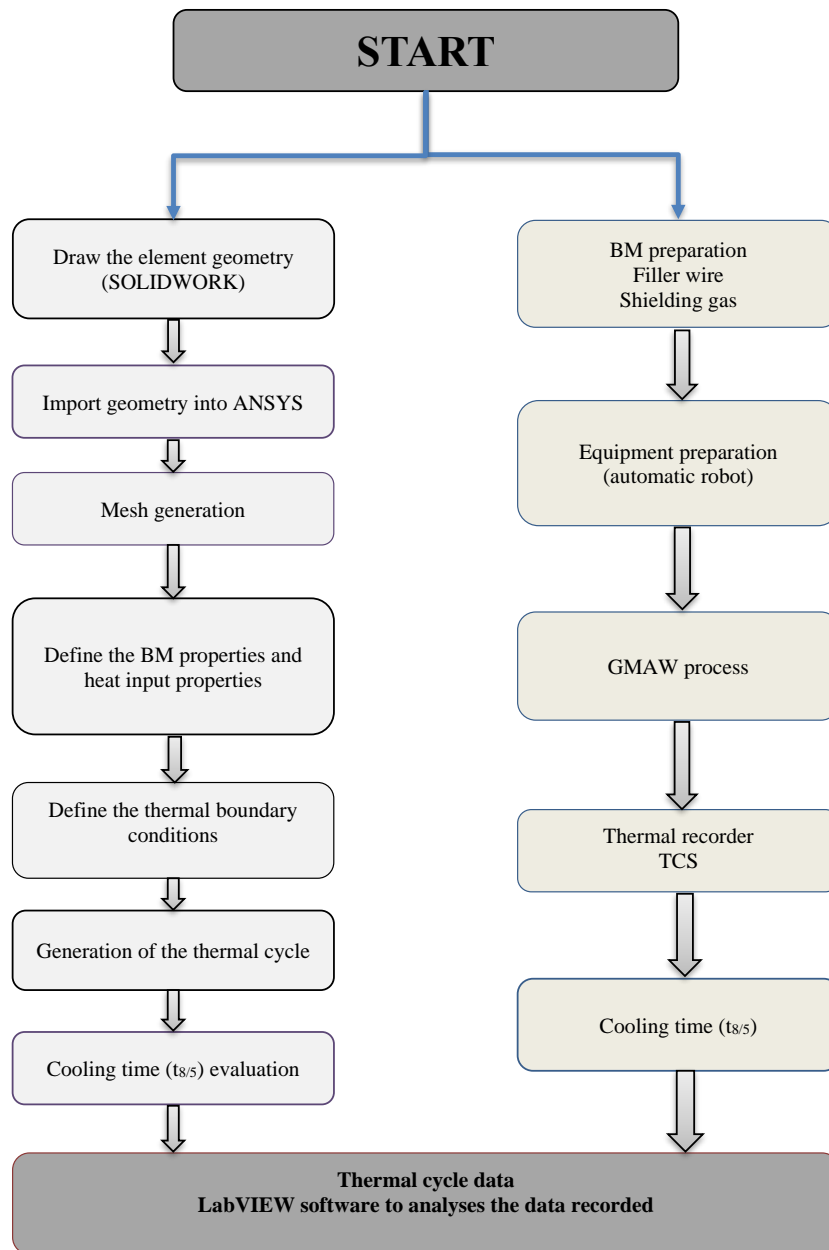


Figure 1.3: Design process for acquiring the thermal cycle data.

In all the tests in this thesis, the joints had V-geometry and the process used was GMAW. Heat dissipation due to conduction, convection, and radiation was investigated using ANSYS19.2 finite element software.

1.5 Scientific contribution to material and welding technology

The scientific contribution of the research carried out in this thesis can be described as follows:

The first contribution is an analytical model based on an element free Galerkin method is developed and an extensive database built in order to predict thermal cycles applicable to dissimilar HSS welded joints. The proposed model in this thesis decreases the number of experiments thereby reducing the manufacturing time and production costs.

In the second contribution, the model in ANSYS software is developed further to enable simulation of thermal cycle of dissimilar materials that can be welded, which will enable prediction of an optimal cooling rate for the welding process.

The third contribution develops a methodology for characterisation and measurement of the volume fraction of bainite (B), ferrite (F), martensite (M), and retained austenite (RA) are implemented. The volume fraction measurements were developed using continuous cooling transformation (CCT) diagrams and SEM images, which were uploaded into ImageJ software. The results were satisfying.

The fourth contribution is based on Scanning electron microscopy (SEM) images, which are analysed using electron dispersive spectroscopy (EDS X-ray) to evaluate the alloying element composition in the weld metal and the CGHAZ, which affects precipitation strengthening.

The fifth contribution develops a Vickers-hardness measurement methodology, which is proposed for evaluation of the softened area, which can affect the strength of the HAZ when welding dissimilar HSS of the range of 690 to 960 QT and TMCP steel. The results clearly show the impact of heat input and weld metal in the HAZ of the dissimilar weld joint and can demonstrate how the performance of the weld joint is dramatically affected. Tensile test measurements confirmed the critical role of heat input, which can cause brittle defects, crack propagation and fragility of the weld joint.

Sixth contribution focus on the choice of an optimal welding process was operated, which leads to improving the weldability of dissimilar HSS weld joint.

The research publications (article I-V) produced as part of the doctoral studies examined dissimilar welding of HSS and UHSS. Several analyses were carried out on different samples, most of which were thermomechanical controlled steels and quenched and tempered steels. The welding process and filler wire composition were selected based on requirements from the steel production companies. The filler wire used in the thesis had two characteristics: undermatched filler wire and overmatched filler wire. Their choice was a function of the carbon equivalent, which meets applicable standards. The use of materials that do not have the same chemical and mechanical characteristics can make the welding process somewhat problematic. Not only materials in this thesis are different, but also mechanical and chemical characteristics of these materials are different as well and also manufacturing processes (QT, TMCP). The impact of the wrong choice of heat

source will be observed in the effects on hardness, strength, and deformation. Additionally, irregularities will be seen in the microstructural constituents in some areas of the weld joint.

This thesis suggests procedures and methods necessary to prevent the formation of undesirable phases in the weld joint and defects in dissimilar welds of high strength and ultra-high-strength steel. The numerical analysis of the thermal cycle of the welded materials, information about their mechanical properties and microstructural constituents, and mechanical testing and microstructural analysis in the laboratory provide a more complete picture of the weld and allow satisfactory results to be achieved in welding operations. The study focuses on HSS series 690, S700 and UHSS series 960 (quenched tempered and thermomechanical control process).

Furthermore, this thesis helps to address the problem of the large number of expensive experimental analyses currently required by providing a greater understanding of the phenomena involved and linking thermal input effects with the mechanical properties and microstructure constituents of dissimilar high-strength steel welds. The study examines the effects of heat input from welding processes on welded structures, welding of HSS and UHSS based on different welding standards, codes and procedures, manufacturing processes used in production of high-strength and ultra-high-strength steels, and microstructure characterisation and mechanical analysis. To this end, the study presents data for a numerical model of the thermal cycle, microstructural constituents in the HAZ, tensile stress, and Vickers hardness of butt joints of dissimilar welds of 690-MPa of QT/MC-steels and S700MC/S960QT. The numerical data analysis and experimental test data comprise the results presented in the publications included in this thesis and previously unpublished results from measurements and tests are introduced in sections 4 and 5.

1.6 Structure of the thesis

The dissertation consists of two parts. The first part gives an overview of the state of the art of dissimilar welding and provides the background of the study. In addition, it provides a summary of main findings of publications. The peer-reviewed publications form the second part of the thesis.

Table 1.1: Brief overview of the chapters

Part I	
Chapter	Contribution to the thesis
Introduction	This chapter provides the background and presents the relevance of the study. The research topic is approached from three points of view: heat transfer effect on the microstructure and mechanical properties of HSS and UHSS welds; numerical analysis with ANSYS software to model thermal transfer in dissimilar HSS welds; and characterisation of microstructure transformations in the HAZ of a dissimilar weld joint.
State of the art	This chapter reviews the state of the art in welding of dissimilar HSS and UHSS, showing numerical analysis methods used to estimate optimum thermal cycles for improving strength in the HAZ and sub-zones of HAZ. The effect of heat input and filler wire composition on microstructure and mechanical properties of dissimilar QT and TMCP steel welds is studied as well.
Methods	This chapter introduces the methodology used in the thesis. The welding procedure used, and the chemical composition of the base materials and filler wire are specified. The methods for gathering the experimental data and tools used for analysing the findings are described.
Results	This chapter presents findings of numerical analysis and experimental tests and summarises results in the publications that form the second part of this thesis.
Overview of the publications	This chapter discusses the published papers and recounts the research aims and findings.
Discussion	The chapter discusses data regarding the research tasks and objectives.
Conclusions	This chapter concludes the first part of the thesis by presenting an approach for optimum weld quality in dissimilar welds of HSS and UHSS. The chapter further presents the weld model required for development of a model of thermal cycle that can ensure favourable microstructure behaviour and low softening in the weld joint.
Part II: Published papers	

1.7 Social and environmental impact

Industrial construction of power plants, automotive vehicle production, and industrial plants in the oil industry, and other industries in the energy sector, have considerable social and environmental impact. The use of dissimilar welding of HSS in industries can bring considerable benefits, for example, in motor vehicle preproduction, safety can be improved because of greater strength and more predictable behaviour in crash scenarios. To combine high strength and low weight, a dissimilar weld joint should improve the strength and hardness of the welded joint.

In an industrial application, environmental and climatic conditions need to be considered, for example, a major problem in parts of Central Africa is usually high humidity, with an average ambient temperature of 30 to 40 °C. Based on the results of this research, it can be surmised that HSS manufactured with QT or TMCP processes and welding of such steels will enable an improvement in the life-cycle of industrial structures. These efficiency improvements in turn will enable oil industry companies and other industry players to consider a greater presence in the sub-Saharan area, which will have social and employment benefits.

2 State of the art of dissimilar welding of HSS-UHSS

This chapter presents the classification of HSS, AHSS, and UHSS, the weldability of dissimilar HSS and UHSS, a review of the heat input effect on the microstructure of dissimilar welded joints and resulting mechanical properties based on the literature. The information in this section supplements the review study in publication I. Topics addressed include the structural composition of HSS and UHSS, the heat source formulation, the temperature gradient formulation, the propagation of heat in the weld joint using a simulation model, the effect of cooling rate on joint strength, and the microstructure characterisation depending on the heat input and the type of filler wire used.

2.1 Classification

HSS can be classified into three types: a classification based on chemical composition, mechanical performance (material strength), and production processes. The classification based on chemical composition takes into account the percentage of the alloying element content. In the literature, it can be evaluated by (Glover, 1977) as follows:

- High strength low alloy (HSLA) steels have low alloying element content, the weight percentage of iron can reach up to 96 %.
- High strength low carbon bainitic steels (HSLAB) have niobium (Nb) as the primary alloying element beneficial to the formation of bainitic microstructure.

(Fang, 2009) described the effect of alloying element contents in the precipitation hardening. The higher content of nitrogen in HSS when welding increased the formation of martensite-austenite island, which is worse for the toughness and strength of weld joint. By classifying, based on the thermomechanical production process, (Mvola, 2016), (Bayock, 2019) described the types of HSS, some of which had undergone heat treatment during the manufacturing process. The following HSS and UHSS are classified according to the standards: (EN 10025-6 2009), (EN 10025-6:2004+A1 2009), and (SFS-EN-10149-1 2013).

The transformation induced plasticity steel (TRIP) is principally composed by the formation of ferrite, martensite, bainite in the microstructure. Twinning induced plasticity (TWIP) contains a large amount of manganese (Mn). A large amount of Mn in the microstructure can increasing the strength of the weld joint at the higher temperature which can cause a crack propagation in the weld joints. The microstructure mainly consists of a high amount of martensite and ferrite. Dual-phase (DP) steel is based on ferrite and martensite microstructural constituents. The presence of hard martensite in the microstructure increases the strength of the material. Figure 2.1 shows the mechanical properties and formability of steels having high strength.

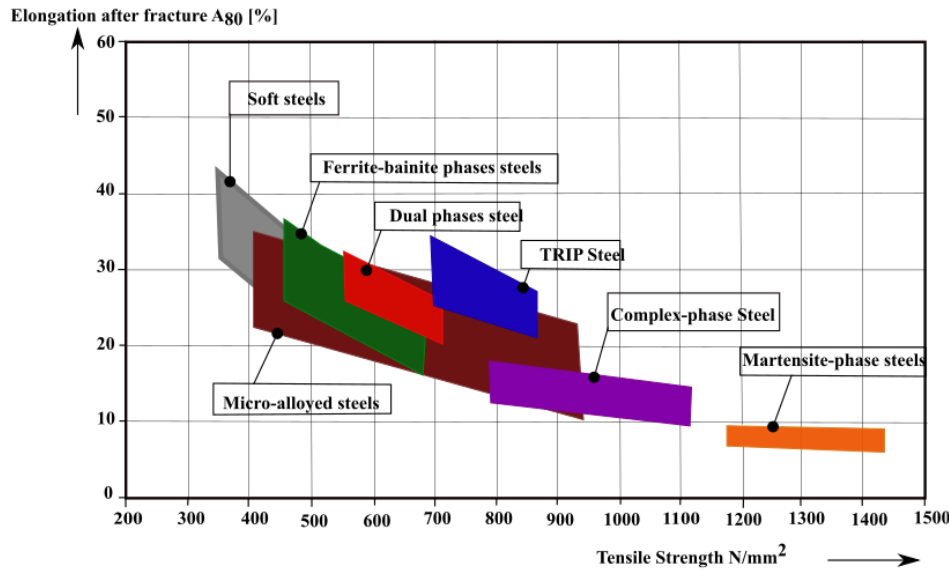


Figure 2.1: Tensile strength and elongation of different HSS grades (Schulze, 2009).

The third classification is according to the mechanical properties of the materials. According to (Mvola, 2016), the steel can be classified as HSS when the yield point (R_e) is in the range of 360 to 690 MPa. Steels with a yield strength of 690-780 MPa are considered to be advanced high-strength steels (AHSS). Steels with yield strength in the range of 780-960 MPa are called ultra-high-strength steel (UHSS).

2.2 Influence of heat input on weldability of dissimilar HSS joints

The transient thermal condition of the weld is an essential factor when welding dissimilar joints. Many types of welding processes have been applied to join different materials together, with the same goal to maintain the optimal mechanical properties of weld and parent materials.

The heat input is one of the most important process parameters affecting the weldability of two different grades of HSS. Studies conducted by (Michailov, 2016), (Cho, 2013), and (Gouldn, 2006) investigated the heat flow formation and its effects on the microstructure of the weld. Experimental data gathered by (Pirinen, 2015) estimated the impact of heat input on the mechanical properties of the weld joints of HSS with a tensile strength of 821-835 MPa. (Coric, 2011) evaluated the influence of the heat input on the hardness and toughness of the heat-affected zone of HSS. Heat input calculation for GMAW

(Michailov, 2016) developed a heat input Q formulation based on the welding machine power per unit length (kJ/cm), which is shown in equation 2.1.

$$Q = \frac{P}{v}. \quad (2.1)$$

Alternatively, P (kW) represents the power source, v (cm/s) being the speed with the heat source moves along the weld joint. The analyses are performed using arc welding, in which the evaluation of the power source was based on the current I and voltage U of the arc, the equation is

$$P = UI. \quad (2.2)$$

When the two equations are combined, the (see eq. 2.3) equation for heat input Q becomes:

$$Q = \frac{UI}{v}. \quad (2.3)$$

Considering certain losses such as heat dissipation and thermal convection, it becomes important to define the part of the heat input that is used in the melting process.

(Radaj, 2003) generated some approximate values for arc efficiency influencing the final value of the heat source (presented in Table 2.1). Based on analysis of experiments, the exact part of heat transferred to the weld zone was defined to be $\eta_{eff} \cdot \eta_{eff} \leq 1$.

Table 2.1: Approximate values of arc efficiency (D. Radaj 2003)

Welding method	SMAW	GMAW	GTAW	SAW	EBW	LBW
η_{eff}	0.65-0.90	0.65-0.90	0.30-0.50	0.85-0.95	0.95-0.97	0.30-0.95

Equation (2.4) gives the final value of the required heat input Q_1 for electric arc weld:

$$Q_1 = \eta_{eff} Q = \eta_{eff} \frac{UI}{v}. \quad (2.4)$$

In real-time, the propagation of the temperature gradient is following a trajectory that can take several forms. In this section, several analytical methods for assessing temperature gradient in welding are discussed. (Karkhin, 2015) (Michailov, 2016) have developed several fundamental solutions, which define the expressions of temperature gradients. Altogether, four models of temperature gradient were developed: momentary temperature gradient, continuous stationary temperature gradient, moving temperature gradient, and rapidly moving temperature gradient. In Table 2.2, the different equations that characterise the temperature gradient movement in the weld joint are shown. Table 2.1

shows equations used to describe the types of semi-infinite solid, point source in an infinite layer, line source in an infinite plate, area source in an infinite rod.

Table 2.2: Heat source formulation in the literature (Goldak, 1996) and (Chen, 2014)

Temperature gradient	Model of temperature field	Equation and comments
Momentary temperature source	Momentary source point on a semi-infinite solid	$T_{(x,y,z,t)} - T_0 = \frac{2Q_0}{c\rho(4\pi at)^{3/2}} e^{-\frac{R^2}{4at}} \quad (2.5)$ <p>when $x = y = z = 0$ the temperature increase is</p> $T_{(0,0,0,t)} - T_0 = \frac{2Q_0}{c\rho(4\pi at)^{3/2}} \quad (2.6)$
	Momentary point source in an infinite layer	$T_{(r,z,t)} = \frac{Q_0}{c\rho(4\pi at)^{3/2}} e^{-\frac{r^2}{4at}} \sum_{i=-\infty}^{\infty} \sum_{j=-1,1} e^{-\frac{(z-j\zeta-2ih)^2}{4at}}, \quad (2.7)$ <p>where</p> $r^2 = (x - \xi)^2 + (y - \eta)^2 \quad (2.8)$ <p>The equation will be changed when the heat source is located on the layer in the frame origin. In that case, $\xi = \eta = \zeta = 0$, the equation becomes</p> $T_{(r,z,t)} = \frac{2Q_0}{c\rho(4\pi at)^{3/2}} e^{-\frac{R^2}{4at}} F(z, t) \quad (2.9)$ <p>with</p> $F(z, t) = \sum_{i=-\infty}^{\infty} e^{-\frac{ih(ih-z)}{at}}. \quad (2.10)$
	Momentary source point in an infinite plate	$T(r, t) - T_0 = \frac{Q_1}{c\rho(4\pi at)} e^{-\frac{r^2}{4at} - bt}, \quad (2.11)$ <p>where $r^2 = x^2 + y^2$</p> <p>and</p> $b = (\alpha_1 + \alpha_2) / cph,$

		<p>b represents the heat exchange due to the exchange and thermal radiation when the cooling time is long.</p> <p>When $r = 0$,</p> $T(0, t) - T_0 = \frac{Q_1}{c\rho(4\pi at)} e^{-bt} . \quad (2.12)$
	Momentary area source in an infinite rod	$T(r, t) - T_0 = \frac{Q_2}{c\rho(4\pi at)^{1/2}} e^{\frac{r^2}{4at} - bt}, \quad (2.13)$ <p>where</p> $b = \alpha p / (c\rho A) . \quad (2.14)$ <p>p is a perimeter, and A is the area of the rod cross-section.</p> <p>If $x = 0$, the temperature will change itself in the cross-section and become</p> $T(0, t) - T_0 = \frac{Q_2}{c\rho(4\pi at)^{1/2}} e^{-bt} . \quad (2.15)$
Continuous stationary temperature source	Continuous source point on a semi-infinite solid	$dT(R, t) = \frac{2q_0(\tau)d\tau}{c\rho[4\pi a(t-\tau)]^{3/2}} e^{\frac{R^2}{4a(t-\tau)}} (t - \tau) , \quad (2.16)$ <p>where q_0 is a heat input power.</p> <p>When $q_0(\tau) = q_0 = const$, the temperature change becomes</p> $T(R, t) - T_0 \int_0^t \frac{2q_0}{c\rho[4\pi a(t-\tau)]^{3/2}} e^{\frac{R^2}{4a(t-\tau)}} d\tau = \frac{q_0}{2\pi\lambda R} \left[1 - \Phi\left(\frac{R}{\sqrt{4at}}\right) \right]. \quad (2.17)$ <p>Due to the Gaussian probability, integral Φ is evaluated as</p> $\Phi(u) = \frac{2}{\sqrt{\pi}} \int_0^u e^{-u^2} \quad (2.18)$ <p>, if $\lim_{\infty} t$</p> $T(R, \infty) - T_0 = \frac{q_0}{2\pi\lambda R} . \quad (2.19)$ <p>The temperature will decrease hyperbolically with power $1/R$.</p>
	Continuous stationary point source in an	$T(x, y, z, t) - T_0 = \frac{q_0}{4\pi\lambda} \sum_{i=-\infty}^{\infty} \sum_{j=-1,1} \frac{1}{R_{i,j}} \left[1 - \Phi\left(\frac{R_{i,j}}{\sqrt{4at}}\right) \right], \quad (2.20)$

	infinite plan layer	<p>where</p> $R_{i,j} = \sqrt{(x - \xi)^2 + (y - \eta)^2 + (z - j\zeta - 2ih)^2} .$ <p>(2.21)</p>
	A continuous stationary source in an infinite plate	$T(r, t) - T_0 = -\frac{q_1}{4a\lambda} \text{Ei}\left(-\frac{r^2}{4at}\right),$ <p>(2.22)</p> <p>where Ei is the exponential integral</p> $Ei = -\int_{-u}^{\infty} \frac{e^{-u}}{u} du .$ <p>(2.23)</p>
	Continuous area source in an infinite rod	$T(x, t) - T_0 = \frac{q_2 x }{2\lambda} \left\{ \frac{1}{\sqrt{\pi}} \sqrt{\frac{4at}{x^2}} e^{\frac{x^2}{4at}} - \left[1 - \Phi\left(\sqrt{\frac{x^2}{4at}}\right) \right] \right\}$ <p>(2.24)</p>
Moving temperature sources	Moving point source on a semi-infinite solid	$dT(x, y, z, t) = \frac{2q_0 d\tau}{c\rho[4\pi a(t-\tau)]^{3/2}} e^{\frac{R_1^2}{4a(t-\tau)}}, \quad \text{where } R_1^2 = x^2 + [v(t - \tau)]^2 + y^2 + z^2.$ <p>(2.25)</p> <p>And $t - \tau$ is the heat propagation time. When $t = \infty$, the equation becomes $T(x, R, \infty) - T_0 = \frac{q_0}{2\pi\lambda R} e^{\frac{v(x+R)}{2a}}$.</p> <p>(2.26)</p> <p>Because of the stationary continuous point source $v = 0$ and $t \rightarrow \infty$, and x, the equation becomes</p> $T(R, \infty) - T_0 = \frac{q_0}{2\pi\lambda R} e^{\frac{vR}{a}} .$ <p>(2.27)</p>
	Moving point source on an infinite plane layer	$T(x, y, z, \infty) - T_0 = \frac{q_0}{4\pi\lambda} e^{\frac{v(x-\xi)}{2a}} \sum_{i=\infty}^{\infty} \sum_{j=1,1} \frac{1}{R_{i,j}} e^{\frac{vR_{i,j}}{2a}},$ <p>(2.28)</p> <p>where</p> $R_{i,j} = \sqrt{(x - \xi)^2 + (y - \eta)^2 + (z - j\zeta - 2ih)^2}.$ <p>(2.29)</p>

	Moving line source in a thin plate	$dT(x, y, t) = \frac{q_1 d\tau}{c\rho[4\pi a(t-\tau)]} e^{\frac{[x+v(t-\tau)]^2+y^2}{4a(t-\tau)} - b(t-\tau)} \quad (2.30)$ <p>The integration of the equation from $\tau = 0$ to $\tau = t$, the equation becomes</p> $T(x, r, t) - T_0 = \frac{q_1}{2\pi\lambda} e^{\frac{vx}{2a}} \int_0^t \frac{1}{t-\tau} e^{-\frac{r^2}{4a(t-\tau)} - \left(\frac{v^2}{4a} + b\right)(t-\tau)} d\tau. \quad (2.31)$ <p>The quasi-stationary temperature can reach when $t \rightarrow \infty$</p> <p>The equation becomes,</p> $T(x, r, \infty) - T_0 = \frac{q_1}{2\pi\lambda} e^{-\frac{vx}{2a}} K_0 \left(\frac{vr}{2a} \sqrt{1 + \frac{4ab}{v^2}} \right). \quad (2.32)$
	Moving area source in an infinite rod	$T(x, \infty) - T_0 = \frac{q_2}{c\rho v \sqrt{1 + \frac{4ab}{v^2}}} e^{\frac{v}{2a} \left(x + x \sqrt{1 + \frac{4ab}{v^2}} \right)}, \quad (2.33)$ <p>where the expression of $\sqrt{1 + \frac{4ab}{v^2}}$ is the dimension number of the heat transfer.</p>
Rapidly moving temperature sources	Rapidly moving point source on a semi-infinite solid	$T_{(r,t)} - T_0 = \frac{q_0/v}{2\pi\lambda} e^{-\frac{r^2}{4at}}, \quad (2.34)$ <p>if the substitution of $t = -x/v$, the equation becomes:</p> $T(x, r) - T_0 = -\frac{q}{2\pi\lambda x} e^{\frac{r^2 v}{4ax}}. \quad (2.35)$ <p>The weld pool length can be evaluated by substituting the melting temperature T_L and $r = 0$ as follows:</p> $L = \frac{q}{2\pi\lambda(T_L - T_0)}. \quad (2.36)$
	Rapidly moving line source in a plate	$T(y, t) - T_0 = \frac{q/(vh)}{c\rho(4\pi at)^{1/2}} e^{-\frac{y^2}{4at} - bt}, \quad (2.37)$ <p>where $b = (\alpha_1 + \alpha_2)/(c\rho h)$.</p> <p>The weld pool length L can be developed by assuming $b = 0$ and $T = T_L$</p>

		$L = \frac{1}{4\pi a} \left(\frac{q/h}{c\rho(T_L - T_0)} \right)^2 \frac{1}{v} \quad . \quad (2.38)$
--	--	---

The shape of the temperature gradient plays a significant role in welding of metal. The thermomechanical characteristics of the base materials have to be well-known to be able to define a proper heat input parameter. When producing the temperature gradient, the heat propagation creates conduction of the temperature in the weld joint. Figure 2.2 shows the thermal exchange (convection, radiation, conduction), and vaporisation occurring during welding of metals. The numerical model is presented in Figure 2.2 and schematic drawing of the experimental configuration in Figure 2.3. With GMAW, the temperature gradient and metal transfer occur from cathode to anode. In the numerical modelling of a temperature gradient, (Chattopadhyay, 2000) claimed that thermal transfer by radiation is often overlooked and confirmed the statement by showing that transfer of thermal radiation can only count as around 5% of the entire temperature gradient and should not be neglected when modelling the process. The shape showing the arc produced using GMAW process was developed by (Gilles, 2009) in Figure 2.3.

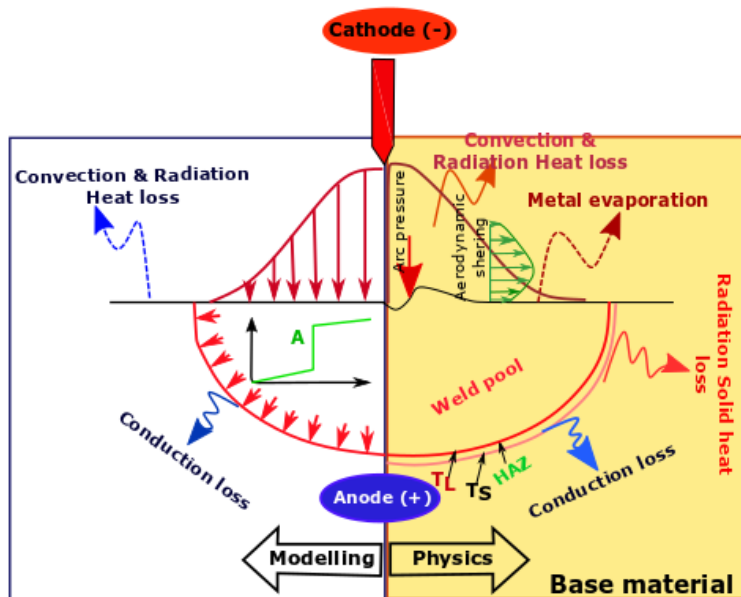


Figure 2.2: Thermal exchange in the weld joint.

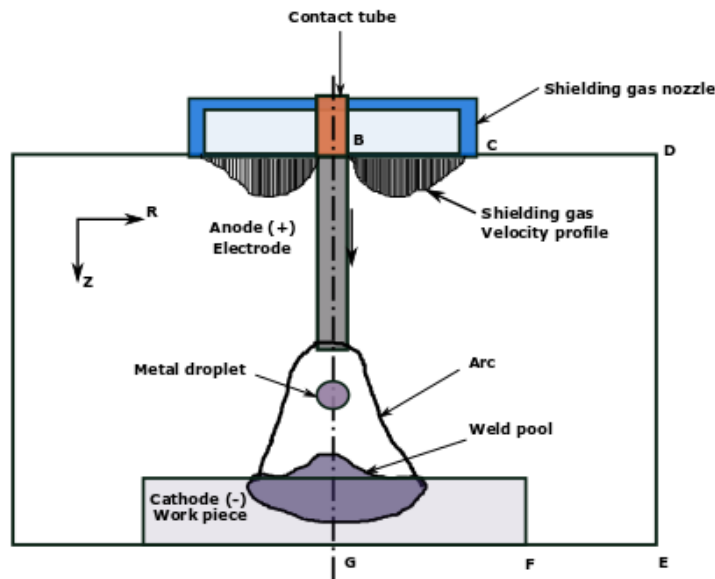
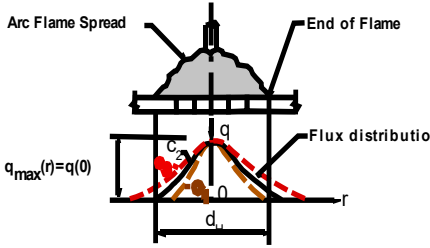
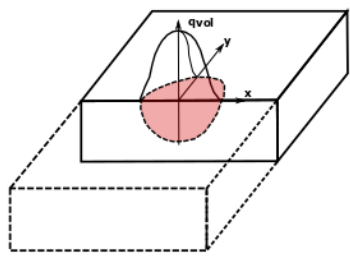


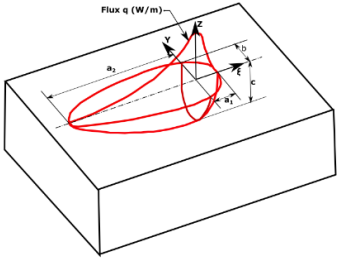
Figure 2.3: Gas metal arc welding (Gilles 2009).

(Rosenthal, 1946), (Rykalin, 1974) developed an analytical heat flow solution, which was compared with experimental data from welding processes. The results were not satisfactory, especially in the formulation of the temperature model in the fusion zone. In an attempt to eliminate these errors, (Friedman, 1978) improved Rosenthal's model by applying the finite element method (FEM) to discretise on element surface and determine a more appreciable heat flow distribution model for fusion zone in the weld joint. From the model developed by Friedman, (Pavelic, 1979) suggested the application of the Gaussian distribution model of the heat flow on the welding parts.

Focusing on the Gaussian distribution model proposed by (Pavelic, 1979), the temperature gradient follows the shape of the Gaussian distribution on a flat surface. The relationship that determines the surface thermal flow is presented in Table 2.3 (equation 1). An alternative method has been presented by (Krutz, 1978), which did not take into account the gradient temperature displacement function of the coordinates system (x , y , z). This approach was not satisfactory, especially when the experiment process was applied because the error had a huge gap with a numerical modelling. Further developing of double semi-ellipsoidal temperature gradient was conducted (Goldak, 1984), (Goldak, 1995). Based on the volumetric Gaussian model, the authors developed a double ellipsoidal power density distribution. Table 2.3 presents the temperature gradient formulation using a double ellipsoidal model, which is most used in the simulation of GMAW process.

Table 2.3: Temperature gradient formulation

Author s	Scheme	Formulation
(Pavelic , 1979)	<p>A circular disc heat source</p>  <p>The diagram illustrates a circular disc heat source on a workpiece. It shows the arc flame spread, the end of the flame, the flux distribution curve, and the radial distance r from the center. The maximum flux at the center is labeled $q_{max}(r)=q(0)$.</p>	$q(r) = q(0)e^{-Cr^2}, \quad (2.39)$ <p>where:</p> <p>$q(r)$ surface flux at radius r(W/m²)</p> <p>$q(0)$ maximum flow at the centre of the heat source (W/m²)</p> <p>C distribution width coefficient (m⁻²)</p> <p>radial distance from the centre of the heat source.</p>
(Krutz, 1978)	<p>Ellipsoidal Power Density Distribution</p>  <p>The diagram shows a 3D representation of an ellipsoidal power density distribution on a rectangular block. The ellipsoid is centered on the top surface of the block, with its major axis along the x-direction and its minor axis along the y-direction. The vertical axis is labeled q_{vol}.</p>	$q(x, \xi) = \frac{3Q}{\pi c^2} e^{-3x^2/c^2} e^{-3\xi^2/c^2} \quad (2.40)$ <p>Q =is the energy input rate (W)</p> <p>c is the characteristic radius of heat flow distribution (m), $\xi = z + v(\tau - t)$, v the welding speed (m/s), the coordinate system (x, y, z) will take the form:</p> $q = (x, z, t) = \frac{3Q}{\pi c^2} e^{-3x^2/c^2} e^{-3[z+v(\tau-t)]^2/c^2}. \quad (2.41)$

(Goldak, 1995)	<p>Double Ellipsoidal Power Density Distribution</p> 	$q(x, y, z, t) = \frac{6\sqrt{3}f_f Q}{abc\pi\sqrt{\pi}} e^{-3x^2/a^2} e^{-3y^2/b^2} e^{-3[z+v(\tau-t)]^2/c^2} \quad (2.42)$ $q(x, y, z, t) = \frac{6\sqrt{3}f_r Q}{abc\pi\sqrt{\pi}} e^{-3x^2/a^2} e^{-3y^2/b^2} e^{-3[z+v(\tau-t)]^2/c^2} \quad (2.43)$ <p>f_f and f_r are the fraction of the heat deposited in the front and rear quadrants are needed.</p> <p>The equations become beyond when $f_f + f_r = 2$.</p>
----------------	--	---

2.2.1 Numerical formulations of the heat cycle in the HAZ

All numerical models of thermal transfer in the weld joint are based on the continuity equation, the expression of the heat source (analysed in Table 2.2), the boundary conditions, thermo-mechanical properties of the materials (heat capacity, thermal expansion, thermal conductivity). Thermal transfer in the weld pool by convection and radiation are generally incorporated into the prescribed temperature field and do not need to be included in the weld model (Bayock, 2019), (Van Wachem, 2008).

The general conduction thermal transfer equation can be expressed as Figure 2.44 and 2.45 shows (Z. Kumar, 2005) (D. Kumar, 2007).

$$\rho c \frac{\partial T}{\partial t} = \nabla(k \Delta T) + Q \quad (2.44)$$

$$\rho c \frac{\partial T}{\partial t} = \frac{\partial}{\partial x} \left(k_x \frac{\partial T}{\partial x} \right) + \frac{\partial}{\partial y} \left(k_y \frac{\partial T}{\partial y} \right) + \frac{\partial}{\partial z} \left(k_z \frac{\partial T}{\partial z} \right) + Q \quad (2.45)$$

k_x, k_y, k_z are thermal conductivity, W/m°C in the x, y, z directions.

c is the specific heat capacity unit and, ρ is the density (kg/m³).

$T(x, y, \text{ and } z)$ is the temperature field, and x, y, and z represent the welding directions in longitudinal, transverse, and thickness directions.

The second phase of the equation describes boundary conditions. Equation (2.45) presents the sum of conduction, convection, and radiation equations, which contribute to charge and discharge of temperature in the welded structure.

$$k \frac{\partial T}{\partial x} l_x + k \frac{\partial T}{\partial y} l_y + k \frac{\partial T}{\partial z} l_z + q_z + h_{conv}(T_s - T_0) + \sigma \epsilon (T_s^4 - T_0^4) = 0. \quad (2.46)$$

The expression represents thermal convection, which represents $h_{conv}(T_s - T_0)$ heat transfer coefficient for convection. q_z is the boundary heat source, T_s and T_0 are the input temperature and ambient temperature for convection and radiation, respectively..

The expression of $\sigma \epsilon (T_s^4 - T_0^4)$ shows the heat loss by radiation. σ represents the Stefan-Boltzmann constant, and $\sigma = 5.67 \times 10^{-8} \frac{W}{m^2} \cdot ^\circ C$. ϵ is the emissivity (0.75).

The digital model is written using an element free Galerkin model, which can transform the equation into:

$$\int_v \left(\frac{1}{2} \right) \left[k_x \frac{\delta^2 T}{\delta x^2} + k_y \frac{\delta^2 T}{\delta y^2} + k_z \frac{\delta^2 T}{\delta z^2} \right] - 2 \left(Q - \rho c \left[\frac{\delta T}{\delta t} \right] \right) dv + \int_{s_1} q T ds + \frac{1}{2} \int_{s_2} h (T - T_\infty)^2 ds = 0. \quad (2.47)$$

The first integral gives the thermal stiffness matrix due to conduction $[K_{cond}]$, the body internal heat generation $\{Q_{body}\}$, and the body heat capacity matrix $[C]$. The second integral gives the thermal load due to heat flux on the surface q . The third integral gives the convection load due to the film coefficient $\{h\}$.

In general, the element transient heat equation can be according to the equation below:

$$[K(T)]\{T\} + [(T)] \left\{ \frac{\partial T}{\partial t} \right\} = \{Q(T)\}. \quad (2.48)$$

The element free Galerkin (EFG) FEM method has been described in the Materials and Methods chapter of this thesis and applied to analyse the temperature distribution in GMAW using double pass process on dissimilar HSS.

2.2.2 Cooling rate after the welding process

According to Karkhin (Karkhin, 2016), the evaluation of the cooling rate is a function of the different parameters: cooling lime ($t_{8/5}$), heat source (Q), the peak temperature (T_{max}), thermal conductivity (λ), welding speed (v), the preheat temperature T_0 , and the thickness of the weld joint (h). The equation is as follows:

$$\Delta t_{8/5} = \frac{P/v}{2\pi} \left[\frac{1}{T_2 - T_1} - \frac{1}{T_1 - T_0} \right]. \quad (2.49)$$

When the heat source has a rapid movement on a source line in the infinite flat surface, using equation 2.37 of Table 2.2, the cooling time $\Delta t_{8/5}$ of T_1 a T_2 can be expressed as:

$$\Delta t_{8/5} = \frac{\left[\frac{P}{vh}\right]^2}{4\pi\lambda c\rho} \left[\frac{1}{(T_2 - T_0)^2} - \frac{1}{(T_1 - T_0)^2} \right]. \quad (2.50)$$

When estimating the cooling time from 800 to 500 degrees Celsius, (Michailov, 1996) has developed the relation of cooling time $\nabla t_{8/5}$ for:

$$\Delta t_{8/5} = (0.043 - 4.3 \cdot 10^{-5} T_0) \left(\frac{Q}{vh} \right)^2 \left(\frac{1}{(500 - T_0)^2} - \frac{1}{(800 - T_0)^2} \right). \quad (2.51)$$

(Karkhin, 2015) and (Poorhaydari, 2005) formulated the expression of maximum temperature which allows to evaluate the cooling rate at 500 °C knowing the cooling time as follows:

$$T_{max}(y) - T_0 = \frac{1}{\sqrt{2\pi e}} \frac{\frac{P}{(vh)}}{c\rho} \frac{1}{y}, \quad (2.52)$$

where y is the distance from the weld line in the HAZ (mm), e is the thickness of the workpiece (mm), and $c\rho$ is the specific heat capacity per unit of volume (0.005 J/mm³K), $\frac{P}{(vh)}$ is the heat input per unit length.

Knowing the mode of heat propagation of the preheat temperature T_0 and the expression $\frac{P}{(vh)}$, the cooling rate can be defined by:

$$\frac{\partial T(0,T)}{\partial t} = -2\pi\lambda c\rho \frac{(T_{max} - T_0)^3}{\left[\frac{P}{(vh)}\right]^2}. \quad (2.53)$$

2.3 Microstructure characterisation of dissimilar HSS welds

In fusion welding of a dissimilar HSS joint, the base metal near the fusion zone is subjected to typical temperature cycles. These particular parts of BM undergo a fast increase in temperature, reaching the melting temperature, followed by a gradual temperature decrease during cooling. The maximum temperature experienced decreases with the distance from the centre line of the weld metal. The chemical composition of the BM is one of the most important data to consider when welding dissimilar HSS. Because of the dissimilarity between materials, informed choice of welding parameters and filler wire becomes essential to minimize different thermally induced changes in the microstructure and properties of the weld metal and HAZ. The filler wire can be characterized based on two key characteristics: alloying element composition and mechanical properties.

Based on the alloying element composition, the choice of filler wire refers to the carbon equivalent (CEV). Filler wire with the same mechanical properties as BM is referred to as a matched filler wire. When the mechanical properties of a filler wire are higher than BM, it is referred to as an overmatched filler wire (Tian, 2018). Figure 2.4 illustrates the microstructure formation over the weld and HAZ. It can be seen that the most critical zone (CGHAZ) which is partially melted can develop some crack propagation and corrosion after welding (Cota, 2000).

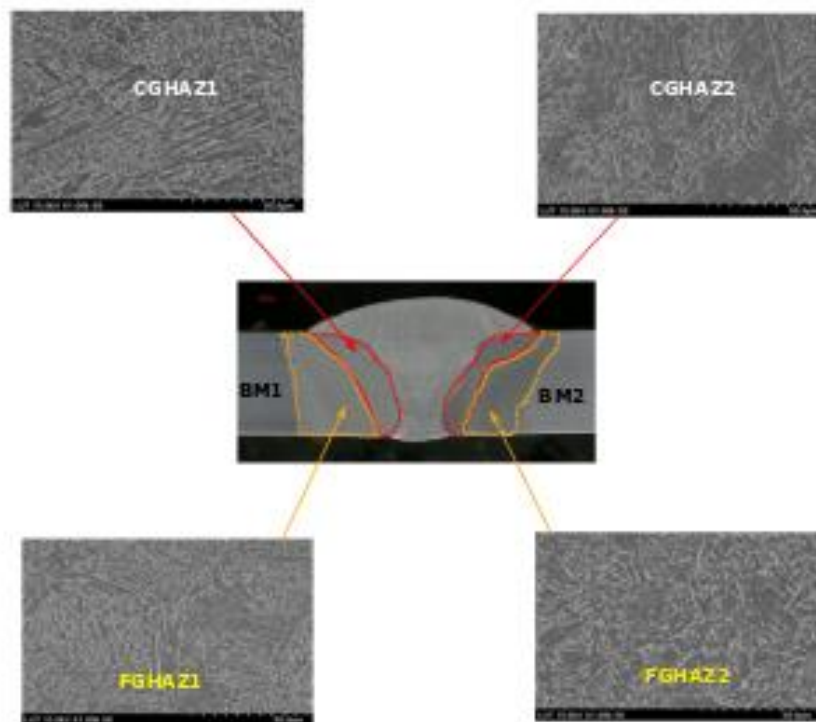


Figure 2.4: Microstructure formation of dissimilar S700MC/S960QC steel welded joint using GMAW and filler wire (Nicro700).

The peak temperature is produced from the weld metal (WM) and distributed along the HAZ (CGHAZ, FGHAZ, SCHAZ), and BM. In this thesis, the analysis will be focused on dissimilar high strength low alloy steel (HSLA). The particularity of this kind of steel is the low carbon content. The strength of the steel is compensated by the alloying element composition such as Manganese (Mn), Chromium (Cr), Nickel (Ni), Silicon (Si), and aluminium (Al).

In the literature, several approaches were developed to predict microstructural constituents when applying the welding process and heat treatment in the HSS structures. The effect of micro-alloying elements (Si, Nb, C, Mn, and Mo) in the microstructural constituents was analysed using several experiment procedures. The analysis performed by (Fang, 2009), (Yan, 2019), and (Chen, 2019) showed the existent correlation between the increase of Si, Mn, Nb, and the increase or not of the proportion of bainite constituent in the austenite grain of microstructure. They noticed that the increase of the heat input influenced the formation of cementite in the austenite grain, which affected the strength of the zone analysed. The decrease of the heat input reduced the cooling time, allowing an increase of bainite and martensite constituent in the cross-section of microstructure. By reducing the heat input when welding high strength low alloy steel, the major issue is a risk of increased hardness, causing hydrogen cracking. (Zhang, 2019), (Zhou, 2017) analysed a specific alloying element (Si). By using a transmission electron microscopy and electron backscatter diffraction (EBSD) images, the authors observed the dependence of granular bainite, acicular ferrite, low bainite and martensite/austenite constituents with Si content in the CGHAZ when welding HSLA steels. The authors noted also that when increasing Si content in the microstructure, the amount of acicular ferrite will increase in the inter critical coarse grain heat-affected zone, affecting the microstructural constituents inside the CGHAZ. The direct effect will be an increase of softening in the heat-affected zone and few brittle zones, which, in turn, will reduce the strength of the joints. A similar analysis was performed by (Navarro-Lopez, 2017), (Mas, 2016), which by using scanning electron microscopy and EBSD characterised of bainite-martensite constituents in the microstructure of HSLA steels. The authors observed that when applying the temperature treatment below the martensite start transformations ($380\text{ }^{\circ}\text{C}$), the formation of bainite-ferrite decreases. The result of an increase of martensite constituent in the austenite grain greater than that in the BM affected by the hardenability of the metal.

During the welding process, the microstructure has its origins in two thermal processes: heating and cooling phase. The heating phase corresponds to austenite grain growing, which increased up to the peak temperature. The cooling phase developed the reconstructive phase. The HAZ of low-alloy steel can have the following sequences: grain growth, carbide dissolution, phase transformation, recrystallisation (martensite formation). Continuous cooling transformation (CCT) diagram provides information on the microstructural transformations in dependence on the cooling rate or cooling time ($t_{8/5}$). During the cooling phase, the austenite grain size will reduce, which at the temperature of below $850\text{ }^{\circ}\text{C}$, will start by the proportion of few ferrites (F), bainite (B), and martensite (M). Figure 2.5 presents an approach of microstructure modelling in the HAZ.

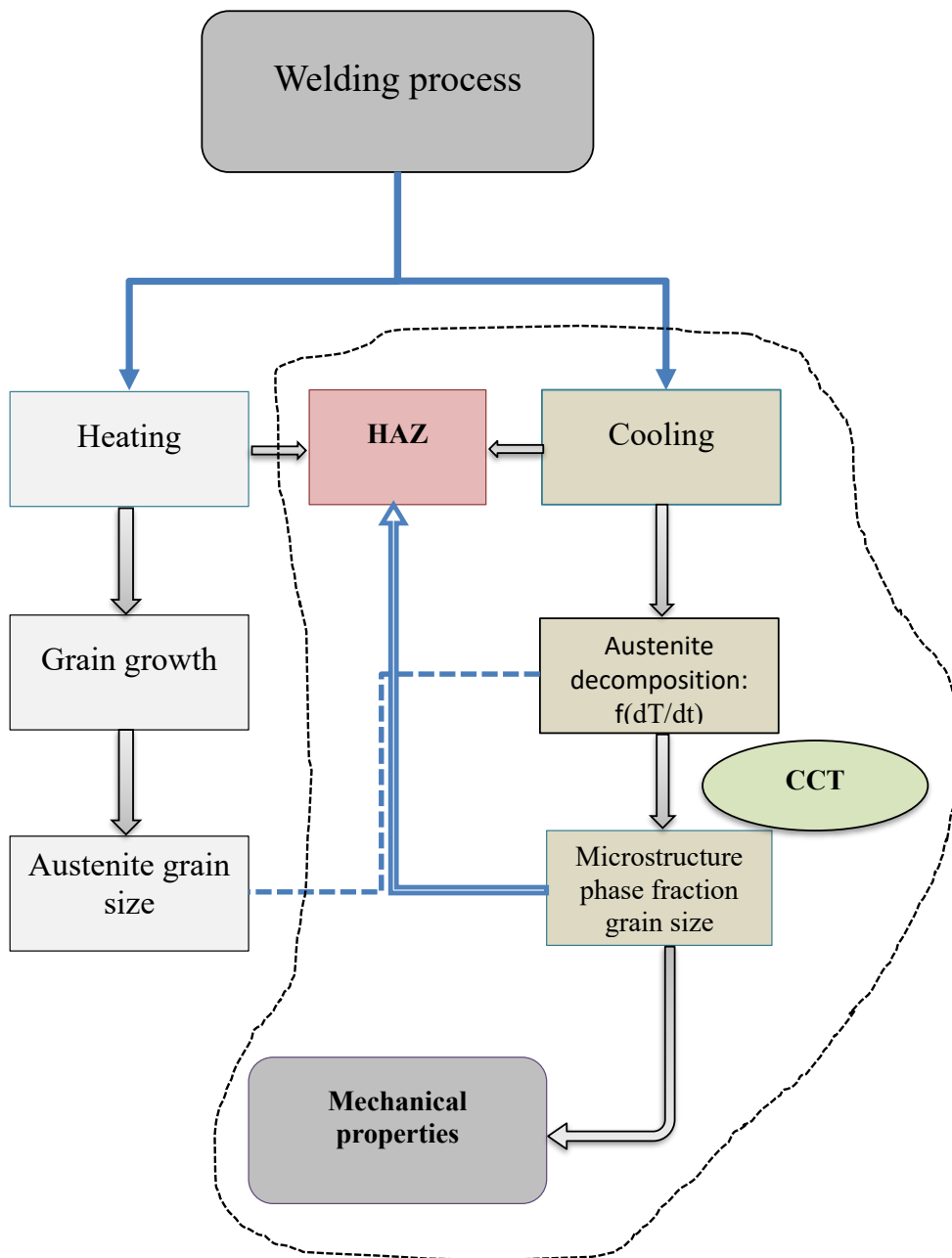


Figure 2.5: Microstructure modelling configuration in the HAZ.

The model started by the welding process, which with a dissimilar joint was heated and cooled. The welded joint was characterised during a cooling phase, showing a

recrystallisation of the austenite grain in the CGHAZ, the microstructure transformation. The mechanical properties evaluations are based on the microstructure phase fraction, which leads to the increase of hardness at the different zones, causing stress and deformation of the welds. Numerical modelling of a neural network of bainite start (B_s) and martensite start (M_s) constituent was developed by (Dongsheng, 2011) (Bhadeshia, 1999). The researchers performed two equations, which allowed evaluation of M_s and B_s formation function of alloying element compositions and the mechanical properties of materials. Hot-rolled extra high strength steel plates were used as an HSS in their analysis. The increase of B_s and M_s transformations caused by a higher heat input will certainly developed softening areas in the HAZ and create a brittle zone in the microstructures.

$$M_s(^{\circ}\text{C}) = 764.2 - 302.6C - 30.6Mn - 16.6Ni - 8.9Cr + 2.4Mo - 11.3Cu + 8.8Co + 7.4W - 14.5Si \quad (2.54)$$

and

$$B_s(^{\circ}\text{C}) = 745 - 110C - 59Mn - 39Ni - 68Cr - 106Mo - 17MnNi + 6Cr^2 + 29Mo^2 \quad (2.55)$$

The researchers did not use the welding parameters in their models, which could influence the final model.

This research focused on the cooling phase, which analysed the microstructural constituents based on the CCT diagram, evaluated the austenite grain size, and the micro-alloying element composition when undermatched and overmatched filler wire were used.

2.4 Mechanical properties of dissimilar HSS welds.

To improve the mechanical properties of the joint when welding dissimilar HSS, several parameters must be used to follow the requirement: the welding parameters, the geometry of the weld joint, the mechanical properties of base material and filler wire, the choice of the filler wire composition. The welding process should be applied according to the welding procedure specification (WPS) in accordance with the ISO 15614-1:2017 standard.

The particularity of welding dissimilar HSS is based on the difference between both materials (mechanical properties and microstructure composition). Using the GMAW process, the use of filler wire becomes a third material that will affect the mechanical stability of the welded joint. The effects of welding process selection on the weld geometry were analysed by (Mvola, 2015), (Mvola, 2016). The authors presented the parameters that must be taken into consideration when welding dissimilar HSS. In Figure 2.6, the same authors showed the factors that influence the weld quality for welding of dissimilar joints. Figure 2.6 points out the interrelation between the service considerations, the fundamentals parameters, filler wire selection, and the welding process selection.

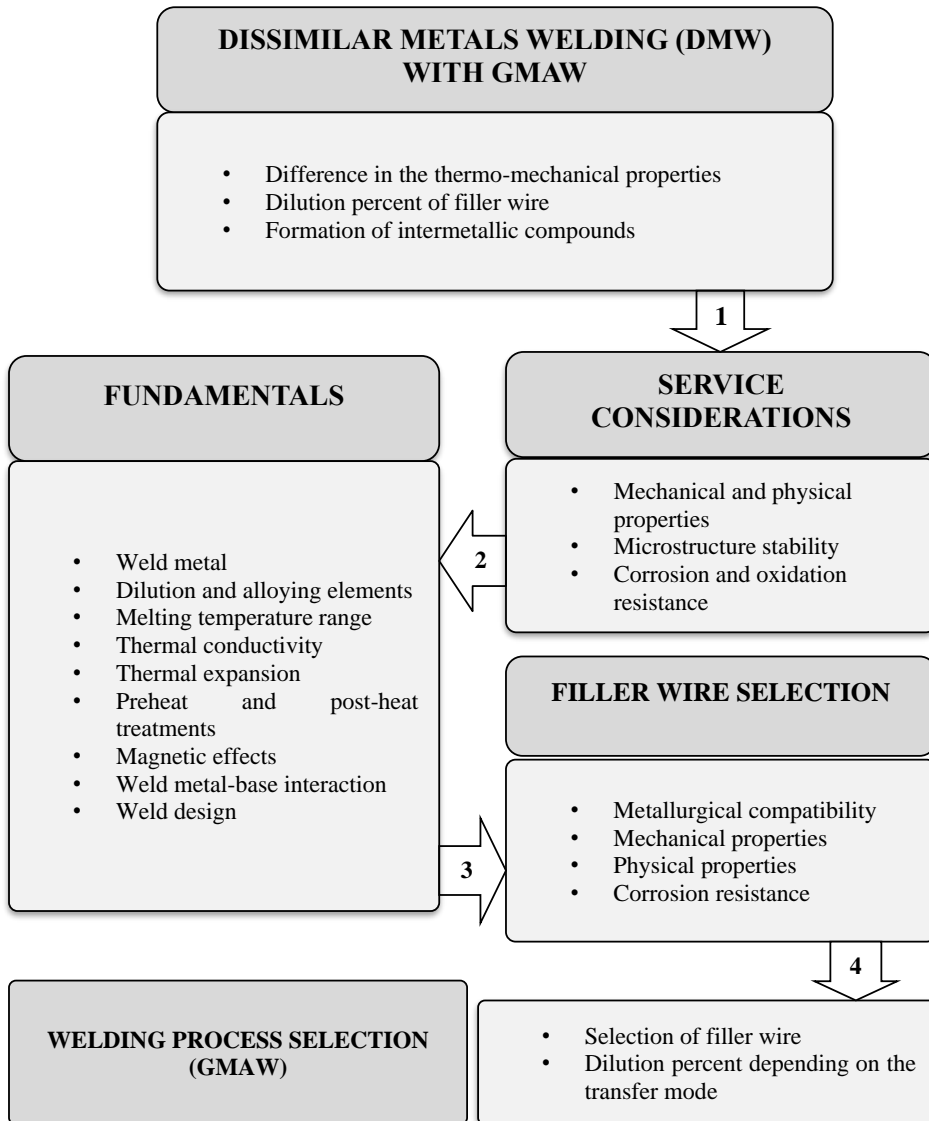


Figure 2.6: DMW factors that influence the quality of the weld joint (Mvola, 2015) and (Kah, 2011).

There is a direct relationship between the mechanical properties of the materials and the heat input during the welding process. In this analysis, (Gorka, 2018) (Lahtinen, 2019), evaluate the mechanical properties of weld joints such as the hardness, tensile strength, and toughness in their heat-affected zones. The authors investigated the mechanical

properties of the HSS of 690 MPa, 700 MPa manufactured by a thermomechanical controlled process (TMCP) and quenching and temper (QT). They used several heat input values, which had a direct effect on the mechanical properties of the welds of steel. The authors noticed the sensitivity of the materials when the heat input was increased, which increases softening in the heat-affected zone. The reduction of the heat input resulted in an increase of hardness, causing several hydrogen cracks in the weld zone.

The optimal choice of welding parameters such as heat input, welding speed, torch position and the required filler wire composition will be analysed in this thesis. Table 2.4 summarises the experimental investigation that has developed to evaluate the influence of the heat input parameters.

Table 2.4: Summary of experimental investigations articles on the influence of the heat input and PWHT on the microstructure and mechanical properties of dissimilar weld structures

Materials	Strategy	Findings	Citation
ASTM E112-10 QT, TMCP, OK Autrod 13.51 GMAW (15% CO ₂ and 85% Ar)	The measurement of the mechanical properties in the HAZ of the dissimilar S690QT/TMCP steel welded.	-The weld of HSS with the heat input of 10 kJ/cm has improved a microstructural constituent in the HAZ. -The heat input of 10 kJ/cm improves strength and impact toughness of the welded joint.	(Pirinen, 2015)
Welding Optim 960 QC and Duplex Stainless steel (UNS S32205) with austenitic filler wire GMAW 350x150x5 mm	Determine the accurate heat input that can improve the strength of the weld joint of dissimilar S960QC/UNS S32205 steel.	- A heat input of 20 kJ/cm caused the crack propagation in the weld joint when welds S960QC steel. The microstructure is formed by more carbide in the austenite grain. -The heat input recommended is 8.6 kJ/Cm, in order to reduce carbide in the microstructure, and improve the strength of the weld joint.	(Tasalloti, 2017)
22MnB5, ENGTS-1000-5, and Docol 1400 M, Rapid Hot Forming Processes	Develop a new methodology of heat treatment of conventional HSS (22MnB5, DP1000, Docol 1400M9 and evaluate their effects on mechanical properties and microstructure characterisation.	- The increase of strain to 31% was observed when heating 22MnB5 at 100 K/s and the tensile reduced by only 9%. - The ductility of the Docol 1400M increased by 75% when the austenisation is conducted (100 K/s).	(Löbbe, 2016)
13CrMo4-5/10CrMo9-10 use GMAW and Cold Metal Transfer (CMT)	Evaluate the potential advantages of cold metal transfer welding using the GMAW process.	- It was an incomplete carbide dissolution, limited carbon diffusion. - An incomplete transformation to austenite was observed.	(Frei, 2016)
ENGTS 1000-5 uses Laser beam welding:0,4 and 2,0 kW and the speed of 20 and 150 mm/s.	Evaluate the mechanical properties and microstructural constituents based on the welding parameters: 0.4 kW and 2.0 kW; 20 mm/s and 150 mm/s.	- The optimal welding condition was when used 2.0 kW and 150 mm/s. - The choice of the condition minimises softening and increases the strength of the welds.	(Alves, 2018)
Hardox 450, Optim 700MC using GMAW process	Investigate the effect of post-weld heat treatment on the mechanical properties of tempered of martensitic steel and high-strength steel joints.	-Hardness decrease in Hardox450 when applying heat treatment of 450 °C for 2 hours. - The hardness of Optim700MC was not affected by post-weld heat treatment.	(Usunali, 2015)

EN 1564 grade EN-GJS-800-8/ GMAW process	Estimate the heat input and PWHT effect on the mechanical properties and microstructure transformation.	- Changes of heat input parameters (current, voltage, and wire-speed) will affect the whole welds area, which modifies their mechanical properties and microstructural constituents.	(Chennaiah, 2016)
42SiMn steel, Soaking hold and annealing hold	Evaluate the effect of two-step heat treatment parameters on microstructure and mechanical properties.	- The most suitable microstructural constituent and the best combination of strength- elongation were resulting in the processing by the heating temperature of 850 °C with a cooling rate of 30 °C/s. - The elongation obtained was 40%, the final microstructure contained 16% of retained of austenite; the rest was the formation of ferrite and bainite.	(Kurcerova, 2017)

3 Materials and Methods

In this section, the material and methods used in simulation and experimental procedures of thermal cycle are described. The numerical model was developed using element free Galerkin (EFG) and finite element model (FEM) in ANSYS software. The experimental procedure based on the design of experiments (DOE) was developed. It contains a description of the welding station used, the weld joint geometry, microstructure and alloying element compositions analysis, hardness tests, and tensile tests used. Tables presenting used steels and filler wire, their classifications, and chemical compositions as well as nominal mechanical properties can be found in sub-section 3.3.2: Table 3.3, Table 3.4, and Table 3.5.

3.1 Numerical simulation procedure of GMAW process

In this sub-section, the numerical model of the GMAW process was developed using a finite element method (FEM) and an element free Galerkin model (EFG). The implementation was performed using two specimens: dissimilar joint of steels S690QT-TMCP and dissimilar joint of steels S700MC/S960QC. During the process, several parameters had to set-up in the program of ANSYS software; the weld geometry of the sample, as well as the thermal conductivity as the function of the temperature, the thermal expansion coefficient, and the mechanical properties of all base materials. The welding process used in this modelling was the GMAW process. Figure 3.1 shows the required input parameters, the processes of modelling in the software, and the output of the system describing the thermal cycle obtained for the subsequent analysis.

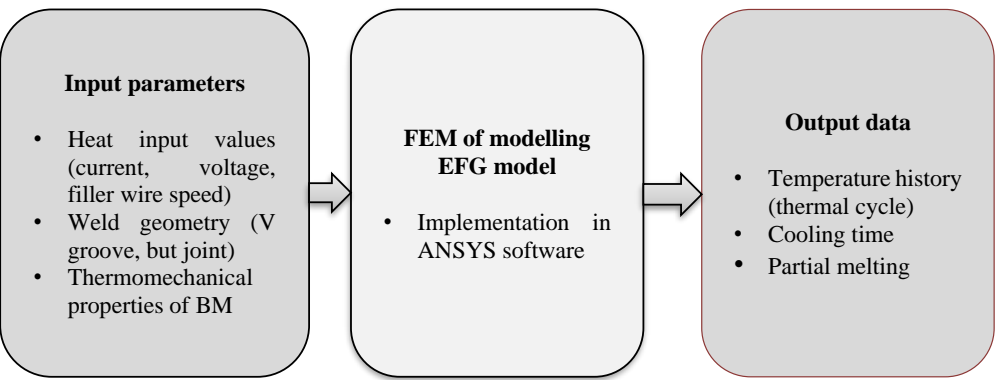


Figure 3.1: Welding modelling showing the input parameters, EFG model and output data.

3.1.1 Geometry design and materials

The geometry of the specimen was conducted using Solid Work software. The dimensions used in this modelling were 150 mm x 50 mm x 8 mm. The joint was V-groove butt joint with an angle of 60° , and 2 mm of a gap. Figures 3.2 and 3.3 present the discretisation of the weld metal within the weld geometry.

The commercial FEM software ANSYS R19.2 was employed for a numerical solution. The calculation domain was discretised into a finite number of control volumes and general conservation equations were solved on the set of control volumes.

The domain size and time step size were investigated to obtain high accuracy of the numerical solution. The domain size of the numerical model was shown to be large enough to eliminate the boundary effect on the formation of melting pool. During the modelling process, each part was removed/deactivated and reactivated successively step by step with the moving heat source along with the weld sample (Figure 3.3). The welding process was developed from point A to point B (Figure 3.3).

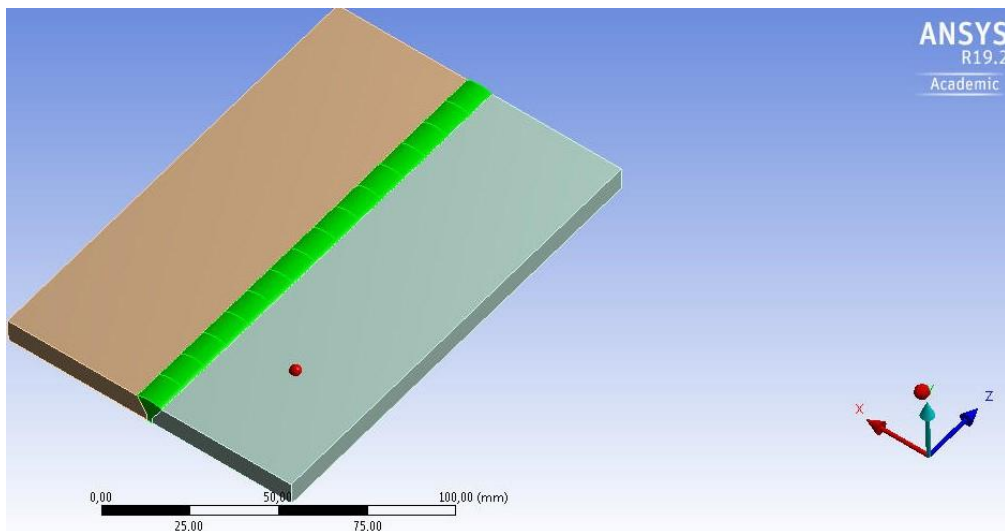


Figure 3.2: Model showing in ANSYS software.

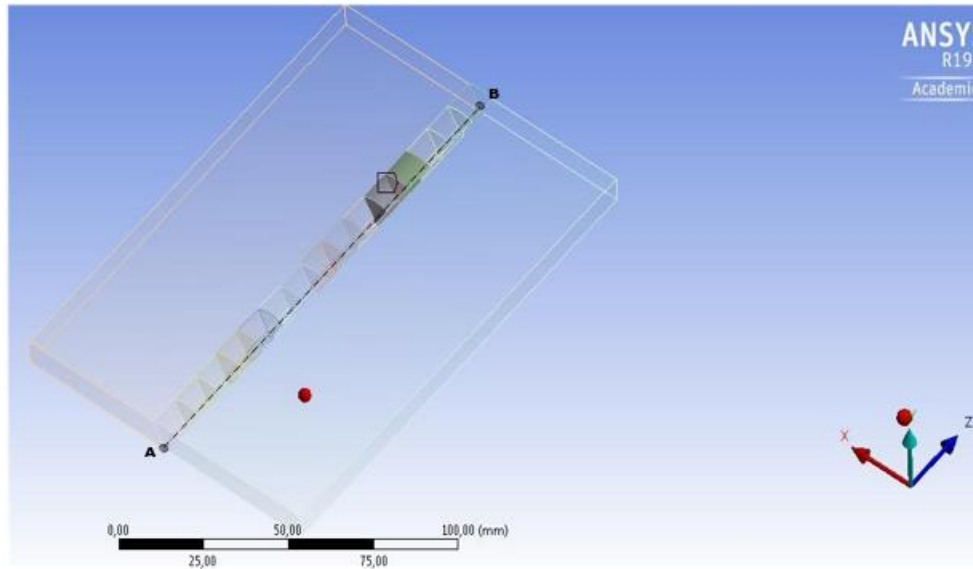


Figure 3.3: Geometry model showing the weld metal discretisation as a weld joint.

In this modelling process, four base material and two filler wire compositions were used. Table 3.3 shows the mechanical properties and chemical composition of the different BM and filler wire. This table presents a chemical composition of 690-MPa of both QT and TMCP steels, the filler wire used, and the carbon equivalent (CEV) of each material following the mechanical properties of the different materials that are shown in the same table.

This table presents a yield strength, ultimate tensile strength, and a limit elongation of the different materials used. To be able to develop the model, the welding parameters, the geometry of the sample, and boundary conditions were uploaded in the software. The software was running, performed a mesh generation (nodes and elements) in the weld geometry. The heat input was applied in the weld metal step by step, and the thermal conduction was developed in the HAZ of both materials. Table 3.1 shows the welding process data used during the modelling process.

The model considered the thermal properties of materials, the thermal conductivity, and the specific heat. By using JMat software, an estimation curve of thermal conductivity and specific heat were performed. Based on the chemical composition, temperature fields, and the mechanical properties of materials, JMat software generated an estimation curve of the thermal conductivity and specific heat of each material. The results are presented in Figure 3.4 for thermal conductivity and in Figure 3.5 for specific heat.

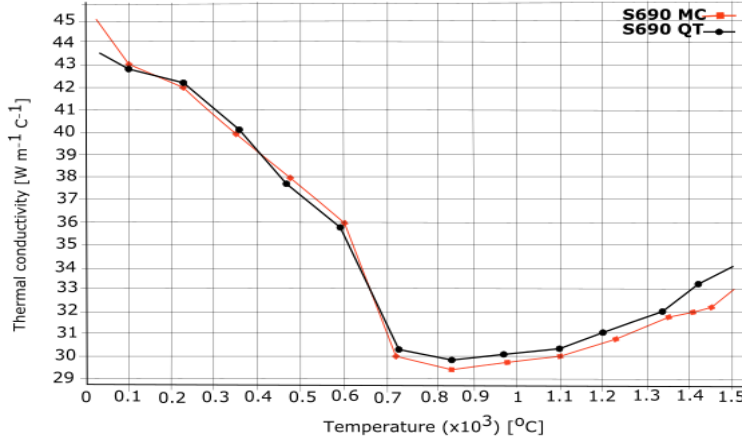


Figure 3.4: Thermal conductivity data of both 690-MPa-steels.

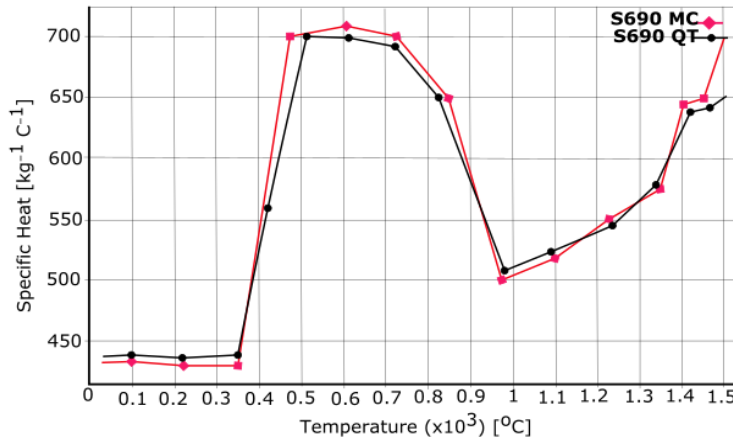


Figure 3.5: Specific heat data of both 690-MPa-steels.

3.1.2 Model and algorithm

The transient heat conduction formulation (3D) used in this thesis is the function of the heat source and movement at a constant speed. The quasi-stationary temperature field is given by (Kumar, 2007) as the discrete equation:

$$\frac{\partial}{\partial x} \left(k_x \frac{\partial T}{\partial x} \right) + \frac{\partial}{\partial y} \left(k_y \frac{\partial T}{\partial y} \right) + \frac{\partial}{\partial z} \left(k_z \frac{\partial T}{\partial z} \right) + Q = \rho c \frac{\partial T}{\partial t}. \quad (3.1)$$

A three-dimensional steady-state heat conduction equation for the material is

$$k(T_{,xx} + T_{,yy} + T_{,zz}) + Q = 0, \quad (3.2)$$

where Q is the heat input per unit of volume.

The model using EFG requires moving at least square approximation. The moving least square approximation was developed based on three components: a weight function with a different node, a polynomial basis, and a non-constant coefficient. The element geometry is showed in Appendix A: (Element model in 3D).

The weighted integral from equation 3.1 is giving by

- Boundary conditions.

At surface $x=0$, (S_1), $T = T_{s_1}$

At surface $x=X$ (S_2), $-kT_{,x} = h(T - T_s)$

At surface $y=0$ (S_3), $-kT_{,y} = h(T - T_s)$

At surface $y=Y$ (S_4), $-kT_{,y} = h(T - T_s)$, (3.3)

At surface $z=0$ (S_5), $-kT_{,z} = h(T - T_s)$,

At surface $z=Z$ (S_6), $-kT_{,z} = h(T - T_s)$

where

X is the length

Y is the width

Z is the height

h is a convective heat transfer coefficient ($W/m^2\text{°C}$)

k is a coefficient of thermal conductivity ($W/m\text{°C}$)

Q heat input (kJ/cm)

T_s is a surface temperature (°C)

T is an internal temperature (°C).

- Weight function with a different node will be given as follows:

By applying a weight function with a different boundary condition (equation 3.3), the equation (3.2) becomes:

$$\int_v [k(w_{,x} T_{,x} + w_{,y} T_{,y} + w_{,z} T_{,z})] dV - \int_v w Q dV + \int_{s_2} wh(T - T_s) dS + \int_{s_3} wh(T - T_s) dS + \int_{s_4} wh(T - T_s) dS + \int_{s_5} wh(T - T_s) dS + \int_{s_6} wh(T - T_s) dS. \quad (3.4)$$

The functional $I(T)$ is written as:

$$I(T) = \int_v \frac{k}{2} [T_{,x}^2 + T_{,y}^2 + T_{,z}^2] dV - \int_v T Q dV + \int_{s_2} \frac{hT^2}{2} dS + \int_{s_3} \frac{hT^2}{2} dS + \int_{s_4} \frac{hT^2}{2} dS + \int_{s_5} \frac{hT^2}{2} dS + \int_{s_6} \frac{hT^2}{2} dS - \int_{s_2} hTT_s \cdot dS - \int_{s_3} hTT_s \cdot dS - \int_{s_4} hTT_s \cdot dS - \int_{s_5} hTT_s \cdot dS - \int_{s_6} hTT_s \cdot dS. \quad (3.5)$$

By using Lagrange user λ to reinforce the boundary conditions, the function I^* is obtained as

$$\begin{aligned}
I^*(T) = & \int_v \frac{k}{2} [T_{,x}^2 + T_{,y}^2 + T_{,z}^2] dV - \int_v T Q dV + \int_{s_2} \frac{hT^2}{2} dS + \int_{s_3} \frac{hT^2}{2} dS + \\
& \int_{s_4} \frac{hT^2}{2} dS + \int_{s_5} \frac{hT^2}{2} dS + \int_{s_6} \frac{hT^2}{2} dS - \int_{s_2} hTT_{s,} dS - \\
& \int_{s_3} hTT_{s,} dS - \int_{s_4} hTT_{s,} dS - \int_{s_5} hTT_{s,} dS - \int_{s_6} hTT_{s,} dS + \int_{s_1} \lambda(T - T_{s_1}) dS.
\end{aligned} \tag{3.6}$$

By applying Variational method, the equation (3.6) becomes

$$\begin{aligned}
\delta I^*(T) = & \int_v (T_{,x}^T k \delta T_{,x} + T_{,y}^T k \delta T_{,y} + T_{,z}^T k \delta T_{,z} - Q \delta T) dV + \int_{s_2} hT \delta T dS + \\
& \int_{s_3} hT \delta T dS + \int_{s_4} hT \delta T dS + \int_{s_5} hT \delta T dS + \int_{s_6} hT \delta T dS - \int_{s_2} hT_s \delta T dS - \\
& \int_{s_3} hT_s \delta T dS - \int_{s_4} hT_s \delta T dS - \int_{s_5} hT_s \delta T dS - \int_{s_6} hT_s \delta T dS + \int_{s_1} \lambda \delta T dS + \int_{s_1} \lambda \delta (T - \\
& T_{s_1}) dS.
\end{aligned} \tag{3.7}$$

When applying equation 1 (Appendix A: additional equations (10)), with equation (3.7), the steady-state heat conduction equation was solved as:

$$\begin{bmatrix} K & G \\ G^T & 0 \end{bmatrix} \begin{Bmatrix} T \\ \lambda \end{Bmatrix} = \begin{Bmatrix} R \\ q \end{Bmatrix}, \tag{3.8}$$

where

$$\begin{aligned}
K_{IJ} = & \begin{bmatrix} \Phi_{I,x} \\ \Phi_{I,y} \\ \Phi_{I,z} \end{bmatrix}^T \begin{bmatrix} k & 0 & 0 \\ 0 & k & 0 \\ 0 & 0 & k \end{bmatrix} \begin{bmatrix} \Phi_{J,x} \\ \Phi_{J,y} \\ \Phi_{J,z} \end{bmatrix} dV + \int_{s_2} h \Phi_I^T \Phi_J dS + \\
& \int_{s_3} h \Phi_I^T \Phi_J dS + \int_{s_4} h \Phi_I^T \Phi_J dS + \int_{s_5} h \Phi_I^T \Phi_J dS + \int_{s_6} h \Phi_I^T \Phi_J dS
\end{aligned} \tag{3.9}$$

$$\begin{aligned}
R_I = & \int_v Q \Phi_I dV + \\
& \int_{s_2} hT_s \Phi_I dS + \int_{s_3} hT_s \Phi_I dS + \int_{s_4} hT_s \Phi_I dS + \int_{s_5} hT_s \Phi_I dS + \int_{s_6} hT_s \Phi_I dS
\end{aligned} \tag{3.10}$$

$$G_{IK} = \int_{s_1} \Phi_I N_K dS \tag{3.11}$$

$$q_K = \int_{s_1} T_{s_1} N_K dS \tag{3.12}$$

Figure 3.5 shows the mesh generated by ANSYS software along with the geometry. The results are presented in chapter 4.

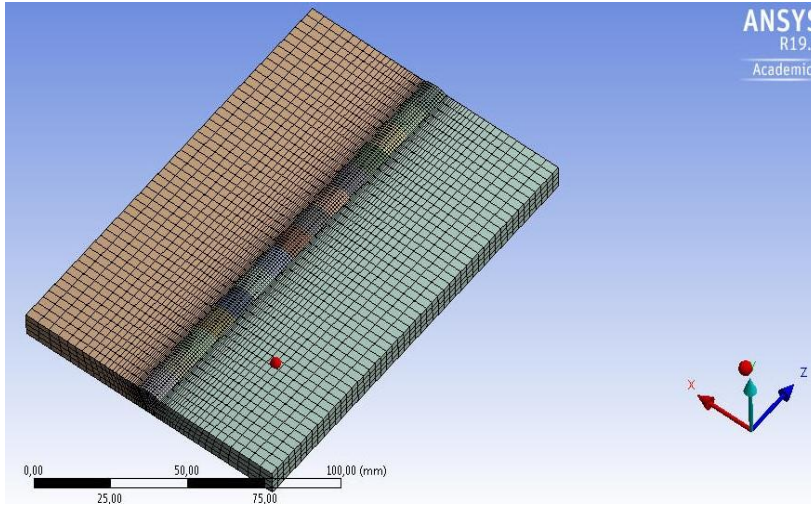


Figure 3.5: The geometry showing a discretisation with a total of 189,202 and 38,100 individual nodes and elements.

3.2 Experimental setup

In this sub-section, the design of the experiment (DOE) was performed. Based on pre welding procedure specification (pWPS), the details of the welding process (GMAW) are presented. The workstation used is a GMAW process station. The robot arm manipulator and controller are ABB IRB-A1600 and ABB IRC5 M2004, respectively. The power source is a Fronius Pulls Synergic 5000 connected to a unit wire feeder. The system acquires data from a number of different measurement points. A thermal cycle sensor (TCS), which is immediately behind the welding torch, captures the thermal cycles during solidification of the welding seam before the seam is cooled. The thermal cycle data was recorded in the central control unit and analysed using LabVIEW software. Table 3.1 shows the welding parameters used to perform the DOE. The interpolation used to design the experiment was $[-1, 0, 1]$. The complete table is shown in Appendix B (Table 2) of this thesis. The whole samples are presented in that table. To perform the experiments, two groups of specimens were welded (S690QT-TMCP) and S700MC-S960QC. The experiment carried out using S690QT-TMCP had six samples and was not performed based on the DOE method. The second specimen (S700MC-S960QT) was performed based on the DOE method for the estimation of samples.

Table 3.1: Input values used in DOE

	Value -1	Value-0	Value+1
Heat input (kJ/cm)	7	12	17
Thickness, e (mm)	8	9	10
Pass weld number	1	1.50	2
Torch angle (°)	8	11.50	15

The input data, the type of filler wire, BM were inserted in the custom design platform of DOE at JMP software. The JMP software is a computer program that analyses statistically the data. The resulting matrix contained twelve runs of experiments, six for each of dissimilar welds (S690QT-S690TMCP and S700MC-S960QC). Table 3.2 presents one of the series of experiments running in the JMP platform.

Table 3.2: Experiment run containing twelve samples of dissimilar S700MC-S960QC weld joint

Experiment (run)	Heat input (kJ/cm)	Torch angle (°)	Pass weld number	Thickness (mm)	Filler wire
1	7	8	1	8	1
2	7	10	1	8	1
3	10	15	1	8	1
4	10	8	1	8	1
5	15	10	1	8	1
6	15	15	1	8	1
7	7	8	2	10	2
8	7	10	2	10	2
9	10	15	2	10	2
10	10	8	2	10	2
11	15	10	2	10	2
12	15	15	2	10	2

3.2.1 Experimental set-up

The welding station was principally composed of GMAW process using robotic MAG welding, a welding machine manufactured by Kemppi, and thermal cycle sensor (TCS). TCS was installed behind the welding torch-allowing to record a cooling time during the solidification phase of the welded joint. The thermal cycle data recorded during the solidification phase will be uploaded in the LabVIEW software (LabVIEW 2018, NI, Austin, TX, USA) for analysis. An ABB IRC 5 robot control unit, which leads to saving the whole program and performs the welding process. Figure 3.6 shows a general configuration of a work-station composed by power source, an automatic robot, a thermal cycle sensor, workpiece, and data acquisition equipment.

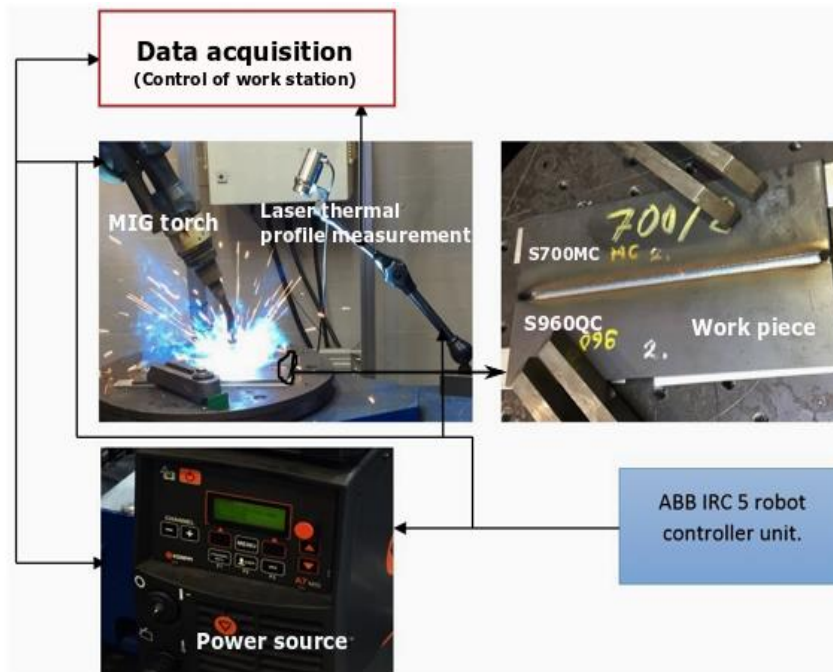


Figure 3.6: Automatic robot GMAW process using a thermal sensor for the measurement of thermal cycle, ABB IRC 5 robot control unit.

3.2.2 Measurement of thermal cycles

The thermal cycle sensor (TCS) used an infrared thermography sensor recorder (HKS-Prozesstechnik 2016) temperature distribution after welding procedure. The measurement range of the TCS ranges from 600 to 1,350 °C which restrains its position. TCS was set at 34 mm from the tips of electrode. Because this device has a frequency of 400 profiles per second, it is suitable for the line speeds used for induction welding, typically welding at 15.2 meters per minute (m/min). The conception of the system was made to minimise the effect of welding spatters on thermal cycle data evaluation, by configuring a filters system. The results from TCS measurement are presented in chapter 4 of this thesis. Figure 3.7 shows the locations of the thermal cycle measurement during welding. Location A and B represent the temperature recorded in S690 TMCP and S690 QT side, respectively, at the distance of 7 mm away from the centreline of the weld. It is the distance to the fusion boundary (± 0.1 mm from the fusion boundary).

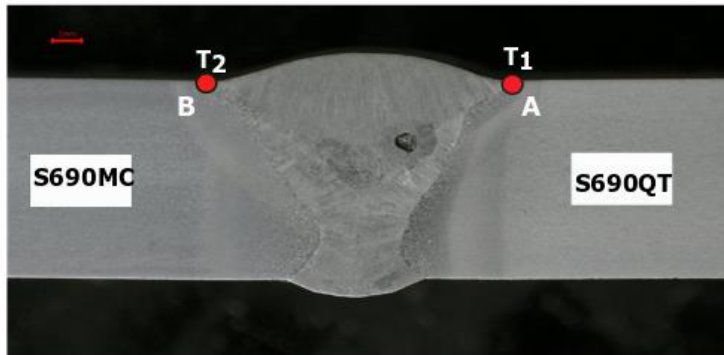


Figure 3.7: Temperature measuring locations in the fusion line of both HAZs: (A) point location of temperature T_1 in the S690QT, (B) point location of temperature T_2 for S690TMCP side (± 0.1 mm from the fusion boundary).

3.2.3 Microstructure analysis

In order to ensure safe and reliable operations at extreme temperatures, welded joints and especially HAZ should be examined. Scanning electron microscopy (SEM), and an energy dispersive spectroscopy (EDS) X-ray spectrum were applied. SEM test includes the identification of microstructural constituents and the evaluation of volume fractions of microstructure formed in the HAZ. EDS analysis includes the alloying element composition in the HAZ and the WM. To perform the test, the specimens were etched on 4% solution of HNO_3 and ethanol to ensure any impurities were removed. The images obtained from SEM were analysed in ImageJ and Origin software which evaluated the volume fraction of microstructural constituents.

3.2.4 Vickers-hardness and tensile strength test set-up

A Vickers-hardness test was conducted across the weld samples using a Wilson Wolpert 452SVD Vickers-hardness tester (ITW, Chicago, IL, USA) according to ISO 6507-1:2018 standard. For the whole sample, the measurement was made on one line per sample and point-by-point over the entire length of the sample. Two calibrations were used to perform a hardness test of samples. The sample using a welded joint of S690QT-TMCP (six samples) was used with a load of 0.025 kgf, the loading rate of 0.0025 N/min, and the unloading rate of 0.0025 N/min. With the dissimilar S700MC-S960QC (HV) weld joint, the measurement was performed using the load of 5 kgf, the loading rate of 0.50 N/min, and the unloading rate of 0.50 N/min. The dwell time of measurement was 20 s. A total of eighteen samples was tested in this section.

The tensile tests were conducted using a ZWICK/ROZ Z 330 RED test machine. The whole test of the specimens was conducted according to EN ISO 6892-1:2010 and (SFS-

EN ISO 4136 2012) standards. From each specimen, two samples were prepared for tensile tests (Test A and Test B). From the 8 mm thick plate, 6 samples were prepared for testing dissimilar S700MC/S960QC with undermatched filler wire, and 6 other samples were prepared to test a dissimilar weld with overmatched filler wire. A total of 12 samples were prepared to conduct tensile tests.

3.3 Schematic cross-section of the weld, materials, and filler wire

This sub-section presents a welded design used in this thesis, the materials used, and the different filler wire compositions. First, two dissimilar types of material were used, namely 690-MPa-TMCP-QT and S700MC/S960QC. The first geometry concerns dissimilar weld joints of 690-MPa TMCP-QT steels. The cross-section shows the weld joint geometry of the V-groove butt joint with dimensions of 150 mm x 50 mm x 8 mm, a 60° angle, and 2 mm gap. The second weld specimen is a dissimilar weld of S700MC/S960QC steels which has dimensions of 300 mm x 150 mm x 8 mm and a V-groove butt joint with an angle of 60° and 2 mm gap. The second weld specimen is the composition of dissimilar S700MC/S960QC steels, which has a dimension of 300 x 150 x 8 mm³ and a V-groove butt joint with an angle of 60° and 2 mm of gap (Figure 3.8).

3.3.1 Schematic cross-section of the weld

In this analysis, a butt joint was welded. Figure 3.8 shows the weld joint configuration, presented to illustrates a different weld pass and the dilution zone of the welded joint. From this figure, a front view of the joint was showed and the limitation of the weld pass.

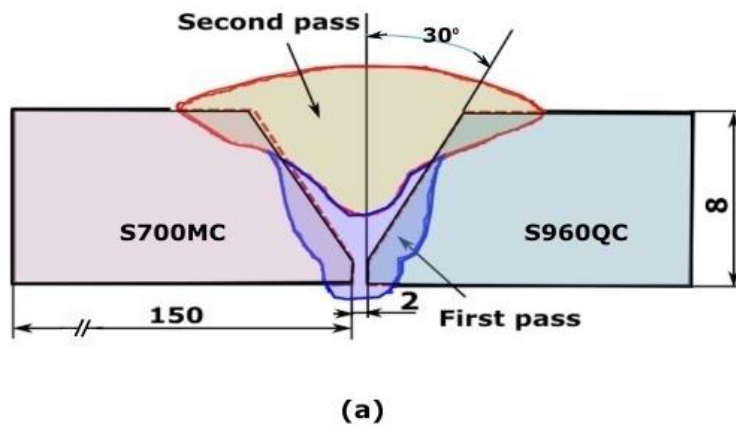


Figure 3.8: Cross-section of the weld showing weld passes and groove geometry.

3.3.2 Materials and filler wire

The specimens were prepared according to ISO EN 17637-2017 standard. The welding process used was GMAW using shielding active gas (Ar +18%CO₂) with a flow rate of 17 l/min. The steel grades used were: S690QT (EN 10025-6), S690TMCP, S700MC (EN 10149-2), and S960QC (EN 10051). To weld dissimilar joints, three different filler wires were used. The first (Mn4Ni1.5CrMo) had the same mechanical properties as both parent materials (S690QT and TMCP). The second one was an undermatched filler wire (NiCrMo700) having lower mechanical properties than both base materials. The third one was an overmatched filler wire (Mn4Ni2.5CrMo). Table 3.3 presents the chemical composition, the mechanical properties, and the CE of the steels. Chemical composition and mechanical properties of filler wires are shown in Table 3.4. Table 3.5 shows the parameters used to carry out the experiments.

Table 3.3: Chemical composition and mechanical properties of S690QT, S690TMCP, S700MC, and S960QC

Chemical composition, wt %																
Materials	C	Si	Mn	Al	B	Nb	Ti	V	Cu	Cr	Ni	Mo	N	P	S	CE
S700MC (EN10149-2)	0.056	0.16	1.18	0.027	0.002	0.044	0.12	0.006	0.002	0.062	0.066	0.0150	0.005	0.001	0.005	0.38
S960QC (EN10051)	0.09	0.21	1.05	0.03	0.002	0.003	0.032	0.008	0.025	0.82	0.04	0.158	0.175	0.001	0.004	0.49
S690QT (EN10025-6)	0.137	0.28	1.39	0.061	0.002	0.021	0.002	0.001	0.002	0.062	0.066	0.029	0.005	0.013	0.013	0.41
S690TMCP	0.049	0.17	1.86	0.025	-	-	0.005	-	0.30	0.20	1.60	0.45	0.005	0.012	0.002	0.55
Mechanical properties																
Materials	Yield strength, MPa		Ultimate tensile strength, MPa		Elongation A ₅ , %		Vickers-Hardness HV5									
S700MC	768		822		12		280									
S960QC	960		1000		18		320									
S690QT	793		835		16.3		270									
S690TMCP	761		821		20		290									

Table 3.4: Chemical composition and mechanical properties of filler wires used

Symbol	Chemical composition (wt%)												CE
	C	Si	Mn	P	S	Ni	Cr	Mo	Cu	Al	Ti+Zn		
16834-A G 69 6 M21 Mn4Ni1,5CrMo	0.07	0.50	1.70	0.012	0.002	1.60	0.20	0.45	0.30	-	0.05		0.55
NiCrMo700	0.056	0.16	1.18	0.001	0.005	0.066	0.062	0.015	0.002	0.027	0.12		0.38
EN ISO 16834-A - G 89 5 M21 Mn4Ni2,5CrMo AWS A5.28: ER120S-G	0.12	0.21	1.9	-	-	2.35	0.45	0.55	0.30	-	-		0.34
Mechanical properties													
Symbol	Yield strength, MPa		Ultimate tensile strength, MPa		Elongation A ₅ %		Vicker-Hardness HV5						
16834-A G 69 6 M21 Mn4Ni1,5CrMo	780		830		17		270						
EN ISO 16834-A - G 89 5 M21 Mn4Ni2,5CrMo AWS A5.28: ER120S-G	960		1038		20		390						

Table 3.5: Welding parameters of the different specimens

Weld samples	Pass 1							Pass 2				
	Filler wire	Current [A]	Voltage [V]	Weld speed [cm/min]	Q [kJ/cm]	Torch angle (°C)	Shielding gas	Current [A]	Voltage [V]	Weld speed [cm/min]	Q [kJ/cm]	Torch angle
Dissimilar 690-MPa-QT/TMCP												
Sample 1	16834-A G 69 6 M21 Mn4Ni1,5CrMo	230	25.60	27.18	10	15	Ar + 18% CO ₂	268	29.00	27.12	14	15°
Sample 2		230	25.60	27.18	10	15		230	25.60	27.18	10	15°
Sample 3		230	25.60	27.18	10	15		258	30.60	22.26	17	15°
Dissimilar S700MC/S960QC												
WS1	16834-A G 69 6 M21 Mn4Ni1,5CrMo	215	25.30	37.30	7	5	Ar + 18% CO ₂	210	26.70	18.00	15	5°
WS2		215	25.30	37.30	7	5		203	26.50	37.50	7	5°
WS3		215	25.30	37.30	7	5		206	26.70	24.00	10	5°
WS4	EN ISO 16834-A - G 89 5 M21	215	25.30	37.30	7	5	Ar + 18% CO ₂	210	26.70	37.50	7	5°
WS5		215	25.30	37.30	7	5°		203	26.50	24.00	10	5°
WS6		215	25.30	37.30	7	5°		206	26.7	18.00	15	5°

4 Test results

The section presents the results of thermal cycle data (numerical and experimental) on welding of dissimilar HSS butt joints. This section includes an evaluation of the effect of the thermal cycle on the structure of the dissimilar weld joints. The section includes four sub-sections: thermal cycle results, microstructural characterization, Vickers-hardness results, and tensile test results.

4.1 Thermal cycle analysis

The evaluation of temperature distribution was carried out using numerical and experimental methods. The numerical modelling was performed using finite element model (FEM) with an element-free Galerkin model (Kumar, 2007). The model was uploaded in ANSYS software. After more than eight hours of running, the results of the thermal cycle data were obtained.

The numerical modelling was done on a dissimilar joint of 690-PMa-QT/TMCP, applying three energy values: 10 kJ/cm, 14 kJ/cm and 17 kJ/cm. A total of 189,202 nodes and 38,100 elements were included in the simulation, different time steps were recorded during the process. During the four-hour simulation of the model in ANSYS software, the following steps were performed:

- SolidWorks was employed to model the solid geometry.
- ANSYS Meshing was used to divide the slab into finite elements.
- ANSYS Fluent was used to define the model and calculations
- ANSYS CFD-post was used for post-processing and results analysis.

Figure 4.1 shows different time steps recorded during the simulation processes. The process started at $t=0$ (Figure 4.1a). Figure 4.1b corresponds to the welding position after 15 s. Figure 4.1c presents the welding position after 45 s, and the end of the welding procedure is shown in Figure 4.1d.

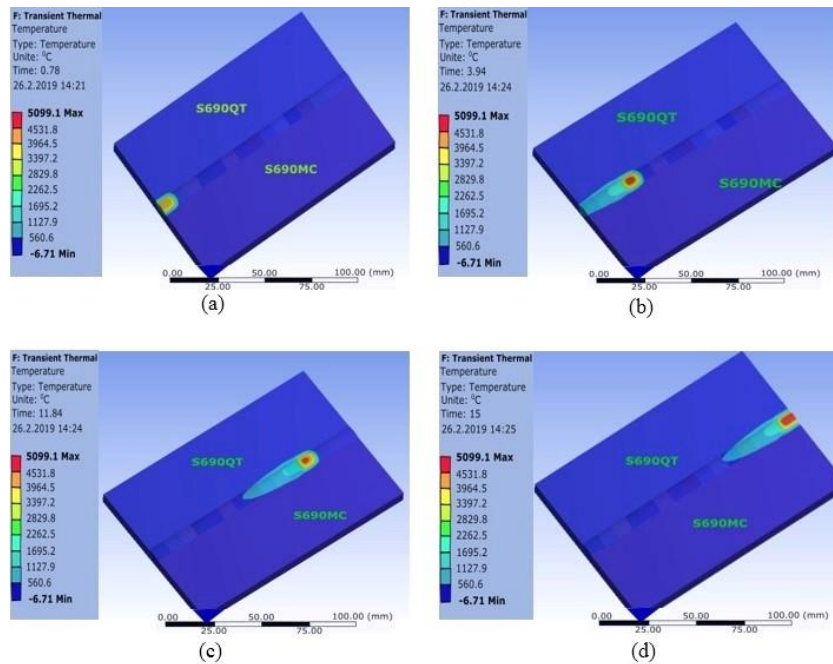


Figure 4.1: Numerical simulation showing the moving heat source. (a) start of welding, (b) welding position after 15 s, (c) welding position after 45 s, and (d) welding position at the end.

Figures 4.2a-c show the numerical results of the thermal cycle in the weld seam of both materials. The heat sources applied to this simulation were 10, 14, and 17 kJ/cm. The first step was considered constant in all three samples. Figures 4.2d and 3a, b present the results of the thermal cycle allowing the cooling time evaluation for both materials. Approximately 1,450 measurement points were recorded for each numerical and experimental analysis process.

Figures 4.3c-e interpret the results of different thermal cycles (numerical and experimental) for each material. It was found that, when a heat input of 10 kJ/cm was applied, the numerical results indicated that the maximum measured temperatures in the QT steel and TMCP steel were approximately 1,320 (T_1) and 1,200 °C (T_2), at the distance of 7 mm away from the centreline of the weld (Figure 3.7). The average cooling time of both materials was 14.5s. During the experimental procedure, the average of cooling time was 18s. Using the heat input of 14 kJ/cm, the numerical results indicated that the maximum temperature in the QT steel and TMCP steel was approximately 1,400 °C (T_1) and 1,300 °C (T_2). The respective numerical and experimental cooling time results gave 24.85 and 30.45 s. when a heat input of 17 kJ/cm was applied, the numerical results indicated that the maximum measured temperatures in the QT steel and TMCP steel were about 1,600 and 1,400 °C, with average values of the respective numerical and experimental cooling time of 29.45 and 36 s.

From both results (numerical and experimental), a considerable gap between a numerical and experimental data was observed. The average of the deviation was estimated at 12% high in the experimental data. Figures 4.3c, d, and e showed a comparison between numerical and experimental curves. The average cooling time increased to 8.5% compared to numerical modelling when it was applied to an experimental process. This gap is considered acceptable if the analysis takes into account the sensitivity and the recordability of the temperature (600-1,350 °C) of the TCS. The modelling method was applied to other dissimilar materials used in this thesis. The results are presented in Table 4.2. For example, the numerical cooling time calculated was 29.45 s, when using the heat input of 10 kJ/cm, less compared to experimental results measured (31.00 s). The outcome from this result is the reduction of the gap between both methods.

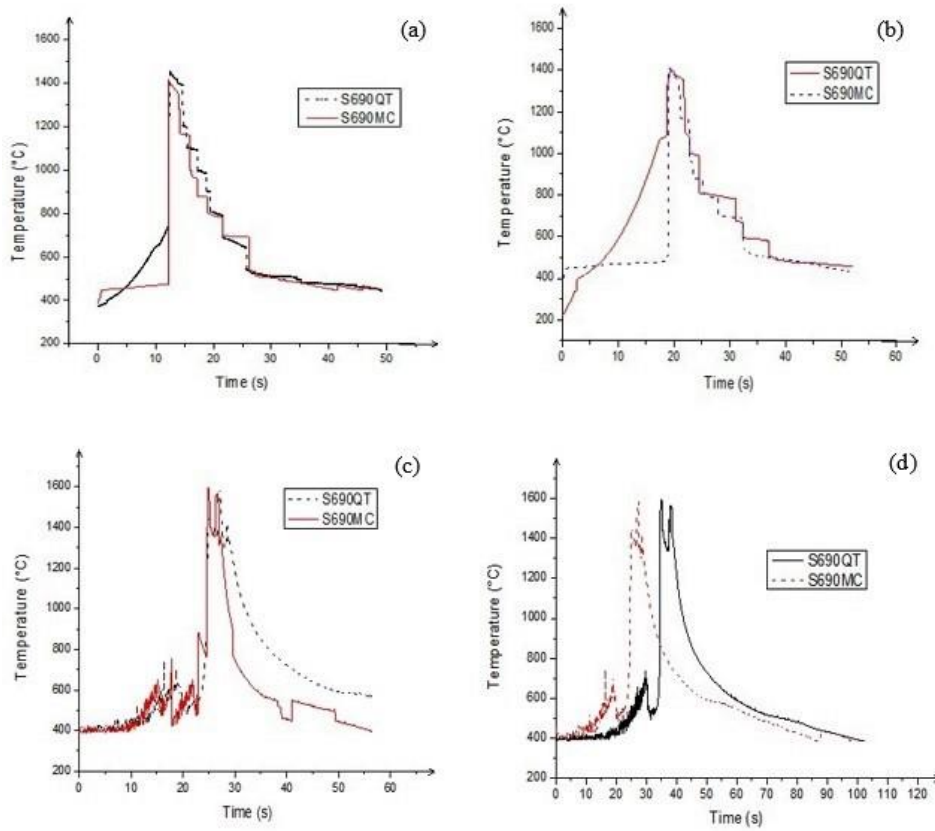


Figure 4.2: Thermal cycle data from modelling and experimental results: (a) thermal cycle data from modelling using 10 kJ/cm of heat input, (b) thermal cycle data from modelling using 14 kJ/cm of heat input, (c) thermal cycle data from modelling using 17 kJ/cm of heat input, (d) thermal cycle data from the experiment using 10 kJ/cm of heat input.

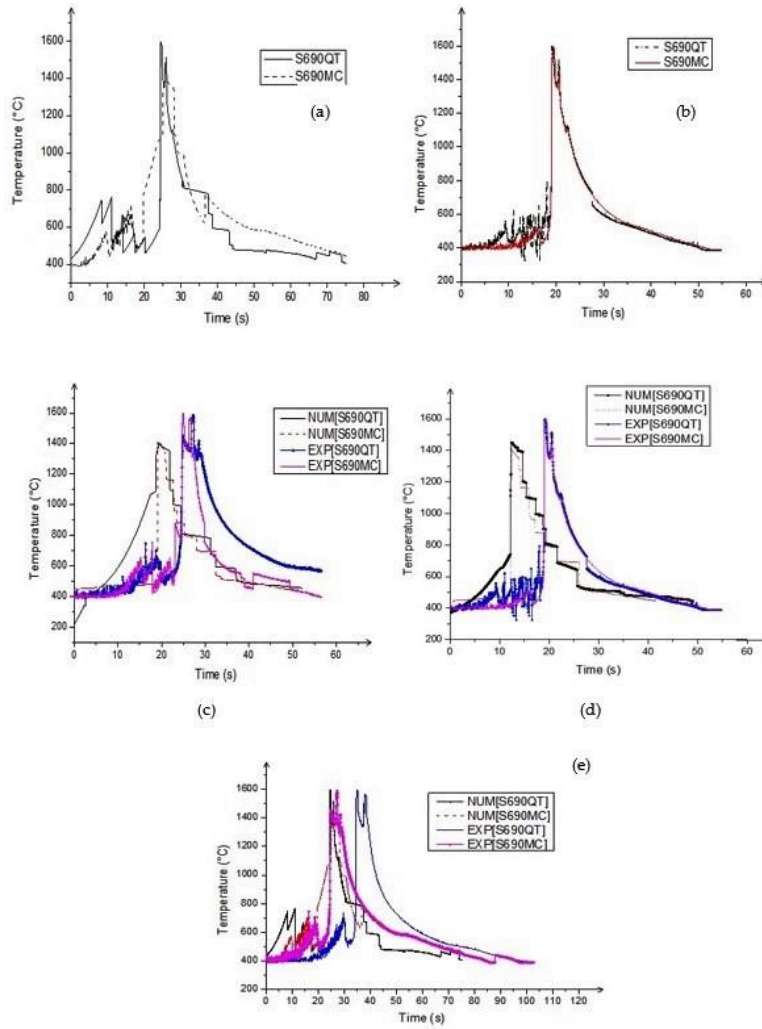


Figure 4.3: Comparison between thermal cycle data obtained using modelling and experimental results: (a) experimental results using 10 kJ/cm, and (b) experimental results using 14 kJ/cm. (c) comparison using 10 kJ/cm of heat input, (d) comparison using 14 kJ/cm, and (e) comparison using 17 kJ/cm of heat input.

From the thermal cycle, any specific details related to the difference in coefficient of thermal expansion or thermal diffusion between two metals are not observable. It was observed an unsymmetrical temperature distribution in the HAZ of both materials, which is due to the sensibility of the equipment and the effect of dilution areas between weld metal and different HAZ. It is assumed that the increase of heat input was the result of change of the physical distance (7 mm) from the centreline of the weld to the measurement point. Figure 4.4 presents the cross-section of the weld joint, which shows

the initial weld geometry and the weld metal. It can be seen from the figure that the weld metal influenced the measurement process due to the propagation across the HAZ.

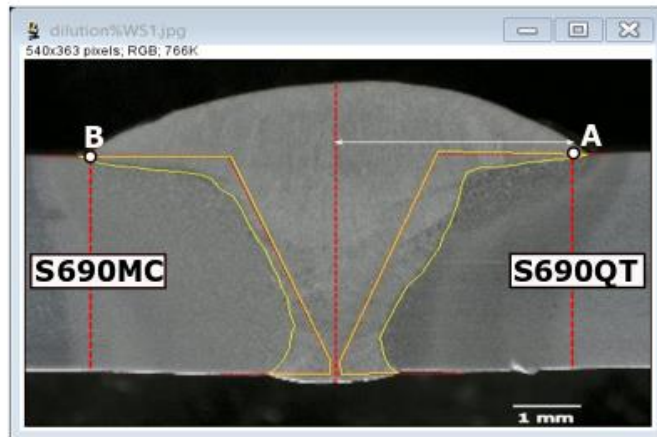


Figure 4.4: Cross-section of the welded joint showing the dilution zone coverage by weld metal and its influence in the unsymmetrical thermal cycle measurement in the HAZ.

Table 4.1 presents numerical and experimental results of cooling time, the maximum temperature evaluated in the CGHAZ of both materials. The temperature was distributed asymmetrically, and the maximum temperature occurred in the S960QC part. The higher temperature (calculated and measured) was evaluated when the heat input was higher (1,200 °C). The grain size, its distribution and the hardness will strongly dependent on the increase or not of the cooling time results.

Table 4.1: Numerical and experimental data showing: the temperature in CGHAZ of each material and the cooling time obtained when dissimilar S700MC/S960QC steels analysed

Filler wire used	Heat Input values kJ/cm	S700MC/S960QC					
		Num. Data			Exp. Data		
		S700MC T ₂ (°C)	S960QC T ₁ (°C)	t _{8/5} (s)	S700MC T ₂ (°C)	S960QC T ₁ (°C)	t _{8/5} (s)
NiCrMo700	7	610.00	745.00	11.52	830.00	910.00	13.00
	10	780.00	980.00	29.45	890.00	1000.00	31.00
	15	850.00	1020.00	42.45	910.00	1100.00	47.00
EN ISO 16834-A - G 89 5 M21 Mn4Ni2,5CrM	7	810.00	900.00	12.58	890.00	940.00	14.12
	10	890.00	980.00	24.89	910.00	1050.00	27.00

o AWS A5.28: ER120S	15	910.00	1200.00	41.58	1000.00	1300.00	45.00
------------------------	----	--------	---------	-------	---------	---------	-------

4.2 Microstructure characterisation

The sub-section presents the results of experiments on dissimilar butt joint welds of S690TMCP/S690QT and dissimilar S700MC/S960QC steels. The experiment is an evaluation of the microstructural constituents and alloying elements formed in the HAZ and weld metal. The sub-section presents optical microscopy, SEM microscopy test, EDS mapping, and the relation between the thermal cycle and hardness in the HAZ.

4.2.1 Microstructure of dissimilar S690QT-TMCP steels

Figure 4.5 describes the cross-section of the weld sample with a different subdivision of the HAZ of both materials, which presents the microstructure of the QT and TMCP steels. The figure indicates four subzones which include the base material (BM), subcritical HAZ (SCHAZ), inter-critical HAZ (ICHAZ), fine grain HAZ (FGHAZ), coarse grain HAZ (CGHAZ), and weld metal (WM).

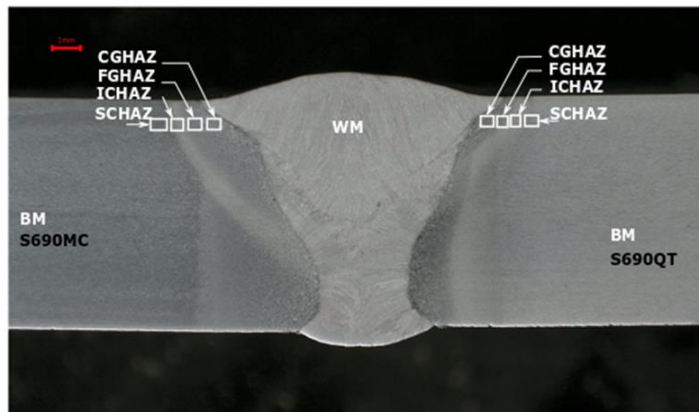


Figure 4.5: Cross-section of the weld joints indicating four subzones used for SEM and optical microscopy investigations.

The microstructural constituents in the HAZ of QT steel are shown in Figure 4.6 and its microstructure varied continuously with local temperature. The typical microstructure of QT steel, consisting mainly of martensite and bainite, is shown in Figure 4.6a. According to ASTM E112-13, the initial austenite grain corresponds to grain size 12 (5.6 μm). BM microstructure is homogeneous, and in-equigranularity is not observed. Because of its limited carbon content of up to 0.15, lath martensite is produced, and the formation of twinned martensite is prevented.

SCHAZ (Figure 4.6b) was the region of the HAZ that has been subjected to peak temperatures below the lower critical point (500 - 750 °C). Processes of nucleation and spheroidisation of carbides occur in this zone. Black cementite conglomerates can be identified. The agglomeration of spheroidised cementite particles at grain boundaries and triple junctions emphasizes the role of grain boundaries as high diffusivity channels for carbon at these low temperatures. The ICHAZ (Figure 4.6c) refers to the HAZ regions that have been subjected to peak temperatures between the lower and upper critical points (Ac_1 and Ac_3), typically between about 750 °C and 850 °C. In this region, the austenite regions decompose to different degrees and thus to different transformation products. The microstructure in this region consists of a mixture of bainite, martensite, and some trace of pearlite. Spheroidization and coagulation of carbides, mostly cementite, also occur. The FGHAZ (Figure 4.6d) refers to the HAZ which was subjected to peak temperatures between the upper critical point Ac_3 and the austenite grain coarsening temperature, typically between about 850 and 1100 °C. The CGHAZ and FGHAZ are both zones that have become fully austenitic due to the weld thermal cycle (1100 - 1500 °C). After γ to α transformation, the microstructure of these zones changed progressively depending on the previous austenite grain size.

During the cooling process, a large transforming grain broke down to form fine grains at a temperature of around 720 °C. Two main grains were identified: bainite and lath martensite (with low carbon). Martensite and bainite were distinguished by their entirely different etching susceptibilities, as shown by the optical micrographs (Figure 4.6e). Since the bainitic transformation occurs at a higher temperature compared to the martensitic transformation, carbon can diffuse to a greater extent, either to the remaining austenite islands or the boundary between laths. The martensitic transformation is characterised by the reaction that takes place in the microstructure during cooling phase causing the formation of the acicular structures called “martensite”. The WM is exposed to a temperature above the liquidus line, which is called the weld interface. This zone is in a partially melted state at such temperatures. After cooling, the weld interface has a mixed microstructure that contains bainite and polygonal ferrite (Figure 4.6f).

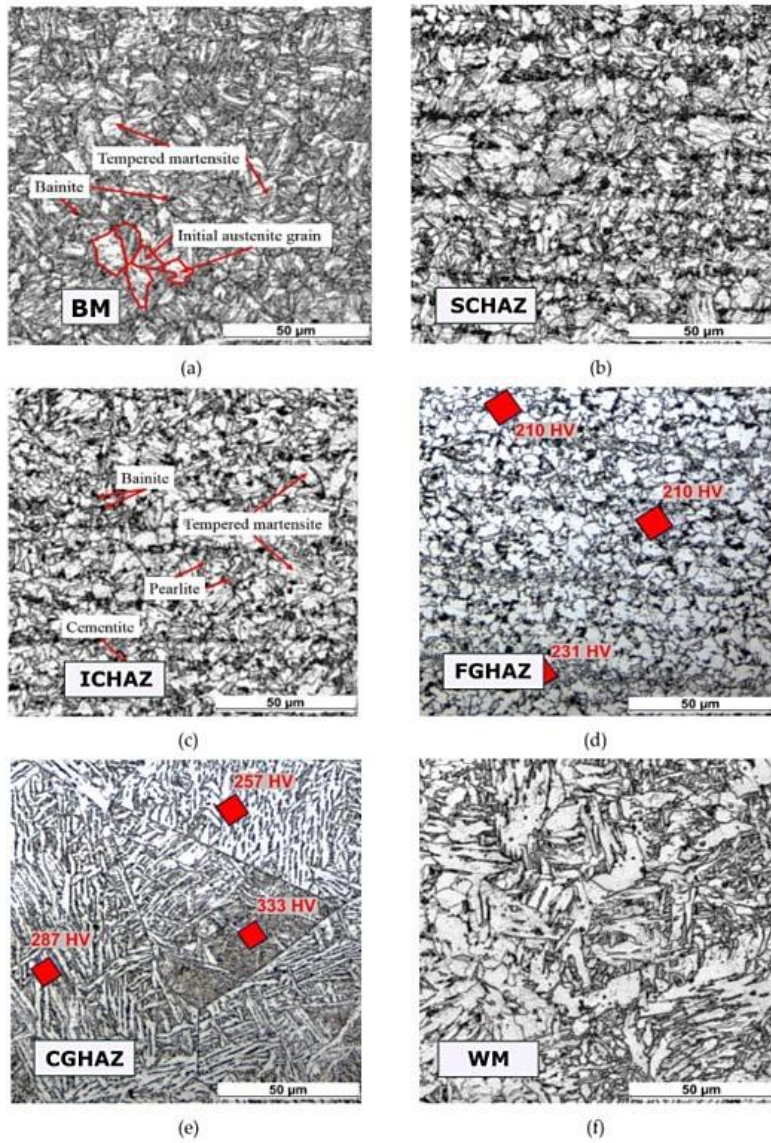


Figure 4.6: Optical micrograph of sample cooling at 31 s. Microstructure of S690QT-steel in the different parts of the HAZ showing: (a) the base material composed by B and M, (b) subcritical HAZ, (c) apparition of cementite, pearlite B and M in the inter-critical HAZ, (d) fine-grain HAZ, (e) austenite form in the coarse grain HAZ, and (f) bainite and polygonal ferrite in the weld metal.

The TMCP steel in this thesis was a high-strength low alloy structural steel manufactured by thermo-mechanically controlled processing. This steel contained about 0.05% less carbon than QT steel (Table 3.3). The reduction in carbon content allowed considerable

improvement in the low toughness of the BM. The microstructure of the BM consists of 70% bainite and 30% ferrite (Figure 4.7a). The effective grain size of the BM corresponds to ASTM E112 grain size 14 (3.0 μm). The SCHAZ and ICHAZ regions of the TMCP steel can be hardly distinguished, unlike the HAZ of the QT steel (Figure 4.7b-c). The reason for this view is the low carbon content in the TMCP steel, which means that heating to temperatures around critical point A_{c1} does not produce large-scale nucleation of cementite and its coagulation. The finest grain and uniform structure within the HAZ of the TMCP steel is observed in the FGHAZ (Figure 4.7d). The microstructure contains mostly polygonal ferrite and dispersed islands of bainite forms.

The microstructure of the CGHAZ (Figure 4.7e) formed during the welding thermal cycle consisted of the products of bainite formation in the austenite grain. These microstructures were classified as bainite, which can take many morphologies. Bainitic ferrite, which consists of a carbide-free ferrite matrix with well-defined islands of the retained of austenite or martensite-austenite (M-A) constituent, was one of the microstructures commonly found in the HAZ of the welds in this thesis. The microstructure of ferrite contains dispersed retained austenite or M-A constituent in the featureless matrix many of which retain the prior austenite grain boundary structure. In the micrographs, most prior austenite grain boundaries are visible, allowing the mean austenite grain size to be measured. The weld metal (Figure 4.7f) is the zone generally subjected to the peak temperature. Initial columnar grains formed by epitaxial growth are seen, indicated by the presence of grains of polygonal ferrite and Widmanstätten ferrite along the former grain boundaries. However, the main constituent is an acicular ferrite.

The first phase forming at prior austenite grain boundaries during cooling below A_{c3} temperature is referred to as polygonal ferrite. At relatively low undercooling, Widmanstätten ferrite formation occurs. The ferrite plates grow rapidly with a high aspect ratio, resulting in parallel arrays. Widmanstätten ferrite plates grow directly compared with a prior austenite grain boundary or polygonal ferrite at the grain boundaries. Acicular ferrite is recognised as an intragranular nucleated morphology of ferrite in which there are multiple impingements between grains. Acicular ferrite nucleates were observed on inclusions inside the prior austenite grains during the cooling process. Provided there is a high density of inclusion, a fine interlocking structure is produced.

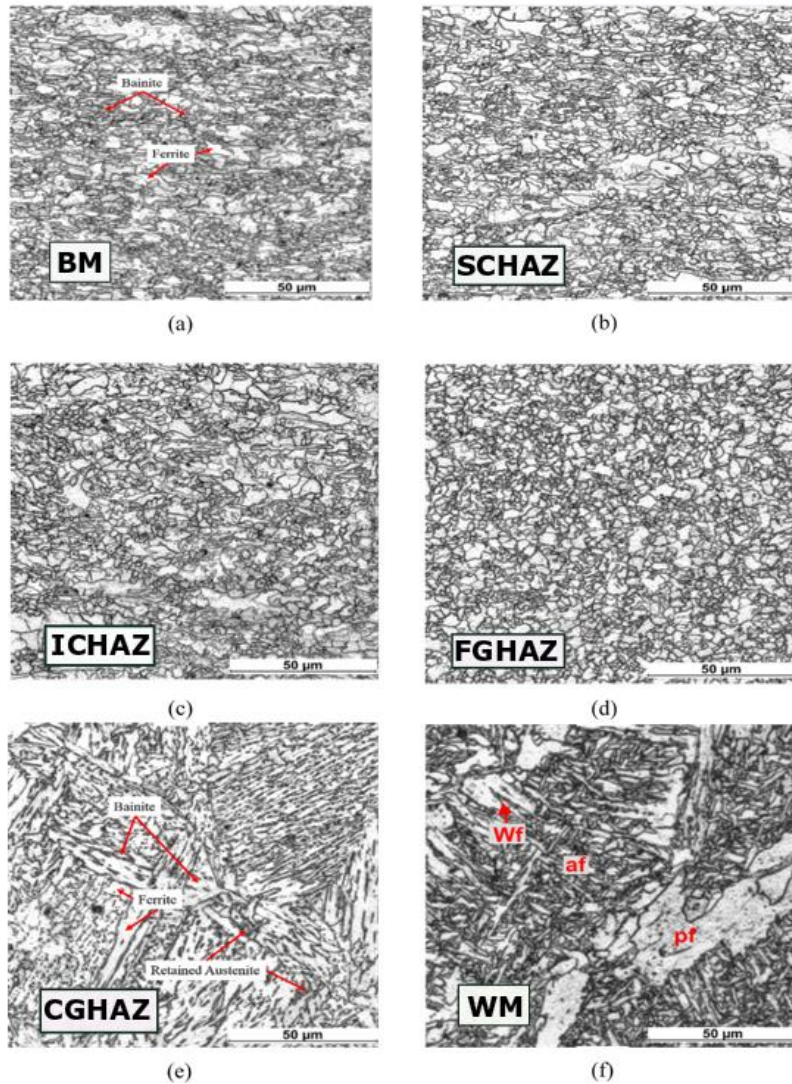


Figure 4.7: Optical micrograph of sample cooling at 31 s. Microstructure of S690TMCP steel HAZ showing: (a) microconstituent of Bainite and ferrite in the base material, (b) the same microconstituent in the subcritical HAZ, (c) mostly polygonal ferrite and dispersed islands of bainite forms in the inter-critical HAZ, (d) same configuration in the fine grain HAZ, (e) mostly bainite with carbide-free ferrite matrix and some retained of austenite in the coarse grain HAZ, (f) widmanstätten ferrite, polygonal ferrite and acicular ferrite in the weld metal.

4.2.2 Microstructure of S700MC-S960QC weld sub-zones using undermatched filler wire

Figure 4.8 shows the cross-section of the welded joint of dissimilar S700MC/S960QC steels. In HAZ on both sides of the WM, distinctive subzones of different microstructure constituents can be distinguished. The subzone showing the coarse grain HAZ is indicated in red colour (A) and the fine grain HAZ in yellow colour.

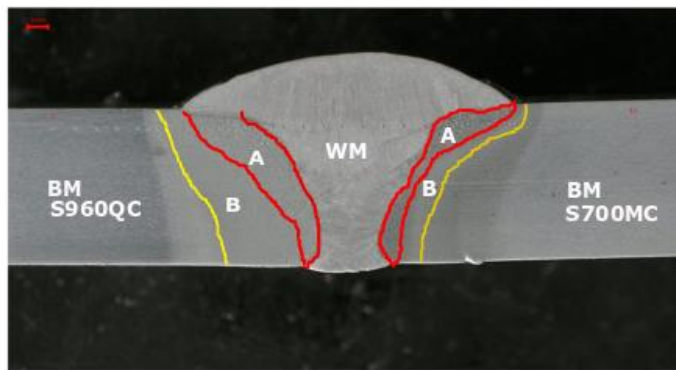


Figure 4.8: Weld joint cross section showing different subzone used for SEM and EDS microscopy investigations. (A) coarse grain HAZ area, (B) fine grain HAZ area.

Figure 4.8 shows a direct microstructural constituent and a comparison between the HAZ and base metal microstructures of S700MC steel using undermatched filler wire. In S700MC steel, the microstructure is a mixture of 70% of bainite and 30% of ferrite. The special characteristic of the manufacturing of this steel is the microstructural control technique, which is a combination of controlled rolling and controlled cooling during production. The microstructure is described as sub-zones, which were identified in this analysis as a CGHAZ (Figures 4.9c, d) and FGHAZ (Figures 4.9e, f). The WM and CGHAZ were subjected to the peak temperatures, which can lead to re-austenisation of the grain structure. Figure 4.9b presents an OM image of the CGHAZ of S700MC, which resulted from high temperature above the austenisation temperature (1,100 °C) over an extended period and generated increased grain size.

Evaluation of the percentages of the microstructural constituents showed that a bainite constituent (40% of volume fraction), grain boundary ferrite (50%) and some trace of retained austenite (10%) in the CGHAZ. The percentages of the microstructural constituents in the FGHAZ showed that the S700MC steel contained more bainite (60%), some carbide-free ferrite (30%), and some amount of retained austenite (10%). So, the relative proportion of ferrite decreased as a result of the limited temperature in that area of HAZ.

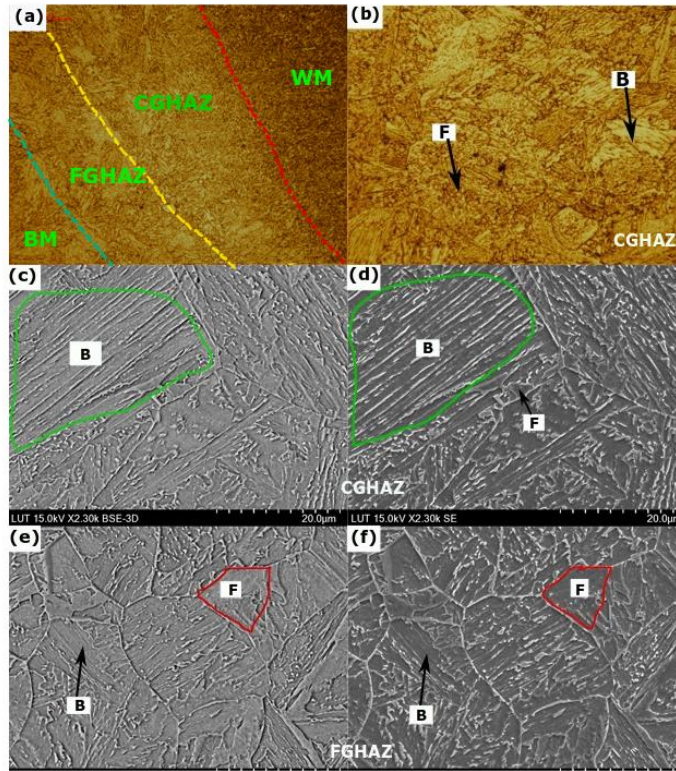


Figure 4.9: Optical micrography and SEM micrography of sample cooling at 31 s. Microstructure of the cross-section of S700MC in sub-zones of the HAZ showing: (a) different sub-zones, (b) coarse grain heat affected zone of optical micrography images, (c), (d) bainite, grain boundary of ferrite and some island of retained of austenite in the coarse grain heat affected zone, (e), (f) bainite, some carbide-free ferrite and retained of austenite in the fine grain heat affected zone.

The 960QC steel was quenched and tempered at 960 MPa and had a composition of 60% bainite and 40% martensite. The sub-regions inspected in the HAZ were the BM, CGHAZ, and FGHAZ.

In the CGHAZ of test sample, bainite, some trace of martensite with and primary grain boundary ferrite were the main microconstituents. The formation of microstructure with high bainite content is especially favourable for mechanical properties of the weld and the HAZ. The percentages of the microstructural constituents in the FGHAZ showed that S960QC steel contained more martensite. It was observed some retained of austenite in the microstructure. Figures 4.10e, f illustrate the microstructural constituents over the FGHAZ.

Figures 4.10g, h show the microstructure of WM, where two types of ferrite were observed in the transformation: pro-eutectoid ferrite (PF) and acicular ferrite (AF) at the temperature of approximately 1,100 °C, at which solidification starts.

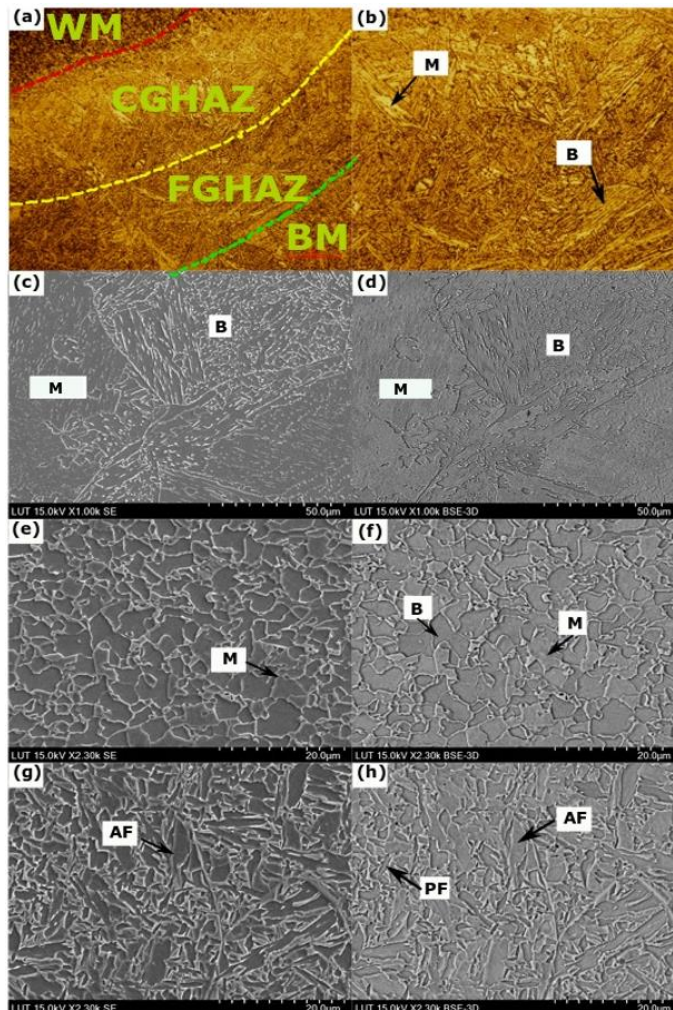


Figure 4.10: Optical microscopy and SEM micrographs of sample cooling at 31 s. Microstructures of cross-section of S960QC in sub-zones of HAZ showing : (a) different sub-zones, (b) coarse grain heat affected zone using optical microscopy images, (c), (d) mixture of bainite-martensite in the coarse grain heat affected zone, (e), (f) martensite with some bainite forms in the fine grain heat affected zone, (g), (h) polygonal and acicular ferrite in the weld metal.

Based on SEM micrograph samples, measurements were carried out directly on the images of both materials focusing on the CGHAZ and FGHAZ areas. The images were uploaded to the image processing software (ImageJ Pro) which analysed different volume fractions of grain (Bayock F, 2019). Figure 4.11 shows the volume fraction of microstructure constituents of bainite, ferrite, martensite and retained of austenite evaluated during the process. A continuous cooling transformation (CCT) diagram compiled from different measurements for S700MC and S960QC are presented in Appendix C: Figures 4 and 5. The bainite start (B_s) and martensite start (M_s) temperature have been estimated using empirical equations (Honeycombe, 1995).

For S700MC steel with cooling time of 13s and 31s, bainite start transformation began between 420 and 500 °C, while for $t_{8/5}$, B_s increased slightly to the temperature of 615 °C. Figure 4.11a shows the maximum value of the volume fraction of bainite (60%) which was observed at the temperature of 500°C. Figure 4.11b presents two results separately: the volume fraction of ferrite, which had a maximum value of 43% observed at the temperature of 615 °C, and the volume fraction of retained of austenite with a maximum value of 15% at 615 °C. Figure 4.11c shows the volume fraction of bainite, evaluated in S960QC side, which peaked at around 55% at the temperature of 550 °C. Figure 4.11d has two graphs which show the respective volume fractions of martensite and retained of austenite. The volume fraction of martensite increased (58%) at a temperature of 400 °C, which corresponded to the cooling time of 13s.

This result confirmed the choice of thermal cycle when the heat input of 10 kJ/cm ($t_{8/5}$ of 31 s) was used, which developed the best combination of bainite (55%), ferrite (25%) and retained austenite (20%) microstructural constituents for S700MC, and bainite (50%), martensite (40%), retained of austenite (10%) microstructural constituents for S960QC.

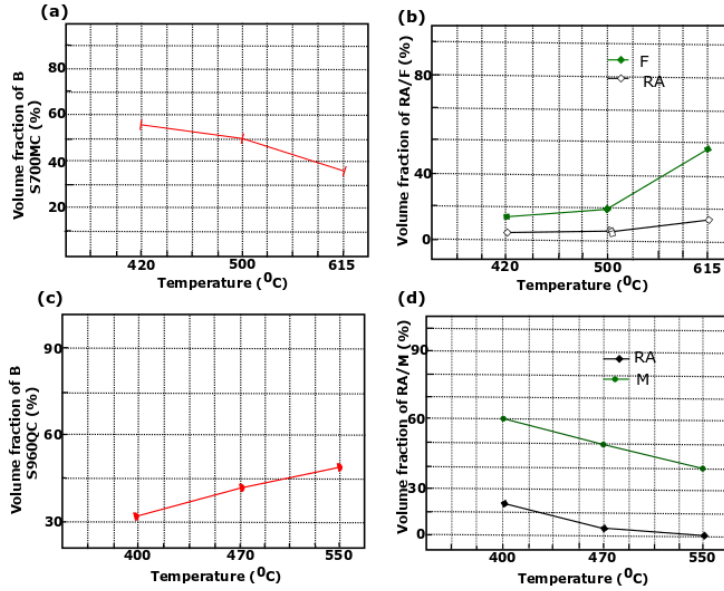


Figure 4.11: Distribution of volume fraction of microconstituents for different cooling conditions (undermatched filler wire). (a) volume fraction of B for S700MC; (b) volume fraction of RA and F for S700MC; (c) volume fraction of bainite of S960QC; (d) volume fraction of martensite of S960QC.

The alloying elements composition in the CGHAZ of both materials and weld metal (WM) was analysed using EDS spectrum. The specimens were measured with point surface analysis. Figure 4.12 shows the mapping and spectra records for alloying elements in S700MC (Figure 4.12a) and the same information for S960QC (Figure 4.12b). The data were recorded in weight %, which presents the percentages of C, Ni, Mo, Cr, Mn, Si, and Fe. The result showed that a higher carbon content measured in both sides can be justified by two possibilities: the presence of contamination which is caused by the pollution of the sample surface. But the samples were polished and cleaned using an ultrasonic bath of hot C_3H_6O and C_2H_6O to ensure any impurities were removed. The second reason is the measurement method itself. The method used in these experiments was point surface. The responsible content of carbon in the case in point can be a small peak, for example for cementite or carbides. Based on this sample, the error is respectively big in comparison to the other elements. The alloying element composition resulting from another test area of CGHAZ showed stability of allowing element composition compared to the BM alloying element composition (Appendix C: Figure 7).

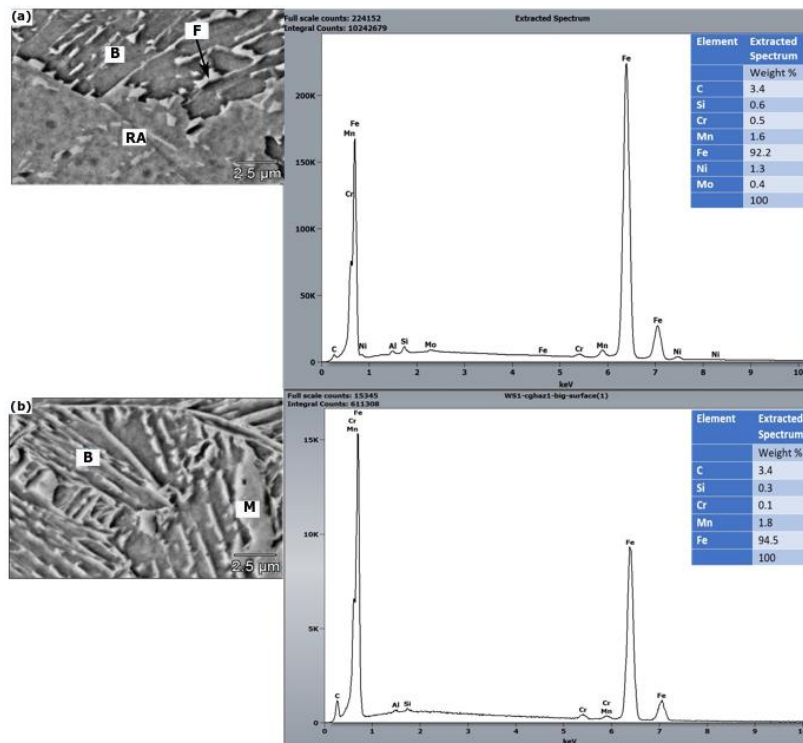


Figure 4.12: SEM micrograph of sample cooled at 31 s and EDS spectra from different positions of the weld joint, indicating chemical composition of different allowing elements of dissimilar S700MC/S960QC using undermatched filler wire: (a) increase of Ni (1.3%) in the coarse grain HAZ of S700MC, (b) increase of Mn (1.8%) in the coarse grain HAZ of S960QC.

4.2.3 Microstructure of S700MC-S960QC weld sub-zones using overmatched filler wire

Selected results from microstructure investigation with SEM micrographs are presented in Figure 4.13. It was found that, at the cooling time of 31 s, the microstructure changed from that of a very fine scale morphology to one with more coarse grains. A direct comparison was performed between the HAZ and BM microstructures of S700MC and S960QC using overmatched filler wire.

The two steels show some differences in the higher thermal cycle HAZ. The microstructure of S700MC was more bainite (70%) with some ferrite (30%). In the S960QC grade, the microstructure was a mixture of bainite and martensite. Figure 4.13 (a) shows the microstructure of the FGHAZ of S700MC at a distance of 2 mm from the fusion boundary. The micrograph shows the austenite grain size can be identified in the fine grain. Moreover, it appears that the amount and morphology of the formed phase have, to some extent, been influenced by the thermal cycle. Bainitic phase is dominant in

this microstructure. On the S960QC side (Figure 4.13b), martensite dominates in the FGHAZ. The bainitic phase dominated in the CGHAZ of S700MC (Figure 4.13c). It can be seen in the figure that the coarse laths of lower bainite (B_L) generally partition the prior-austenite grains intersecting each other (Guo 2010). Figure 4.13(d), which refers to the CGHAZ of S960QC the micrograph, indicates a two-phase structure consisting of mixed bainite-martensite and some retained austenite. The microstructure constituent in the WM metal (Figure 4.13e) is mainly formed by WF and AF.

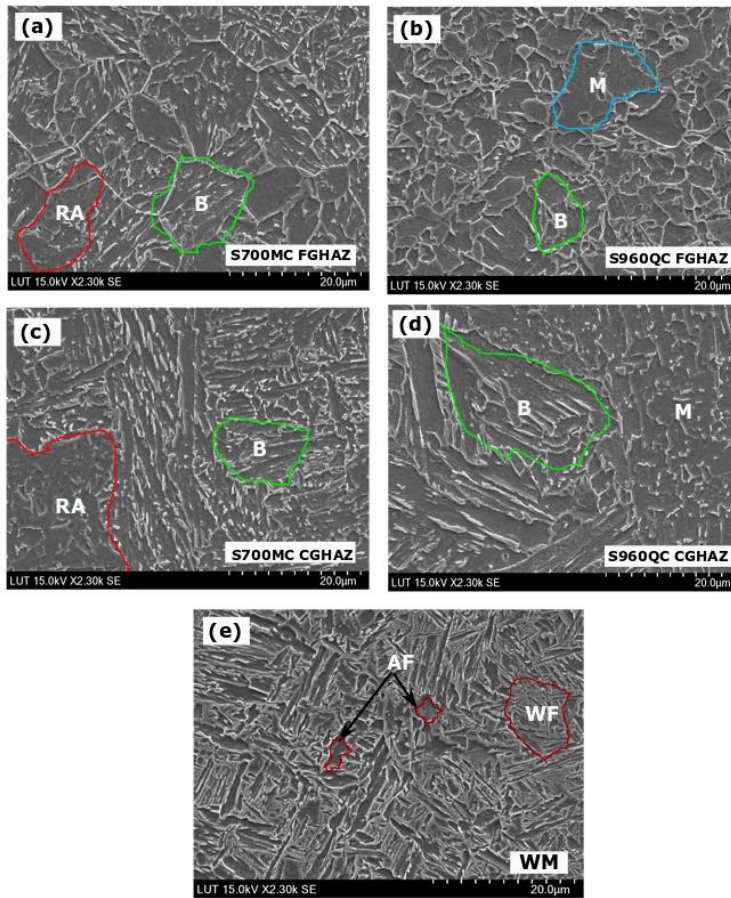


Figure 4.13: SEM micrograph of sample cooling at 31 s. Microstructure of dissimilar weld joint using overmatched filler wire: (a) bainite formation and some retained of austenite in the fine grain HAZ of S700MC, (b) mixture of bainite-martensite in the fine grain HAZ of S960QC, (c) ferrite and some bainite islands in the coarse grain HAZ of S700MC steel, (d) bainite formation and some trace of martensite in the coarse grain HAZ of S960QC steel, and (e) widmanstätten ferrite and some acicular ferrite island in the weld metal.

Figure 4.14 shows the ratios of the microstructural constituents of ferrite (F), bainite (B), martensite (M), retained of austenite (RA), and A_{C1} temperature of both steel welds during determination in the simulations. The plots indicate the ratios of ferrite, bainite, and martensite determined in the welded joint HAZ of both steels. Figure 4.14a suggests that, at A_{C1} (500 °C) point, bainite has a ratio of 60%, ferrite a ratio of 30%, and retained austenite a ratio of 10%. Within the temperature range from 615 °C, which is obtained with an increase of the heat input at 15 kJ/cm, the ratio of ferrite increases (50%), and the ratio of bainite decreases to 40%. The ratio of retained of austenite will remain at 10%.

On the other side, the bainite martensite is distributed in the S960QC steel HAZ. At 550 °C, most bainite is determined, having a ratio of 55%. The martensite ratio in that point was 30% and the retained of austenite has a ratio of 15% which late will be transformed into martensite-austenite (M-A) microstructural constituents.

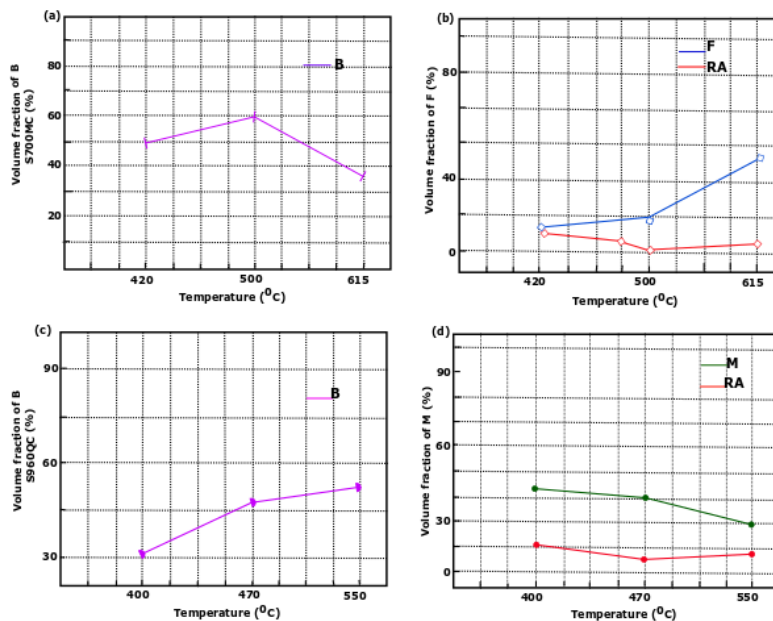


Figure 4.14: Distribution of volume fraction of microconstituents for different cooling conditions (overmatched filler wire). (a) volume fraction of B for S700MC, (b) volume fraction of F of S700MC, (c) volume fraction of B of S960QC, (d) volume fraction of M of S960QC.

Figures 4.15(a) (b) and (c) present an EDS scanning of dissimilar weld joint of S700MC/S960QC using overmatched filler wire. The mapping of the major alloying elements (Cr, Si, Mn, Ni, Mo) in the measured point of the weld metal is presented in (Figure 4.15a). It should be pointed out that C is excluded in the analysis due to uncertainty as a result of light element character. EDS spectrum of WM measured point (close to the fusion line between WM and CGHAZ) of S960QC side showed an increase of Ni content compared to the BM, which provides further evidence for diffusion of Ni

from weld metal into the area. Figure 4.15(b) provides a comparison between the alloying element composition of CGHAZ of S700MC and BM. It should be noted that wt.% of C is excluded from the results for the reasons mentioned above. The results revealed that the solidification occurs with the relation Cr_{eq}/Ni_{eq} . Figure 4.15(c) shows the EDS measurement of CGHAZ of S960QC. The results presented an increase of Mn and the absence of Cr alloying element composition. Other tests showed some stability in the composition of alloying elements compared to the BM (Appendix C: Figure 8). The composition of the weld metal was more homogeneous when the heat input of 10 kJ/cm was applied. The decrease of this heat input caused considerable disparities in the composition of alloying elements (Cr, Mn, Ni, and Mo).

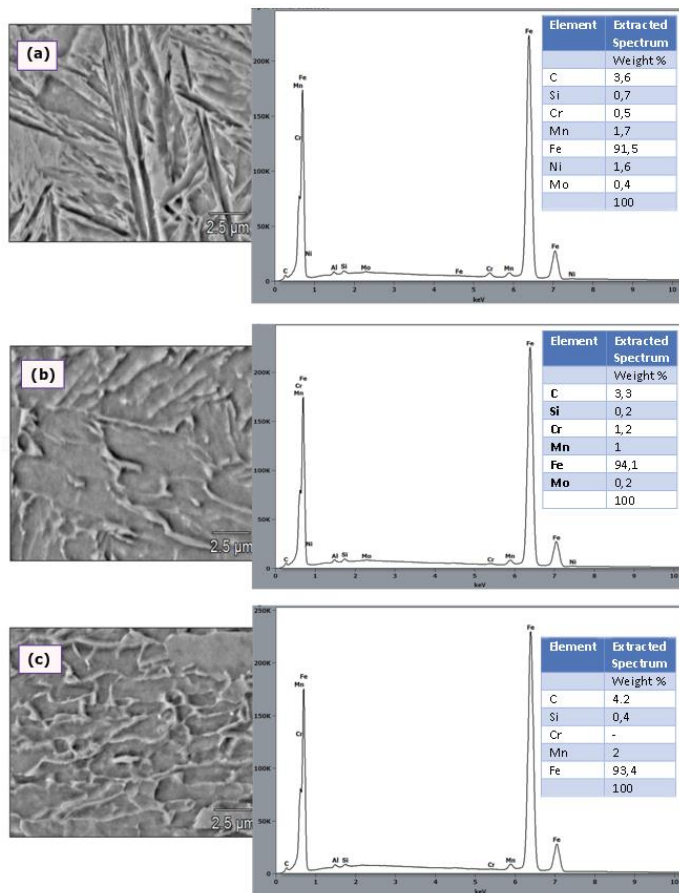


Figure 4.15: SEM micrograph of sample cooled at 31 s and EDS spectra from different positions of the weld joint, indicating chemical composition of different alloying elements of dissimilar S700MC/S960QC using overmatched filler wire: (a) weld metal, (b) Mn decrease (1%) in the coarse grain HAZ of S700MC, (c) Mn increase (2%) in the fine grain HAZ of S960QC.

4.3 Vickers-hardness results

The sub-section presents the results of experiments on dissimilar HSS of S690TMCP/S690QT and S700MC/S960QC weld joints. The experiment is an evaluation of softening in the HAZ caused by the heat input variations. The sub-section provides the hardness results along the weld joints. Micro hardness and Vickers-hardness tests were applied in this analysis.

4.3.1 Micro-hardness of dissimilar S690QT-TMCP steels

The experimental data show that the HAZ of the same grade steels with different chemical composition and initial microstructure can differ significantly for the same welding conditions. Naturally, the local mechanical properties of the HAZ and consequently the mechanical properties of the weld joints can also be substantially different. The microhardness profile shows the heterogeneity of the welded joints (Figure 4.16). Figure 4.16 shows the microhardness of both steels, which is about 270 HV0.1 for S690QT and 290 HV0.1 for S690MC. The hardness of the weld metal is also virtually identical (230 HV0.1). The weld metal is undermatched, and the yield stress of the filler metal is 72% of that of the base metal. Coarse grain regions are very different for the two steels: 268 → 310 HV0.1 for the QT steel, and 248 → 260 HV0.1 for the TMCP steel.

In the first case, the sharp increase in hardness can be explained by the formation of bainitic martensitic microstructure constituents and grain growth. In the second case, the hardness drop is caused by primary recrystallization of the microstructure and the formation of more equilibrium products of austenite decomposition during cooling. Both steels show lowest hardness in the fine grain region due to the formation of predominantly polygonal ferrite. With heating between A_{C1} and A_{C3} (ICHAZ), the austenite composition in the microstructure varies from 0 to 100% depending on the local peak temperature. As the austenite transforms into ferrite during cooling, its fraction determines the hardness at the inter-critical heating region. The sub-critical HAZ (SGHAZ) area was much more impacted, with a meagre hardness value of 180 HV0.1 when the cooling time was high (36 s).

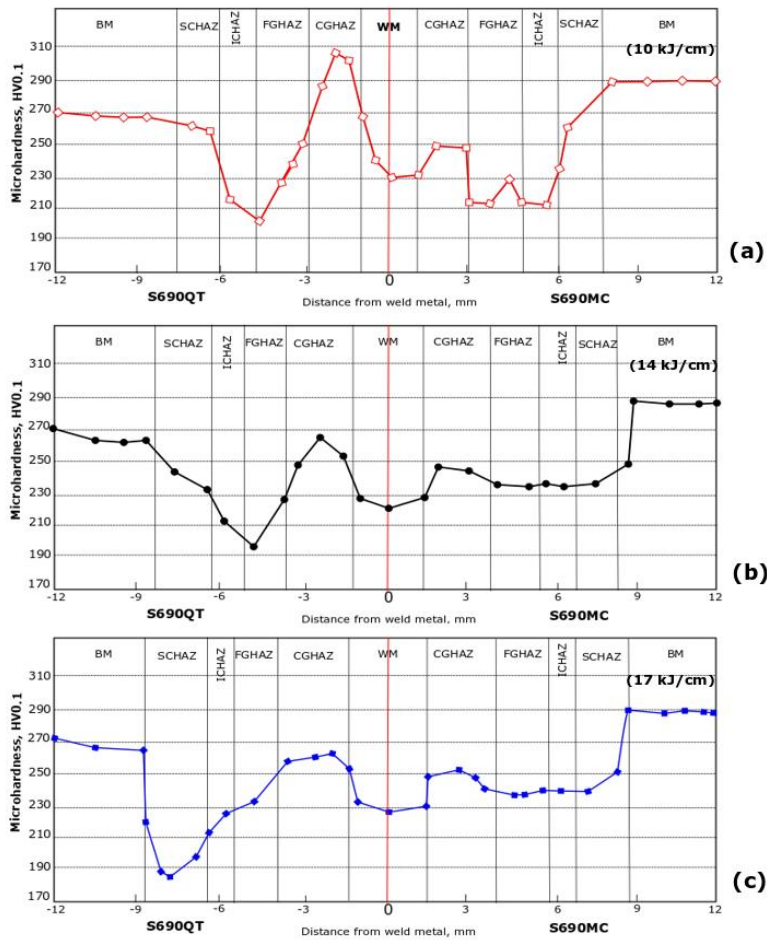


Figure 4.16: Microhardness profile of dissimilar weld joints of 690MPa of QT and TMCP steel: (a) hardness profile of 10 kJ/cm, (b) hardness profile of 14 kJ/cm, (c) hardness profile of 17 kJ/cm.

The width of the SGHAZ is different in both steels: in the QT steel, it is mainly determined by the width of the FGHAZ region, and in the TMCP steel, by the total width of the CGHAZ and FGHAZ regions. With increasing heat input from 10 to 17 kJ/mm (reducing the cooling rate), the hardness of the CGHAZ in the QT steel decreases from 300 to 250 HV0.1. The hardness of the HAZ metal heated slightly below A_{c3} decreases by 30% to 190 HV0.1. The TMCP steel shows almost the same hardness in the CGHAZ. In the FGHAZ, the hardness of the steel undergoes a greatest decrease, a 20% drop to 235 HV0.1. The width of the HAZ and its subzones significantly increase with increasing heat input. The width of the soft subzone in the TMCP steel is directly proportional to the heat input. With the growth in heat input from 10 kJ/mm to 17 kJ/mm, the region of reduced hardness (215-235 HV0.1) increases by 73%. HAZ softening phenomena can lessen the

strength of welded joints. The main reason for HAZ softening is high heat input, and heat input should be controlled and limited, especially for thick plates, as the softening effect of the welded joint is proportional to the plate thickness (Kim, 1999).

4.3.2 Vickers-hardness using undermatched filler wire

The hardness tests for welds with undermatched filler wire showed a decrease of hardness in the weld metal in comparison to the base material (Figure 4.17). Figure 4.17a (left) presents the hardness profile, which had a different area of the HAZ for both materials and weld metal. On the right side, the figure presents, in red, the measurement line at 2 mm from the top of the weld joint.

For the first sample (heat input of 15 kJ/cm), the lowest hardness occurred in the FGHAZ of S700MC, with a value of 210 HV5. The average hardness in the HAZ was 225 HV5. For S960QC, the lowest hardness occurred in the CGHAZ (240 HV5) in the fusion line (line between CGHAZ and WM). The hardness value in the WM area was not significantly increased (260 HV5). When comparing the two BM, the impact of the heat input was mostly seeing in the S700MC FGHAZ side. The use of undermatched filler wire also leads to a significant hardness drop in the HAZ of both materials and weld metal area (Guo, 2016).

Figure 4.17b shows the HAZ hardness map of dissimilar S700MC/S960QC using the heat input of 7 kJ/cm. The cross section of weld joint is represented in the right of the figure. The results clearly show that the average hardness value decrease of 8% (260%) in the CGHAZ of S700MC side compared to its BM. On the S960QC side, the average hardness measured was 300 HV5 lower compared to the BM (320 HV5). In the weld metal area, the hardness value was increased compared to the previous heat input.

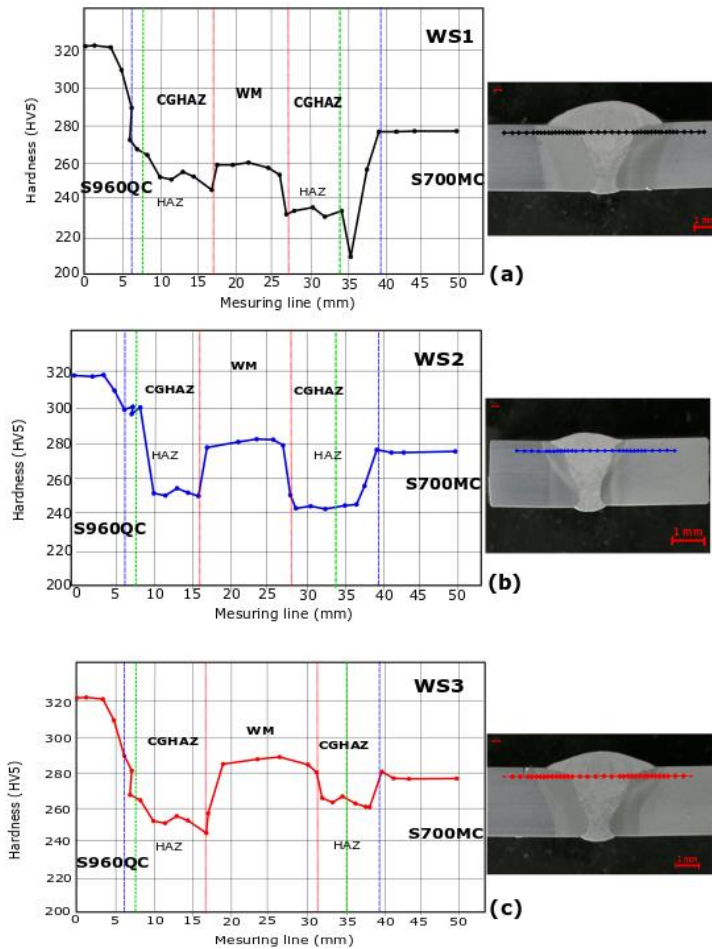


Figure 4.17: Hardness distribution on a cross section of S700MC/S960QC at the distance of 2 mm from the top of the weld joint using undermatched filler wire in the weld joint: (a) hardness profile of WS1, (b) hardness profile of WS2, (c) hardness profile of WS3.

4.3.3 Vickers-hardness using overmatched filler wire

Figure 4.18 shows the hardness (HV5) distributions of dissimilar S700MC/S960QC weld joints using overmatched filler wire. The S700MC HAZ has a region with lower hardness than the S960QC, i.e., a softening zone. The region is located in fine grain HAZ (FGHAZ) which is around 16% lower than the BM. Figure 4.18a shows the hardness distribution when the heat input of 7 kJ/cm was applied. The hardness of the weld metal was increased by 205 to 420 HV5. It can be noticed from the hardness distribution that HAZ softening is less severe in the S700MC side, with less than 5% decline in hardness at the lowest hardness level, close to the fusion boundary. This stability is due to the lower heat input value which causes a rapid cooling of the HAZ and forming hard and brittle structures

that can cause cracks (Coric 2011). In the S960QC side, the same stability was observed. The reason may be correlated with the martensitic phase in the microstructural constituents. In the CGHAZ toward the fusion boundary, the hardness values were stabilised in both sides.

Figure 4.18b shows the variation of hardness when the heat input of 10 kJ/cm was applied. The substantial reduction of hardness in some areas was observed, notably in the FGHAZ of S700MC and in the CGHAZ of S960QC. The hardness of these softening zones varies between 220- 240 HV5 in S700MC side, 250- 260 HV5 in S960QC side observable in Figure 4.18b. The significant contributors could be the attenuation of the dislocation of the new coarse grains formed from the inter-critical austenite at these regions (Guo, 2010) (Gorka 2018).

As can be seen in Figure 4.18c, it can be noticed from the hardness distribution that softening is more severe in this figure than previously. The reason is because of the increase of the heat input to 15 kJ/cm, which can lead to the formation of higher thermal cycle in the HAZ of both steels causing the increase of ratio of ferrite to austenite in the HAZ.

The weld metal has a higher hardness level, in the range of 380- 420 HV5 for the whole samples. The reason is the chemical composition of the fusion zone causing some macro segregation in the weld zone impacting the hardness measurements.

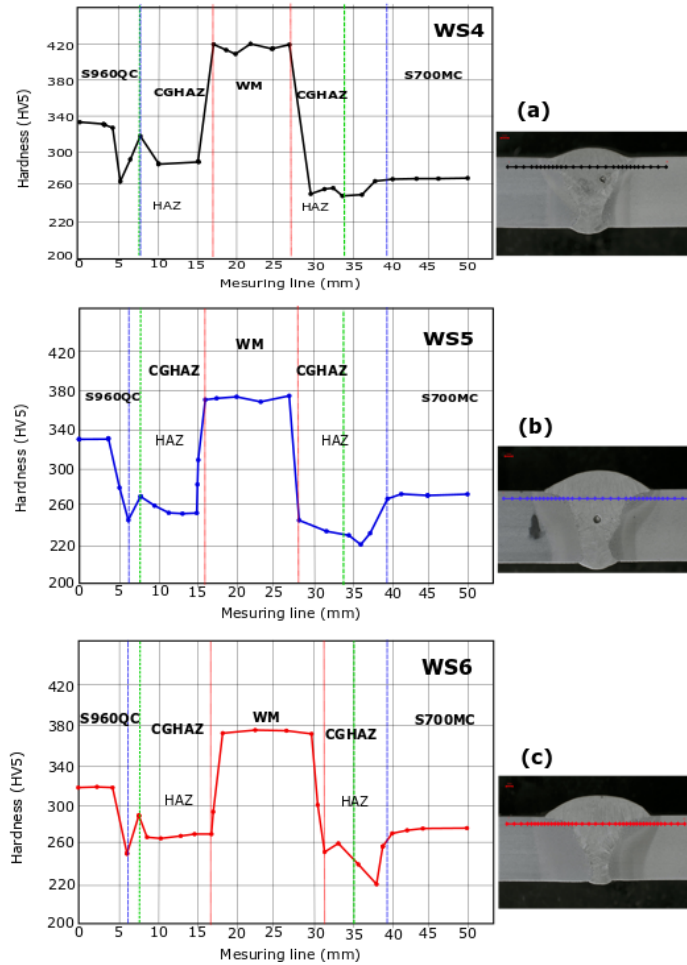


Figure 4.18: Hardness distribution at the distance of 2 mm from the top of the weld joint using overmatched filler wire in the weld joint: (a) hardness profile of WS4, (b) hardness profile of WS5, (c) hardness profile of WS6.

4.4 Tensile test results

The different yield strength (YS) and ultimate tensile strength (UTS) are shown in Table 4.2. Figure 4.19 displays the tensile test results, which reveal a failure in the fine grain HAZ of S700MC side. This may be a result of stress concentration at this soft region. As can be seen in Figure 4.19, increase in strength shows a direct relation with decrease of heat input. This result confirms the analysis that was conducted in the hardness profile (Figure 4.17 and 4.18).

There is a reduction in yield strength from the original 768 to 699 MPa for weld sample (WS1), from 768 to 756 MPa for WS2, from 768 to 707 for WS3, from 768 to 774 for WS4, from 768 to 755 MPa for WS5, and from 768 to 711 for WS6. In comparison, the ultimate strength of the specimens was 18% - 24% lower than that of the S960QC and sensibly the same than that of the S700MC.

Table 4.2: Yield strength and ultimate tensile strength. Tensile test results obtained from two replicates (Test A and Test B) for each sample. The average (Av.) quantities are calculated from Test A and Test B. The base materials values are also mentioned (data was taken from the manufacturing steel companies).

Specimen	Yield strength (N/mm ²)			Ultimate tensile strength (N/mm ²)			Elongation (%)
	Test A	Test B	Av.	Test A	Test B	Av.	
WS1	692.80	706.30	699.50	769.10	770.30	769.70	6.60
WS2	759.10	753.00	756.10	817.80	813.30	815.50	9.90
WS3	715.70	700.00	707.09	794.40	823.00	808.70	6.90
WS4	753.00	795.00	774.00	841.90	831.50	836.70	11.10
WS5	749.00	761.10	755.00	794.60	795.40	795.00	9.50
WS6	702.08	720.00	711.00	772.10	773.50	772.80	6.70
S700MC			768.00			822.00	12.00
S960QC			960.00			1005.60	18.00

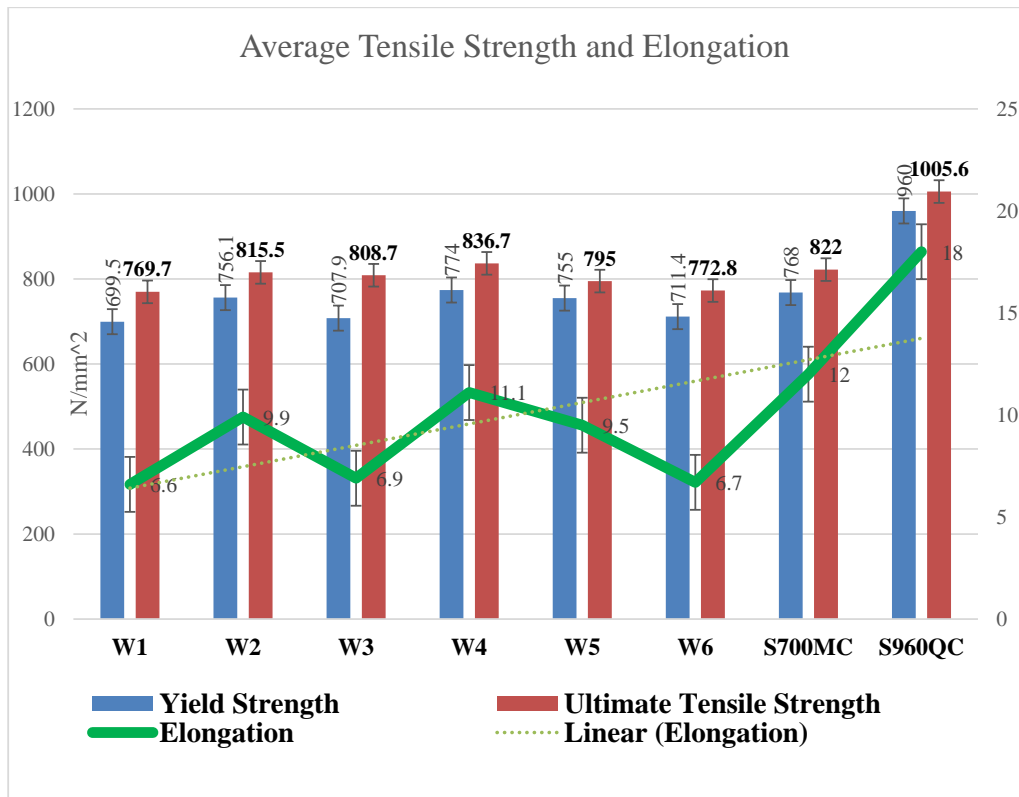


Figure 4.19: Comparison between the weld samples with the BM in terms of yield strength, ultimate Tensile strength as well as elongation (%).

The variation of elongation (%) of the specimen was important and did not show a clear correlation to the cooling time. Because of the significant mismatch between the mechanical properties of the BM and the WM, it will be interesting to analyse the elongation of the weldment through a standard tensile test. The concentration of strain and plastic deformation was mainly at the fine grain HAZ area of S700MC, which constitutes the softest region.

5 Overview of the publications

This section presents an overview of the publications used in this thesis. A more detailed description of the individual work can be found in the articles, *Publications I-V*. This section further summarises the findings of *I* and presents the results of *Publication II, III, IV*, and *V*.

Publication I: Experimental review of thermal analysis of dissimilar welds of high-strength steel.

Review of previous studies:

Previous studies in this article include reports published in scientific journals and other scientific literature. In addition, industrial reports and interviews having scientific value are also included.

Findings:

The dependency of life service of dissimilar HSS upon the mechanical and physical properties, microstructural stability (typically when the heat input change), and the resistance to oxidation and corrosion. The compatibility of filler metal with the selected base metals. The microstructural changes in the HAZ of dissimilar high strength steels can be severely observed when higher heat input is applied using GMAW process. The HAZ could be a characteristic of softening suppression due to the microstructural changes caused by the increase of cooling time. Applying a lower heat input could increase hardness and developed crack propagations in the weld metal.

Publication II: Numerical and experimental investigation of the heat input effect on the mechanical properties and microstructure of dissimilar weld joint of 690-MPa QT and TMCP steel.

Research objectives:

In this publication, numerical and experimental approach of thermal cycle measurement were developed. The method used dissimilar joint of 690-MPa QT and TMCP steel, which was carried out using three heat input values (10, 14, and 17 kJ/cm). The experimental method using GMAW process, thermal cycle sensor (TCS) was carried out to verify the numerical approach in order to improve the weldability of dissimilar HSS weld joints. The effect of heat input in the microstructure and Vickers-hardness of the HAZ were scientifically evaluated. The impact of hardness in the microstructural constituents of the HAZ was also analysed, which leads to minimising softening by proposing the required heat input that must be applied to improve the reconstructive transformation in the coarse grain HAZ (CGHAZ) of both steels.

Results:

The numerical model showed an acceptance confirmation with experimental validation of thermal cycles within a range of 7-19%. Table 5.1 shows comparative results of cooling time, average micro hardness, and microstructural constituents in the coarse grain heat affected zone (CGHAZ) of both materials.

The results show that it is possible to considerably apply the heat input of 10 kJ/cm which has a favourable response in terms of softening and HAZ microstructure change. The average peak temperature in the melting zone was approximately 1,100 °C and the respective temperature in the CGHAZ and FGHAZ was 850 °C. Compared to the experimental process, the standard deviation was estimated to 12%. The microstructural constituent in the coarse grain HAZ of S690TMCP was essentially based on the mixture of bainitic-ferrite with some free carbide-free across the austenite grain boundary. In the S690QT side, the austenite grain was mainly constituted by the formation of bainite and lath martensite.

The microhardness point tests were performed within the HAZ of both materials. On the S690TMCP HAZ side, the average hardness of 230 HV0.1 was measured, which was acceptable compared to the BM. In the S690QC side, the average hardness measured was 290 HV0.1.

A direct correlation between heat input, microstructure change, and improvement of harder structure in the CGHAZ was noticed. Accordingly, the reasonable hardness was recorded for the specimen made with the heat input of 10 kJ/cm.

Table 5.1: Cooling time, microstructure characterisation, and average microhardness in the HAZ recorder from numerical and experimental data

Heat input values (kJ/cm)	Method	Cooling time (s)	Microstructural constituents		Average hardness values Measured in the HAZ (HV0.1)	
			S690TMCP	S690QT	S690TMCP	S690QC
10	Numerical	14.50	- Increase of bainite. - Decrease in ferrite - Less retained austenite	- Decrease of bainite. - Increase of martensite	230	290
	Experimental	18.84				
14	Numerical	24.85	- Increase of ferrite. - Decrease of bainite - Some amount of retained austenite	- Increase of bainite. - Formation of martensite - Some amount of retained austenite	210	260
	Experimental	30.45				

17	Numerical	29.45	- Increase of ferrite. Decrease of bainite.	- Increase of bainite - Decrease of	180	230
	Experimental	36.00	- Formation of carbide in the austenite grain	- Formation of martensite - Formation of carbide		

Relation to the whole dissertation work:

The paper contained here has contributed to developing the model that can predict an optimum heat input based on the FGM method, which will improve the weld joint quality.

Paper-II is a study developed using FGM in the FEM, which is introduced in the ANSYS software to generate a thermal cycle using different heat input values. The numerical model is used for any dissimilar weld joint. The geometry of the weld joint is uploaded in the ANSYS software, the chemical composition of BM and filler wire is also introduced in the software. The mechanical properties, thermomechanical data are introduced in the software. After calculations, the software will generate the results, which will be treated and compared with the experimental data. The last relation is the method that was used to evaluate the microstructural constituents in the dissimilar weld joint of HSS. Optical microscopy tests were carried out, and the different connections were linked between the bainite, martensite proportions formed in the CGHAZ of QT-steel and the ferrite, bainite, retained of austenite constituents in the microstructure of TMCP steel.

Publication III: **Effect of heat input and undermatched filler wire on the microstructure and mechanical properties of dissimilar S700MC/S960QC high-strength steels.**

Research objectives:

In this study, the aim was to investigate the effect of heat input and undermatched filler wire on the microstructural behaviour and thus resulting in mechanical properties of the HAZ of dissimilar S700MC/S960QC steels. From this analysis, it was possible to link the relationship between the heat input, the ferrite, bainite, tempered martensite and retained austenite constituents in the HAZ, and the mechanical properties of the weld joint. The experimental analysis was performed using a welding process GMAW, a microstructure characterisation using a scanning electron microscopy (SEM) micrograph and CCT diagrams to evaluate microstructure constituents close to the weld metal, the energy dispersive spectroscopy (EDS) to evaluate an alloying element composition and the repartition along with the weld joint, a Vickers-hardness of whole samples, and a tensile test to evaluate the strength and elongation of samples.

Results:

The results showed that the use of heat input of 7 kJ/cm results in a fast cooling rate (33 °C/s), which slightly decreases the average hardness in the HAZ of both materials. The

decrease hardness observed in the S700MC side was 11% to 245 HV5 versus 270 HV5 for the base material (BM). For S960QC steel, the lowest hardness was found at the FGHAZ, which was decreased by 22% compared to that of base material. Using the heat input of 10 kJ/cm, which resulted in a cooling rate of 21 °C/s, the bainite-ferrite microstructural constituents were formed in the austenite grains of the CGHAZ of S700MC, and the S960QC; the proportion of more bainite (55%) and less martensite (27%) with several fractions of retained of austenite (18%) constituted the CGHAZ microstructure. The best combination of hardness and strength was achieved by choosing a cooling rate of 21 °C/s (heat input of 10 kJ/cm). This resulted in an equilibrium of bainite, ferrite, and martensite constituents in the microstructure of dissimilar S700MC/S960QC weld, reducing the formation of pro eutectoid grain boundary carbide. Table 5.2 presents the results obtained during this experimental analysis. The increase of the volume fraction of bainite with the decrease of the heat input was observed for S700MC steel side of the weld joint. In the S960QC side, the decrease of the heat input caused an increase in the volume fraction of martensite, which occasioned the formation of brittle zones in the HAZ.

Table 5.2: Experimental data recorder from applying heat input in the dissimilar HSS of S700MC/S960QC: cooling rate, microstructure characterisation, alloying element composition, Vickers-hardness, and at tensile strength average in the weld joint

Heat input value (kJ/cm)	Cooling rate (°C/s)	HSS	Volume fraction evaluated (%)	Hardness values (HV5)	Tensile strength average (MPa)
7	33	S700MC	V_f of bainite (70) V_f of ferrite (20) V_f of retained of austenite (10)	210	769.70
		S960QC	V_f of bainite (45) V_f of martensite (40) V_f of retained of austenite (15)	268	
10	21	S700MC	V_f of bainite (60) V_f of ferrite (35) V_f of retained of austenite (5)	245	815.50
		S960QC	V_f of bainite (55) V_f of martensite (27) V_f of retained of austenite (18)	280	
15	10	S700MC	V_f of bainite (30) V_f of ferrite (55) Few Carbides (15)	180	808.70
		S960QC	V_f of bainite (60) V_f of martensite(20) TMA (15) V_f of retained of austenite (5)	240	

Relation to the whole dissertation work:

The paper shows the impact of heat input when welding dissimilar weld joint of HSS of S700MC/S960QC on the microstructural constituents, mechanical properties of the weld

joint. The paper supported the findings of article III. It evaluates with exactitude the heat input and filler wire that is required to weld dissimilar S700MC/S960QC in order to predict optimum microstructural constituents and strength in the HAZ.

Publication IV: Characterisation of bainite-ferrite structures formed on the heat-affected zone of dissimilar welds of high-strength steel (S700MC/S960QC) and their dependency on cooling time.

Research objectives:

The research of this study was characterised by the bainite-ferrite, martensite structure formed on the HAZ of dissimilar high-strength steel welded using overmatched filler wire. The experimental method was performed using the GMAW process of dissimilar S700MC/S960QC steel. With these objectives, the characterisation model was developed based on SEM images, which were uploaded in the ImageJ software. The volume fraction of bainite, ferrite, martensite, and retained of austenite was evaluated in the microstructure of dissimilar welds. Electron dispersive spectroscopy (EDS) micrograph was also performed in others to evaluate the alloying element composition in the HAZ of both materials when overmatched filler wire was used.

Results:

The results showed the formation of granular bainite (GB) at 615, 500, and 420 °C with a respective volume fraction of 38, 58, and 20% in the S700MC side. The rest of the formation was the formation of ferrite (40, 28, and 20%), and retained of austenite (12, 10, and 20%). In the S960QC side, the morphology of the microstructure was the formation of bainite, tempered martensite, and few carbides around the austenite grain boundary, which will be transformed into retained of austenite. At the temperature transformation of 550 °C, 470 °C, and 400°C, the volume fraction observed in the austenite grain was 42%, 55%, and 33% for bainite formation, 30%, 25%, and 45% for martensite formation, and 28%, 20%, 22% for retained of austenite formation. The analysis using EDS X-ray spectroscopy showed the absence of alloying elements such as Ni and Mo in the CGHAZ of S960QC steel, but in the same area of S700MC steel with the value of 1.3Ni, and 0.4Mo, respectively. This finding confirms the correlation between the microstructural analyses with the softening in the HAZ, causing a brittle zone in the weld samples. The noticeable presence of 1.3Ni, 0.4Mo, and 1.6Mn (S700MC) confirmed the temperature rise in the HAZ, as did the production of bainite with the significant intrusion of F and Cementite. The structure morphologic of B, F, and TMA are shown in Table 5.3. In the same table, the microstructure characterisation at the cooling temperature and the correspondent of microstructural constituents are showed as well.

Table 5.3: Structural feature and microstructure characterisation in the HAZ of dissimilar S700MC/S960QC

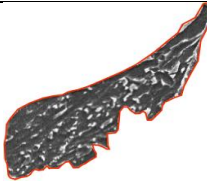

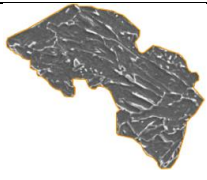
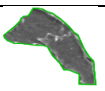
Type of steel	Structural Feature	Characteristic	Cooling at 615 °C	Cooling at 420 °C	Phase transformation
S700MC		granular boundary ferrite (GBF)	Bainite + Ferrite + Cementite		Bainitic Phase
		RA		Bainite+ RA	Bainitic phase
S960QC		Granular bainite	470 °C bainite transformation at 550 °C	400 °C	Bainitic Phase
		TMA		RA to TMA	
					Martensitic + Retained Austenitic

Table 5.4 also presents the alloying element composition in the CGHAZ of both materials, which play a significant role in the hardness of the weld joint.

Table 5.4: Micro-alloying elements composition in both sides of the dissimilar welded joint of S700MC/S960QC

Elements (%)	C	Si	Cr	Mn	Fe	Ni	Mo	Total %
S700MC (CGHAZ area)	3.3	0.6	0.5	1.6	92.2	1.3	0.4	100
S960QC (CGHAZ area)	3.4	0.3	0.1	1.8	94.2	-	-	

Relation to the whole dissertation work:

This paper supported the findings of paper II and Paper III, which characterised the formation of bainite, ferrite, and tempered martensite on the microstructure of dissimilar joint of S700MC/S960QC steel using undermatched filler wire. The evaluation of the influence of heat input and the filler wire composition in the performance of the weld joint was analysed. The papers contributed to the whole thesis as a critical study on the effect of heat input and overmatched filler wire in the microstructure characterisation of the dissimilar HSS.

Publication V: A Feasibility study of welding dissimilar Advanced and Ultra High Strength Steels.

Research objectives:

In this article, the objective was to choose the optimum welding process with the required welding parameters, which will achieve a high quality of dissimilar HSS welded samples. Based on the analysis of dissimilar welds of HSS, AHSS and UHSS, experimental analysis was performed using the GMAW welding process, to join a dissimilar joint of steels S700MC and S960QC using overmatched filler wire. The influence of welding parameters and overmatched filler wire were analysed to improve the strength of the welded joint and to propose the optimal welding process that can be applied.

Results:

Based on the results from the literature review and the experiment that was done, two issues were recognised when welding dissimilar AHSS and UHSS materials: cold cracking and material softening, especially in the fine grain heat-affected zone (FGHAZ). It is advised to have accurate control of heat input during the welding process. The welding specimen of dissimilar S700MC/S960QC using overmatched filler wire confirms the implication of the filler wire mechanical properties and chemical characteristics on the performance of the weld joint. Based on different types of dissimilar HSS/UHSS welded, good behaviour of bainite-ferrite steel is noted, which has the best weldability. GMAW process and Laser welding are the most common methods used and have shown good weldability when dissimilar AHSS/UHSS is used.

Relation to the whole dissertation work:

The paper supported the findings of paper III, IV, which evaluated the mechanical and microstructural constituents in the dissimilar S700MC/S960QC weld joint using overmatched filler wire. A Vickers-hardness, SEM micrograph and EDS X-ray spectrum

mapping were performed to evaluate the implication of overmatched filler wire and heat input values on the strength of the weld joint.

6 Discussion

High strength steels (HSS) are special steel that is sensible to the welding parameters, which stem directly from the thermomechanical properties of the materials. In the case of dissimilar joint of different HSS, the attention must be paid on the parameters guaranteeing adequate properties for both steels to be joined. In this thesis, the softening problems are always pointed out when welding dissimilar high-strength steels. The challenge that many welding companies are facing is to maintain the mechanical properties of the weld joint of dissimilar HSS at a reasonable level. The analysis in this thesis focuses on improving the mechanical properties of the heat-affected zone of the welds. To solve the issue, a numerical modelling method was developed. Based on the welding parameters (current, voltage, wire-speed, torch position, welding speed), joint geometry, and mechanical properties of a different base material, a thermal cycle of welding process in a weld joint was developed. The application of an experimental procedure was performed to determine an optimal cooling rate favourable to reduce softening in the weld joint. The microstructural analysis was performed using SEM/ EDS images, which developed the influence of the thermal cycle on the microstructural constituents in the HAZ. Mechanical tests (Hardness test, tensile test) were applied to determine the most softening area affected during welding and proposed the required heat input and filler wire.

6.1 State of the art of weldability of dissimilar high strength steel

Welding dissimilar HSS joint is a critical task, joining a well-known heat composition to the material properties. In order to weld dissimilar HSS, welding parameters, weld geometry, filler wire composition must be applied as a function of the mechanical properties of base materials, and chemical composition. The cooling rate is the result of the welding process, which affects the microstructural constituents and thus mechanical properties of the weld joint. The analysis in paper I developed the relation between welding parameters (heat input), mechanical properties and microstructural behaviour of base materials, and both chemical and mechanical properties of the filler wire. The results showed the influence of thermal cycle and filler wire composition on the mechanical properties of the weld joint. Depending on the material used, (Pirinen, 2015) recommended post-weld heat treatment after welding phase. This process will help a HAZ to recover the original mechanical properties. The same methodology was applied by (Löbke, 2016) to regain the mechanical stability of the weld joint. Paper I noted the increase of hardness due to abnormally high thermal cycle. To correct the irregularities regarding the mechanical behaviour of welds, a suitable selection of post-weld heat treatment processes is essential to obtain specific weld joint properties. Paper I recommended the choice of a correct category of welding process parameter and weld joint geometry for dissimilar HSS, which will help to avoid weld defects such as cracks and softening.

6.2 Thermal cycle model and mechanical properties of the weld joints

The main issue when welding dissimilar HSS is the selection of the welding parameters and filler wire. Because of the difference existing between both materials, it is important to develop a model that helps to have a good understanding. In paper II, a model based on the heat input, the geometry of the weld joint, base material mechanical properties and chemical composition was developed. The thermal cycle was developed to estimate the proper heat input, which will give high weld quality and minimise softening in the HAZ. In paper II, the results showed the best heat input value to be 10 kJ/cm when welding dissimilar HSS which was shown in cases of S690QT/TMCP, S700MC/S960QC with undermatched filler wire and S700MC/S960QC overmatched filler wire. SEM test and continuous cooling transformation (CCT) diagram were performed to identify the different temperature start and end transformations and the microstructural constituents in different areas of the weld joint. The area used was weld metal (WM), coarse grain high affected zone (CGHAZ), fine grain heat-affected zone (FGHAZ). The increase of the heat input at 17 kJ/cm in the dissimilar joint of S690QT-TMCP developed a presence of tempered martensite, the cementite in the initial austenite grain of QT-steel. In the S690TMCP side, a slide ferrite was identified, and few retained austenite at the end of the transformation. The use of the heat input of 10 kJ/cm maintained the hardness value in the HAZ of both materials with the average difference from 7 to 10% compared to the initial values.

The heat input recommended can be applied to weld dissimilar S690QT-TMCP steel according to the norm (EN 10025-6 2009). Sometimes, the welded joint can be applied for post-weld heat treatment (Gorka, 2018) to improve the mechanical properties. The microstructure characterisation was defined in paper II. The results also reveal the grain growing in the QT-steel. The average size of grain growth was $12.72 \mu\text{m}^2$, whether 10% biggest according to ASTM E112-13 standard. In the TMCP side, the average grain size was $4 \mu\text{m}^2$, 7% most significant than the original grain. From this analysis, the results can help to define a proper heat input value that will improve a material property in the heat-affected zone of this dissimilar S690QT-TMCP steels.

6.3 Microstructure and mechanical properties using undermatched WM

Paper III investigated the weldability of dissimilar S700MC-S960QC using undermatched filler wire. The influence of the welding parameter was analysed. By applying GMAW process, the cooling time was determined. The influence of cooling rate on the microstructure constituents and the mechanical properties of the welded joint were observed. By applying three heat input values (10, 7, and 15 kJ/cm), the cooling rate of 21°C/s was the best result that reduces softening in the HAZ of both sides. The average hardness was only 7% lower than the base materials. SEM analysis results in the presence

of 55% of bainite, 27% of martensite, and 18% of retained of austenite on the FGHAZ of S960QC. In the S700MC, the presence of ferrite (36%), bainite (50%) and retained of austenite (14%) was observed on the microstructure. The presence of undermatched filler wire was the composition of alloying elements such as 1.3Mi, 0.4Mo, and Mn in the S700MC. A supplementary EDS analysis in the same CGHAZ revealed the stability of carbon content on both sides of the joint. Tensile test results showed a decrease of an average strength of 6% compared to the BM. The elongation showed a 17% decrease compared to the BM. The reason for the decrease of the strength was the choice of the filler wire composition. The microstructural constituents during the cooling phase impacted the mechanical properties of the welded joint. To maintain the strength of the joint, an increase of alloying elements of filler wire is required. The recommendation was supported by (Ali, 2019), which added the fact that the increase of the strength is caused by the refinement of prior austenite grain size. The HAZ strength level is sensitive to the heat input value which participate in the determination of the thermal cycle. It is important to notice that the hardenability of the HAZ is high enough to facilitate a local strength increase near the fusion boundary.

From this analysis, this thesis recommends a cooling rate of 21 °C/s, which will provide the best combination of hardness and strength. This combination achieved an equilibrium proportion of bainite, ferrite, martensite in the microstructural constituents of dissimilar welded joint of S700MC/S960QC.

6.4 Microstructure and mechanical properties using overmatched WM

Paper IV and V showed the welded samples of dissimilar S700MC/S960QC using overmatched (mechanical properties higher than the BM) filler wire. The challenge to weld this dissimilar joint is the filler wire composition, which is not suitable to be used in this sample.

The process needed a suitable welding parameter, which can avoid crack propagation at the interface of the fusion line. The results from paper IV and V presented the increase of average hardness in the weld metal to 22% higher than the BM. The decrease of hardness was observed in the fine grain heat-affected zone, causing a softening area in both materials. The increase of hardness in the fusion zone confirms the argument presented by (Mvola, 2017), who developed the argument that the risk of applying overmatched filler wire on dissimilar HSS weld joint can cause a crack propagations in the weld metal.

The cause of softening was the filler wire composition, which has a mechanical property and carbon content higher than both materials. SEM micrograph showed the variation of microstructural constituent in the HAZ (bainite and ferrite) of in the S700MC function of the thermal cycle developed during welding. S960QC was mainly formed by bainite, lath

martensite and the amount of retained austenite in the microstructure. The increase of weight % of Mn, Mo, Si, and Cr was observed in the HAZ of S700MC, 1, 0.2, 0.2, and 1.2, respectively. In the S960QC side, only the presence of Mn and Si was observed with 2 and 0.4% of the weight, respectively. The increase of Mn than the BM can cause brittle mainly in martensite microstructure constituents (Tempered martensite) in the HAZ of S960QC. The use of overmatched filler wire produced in the weld metal a formation of acicular ferrite (AF) and widmanstätten ferrite (WF) constituents and can be source of crack propagation when the cooling time becomes long.

These types of ferrites promoted a risk of segregation at the interface of the fusion line. The confirmation was made in paper IV and V when the samples were welded. To increase softening in the HAZ, alloying element composition will play a significant role. The increase of Mn, Si, and Ni (weight %) and application of heat input of 10 kJ/cm justified the stability of hardness in the HAZ of both materials. The results were confirmed in paper IV and V. This affirmation was also confirmed by (Zhang, 2019), who analysed the influence of heat treatment on the formation of bainite, ferrite, martensite in the HAZ of the weld joint when welding dissimilar HSS.

6.5 Welding process recommended for dissimilar welding of HSS

To improve the strength when welding dissimilar HSS, paper V developed the following instruction, which shall be applied for industrial use.

- Adjust the welding process (cooling rate) based on the mechanical properties and chemical composition of the materials
- Adjust the geometry of the weld joint
- Mechanical properties of BM shall be in accord with the selection of the proper filler wire.

The use of gas metal arc welding (GMAW) process with Laser beam welding with an optimal parameter will develop a high-quality weld. Comparing with other welding processes, the GMAW process was the welding process that can be controlled most. Its cooling rate is good and has good strength and mechanical properties when the welding parameters are well determined. When associated with Laser beam welding, the softening issues will be solved. The strength of the joint will be excellent. The same paper shows the importance of using GMAW based on weldability. GMAW can be applied for many types of HSS: twinning induced plasticity steel (TWIP), transformation induced plasticity steel (TRIP), duplex phases steel (DP), complex phase steel (CP), martensite steel (MS), bainite ferrite steel (BF), thermomechanical controlled process steel (TMCP), or quenched and tempered steel (QT).

The objective of this research was to improve microstructural constituents and softening of the heat-affected zone when welding dissimilar HSS. The base materials were selected according to their applicability in the extreme conditions in regions like arctic and sub-

Sahara regions. Based on that, a numerical model of the thermal cycle was developed. The result of this thermal cycle was to choose optimal heat input data that will lead to reducing softening in the HAZ when welds sample. An experimental procedure was performed to validate the heat input data. The second issue was the choice of the filler wire that will be required to weld dissimilar HSS of S690QT-TMCP, S700MC/S960QC. Several experimental tests were carried out: the first group was using an undermatched filler wire and the second overmatched filler wire. The choice of welding dissimilar HSS using an undermatched filler was applicable; the heat input value must be estimated at 13 kJ/cm. The weldability of dissimilar HSS using undermatched filler wire was studied in paper III. The analysis of microstructural constituents was balanced using the welded samples selected, and the average hardness decreased to 7% to the BM. By using overmatched filler wire, the heat input should decrease to 10 kJ/cm, and the softening was reduced, leading to the strength of the heat-affected zone close to the BM. The analysis was performed in papers IV and V of the thesis.

7 Conclusions

This thesis investigated softening issues when welding dissimilar high strength steels and ultra-high-strength steels. It is often challenging in terms of achieving defect-free welds with required mechanical properties and research is therefore needed to better understand how the choice of welding method and welding parameters will influence productivity and weld properties. An important issue is control of the thermal cycle, as these steels have rather narrow process parameter windows and are prone to softening in the heat-affected-zone (HAZ).

The novelty of this thesis is to aim at understanding the relationship between the welding parameters and resulting microstructure, determining the mechanical properties, by thermal analysis combining experiments and by numerical modelling. There is also limited information available in the literature on the different combinations of steels investigated which contributes to the novelty and also brings new knowledge about dissimilar welding of high strength steels.

The studies considered welded joint production from the welding process (welding parameters) to materials characterisation. First, an optimal heat input database for numerical modelling of a dissimilar weld joint was chosen. The model was constructed and run using ANSYS software. Experimental analysis was performed using gas metal arc welding (GMAW), which is a suitable welding process when welding dissimilar HSS. The choice of filler wire characteristics was one of the most critical parameters in this research. Filler wire was chosen based on the mechanical properties of the different materials used because of the low carbon content in the materials. The following conclusions can be drawn based on the research presented in this thesis and the published articles.

Many new high strength steels with improved weldability, also at very high strength level, have been introduced in recent years thanks to advances in steel production processes. These steels are increasingly used in many applications where their high strength-to-weight ratio brings benefits. Important fields of applications include vehicles such as cars and trucks, and advanced loads bearing structures, etc. However, it is common to apply the very highest strength grades only where required which is why dissimilar welding becomes inevitable and increasingly important. Understanding how to do this in the best possible way with a minimum of trial and error is therefore needed for practical and economic reasons. All contributions to knowledge about how the weld quality and properties can be improved by an optimized choice and precise control of heat input (control thermal cycles) are therefore of importance.

The results presented in the dissertation are definitely introducing a methodology that can be developed and refined to hopefully become a practical tool for selection of welding methods and parameters in welding of high strength and ultra-high-strength steels.

References

- Ali, M., Porter, D., Kömi, J. 2019. "Effect of cooling rate on microstructure and mechanical properties of ultra high strength steels." *Journal of Iron Steel Research International* 1-15.
- Alves, P., Lima, M., Raabe, D., Sandim, H. 2018. "Laser beam welding of dual-phase DP1000 steel." *Journal of Materials Processing Tech.* 498-510.
- Bayock N., Kah, Layus P., Karkhin, V. 2019. "Numerical and experimental investigation of the heat input effect on the mechanical properties and microstructure of dissimilar weld joints of 690-MPa QT and TMCP steel." *Metals* 1-19.
- Bayock, N., Kah, P., Mvola, B., and Layus, P. 2019. "Effect of heat input and undermatched filler wire on the microstructure and mechanical properties of dissimilar S700MC/S960QC steels." *Metals* 1-20.
- Bayock, N., Kah, P., Mvola, B., Layus, P. 2019. "Experimental review of thermal analysis of dissimilar welds of High-Strength Steel." *Review on Advanced materials science* 58 (1): 38-49.
- Bayock, N., Kah, P., Salminen, A., Mvola, B., Yang, X. 2020. "Feasibility study of welding dissimilar advanced and ultra high strength steels ." *Reviews on Advanced Materials Science* 54-66.
- Belinga, Mvola. 2017. *Effect of adaptative GMAW processes: Performance and dissimilar weld quality*. Lappeenranta: Acta Universitatis Lappeenrantaensis.
- Bhadeshia. 1999. "Neural Networks in Materials Science." *ISIJ International* 966-979.
- Budkin, Y., Redchits, A. 2013. "A criterial approach to evaluating the weldability of material and alloys for welded aircraft structures." *Welding International* 687-689.
- Chan, C.L., Mazumder, J. and Chen, M.M. 1984. "A two-dimensional transient model for convection in laser melted pool." *Metallurgical Transactions* 15A: 2175-84.
- Chattopadhyay, G., Phanikumar, K. 2000. "Modelling of transport phenomena in laser welding of dissimilar metals." *International Journal of Numerical Methods for Heat and Fluid Flow* 11: 156-171.
- Chen, B., Hashemzadeh, M., Soares, C. 2014. "Numerical and experimental studies on temperature and distortion patterns in butt-welded plates." *International Journal of Advanced Manufacturing Technology* 1121-1131.

- Chen, Z., Li, J., Qi, J., Chen, L., Sun, L., and Wang, G. 2019. "Effects of Nb on bainite transformation behavior and mechanical properties of low-carbon bainitic steels." *Steel Research International* 1-10.
- Chennaiah, B., Koumar, N., Prahlada, K. 2016. "Influence of heat input and PWHT on the microstructure and mechanical properties in dissimilar (IS2062-EN8) Welded joints." *Procedia Computer Science* 54-51.
- Cho, D., Na, S., Cho, M., Lee, J. 2013. "A study on V-groove GMAW for various welding positions." *Journal of Materials Processing Technology* 1640-1652.
- Coric, A., Petrovic, Z., Pasic, S. 2011. "Heat input influence to the hardness and toughness of heat affected zone of high strength steel." *International Congress on Advances in Welding Science and Technology for Construction, Energy and Transportation Systems (AWST)*. Antalya: AWST. AWST-11/44.
- Cota, A., Santos, D. 2000. "Microstructure characterization of bainitic steel submitted to torsion testing and interrupted accelerated cooling." *Materials Characterization* 291-299.
- Dongsheng, L., Qingliang, L., Toshihiko, E. 2011. "Microstructure and mechanical properties in hot-rolled extra high-yield-strength steel plates for offshore structure and shipbuilding." *Metallurgical and Materials Transactions A* 1349-1861.
- EN 10025-6. 2009. "Part 6 Technical delivery conditions for flat products of high yield strength structural steels in the quenched and tempered condition, hot rolled products for structural steel."
- EN 10025-6:2004+A1. 2009. "Hot rolled Productions of Structural Steels. Part 6: Technical Delivery Conditions for Flat Products of High Strength Strutural Steels in the Quenched and Tempered Condition;" *Suomen, Standardoimisliitto (SFS): Helsinki, Finland* 24p.
- Fang, F., Qi-long, Y., Cai-Fu, Y., Su, H. 2009. "Microstructure and precipitation behavior in HAZ of V and Ti microalloyed steel." *Journal of Iron and Steel Research International* 68-77.
- Frei, J., Alexandrov, B., Rethmeier, M. 2016. "low heat input gas arc welding for dissimilar metal weld overlays partI: the heat-affected zone." *Welding in the World* 459-473.
- Friedman, E. 1978. "Analysis of weld puddle distorsion." *Welding Journal of Research Suppl.* 161-166.
- Gaspar, M. 2019. "Effect of welding heat input on simulated HAZ areas in S960QL high strength steel." *Metals* 1-14.

- Gilles, P., El-Ahmar, W., Jullien J. 2009. "Robustness analyses of numerical simulation of fusion welding NeT-TGI application: "Single weld-bead-on-plate"." *International Journal of Pressure Vessel and Piping* 3-12.
- Glover, G., McGrath, T., Tinkler, M., Weatherly, G. 1977. "The influence of cooling rate and composition of weld metal microstructures in a C/Mn and HSLA steel." *Welding Research Supplement* 267s-.
- Goldak, D., Chakravarti, A., Bibby, M. 1984. "A finite element model for welding heat source." *Metallurgical Transactions B* 299-305.
- Goldak, J., Breiguine, V., Dai, N., Zhou J. 1996. "Thermal stress analysis in welds for hot cracking." *ASME Journal of Pressure Vessel Technology* 2-10.
- Goldak, J., Gu, M. 1995. "Computational weld mechanics of the steady state, Mathematical modeling of weld phenomena 2." *The Institut of Metals* 207-225.
- Gorka, J., Stano, S. 2018. "Microstructure and properties of hybrid laser arc welded joints (Laser beam-MAG) in thermo-mechanical control processed S700MC steel." *Metals* 1-15.
- Gouldn, E., Khurana, P., Li, T. 2006. "Predictions of microstructure when welding automotive advanced high-strength steels." *Welding Research* 111-116.
- Guo, A., Misra, K., Xub, J., Guob, B., Janstoc, S. 2010. "Ultra high strength and low yield ratio of niobium-microalloyed 900 MPa pipeline steel with nano/ultrafine bainitic lath." *Material Science Engineering* 3886-3892.
- Guo, W., Li, L. 2016. "Laser welding of high strength steels (S960 and S700) with medium thickness." *Journal of Laser Application* 1-10.
- HKS-Prozesstechnik. 2016. *ThermoprofileScanner* [online]. 6. 1. www.hks-prozesstechnik.de/en/products/thermoprofilesScanner.
- Honeycombe, R., Bhadeshia, H. 1995. *Steel microstructure and properties*. London: Edward Arnold.
- Huetter, J. 2017. "Volvo XC40 has two tone option, exterior remains steel, offers all-inclusive ownership model." *Repairer Driven News* 2p.
- J., Lippold. 2015. *Welding metallurgy and Weldability*. John Wiley & Sons, Inc.
- Kah, P., Salminen, A., Martikainen, J. 2011. "The influence of parameters on penetration, speed and bridging in laser hybrid welding." *Mechanical Technologies* 324-333.

- Karkhin, V. 2015. *Thermal processes in welding. 2nd ed.* St. Petersburg: St. Petersburg Polytechnic University Publ.
- Kim, B., Lee, S., Kim, J., Lee, D. 1999. "Microstructure and local brittle zone phenomena in high strength low alloy steel welds. ." *metallurgical Transactions A* 139-142.
- Kinnunen, J. 2016. *controlling full penetration in MAG welding by the application of infrared thermography and neural network.* Lappeenranta: Lappeenranta-Lahti University of Technology.
- Krutz, G., Segerlind, L. 1978. "Finite Element analysis of welded structures." *Welding Journal Research Supplement* 211-216.
- Kumar, A., DebRoy, H. 2007. "Heat transfer and fluid flow during gas metal arc fillet welding for various joint configurations and welding positions." *Metallurgical and Materials Transactions A* 506-519.
- Kumar, A., Zhang, W., Kim, W., DebRoy, H. 2005. "A smart bi-directional model of heat transfer and free surface flow in gas metal arc fillet welding for practising engineers." *Welding in the World* 32-48.
- Kurcerova, L. 2017. "The effect of two-step heat treatment parameters on microstructure and mechanical properties of 42SiMn steel." *Metals* 1-14.
- Lahtinen, T., Vilaca, P., Peura, P., Mehtonen, S. 2019. "MAG Welding Tests of Modern High Strength Steels with Minimum Yield Strength of 700 MPa." *Applied Sciences* 1-18.
- Laitinen, R. 2006. *Improvement of weld HAZ toughness at low heat input by controlling the distribution of M-A constituents.* OULU: University of OULU.
- Löbbecke, C., Hering, O., Hiegemann, L., Tekkaya, A. 2016. "Setting mechanical properties of high strength steels for rapid hot forming processes." *Materials* 1-19.
- Mas, F., Tassin, C., Valle, N., Robaut, F. 2016. "Metallurgical characterization of couple carbon diffusion and precipitation in dissimilar steel welds." *Journal of Materials and Science* 4864-4879.
- Michailov, V., Karkhin, V., Petrov, P. 2016. *Principles of welding.* St. Petersburg: St. Petersburg Polytechnic University Publ.
- Michailov, V., Thomas, K., Wohlfahrt, H. 1996. "Numerical simulation of hydrogen distribution in multipass weld joints." *Welding and Cutting* 44-54.

- Mvola, B., Kah, P., Martikainen, J., and Suoranta, R. 2016. "Dissimilar welded joints operating in sub-zero temperature environment." *International Journal of Advanced Manufacturing Technology* 3619-3635.
- Mvola, B., Kah, P., Martikainen, J., Suoranta, R. 2016. "Dissimilar high-strength steels: fusion welded joint, mismatches, and challenges." *Reviews on Advances Materials Sciences* 146-159.
- Mvola, B., Kah, P., Martikainen, J., Suoranta, R. 2015. "State-of-the-art of advanced gas metal arc welding processes: Dissimilar metal welding." *Proceedings of the institution of Mechanical engineers, Part B: Journal of Engineering Manufacture* 1694-1710.
- Navarro-Lopez, A., Hidalgo, J., Sietsma, J., Santofimia, M. 2017. "Characterization of bainite/martensite structures formed in isothermal treatments below the Ms temperature." *Materials Characterization* 248-256.
- Pavelic, V., Tanbakuchi, R., and Uyehara, O. 1979. "Experimental and computed temperature histories in gas tungsten arc welding of thin plates." *Welding Journal Research Supplement* 295-305.
- Pirinen, M., Martikainen, Y., Layus, P., Karkhin, V., and Ivanov, S. 2015. "Effect of heat input on the mechanical properties of welded joints in high-strength steels." *Welding International* 14-17.
- Poorhaydari, K., Patchett, B., and Ivey, D. 2005. "Estimation of cooling rate in the welding of plates with intermediate thickness." *Welding Journal* 149-155.
- Radaj, D. 1992. *Heat effects of welding-temperature fields, residual stress, distortion*, 2nd ed. Berlin: Springer-Verlag.
- Radaj, D. 2003. *Welding residual stresses and distortion. Calculation and measurement*. Duesseldorf: DVS-Verlag.
- Rosenthal, D. 1946. "The theory of moving sources of heat and its application to metal treatments." *Transactions ASME* 849-865.
- Rykalin, R. 1974. "Energy sources for welding." *Welding in the World* 227-248.
- Schneider, C., Wolfgang, E., Schnitzer, R., Staufer, H., Vallant, R., Enzinger, N. 2017. "Welding of S960MC with undermatching filler material." *Welding in the World* 1-9.
- Schulze, G. 2009. *Welding high strength steel*. New York: Springer Verlag.

- SFS-EN ISO 4136. 2012. "Destructive Tests on Welds in Metallic Materials. Transverse Tensile Tests;" *Suomen, Standardoimisliitto (SFS): Helsinki, Finland*, 21p.
- SFS-EN-10149-1. 2013. "Hot Rolled Flat Products made of High Yield Strength Steels for Cold Forming. Part 1: General Technical Delivery Conditions;" *Suomen, Standardoimisliitto (SFS): Helsinki, Finland*, P. 32.
- Tasalloti, H., Kah, P., Martikainen, J. 2017. "Effect of heat input on dissimilar welds of ultra high strength steel and duplex stainless steel: microstructure and compositional analysis." *Materials Characterization* 29-41.
- Tian, J., Xu, G., Zhou, M., Hu, H. 2018. "Refined bainite microstructure and mechanical properties of a high-strength low-carbon bainite steel treated by austempering below and above Ms." *Steel Research* 1-10.
- Uzunali, U., Cuvalci, H. 2015. "The effect of post weld heat treatment on the mechanical properties of tempered martensite and high strength steel welded joints." *The 2015 world congress on Advances in structural engineering and mechanics (ASEM15)*. Incheon, Korea: ASEM15. 1-20.
- Van Wachem, B., Sasic, S. 2008. "Derivation, simulation and validation of a cohesive particle flow CFD model." *AIChE Journal* ({JOHN WILEY & SONS INC}) 54 (1): 9-19.
- Yamamoto, J., Meguro, S. 2009. "Analysis of martensite transformation behavior in welded joints of low transformation-temperature materials." *Welding International* 411-421.
- Yan, S., Liu, X., liang, T., Chen, J., and Zhao, Y. 2019. "Effect of micro-alloying elements on microstructure and mechanical properties in C-Mn-Si quenching and partitioning (Q&P) steels." *Steel Research International* 1-10.
- Zhang, Y., Shi, G., Sun, R. 2019. "Effect of Si content on the microstructure and the impact properties in the coarse-grained heat affected zone (CGHAZ) of typical weathering steel." *Material Science & Engineering A* 1-10.
- Zhou, M., Xu, G., Hu, H., Yuan, Q., Tian, J. 2017. "The effect of large stress on bainitic transformation at different transformation temperatures." *Steel Research International* 1-7.

Appendix A: List of equations

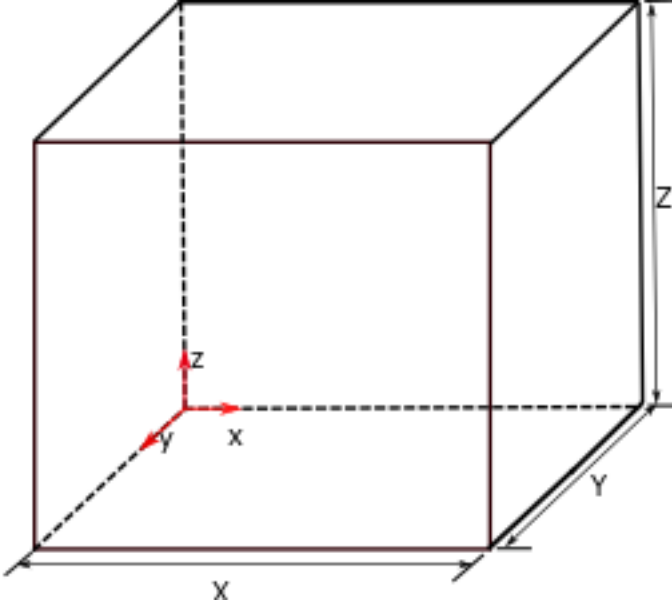


Figure 0: Element model in 3D

Moving least square approximation

Knowing the function $T(x, y, z)$, his approximation can be written in 3D domain as;

$$T^h(x, y, z) \quad (1)$$

$$T^h(x, y, z) = \sum_{j=1}^m p_j(x, y, z) a_j(x, y, z) \equiv p^T(x, y, z) a(x, y, z) \equiv p^T(X) a(X) \quad (2)$$

Where m is the number of terms

$p_j(x, y, z)$ is the monomial basis function

$a_j(x, y, z)$ Non-constant coefficients

$$X^T = [x, y, z], p^T(X) = [1 \quad x \quad y \quad z] \quad (3)$$

To estimate the coefficients $a_j(X)$, the quadratic functional $J(x)$ must be neglected.

$$J(X) = \sum_{l=1}^n w(X - X_l) \left\{ \sum_{j=1}^m p_j(X_l) a_j(X) - T_l \right\}^2 \quad (4)$$

$$A(x)a(x) = B(x)T \quad (5)$$

$$a(x) = A^{-1}(x)B(x)T \quad (6)$$

$$A = \sum_{l=1}^n w(x - x_l)p(X_l)p^T(X_l) \quad (7)$$

$$B(x) = [w(x - x_1)p(x_1), w(x - x_2)p(x_2), \dots \dots \dots w(x - x_n)p(x_n)] \quad (8)$$

$$T^T = [T_1, T_2, \dots \dots \dots T_n] \quad (9)$$

$$T^h(x) = \sum_{l=1}^n \Phi_l(x)T_l = \Phi(x)T \quad (10)$$

$$\Phi_l(x) = \sum_{j=0}^m p_j(x)(A^{-1}(x)B(x))_{jl} = p^T A^{-1}B_l \quad (11)$$

$$\Phi_{l,x}(x) = (p^T A^{-1}B_l)_{,x} = p^T_{,x} A^{-1}B_l + p^T (A^{-1})_{,x} B_l + p^T A^{-1}(B_l)_{,x} \quad (12)$$

Cubic spline weight function

$$w(x - x_1) = w(r) = \begin{cases} \frac{2}{3} - 4r^2 + 4r^3 & r \leq \frac{1}{2} \\ \frac{4}{3} - 4r + 4r^2 - \frac{4}{3}r^3 & \frac{1}{2} < r \leq 1 \\ 0 & r > 1 \end{cases} \quad (13)$$

The gaussian shape function

$$w(x - x_l) = w(r) = \begin{cases} e^{-(2.5r)^2} & 0 \leq r \leq 1 \\ 0 & r > 1 \end{cases} \quad \text{The quartic spline weight function}$$

$$w(x - x_l) = w(r) = \begin{cases} e^{-6r^2 + 8r^3 - 3r^4} & 0 \leq r \leq 1 \\ 0 & r > 1 \end{cases} \quad (14)$$

Reinforcement of essential boundary

$$\lambda(x) = N_l(a)\lambda_l, \quad x \in S \quad (15)$$

$$\delta\lambda(x) = N_l(a)\delta\lambda_l \quad x \in S \quad (16)$$

N_l is a Lagrange interpolation, a is the surface along the essential boundary

Appendix B: List of tables

Table 1: Pre-Welding Procedure Specification



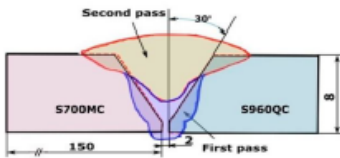
Pre Welding Procedure Specification							PWPS				
Parent material		S700MC and S960QC					 <p>Two weld pass. Air gap is 2 mm</p>				
Material thickness		8 mm									
Outside diameter		-									
Welding process		Robotic MIG									
Welding position		Flat									
Groove preparation		square									
Groove cleaning		-									
Workpiece fixturing		-									
Tack welding		Both ends- TIG welding									
Back gouging		-									
Backing		-									
		Designation of consumables and trade name			Torch angle		P1=8° P2=15°				
	Filler material classification	Esab OK Autrod 16.55 (AWS A5.9: ER 385) for (S960 HSS) Mn3Ni1CrMo (S690) (EN 12534)			Inclination angle						
					Distance contact tube to workpiece						
					Preheating and interpass temperature						
				Preheat temperature		-					
				Interpass temperature		-					
	Flux					Preheating method		-			
	Shielding gas			M21 Ar + 2% CO ₂ Ar +18% CO ₂			Temperature measurement		-		
	Flow rate			14 L/min 16 L/min			Post-weld heat treatment				
	Plasma gas			-			Method		-		
	Flow rate			-			Heating rate		-		
Backing gas			-			Temperature		-			
Flow rate			-			Time		-			
Type of current			DC+			Cooling rate		-			
Polarity						Post-weld treatment		-			
Remarks:					Date and name:						
Sample	Process	Size of filler metal Ø (mm)	Current (A)	Voltage (V)	Travel speed (mm/s)	Wire feed rate (m/min)	Heat input (kJ/mm)	Run-out length (mm)	Weaving frequency (Hz)	Amplitude (mm)	Remarks
1	MIG	1.0	190	24,5	8.0	9.5		18	-	-	

Table 2: weld sample description

Sample	Base material	Heat input (kJ/cm)	Welding Torch Angle.	Filler wires numb.
S1	S700MC-S960QC	7	P1	F1
S2	S700MC-S960QC	10	P1	
S3	S700MC-S960QC	15	P1	
S4	S700MC-S960QC	7	P2	
S5	S700MC-S960QC	10	P2	
S6	S700MC-S960QC	15	P2	
S7	S700MC-S960QC	7	P1	F2
S8	S700MC-S960QC	10	P1	
S9	S700MC-S960QC	15	P1	
S10	S700MC-S960QC	7	P2	
S11	S700MC-S960QC	10	P2	
S12	S700MC-S960QC	15	P2	

Appendix C: List of figures

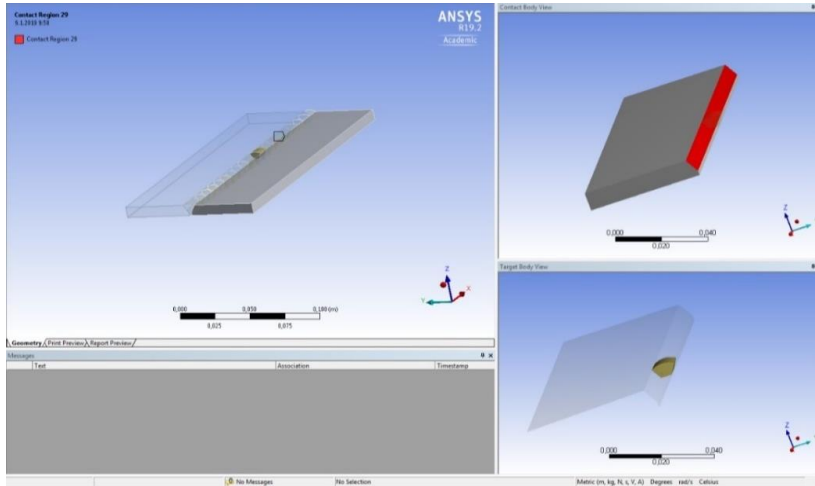


Figure 1: Geometry of weld sample on ANSYS software.

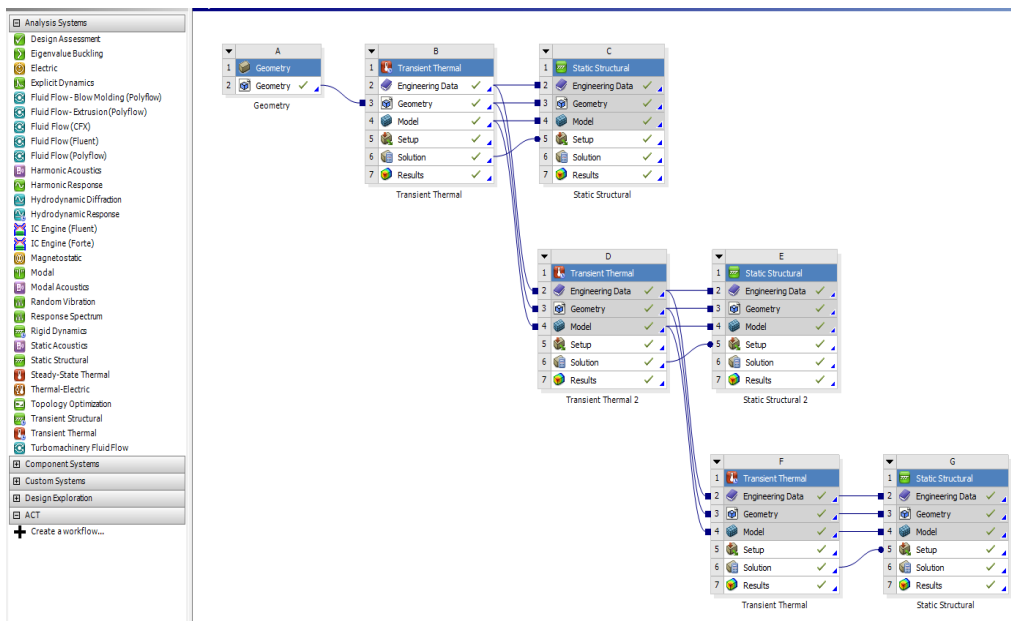


Figure 2: Thermal analysis of weld sample geometry using ANSYS software.

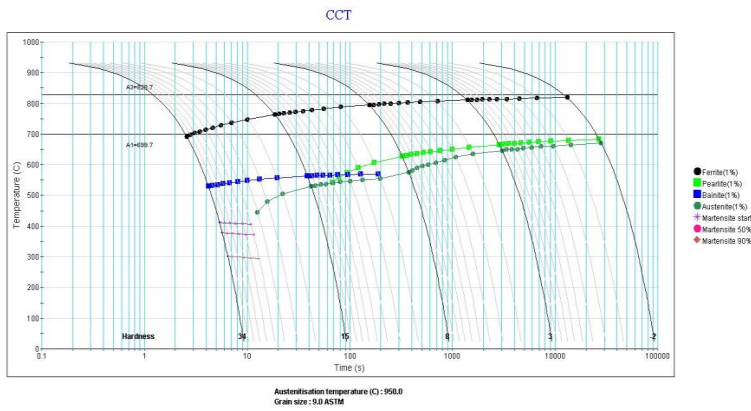


Figure 3: CCT diagram of S690QT steel.

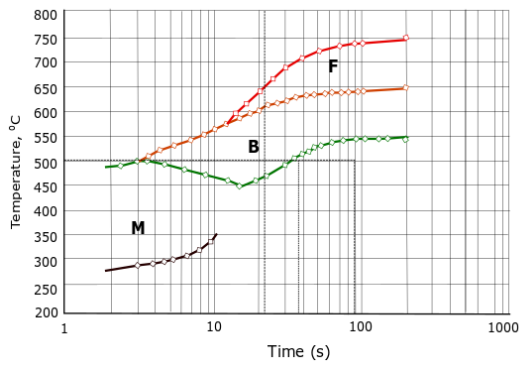


Figure 4: CCT diagram of S700MC steel (Gorka 2018).

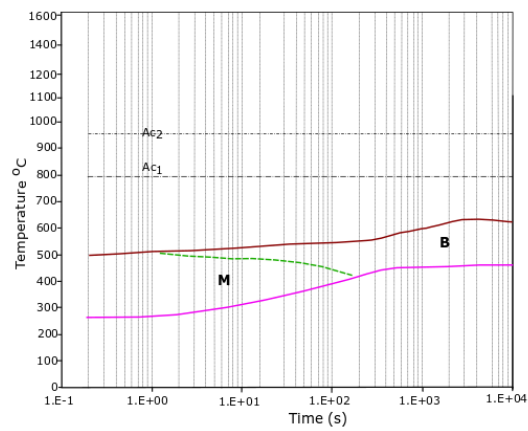


Figure 5: CCT diagram of S960QC steel (Tasalloti 2017)

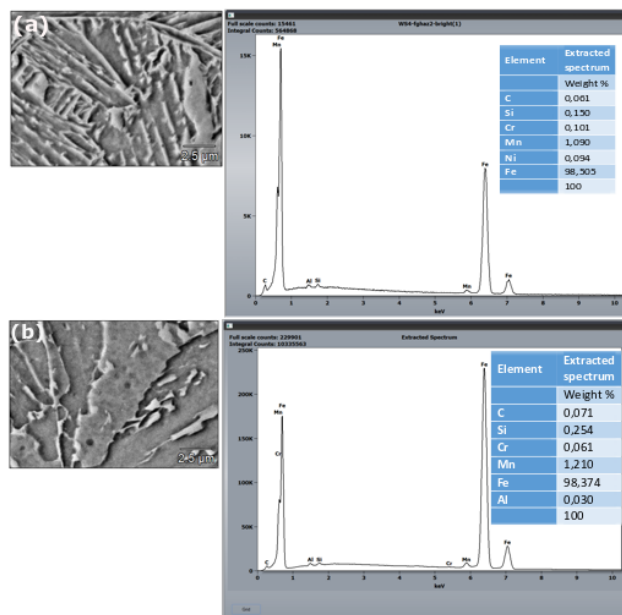


Figure 6: EDS images and alloying elements composition in the CGHAZ using undermatched filler wire: (a) S700MC steel side, (b) S960QC steel side.

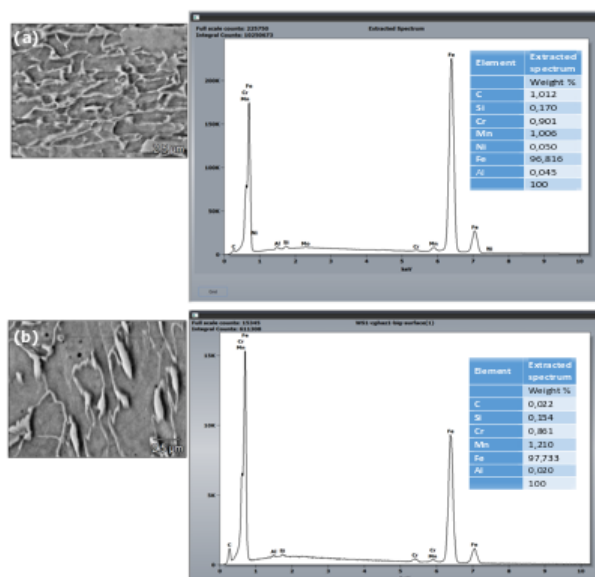


Figure 7: EDS images and alloying elements composition in the CGHAZ using overmatched filler wire: (a) S700MC steel side, (b) S960QC steel side.

Publication I

Bayock, F., Kah, P., Mvola, B. and Pavel, L.

Experimental review of thermal analysis of dissimilar welds of high-strength steel

Reprinted with permission from

Rev. Adv. Mater. Sci.

Vol. 58(1), pp. 38-49, 2019

© 2019, DE GRUYTER

Review

Francois Njock Bayock*, Paul Kah, Belinga Mvola, and Pavel Layus

Experimental review of thermal analysis of dissimilar welds of High-Strength Steel

<https://doi.org/10.1515/rams-2019-0004>

Received May 3, 2018; accepted Oct 4, 2018

Abstract: Dissimilar welding offers exiting benefits for a wide range of engineering applications, such as automotive bodies, piping systems of nuclear power plants, health equipment. The main advantages of dissimilar welding applications are weight reductions, lower costs, unique properties combinations, and improved energy-efficiency. The properties of dissimilar weld depend on the type of welding process used, the accuracy of the process parameters control, the characteristics of the base metal and the heat treatment procedures. The current study reviews the scientific literature on the topic of thermal analysis of dissimilar high-strength steels (HSS) welding. The review of experimental data was carried out to analyze the variable heat input effect on dissimilar welds. The results indicate the welds mechanical properties irregularity and reduction in toughness and tensile strength due to uneven changes in the microstructure. Furthermore, post weld heat treatment (PWHT) often resulted in the formation of intermetallic compounds whose properties are dependent on the duration of treatment. The research results can be used to optimize the heat input of the HSS welding process.

Keywords: High-Strength Steel, Dissimilar Weld, Heat Treatment, GMA Welding Process, Thermal Distribution, PWHT

1 Introduction

Industrial enterprises are increasingly starting to use dissimilar welded joints of high-strength materials in the manufacturing of their products. Dissimilar joints can im-

prove not only product quality and bring cost benefits, but also enable innovative design and provide enhanced structural stability [1]. It is also clear that the mechanical, thermo-mechanical and microstructural properties of materials used in dissimilar welding, play an essential role in the determination of the optimal parameters for a welding process [2–5]. On the other hand, regardless of the welding process, of the introduced heat input will influence the metal during the welding process and also after welding is complete.

A suitable weld depends mainly on the heat source parameter for it to conceal these mechanical characteristics, microstructures. In addition to the heat source, there are also parameters such as the geometry of the weld joint, the filler metal, and the welding process to be applied.

In gas metal arc welding (GMAW) of HSS, the microstructure and mechanical properties of the welded joint are determined by the chemical composition of the weld and the base material, and by the cooling rate, especially in the heat-affected zone (HAZ). The latter depends mostly on the heat input, weld geometry and the thermophysical properties of the metal. Comparative analysis of the HAZ microstructure of HSS shows the dependence of the mechanical properties of the weld on the welding conditions and especially on the heat input [6–10]. All these parameters have a direct effect on the thermal characteristics of the weld joint for dissimilar materials.

This study aims to review analyses of thermal treatment (e.g., heat input during welding and post weld heat treatment) of dissimilar welds of HSS structures produced using different welding processes. Improved understanding of the effects of heat treatment will enable better control of the mechanical properties (hardness, yield strength, and tensile strength), metallurgical compounds and microstructure (martensite, bainite, and ferrite morphology) in the weld joint structure.

The material characteristics and alloy composition of HSS are presented, and the principles underlying the chemical composition of such steels, the manufacturing processes used in HSS production and the weldability of the steels are explained. This knowledge provides the basis for analysis of heat input and posts weld heat

***Corresponding Author: Francois Njock Bayock:** Laboratory of Welding Technology, Lappeenranta University of Technology, P.O. Box 20, 53851, Lappeenranta, Finland;
Email: Francois.Njock.Bayock@lut.fi

Paul Kah, Belinga Mvola, Pavel Layus: Laboratory of Welding Technology, Lappeenranta University of Technology, P.O. Box 20, 53851, Lappeenranta, Finland

Open Access. © 2019 F. N. Bayock *et al.*, published by De Gruyter.



This work is licensed under the Creative Commons Attribution

Brought to you by | Lappeenranta Tiedekirjasto
Authenticated

Download Date | 11/23/19 3:30 PM

treatment, and study of their effects on the mechanical, metallurgical and microstructural characteristics of the weld [11].

2 Background of high-strength steel

Different types and grades of HSS were developed. Steels using yield point (R_e) above 355 MPa are referred to as HSS. Different classifications were put on the market according to the high values of the mechanical characteristics. For those values of high tensile strength ranging from 450 to 800 MPa are considered to be advanced high-strength steel. And that with high tensile strength values above 960 MPa, are classified as ultra-high strength steel [4].

2.1 High-strength steel classification

High-strength steels are grouped based on chemical composition, production method, and the heat treatment process. In the production of high-strength steels or improving others properties, the different alloying composition like carbon (C), Manganese (Mn), Nickel (Ni), Chromium (Cr), Molybdenum (Mo), Vanadium (V), Niobium (Nb), Copper (Cu), Titanium (Ti) or Boron (B) are added with the aim of increasing strength, but increased alloying is not cost effective. Heat treatment is applied to attain desired mechanical characteristics such as tensile strength, yield strength, ductility, and notch toughness to meet the requirements of the relevant standards and specifications. Common heat treatments include normalizing followed by tempering. Highly resistant steels can be classified according to the mode of production. Many production companies developed quenched and tempered (QT) steels, Induced Plasticity steel (TRIP) or thermo-mechanical control Process (TMCP) and many others. This process offers higher strengths with lower carbon equivalent, therefore, better weldability. In automotive engineering, the mechanisms of a controlled transformation of the microstructure have proved particularly interesting because they allow the creation of steels with a favorable combination of mechanical strength and formability. Figure 1 shows a selection of high-strength specialty steels commonly used in automobile production, with their strength properties and ductility. Non-alloyed high-strength, fine-grained structural steel are compared. It is noted that the Dual-phase and multi-phase steels and special alloy steels offer the following advantages:

- Reduced weight while keeping strength level;
- Easy formed cold and hot;
- Good ductility with high processing speeds;
- A strong hardening with large total deformations, resulting in a high energy absorption capacity;
- Good weldability.

Their microstructure depend on the load profile, the chemical composition, the effective hardening mechanisms, and heat treatment status. Flat products made from HSS for cold forming are characterized by different property-determining microstructure states like Two-phase steels, Multi-phase steels, special alloyed steels and other (recently developed) [12, 13].

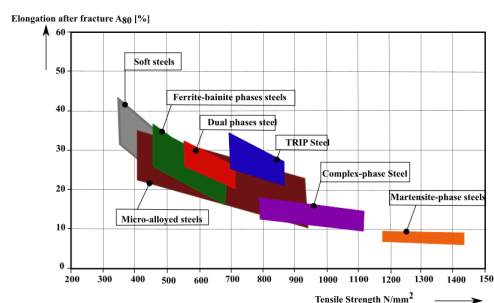


Figure 1: Example selection and properties of currently common hot-rolled high-strength steels for automotive production. G. Schulze // Heidelberg-Dordrecht. (2009). ©2009 Springer Verlag.

2.2 Filler material classification

The choice of filler materials in welding depends on the minimum requirements for the mechanical properties of the base material. To prevent metallurgical notches, filler materials should be used that allows production of a weld metal with mechanical-technological properties that are comparable to those of the base material [2]. Table 1 presents a recommended series of base material features (yield point, type of production) and corresponding elements of filler materials [14].

The most critical parameter in the welding of structural steels is the temperature-time curve. Therefore, the excessive welding heat input degrades HAZ properties by two possible scenarios: A tendency to hardening through martensite formation, thus leading to possible cold cracking, and a tendency to recombine integrated hydrogen and thus to the formation of hydrogen-induced cracking. The

Table 1: Recommendations for base material-filler material allocations with fine-grain structural steels. G. Schulze // Heidelberg-Dordrecht. (2009). ©2009 Springer Verlag.

Base material		Welding Process	Code for yield point	Filler material		The chemical composition of solid wire
Yield point [N/mm ²]	Production			Code number for a test temperature		
275	N,M	E	38, 42	0, 2, 4, 6		-
		G				G3Si1
		S				S3
355	N,M	E	38, 42	0, 2, 4, 6		-
		G				G3Si1
		S				S3Si
420	N,M	E	42, 46	0, 2, 4, 6		-
		G				G3Si1, G4Si1
		S				S3Si, S4Si
460	N, M, Q	E	46, 50	0, 2, 4, 6		-
		G				G4Si1
		S				S4Si
500	M, Q	E	50	0, 2, 4, 6		1NiMo
		G				G3Ni1
		S				S2Ni1Mo
550	Q	E	55	0, 2, 4, 6		1NiMo
		G				-
		S				-
620	Q	E	62	0, 2, 4, 6		Mn1NiMo
		G				-
		S				-
690	Q	E	69	0, 2, 4, 6		Mn2NiMo
		G				-
		S				-
890	Q	E	89	0, 2, 4, 6		Mn2NiMoCrMo
		G				-
		S				-

Q – Quenched and tempered fine grain structural steels;
Q M – Thermomechanical rolled fine grain structural steel;
Q N – Normalising rolled fine grain structural steels and the unalloyed.
Q E–Manual arc welding, **G**–Gas metal Arc welding, **S**–Submerged arc welding.

method used to assess the need for pre-heating is based on the carbon equivalent value (C_{EV}). Accordingly, all structural steel standards from the EN 10025 series contain unique tables detailing, for each material, the extreme acceptable amount of carbon equivalents depend on the material thickness. If the exact equivalent of a batch exceeds these specifications, preheating should be considered.

The temperature-time curve during welding is influenced by the heat input, the relative thermal efficiency of the selected welding process, the sheet thickness, the pre-heating temperature, and the weld shape. Thus, with fusion and resistance welding, quick heating to a specified

peak temperature occurs followed by significantly slower cooling. This process is schematized in Figure 2, and the interaction of the above influencing factors on the HAZ in fine grain structural steels is illustrated. The cooling rate is the parameter that influences the mechanical properties in the coarse grain HAZ (CGHAZ).

The combination of C_{EV} and sheet thickness only indicates the need for pre-heating, it does not, however, define the pre-heating temperature. In order to determine this value, further parameters must be considered. Figure 3 presents the carbon equivalent for the different constitu-

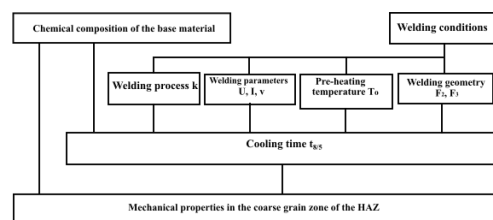


Figure 2: Parameters that affect the mechanical properties of the CGHAZ. With the $t_{8/5}$ cooling time between 800 and 500°C, F_2 , F_3 weld factor for two or three-dimensional heat dissipation, k relative thermal efficiency, U , I (voltage and welding current). Reprinted with permission from Roos *et al.* // Heidelberg-Dordrecht. (2011). ©2011 Springer Verlag.

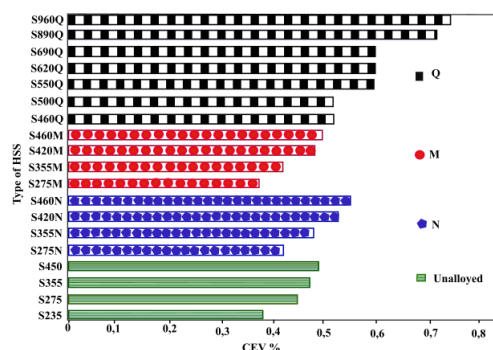


Figure 3: Comparison of the carbon equivalent value (CEV) of the constitution of steel internal composition, EN 10025-3, -4, and -6 with unalloyed steel structures, EN 10025-2. Reprinted with permission from Schulze // Heidelberg-Dordrecht. (2009). ©2009 Springer Verlag.

tion of high strength steel internal composition (EN 10025-3, -4, -6).

When welding thick sheets (> 6 mm), the heat dissipation occurs in three dimensions, the heat applied by the arc dissipates in the sheet surface and the direction of the sheet thickness.

3 Weldability of high-strength steels

Welding two pieces of different mechanical characteristics and microstructures require a certain number of objectives to be achieved. To have a weld of good quality, it is necessary to reduce as much as possible the thermal defects (hot and cold cracks), the mechanical defects (stress, hardness

defect), and defects of the microstructure (hydrogen crack). The weld should have specified values of yield strength, ductility, notch toughness, and the weld should behave appropriately in different uses. When welding the HSS, from the melting zone to the HAZ, all this part is susceptible to high hardness values. When welding the HSS, from the melting zone to the heat affected zone (HAZ), all this part is susceptible to high hardness values. High values of hardness can lead to cracking defects, leading to defects in the weld joint. It would be precious to evaluate the equivalent carbon to determine the appropriate characteristics of the filler metal to identify the more consistent cooling process.

The weldability of HSS and its behavior concerning heat input and PWHT, together with the dependence of the weldability on the base material and the type of welding process will next be considered.

4 Thermal behavior in dissimilar welding of HSS

In the welding process using dissimilar HSS, several parameters are scrupulously taken into account before the operation itself. The geometrical parameters of the weld joint, the chemical characteristics of the base materials, the choice of the filler metal. After that comes the parameters of the heat sources and the cooling rate, which are functions of the speed of the welding process, the voltage, and the current intensity. It is a link between the heat source that depends on the parameters mentioned above and the cooling time. The combination of the two parameters has effects on the mechanical characteristics and microstructures of the weld joint.

First, the mechanical and microscopic behavior of the weld joint will be examined by considering the different sources of heat, and then the results of research into post-weld thermal treatments will be addressed.

4.1 Heat input conditions

In his work, Pirinen *et al.* [6] studied strength, elongation, and hardness of HSS weld manufactured with Shielded Metal Arc Welding (SMAW). Figure 4 shown the plates welded were 8 mm thick HSS (ASTM E112-10) produced by quenching tempered, and thermos-mechanical controlled process (tensile strength 821–823MPa). Welding was done with a 15% CO_2 +85% arc shielding gas and Autrod 13.51 electrode. The dependence on heat input of the strength, elongation, and hardness in the HAZ was determined. It

was found in Figure 5a, b that an abnormal value of heat input will disturb the strength then elongation of the weld joint.

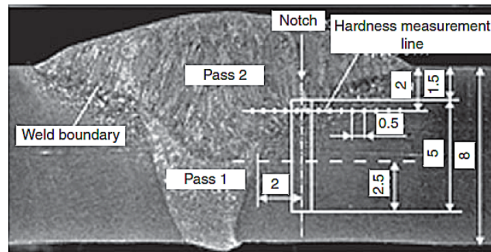


Figure 4: The configuration of V-joint with 2 passes welded joint. Reprinted with permission from Pirinen *et al.* // Welding International. (2015). ©2015 Taylor & Francis.

In other work, **Tasalloti *et al.*** [16] use two basic metals with different mechanical characteristics and microstructures namely S960 and S32205. With the gas welding process, it analyzes the effects of the different values of the heat source on the compositions of the microstructure. Figure 6 shows the different effects of the heat input values in the weld zone. Figure 6a represents the heat input with 0,86kJ/mm, b represents the heat input with 0,64kJ/mm and the last Figure 6c 0,48kJ/mm. It succeeded in determining optimum heat exchange rate favorable to the good behavior of the geometry of phase transformations at the interior of the grains. For the S960, a high heat source helps move a large number of Bainite for Martensite. Figure 7a.

Löbbe *et al.*, [18] in his approach analyze the behavior of the weld joint after welding. The objective here is always to find the mechanical properties of the base materials at the level of the weld joint. It can then evaluate it by acting on the analysis of the microstructure which, they are related to the mechanical properties of the materials. It develops a new approach for reheating the joint after welding, note "hot forming with rapid heating" (Figure 8a, b). Three necessary materials are used for this process (22MnB5, ENGTS-1000-5, and Docol 1400 M). A slight change in the microstructure formation of grain size and undissolved carbide materials has been noted and was found to be excellent compared to conventional treatment. Figure 9 shows the different steps taken by the microstructure when using the new model: step 1 - quenching room temperature, step 2 - quenching at 350°C during 30s, step 3 - formation of carbides without any susceptible deformation

Frei *et al.* [19] used GMAW with Cold Metal Transfer (CMT) to evaluate the effect of low heat input on mechanical and microstructural properties of the HAZ of two high strength steels (13CrMo4-5/10CrMo9-10). The impact of the low heat source on the behavior of the microstructure of these two HSSs was determined. The analyzes were located on the CGHAZ. Compare with a higher heat source, it has been noted some incomplete microstructures transformations (austenite transformation) in this area (CGHAZ).

The weldability analysis of the dual phase of high-strength steel (grade ENGTS1000-5) using laser beam welding was studied by Alves *et al.* [20]. The assumption of the analysis is based on the heat source (0,4 kW and 2kW), and the welding speed is evaluated at the interval 20mm / s and 150mm / s. Figure 10 illustrates the method used to perform the welding and at the same time pick up the temperature profiles. The microstructure analyzes presented a hardness profile represented in Figure 11. The melting zone has the maximum value of the Hardness profile which was 530 HV; this will be justified by the fact that this zone has a high temperature, which is therefore susceptible to hot crack.

For both types of steel, this system guarantees a good quality weld compared to the conventional method. The recommended parameters for welding these materials are (P2.0 / S150).

4.2 Post weld heat treatment condition

Uzunali *et al.* [21] investigated post-weld heat treatment effects on the mechanical properties of tempered martensitic of high-strength steel welded joints. The welded joints were performed in accordance with standards EN 15609, EN 15614, steels Hardox x450 (0,11C, 0,46 Si, 1,39Mn, 0,01P, 0,002S, 0,25S, 0,25Cr, 0,07Ni, 0,017Mo) and Optim 700MC (0,064C, 0,25Si, 1,84Mn, 0,015P, 0,018S, 0,22Cr, 0,25Ni, 0,0001Mo,) were chosen due to their partially high carbon equivalent. Chemical analysis, hardness tests, and microscopic examination were implemented to assess the mechanical properties of the material before the welding process. Figure 12 shows an example of microstructure compartment during heat treatment at 450°C.

Hardness increase due to temperature distribution and cooling rate was determined only in the HAZ of Hardox 450 materials approximately 450-520 Vickers. Hardness increase due to temperature distribution and cooling rate was not defined in the HAZ of Optim700MC. The results show that Hardox450, due to its carbon equivalent ratio, can be subjected to PWHT to decrease the hardness increase in the HAZ.

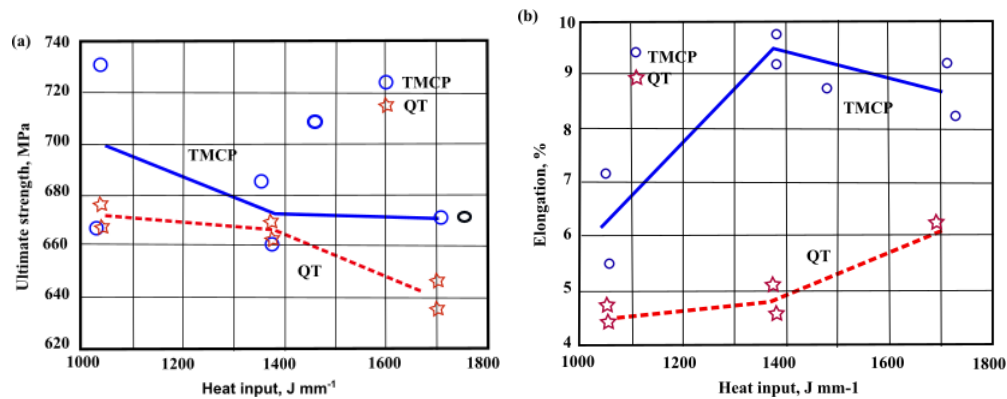


Figure 5: Heat input function of; (a) ultimate strength, (b) elongation. Reprinted with permission from Pirinen et al. // *Welding International*. (2015). ©2015 Taylor & Francis.

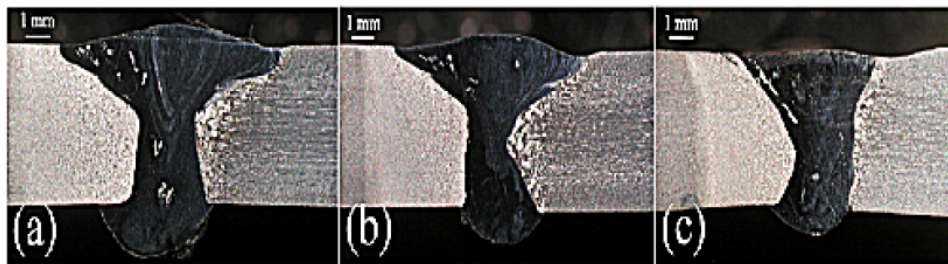


Figure 6: Structure of weld samples of the dissimilar weld of S960/S32205: (a) WS7.1; (b) WS8; (c) WS 9. Reprinted with permission from Tasalloti et al. // *Material Characterization*, 123 (2016). ©2016 Elsevier Inc. All rights reserved.

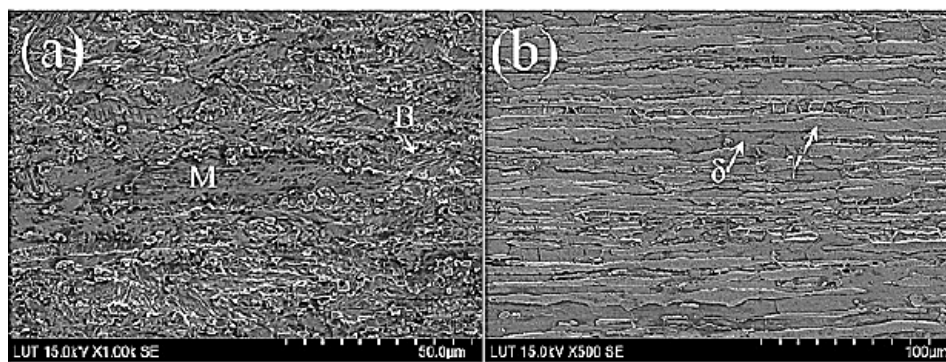


Figure 7: Microstructure of weld sample: (a) S960 and (b) S32205: Reprinted with permission from Tasalloti et al. // *Material Characterization*, 123 (2016). ©2016 Elsevier Inc. All rights reserved.

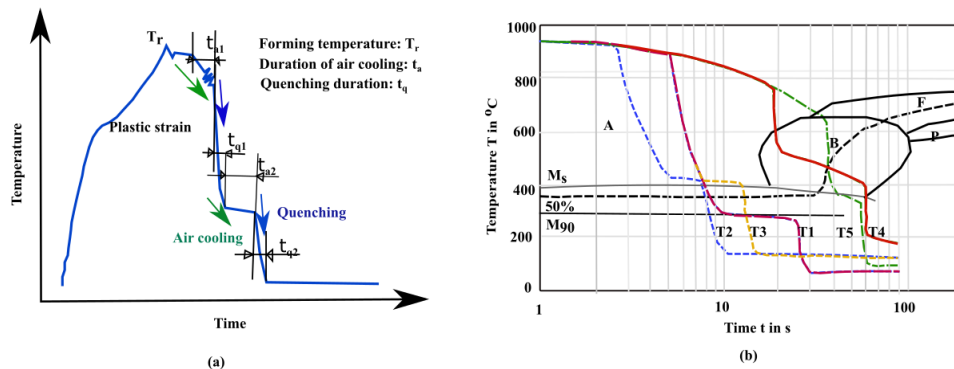


Figure 8: Heat process: (a) Intermittent Process Typical Cooling Cycle, (b) temps temperature of 22MnB5 Reprinted with permission from Christian Löbbeck *et al.*, // Materials, 9 (2016). ©2017 Licensee MDPI, Basel, Switzerland.

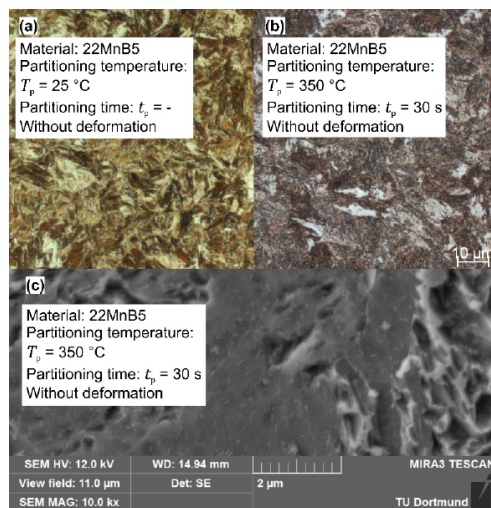


Figure 9: Microstructure analysis of 22MnB5: (a) Step 1: Quenching to room temperature; (b) Step 2: Quenching to 350°C during 30s; (c) Formation of carbides. Reprinted with permission from Löbbeck *et al.*, // Materials, 9 (2016). ©2017 Licensee MDPI, Basel, Switzerland.

Chennaiah *et al.* [22] estimated the effect of the heat source, and PWHT on the mechanical and microstructure behavior IS 2062 and EN 1564 grade EN-GJS-800-8 welds fabricated using a MIG welding process. The variation of alloying elements and physical properties of the material did not change considerably, but the significant change occurred in the mechanical properties. In the dissimilar material, there was an increase in the tensile strength and

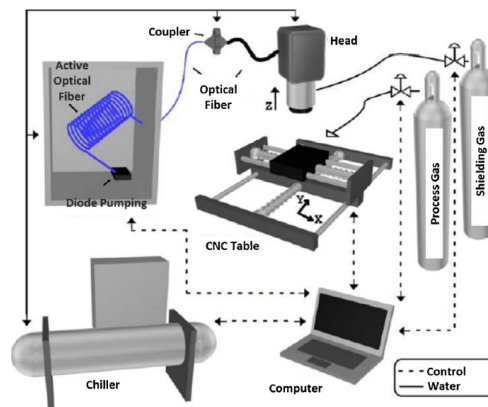


Figure 10: Experimental setup of the Laser welding process. Reprinted with permission from Alves *et al.* // Journal of Materials Processing Tech. ©2017 Elsevier B.V. All rights reserved.

impact strength as the heat input decreased. In addition, the process of evolution of the hardness in this case starts from the zone of fusion, followed by HAZ, towards the base metal. Figure 13 show positive effect of heat treatment for weld carried out with different heat inputs.

Both materials have different basic chemical and mechanical properties. The results after welds and heat treatments have shown that the lower the heat sources, the higher the hardness values. This phenomenon has been observed in IS2062 steel. The variation of the hardness was observed on the HAZ. The same result was obtained when the PWHT was applied. The evolution of the hardness on

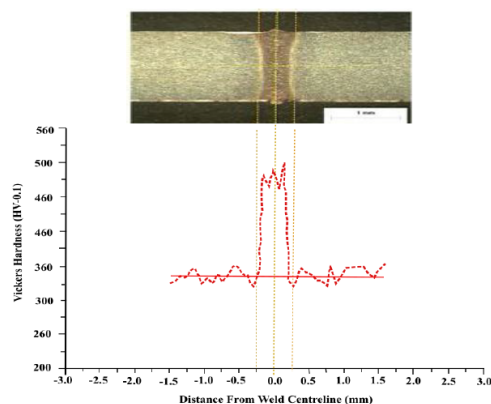


Figure 11: Hardness profile of sample: P2 / S150. Reprinted with permission from Alves *et al.*, // Journal of Materials Processing Tech. ©2017 Elsevier B.V. All rights reserved.

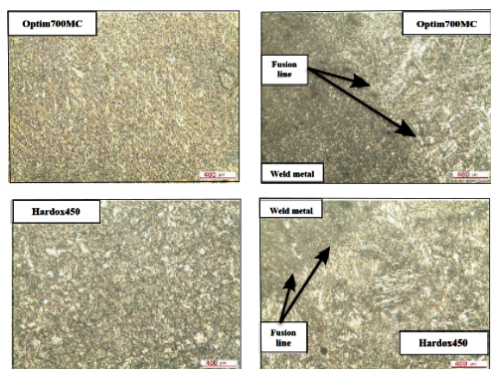


Figure 12: The microstructure of A1 specimen (2 hours of heat treatment at 450°C). Reprinted with permission from Uzunali *et al.*, // Advances in Structural Engineering and Mechanics, ASEM15 (2015). ©2015 ASEM15.

the HAZ can lead to negative effects on the mechanical characteristics of the weld joint.

Two methods of PWHT (retention and tempering annealing at the bainite transformation temperature) were used by Kucerova [23] to determine the behavior of the microstructure and the mechanical properties of the 0.4Mn 0.6Mn 42SiMn steel. 2Si 0.03Nb. A model has been developed to successively analyze the implications of the heat source on the mechanical behavior (tensile strength resulting in elongation), but also on the microstructure phase transformations (Austenite for bainite). It has been found after analysis of the results that for a heat source applied

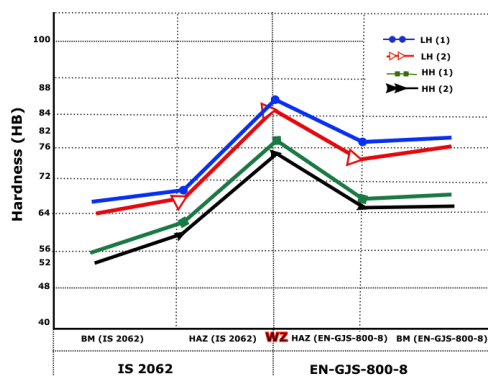


Figure 13: Dissimilar weld of IS 2062/EN-GJS-800-8. Hardness analysis. Normal welding process, (1) Low heat input LH₁, (1) high heat input HH₁. PWHT process. (2) Low Heat LH₂, (2) High heat HH₂. Reprinted with permission from Sergio *et al.*, // Material Research, 5 (2014). ©2014 MR.

to the weld joint, with an interval of 850°C to 1000°C, the reduced cooling time will have an impact on the tensile strength and its elongation. Figure 14a showed the different temperature variations and their impact on tensile strength (R_m), elongation (A) and retained austenite (RA). Based on the variations of the cooling rate, it is found in Figure 14b that the variation of the tensile strength thus resulting in elongation to a value of 930 MPa. It was possible to determine the high value of retained at more than 10%. As a function of bainitic hold temperature, a high value was observed at a temperature of 400°C. Corresponding to a value of retained of 12%. The higher the temperature, the retained austenite values will drop to the value of 0%.

5 Results and discussion

The results vary according to the chemical structure of the base materials and the welding conditions. Table 2 summarizes key results obtained from the literature.

Dissimilar welding of the HSS requires a combination of several analyzes such as the geometrical parameters of the weld joint, the mechanical characteristics of the base materials after the determination of the filler metal obtained after evaluation of the carbon equivalent. The decision of the type of welding process and the value of the heat source will depend on the geometric and mechanical characteristics of the base materials. Table 3 presents some recommended welding procedures based on the mechanical components of the base material. It is noted that for

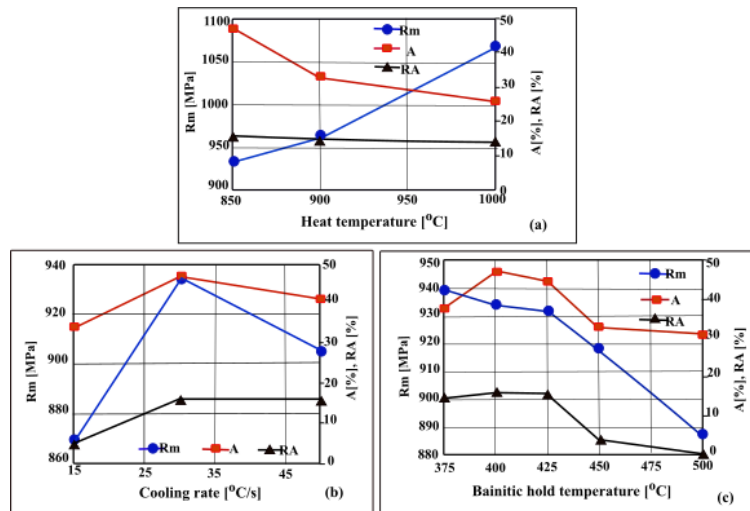


Figure 14: The effect of; (a) heating temperature, (b) cooling rate, and (c) bainitic phase temperature. Reprinted with permission from Kucerova // Metals 7 (2017). ©2017 Licensee MDPI, Basel, Switzerland.

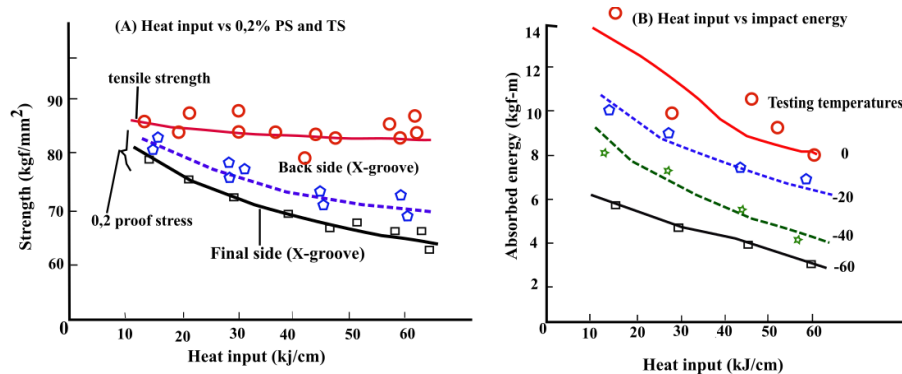


Figure 15: (a) Heat input with strength behavior of 780 MPa (80 kgf/mm²) using SMAW (1 kgf/mm² = 9.8 MPa; 1 kgf-m = 9.8 J). Reprinted with permission from Ikawa *et al.* // Sampo Publication Inc, (1978). © 1978 Sampo Publication Inc.

HSS with a high tensile strength of 610 MPa, the widely used welding processes are as follows:

- Shielded metal arc welding;
- Submerged arc welding;
- Gas tungsten arc welding;
- Occasional use for electrosag welding.

For structural steels with a high tensile strength of 610 MPa, the widely used welding processes include Shielded metal arc welding, submerged arc welding and

gas shielded metal arc welding and occasional use for electrosag welding.

After having chosen the process of welding materials according to their high tensile strength, it is recommended to determine the parameters of the heat source. Figure 15a shows the different heat source values applicable depending on the recommended high tensile strength. It has been noted that for low values of heat source, the values of high tensile strength should be high. The same phenomenon has been observed in Figure 15b. A reduced values of a heat source has a higher energy impact value.

Table 2: Summary of experimental investigations has been done to evaluate the influence of the heat input parameter and PWHT on the microstructure and mechanical behavior of dissimilar weld structures.

Materials	Strategy	Findings	Citation
ASTM E112-10 QT, TMC, OK Autrod 13.51 Shielded Metal Arc Welding (15% CO ₂ and 85% Ar)	Measurement of the mechanical behavior in the HAZ area of the dissimilar HSS.	<ul style="list-style-type: none"> • Variations in heat sources have direct implications on the mechanical characteristics of weld seams. • The heat source with a value of 1.7 can increase the hardness of the weld joint. 	Pirinen <i>et al.</i> [6]
Welding Optim 960 QC and Duplex Stainless steel (UNS S32205) with austenitic filler wire GMAW 350x150x5 mm	Apply three different value heat sources and analyze the mechanical behavior and microstructure	<ul style="list-style-type: none"> • A higher heat source can cause high hardness of the S960 QC HAZ, resulting in hot cracks. • When the heat source is minimal, this can lead to low hardness values and some cold cracks. 	Tasalloti <i>et al.</i> [16]
22MnB5, ENGTS-1000-5, and Docol 1400 M, Rapid Hot Forming Processes	Evaluate the mechanical properties and microstructure evolution during heat treatment.	<ul style="list-style-type: none"> • A slight change in the microstructure formation of grain size and undissolved carbide materials has been noted and was found to be excellent compared to conventional treatment. • For both types of steel, this system guarantees a good quality weld compared to the conventional system. 	Löbbe <i>et al.</i> [18]
13CrMo4-5/10CrMo9-10 use GMAW and Cold Metal Transfer (CMT)	Evaluate the advantages using Low heat input compared to the conventional GMAW	<ul style="list-style-type: none"> • It has been noted some incomplete microstructures transformations (austenite transformation) in this area (CGHAZ). 	Frei <i>et al.</i> [19]
ENGTS 1000-5 use Laser beam welding between 0.4 and 2.0 kW	Using the parameters of the heat source to evaluate the mechanical behavior and microstructure of the welded structure.	<ul style="list-style-type: none"> • The melting zone has the maximum value of the Hardness profile which was 530 HV; this will be justified by the fact that this zone has a high temperature, which is therefore susceptible to hot crack. 	Alves <i>et al.</i> [20]
Hardox 450, Optim 700MC MAG welding method	It investigated PWHT effects on the mechanical behavior of tempered of martensitic steel and high-strength steel joints.	<ul style="list-style-type: none"> • Hardness increasing due to temperature distribution. • The cooling rate determined only in HAZ of Hardox450 materials. • The hardness of the weld metal has not been affected by PWHT 	Uzunali <i>et al.</i> [21]
EN 1564 grade EN-GJS-800-8/ MIG welding process	It estimated the heat input and PWHT, and their influences in mechanical and microstructure properties.	<ul style="list-style-type: none"> • Changes in the parameters of the heat source have a direct impact on the mechanical characteristics of the weld seam. 	Chennaiah <i>et al.</i> [22]
42SiMn steel, Soaking hold and annealing hold	The effect of two-step heat treatment parameters on microstructure and mechanical properties.	Based on the variations of the cooling rate, the variation of the tensile strength thus resulting in elongation to a value of 930 MPa. It was possible to determine the high value of retained at more than 10%. As a function of bainitic hold temperature, a high value was observed at a temperature of 400°C.	Kucerova [23]

Table 3: Welding process with the type of welding consumables [28–32].

Welding process	Type of high-strength steel				
	490-MPa	610-MPa	690-MPa	780-MPa	980-MPa
Shielded metal arc welding	①	①	①	①	②
Submerged arc welding	①	①	①	①	②
Gas shielded metal arc welding	①	①	①	①	①
Gas tungsten arc welding	①	②	②	②	①
Electroslag welding	①	③	④	④	④

Note: ①: Widely used, ②: Used, ③: Occasionally used, ④: Not used

The consequences of a low or very high heat source compared to normal are important for the analysis of stress (cold and hot crack) and also on the microstructure (phase transformation) of HAZ of weld structures. To reduce the high risk of mechanical defects, it is often advisable to proceed to the PWHT.

6 Conclusion

This paper reviewed the literature on the topic of thermal behavior of HSS structures. It was found that different welding processes can be used to weld dissimilar steel materials (high-strength steels and stainless steels). Study of the mechanical properties and microstructure development of the weld joints is significant because the primary purpose of the welding is to actively join the two metals together as a welded structure at precise positions. It is crucial to obtain the tensile strength of the weld and the factors affecting the strength of the weld to maintain the acceptable microstructure of the weld joint. Based on the reviewed literature, a summarizing table was designed which provides a useful at-a-glance overview of current knowledge of dissimilar welding of high-strength steels. The analysis identified the resulting key aspects:

- A significant problem regarding the welding of dissimilar high-strength steels is cold cracking and material softening near the HAZ. Thus, heat input parameters should be controlled precisely during the welding process.
- It should be noted that the higher the heat input, the worse the properties of the HAZ of dissimilar welds of HSS;
- The correct category of the dissimilar HSS materials to be welded can help the manufacturer to select the best-optimized way of the joining processes. Understanding the different mechanisms found in dissimi-

lar welding of HSS will help to avoid defects such as cracks and softening;

- The heat input, the base materials, and the welding process are interlinked, and appropriate parameters are required to ensure the optimum characteristics of the weld joint. When using GMAW for HSS welds, high heat input affects the microstructure of the weld joint and the heat-affected area (causing bainitic transformation on the ferritic side and more martensite). With laser beam welding, the increase in the beam current leads to increasing depths and widths of the welds, and fully austenitic microstructure is produced in the weld zone. The consequence, there is a high cooling rate during the process. It is essential to obtain the optimal beam input current for the welding process and the desired outcome;
- When using PWHT, the weld joint may lose these intermetallic properties if the duration of the PWHT becomes long. With two HSS steels of type Hardox 450-Optim 700MC, the hardness increased due to abnormally high-temperature distribution. With decreased heat input, there is an increase in the tensile strength and impact strength. In the dissimilar welding of high-strength steel structures, suitable selection of the parameters of the PWHT process is significant to obtain specific weld joint properties.

Acknowledgement: The authors wish to express their gratitude to the Finnish National Education Agency (EDUFI), and the ENI CBC project Energy-efficient systems based on renewable energy for arctic conditions “EFREA” for their financial support.

References

- [1] P. Kah, M. Shrestha and J. Martikainen, *Mech. and Materials*, 440 (2014) 269–276.

- [2] American Welding Society, Welding Handbook Part 1, Material and application, Eighth Edition, IV(1987)-IV (1998), pp. 210-450.
- [3] B. Mvola, P. Kah and J. Martikainen, Review Advanced Mater. Science, 38 (2014) 125-137.
- [4] B. Mvola, P. Kah, J. Martikainen and R. Suoranta, Review Advanced Material Science, 44 (2016) 2.
- [5] American Welding Society, Welding Handbook Part 2, metal and their weldability, Eighth Edition, (1982), pp. 312-356.
- [6] M. Pirinen, J. Martikainen, P. Layus, V.A. Karkhin, and S. Yu. Ivanov, Welding International, 4 (2015) 14-17.
- [7] N. Kapustka, Welding Journal, 87 (2008) 135-148
- [8] Y. Shi, Z. Han and J. Fu, International Journal Fract. IV (1998) 91-101.
- [9] O. Balancin, W.A.M Hoffmann and J. Jonas, Metallurgical and Materials Transactions A, 31 (2000) 1353-1364.
- [10] G. Schulze, Welding high-strength steel, Springer Verlag, New York, (2009).
- [11] G. Frank, Berechnung von Vorwärmtemperaturen beim Schweißen, Düsseldorf: SchweißBen und Schneiden, (1988).
- [12] O. Tanaka, Sanpo Publications Inc., (1986) 79-86.
- [13] E. Roos, K. Maile, Werkstoffkunde für Ingenieure (Grundlagen, Anwendung, Prüfung., Berlin, Heidelberg: Springer Verlag, (2011).
- [14] H. Shao, Blank Welding high strength steels (Ph.D. dissertation, The Ohio State University, Columbus, Ohio, 2000).
- [15] M. Pirinen, The effects of Welding heat input on the usability of high-strength steels in welded structures (Doctoral thesis, Lappeenranta University of Technology, Lappeenranta, 2013).
- [16] H. Tasalloti, P. Kah and J. Martikainen, Materials Characterization, 123 (2017) 13-29.
- [17] M. Sadeghian, M. Shamanian, and A. Shafyei, Materials and Design, 60 (2014) 678-684.
- [18] C. Löbke, O. Hering, L. Hiegemann and A. Tekkaya, Materials, 9 (2016) 229.
- [19] J. Frei, T. Alexandrov and M. Rethmeier, Weld World, 60 (2016) 459-473.
- [20] M. Alves, M. Lima, D. Raabe, and Z. Sandim, Journal of Materials Processing Tech. 252 (2017) 498-510.
- [21] U.Y. Uzunali and H. Cuvalci, Proceedings of Advances in Structural Engineering and Mechanics, Korea (2015) 24-30.
- [22] B. Chennaiah, P. Nanda and K. Pahlada, International Journal of Eng. Research & Tech., 2 (2013) 1406-1413.
- [23] L. Kucerova, Metals, 7 (2017) 1-12.
- [24] KOBELCO Welding, The arc welding of specific steels and cast irons, Kobe Steel LTD, Tokyo, (2015).
- [25] G. Hissan, Conference IWW Doc. Prague (1999).
- [26] A. Omar, Welding journal, 2 (1998) 86-93.
- [27] J. Dupont, and C. Kusko, Welding Journal, 2 (2007) 54-57
- [28] H. Ikawa and T. Godai, The Complete Book of Welding, Tokyo, Sanpo Publication Inc., (1978).
- [29] R. Cristoffel, E. Nippes, and H. Solomon, Proceedings of the 5th Bolton Landing Conference, Bolton, (1978).
- [30] M. Pirinen, Welding international, 4 (2014) 13-18.
- [31] David Miller, API Recommended Practice, American Petroleum Institute 941 (1997-1998), rev.2-21-2006.
- [32] The Association for Training Engineers of Smaller Enterprises in Japan, Welding high-strength steel, Utilization of Welding Technology, Tokyo, (1984), pp. 5-912.
- [33] P. Russo, P. Matteis, A. Sanchez, and G. Scavio, Proceedings of 55 Convegno Nazionale IGF XXII, Rome, (2013), pp. 12-20.
- [34] A. Loureiro, Journal of Mat. and Tech., 128 (2002) 240-249.
- [35] V. Kujanpaa, S. David and C. White, Welding Journal, 65 (1986) 171-179.

Publication II

Bayock, F., Kah, P., Layus, P., and Karkhin, V.

**Numerical and Experimental Investigation of the Heat Input Effect on the
Mechanical Properties and Microstructure of Dissimilar Weld Joints of 690-MPa
QT and TMCP Steel**

Reprinted with permission from
Metals

Vol. 9(3):355, pp. 1-19, 2019
© 2019, MDPI

Article

Numerical and Experimental Investigation of the Heat Input Effect on the Mechanical Properties and Microstructure of Dissimilar Weld Joints of 690-MPa QT and TMCP Steel

Francois Njock Bayock ^{1,*}, Paul Kah ¹, Pavel Layus ¹ and Victor Karkhin ²

¹ Laboratory of Welding Technology, Lappeenranta University of Technology, P.O. Box 20, 53851 Lappeenranta, Finland; paul.kah@lut.fi (P.K.); pavel.layus@lut.fi (P.L.)

² Welding and Laser Technologies Laboratory, Peter the Great St. Petersburg Polytechnic University, 195251 St. Petersburg, Russia; victor.karkhin@mail.ru

* Correspondence: francois.njock.bayock@lut.fi; Tel.: +358-46526-7492

Received: 12 February 2019; Accepted: 15 March 2019; Published: 20 March 2019



Abstract: The study evaluates numerically and experimentally the effect of welding heat input parameters on the microstructure and hardness of the heat-affected zone (HAZ) of quenched and tempered (QT) and thermo-mechanically controlled process (TMCP) 690-MPa high-strength steel. Numerical analyses and experimental comparisons were applied using three heat input values (10, 14, and 17 kJ/cm) in order to predict the thermal fields during welding. Experimental analysis was carried out of the microstructure and microhardness behavior in different HAZ areas. The numerical values indicate that the maximum respective values of temperature measured in QT steel and TMCP steel were about 1300 and 1200 °C for a heat input of 10 kJ/cm, 1400 and 1300 °C for a heat input of 14 kJ/cm, and 1600 and 1450 °C for a heat input of 17 kJ/cm. The cooling times resulted, for a heat input of 10 kJ/cm, in numerical $t_{8/5}$ (14.5 s) and experimental (18.84 s) increases in hardness in the coarse-grain heat-affected zone (CGHAZ) of the QT steel (317 HV0.1), due to the formation of bainite and lath martensite structures with grain growth. Decreased hardness in the CGHAZ of TMCP steel (240 HV0.1) was caused by primary recrystallization of the microstructure and the formation of more equilibrium products of austenite decomposition. Increasing the heat input (14 to 17 kJ/cm) led to numerical $t_{8/5}$ (29 s) and experimental (36 s) decreases in hardness in the CGHAZ of QT steel (270 HV0.1) due to the full austenite (thermal weld cycle), and maintained the relative value of TMCP steel (235 HV0.1).

Keywords: thermo-mechanically controlled process steel; quenched and tempered steel; microstructure

1. Introduction

High-strength steel (HSS) is used more and more today in almost all industrial fields. The benefits are enormous in terms of tensile strength and elongation, depending on the area of use. It is often essential to understand the microstructural behavior of materials subjected to dissimilar welds. It would be crucial to know the methods of manufacturing the elements and their uses to begin the analysis of their weldability. The weldability of these materials depends on many parameters such as the geometry of the weld joint, and the mechanical and chemical properties of the different elements [1–3]. After that, the characteristics of the filler metal are used when welding with an electric arc or others. In this analysis, two types of HSS are studied, with the same mechanical properties, but of varied chemical composition and a different method of manufacture—quenching and tempering (QT), and thermo-mechanically controlled processing (TMCP). The first stage of QT steel production is hot-rolling with air-cooling,

followed by reheating above the transformation temperature AC_3 , and then water quenching. High cooling rates suppress diffusion-controlled ferrite and pearlite formation and lead to the creation of the main martensite. Subsequent tempering allows the desired mechanical qualities to be achieved by relieving internal stresses [4–7]. The conditions of the thermomechanical rolling in TMCP steel production depend on the plate thickness and chemical composition of the steel being treated. A high degree of deformation in the temperature range of the suppressed recrystallization ($T_{max} \geq 1150$ °C) results in essential grain refinement of the final microstructure [8,9]. Steel grades with the same value of yield stress (690 MPa) can have significantly different chemical composition. Therefore, the weld joint and the heat-affected zone (HAZ) microstructural and mechanical properties may also differ. The mechanical behavior of the HAZ largely determines the serviceability of a weld joint. Thus, the analysis of the mechanical behavior and the microstructure of dissimilar high-strength steels reveals a particular interest in the field of current research [10–12]. Researchers usually give primary attention to the coarse-grain region of the HAZ (CGHAZ), which is traditionally considered the most unfavorable area of the HAZ. However, such a consideration is not always valid. For example, some areas of the HAZ can contain a relatively soft layer with under-matched mechanical properties, and it is, thus, essential to assess the features of the entire HAZ [13,14]. Successful welding of HSS requires a thorough understanding of microstructural transformations and other phenomena occurring during and after the welding process. A correctly chosen welding heat input will result in a high-quality weld without induced cold cracking and stress corrosion cracking defects, which are often observed in the CGHAZ region [15–17]. In the case of multi-pass welding, deterioration of toughness can be caused by small areas of poor fracture toughness, referred to as local brittle zones. This zone is often situated between the interconnection of two weld passes in CGHAZ [18]. Some authors [19–22] evaluated the mechanical properties (tensile strength, impact energy, and crack opening displacement) in consumable electrode arc welding of QT and TMCP steels. Their results indicated that the tensile strength is higher than 800 MPa [22]. However, they seemed to not consider the effect of the microstructural gradient and the impact of different microhardness in the various HAZ regions. As a result, researchers studied the tensile properties of undermatch welds of QT HSS RQT701 for different heat inputs [23]. It was observed that an increase in the heat input values produces a coarsening of the microstructure of the weld metal (WM) and the HAZ. This microstructure change, in turn, promotes the formation and coarsening of upper bainite in the zones mentioned above with the appearance of some ferrite side plates. Generally, most of the research in this area was conducted without paying attention to microstructural behavior in the different regions of the HAZ [24,25]. In welding simulation, there is an interaction of some disciplines in the physical analysis: the interaction between temperature, mechanical response (residual stress, gap opening, distortion, and hardness), and microstructure (composition, morphology, and chemical reactions). From the analysis of the thermal behavior of the weld joint to the microstructural analysis, there are two phases of heat exchange: the heating phase and the cooling phase. For a numerical analysis of this process, the model using the finite element method can develop the transient heat transfer process. The chemical reactions of materials creating latent heat may be neglected during the process of welding modeling. Goldak [26] modeled the welding simulation using finite element method information to model heat flow as ellipsoidal and double-ellipsoid models. In this study, the values of heat source were applied in the weld joint of two base materials. The numerical analyses of heat source were carried out on the diffusion in the weld joint. Then, thermal conduction was observed from the weld joint to the different base materials. The cooling time ($t_{8/5}$) of each welding operation enabled us to evaluate the different microstructure behavior (grain size) and the mechanical strains (microhardness results). A comparative thermal profile (numerical and experimental) was performed in order to predict the reasonable cooling time and hardness susceptible to having a great morphology of the microstructure in the different HAZ regions (fine-grain HAZ (FGHAZ) and GCHAZ).

2. Materials and Methods

The analyses were conducted on two types of HSS with the same tensile strength of 690 MPa (QT and TMCP). Table 1 represents the chemical composition of the base materials used in this experimental analysis. Figure 1 shows the geometry of the weld joint with dimensions $150 \text{ mm} \times 50 \text{ mm} \times 8 \text{ mm}$, equipped with a weld joint having a V-groove butt joint with an angle of 60° , and a 2 mm gap. Table 2 shows the mechanical properties (yield strength, tensile strength, and elongation) of both base materials and filler material. On the basis of the chemical compositions of the different materials, the carbon equivalence values were determined. The mechanical characteristics of the base materials made it possible to determine the characteristics of required weld metal, allowing the application of the different heat inputs requested in this analysis.

The weld applied in this analysis was Gas metal arc welding (GMAW), using shielding gas Ar + 18% CO_2 , and an automatic robotic system. The digital laser system automatically read the thermal transfer (Figure 2a) from the weld metal line to the base materials. This reading by the laser made it possible to determine the temperatures point by point, and it was possible to evaluate the cooling time which from 800 to 500°C ($t_{8/5}$). The welding parameters were integrated into the central unit, which was interconnected with the servo controller of the robot system and the power source. The welded parts were placed in a cabinet at both ends, and the variations of the heat source automatically changed the speed of the welding process (Figure 2b). Table 3 presents the different parameters applied to the heat source. As the welding used two layers, the first one remained constant at a value of 10 kJ/cm , while the second layer varied; this allowed us to determine the variations of the $t_{8/5}$ time on the different samples. The weld metal was undermatched, and the yield strength of the filler metal was 72% of that of the base metal. The welding conditions are presented in Table 3. The heat input corresponds to an arc efficiency according to ISO 15614-1:2017.

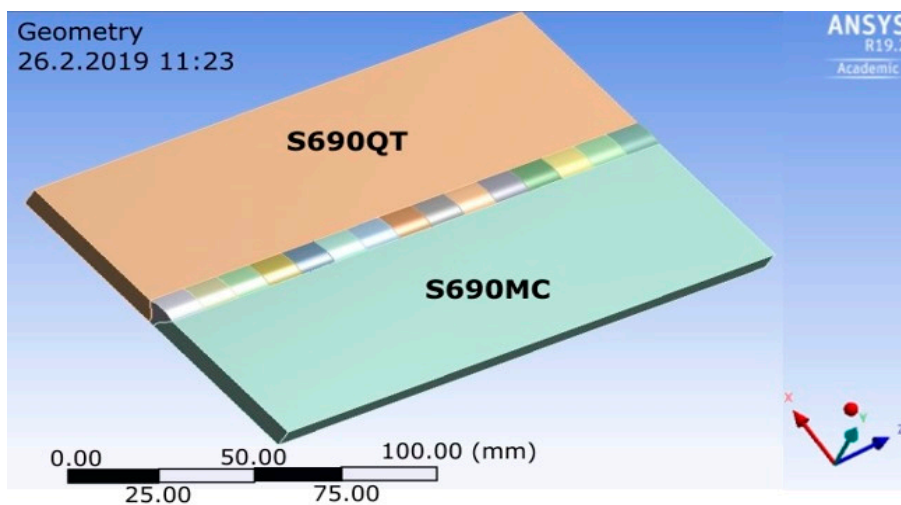


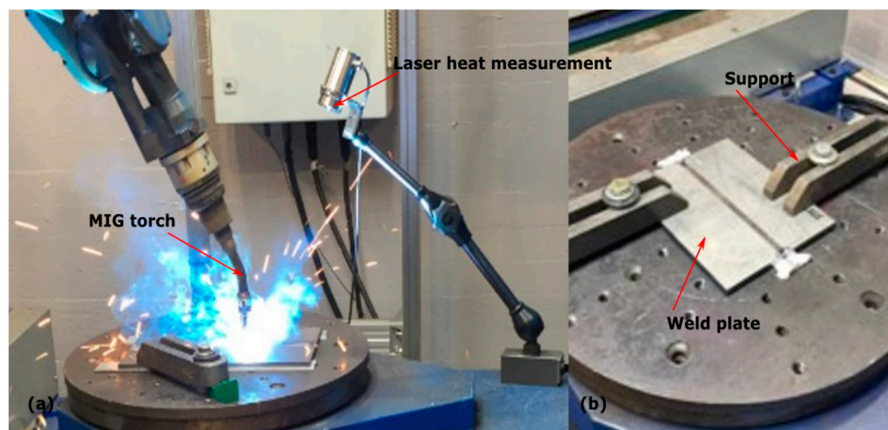
Figure 1. The geometry of the sample.

Table 1. The chemical composition of the quenching and tempering (QT), thermo-mechanically controlled process (TMCP) steels, welding wire (wt %), and the carbon equivalent (CE).

	C	Si	Mn	Al	B	Nb	Ti	V	Cu	Cr	Ni	Mo	N	P	S	CE
Steel																
QT	0.137	0.28	1.39	0.061	0.0021	0.022	0.002	0.001	0.02	0.062	0.066	0.029	0.005	0.013	0.0013	0.41
TMCP	0.049	0.17	1.86	0.025	-	0.081	0.092	0.009	-	-	-	0.008	0.005	0.08	0.004	0.35
16834-A G 69 6 M21 Mn4n1.5CrMo	0.07	0.50	1.70	-	-	-	0.05	-	≤0.30	0.20	1.60	0.45	0.005	0.012	0.02	0.55

Table 2. Mechanical properties of the steels and welding wire.

Steel	Yield Strength (MPa)	Tensile Strength (MPa)	Elongation A5 (%)
QT	793	835	16.3
TMCP	761	821	20
16834-A G 69 6 M21 Mn4ni1,5CrMo	720	780	≥17

**Figure 2.** Gas metal arc welding process: (a) weld torch and laser heat control; (b) workpiece position.**Table 3.** Welding conditions.

No.	Pass	Current (A)	Voltage (V)	Welding Speed (cm/min)	Net Power (W)	Heat Input (kJ/cm)
1	1	230	25.6	27.18	4710	10
	2	230	25.6	27.18	4710	10
2	1	230	25.6	27.18	4710	10
	2	268	29.0	27.12	6218	14
3	1	230	25.6	27.18	4710	10
	2	258	30.6	22.26	6316	17

The microstructure of the joints was revealed by etching the specimens in an initial etchant (4% solution of HNO₃ in ethanol). The microstructure was examined using a Leica DMI5000M light metallographic microscope (Leica Microsystems, Wetzlar, Germany) with magnification up to 1000×. Image analysis was used for accurate determination of grain size according to ASTM E112-13. Hardness measurements according to ISO 6507-1:2018 were conducted with a Wilson Wolpert 452SVD Vickers hardness tester (ITW, Chicago, IL, USA). The microhardness of single phases was measured by a Wilson Wolpert 402MVD microhardness tester (ITW, Chicago, IL, USA) with a diamond pyramid indenter under a load of 0.0025 N. Evaluation of the grain size was made possible by ImageJ software (ImageJ 2013, NIH, Bethesda, MD, USA). Measurements were taken on samples of FGHAZ from the two base materials. The measurements were automatically performed using ImageJ surface area. Table 1 shows the mechanical properties of the different base materials, while Table 2 shows the chemical composition of QT S690 and TMCP S690 steel.

3. Numerical Formulations

In this study, the transient method of heat transfer from the melting point to the base material was applied. The ambient temperature was evaluated at 28 °C. The displacement of the heat source was measured from the thermal diffusion (weld torch) to the weld joint, and from the weld joint to the base material. In this study, flux production was considered constant in its geometry and intensity. Q (W/mm^3), the thermal energy due to the thermal conduction, was analyzed along of the weld joint and was evaluated according to the thermomechanical parameters of each material, i.e., the effect of the thermal conduction on different surfaces of the weld joint.

The heat of the welding arc and molten metal droplets can be considered during the welding process, and the elements representing filler elements in the finite element model are provided in terms of heat input as volumetric and surface heat flux with uniform density. The volumetric heat input q ($\frac{W}{mm^3}$) is determined by Equation (1).

$$q = \frac{\eta UI}{V} b_v + \frac{\eta UI}{A} b_A, \quad (1)$$

where η is the arc efficiency, and it was assumed to be 0.90 for GMAW in this study, U and I are the arc voltage (V) and welding current (A), respectively, and V , A the different volume (mm^3) of elements representing the weld filler material in the finite element (FE) model. In Equation (1), the volumetric heat factors b_v and b_A have no physical interpretation. They are only used to fine-tune the heat flux such that the desired fusion zone and temperature distributions can be archived. The conduction in x -, y -, and z -directions for an orthotropic heat conduction model is given in Equation (2) based on Fourier's law of conduction.

$$\left(\frac{\partial}{\partial x} \left[k_x \frac{\partial T}{\partial x} \right] + \frac{\partial}{\partial y} \left[k_y \frac{\partial T}{\partial y} \right] + \frac{\partial}{\partial z} \left[k_z \frac{\partial T}{\partial z} \right] \right) + \dot{q} = \rho c \frac{\partial T}{\partial t}, \quad (2)$$

where k_x , k_y , and k_z are the thermal conductivity values ($W/m \cdot ^\circ C$) in the x -, y -, and z -directions, T (x , y , and z) is the temperature, and x , y , and z represent the welding directions in longitudinal, transverse, and thickness directions. The essential boundary was defined as shown in Equation (3).

$$k \frac{\partial T}{\partial x} l_x + k \frac{\partial T}{\partial y} l_y + k \frac{\partial T}{\partial z} l_z + q_z + h_{conv} (T_s - T_0) + \sigma \epsilon (T_s^4 - T_0^4) = 0, \quad (3)$$

where, l_x , l_y , and l_z are the direction cosines of the outward drawn normal to the boundary, h_{conv} is the heat transfer coefficient, q_z is the boundary heat flux, ϵ is emissivity whose value was considered as 0.03, and $\sigma = 5.67 \times 10^{-8} W/m^2 \cdot ^\circ C$ is the Stefan-Boltzmann constant. By applying the finite element method for the resolution of the system, Equation (3) was developed according to the model Galerkin's virtual development of the temperature flow according to Equation (4).

$$\int_v \left(\frac{1}{2} \right) \left[K_x \frac{\delta^2 T}{\delta x^2} + K_y \frac{\delta^2 T}{\delta y^2} + K_z \frac{\delta^2 T}{\delta z^2} \right] - 2 \left(Q - \rho c \left[\frac{\delta T}{\delta t} \right] \right) dv + \int_{s_1} q T ds + \frac{1}{2} \int_{s_2} h (T - T_\alpha)^2 ds = 0, \quad (4)$$

where, in the first integral, the first three terms give the thermal stiffness matrix due to conduction, $[K_{cond}]$, Q gives the body internal heat generated, such as the heat vector, $\{Q_{body}\}$, and the last term gives the body heat capacity matrix, $[C]$, in terms of the time derivatives of temperature. The second integral gives the thermal load due to heat flux on the surface q . The first term in the third integral gives the convective load due to the film coefficient $\{h\}$. Finally, the stiffness matrix is given in Equation (5).

$$[K] + [K_{cond}] + [K_{conv}]. \quad (5)$$

Moreover, the load vector is defined in Equation (6).

$$\{Q\} + \{Q_{body}\} + \{q\} + \{h\}. \quad (6)$$

The heat energy equations were written in tensor form, whereby the element transient heat equation was obtained and later summed to get the system equation analyzed with time. Equation (7) shows the derived matrix.

$$[K(T)]\{T\} + [(T)]\left\{\frac{\partial T}{\partial t}\right\} = \{Q(T)\}. \quad (7)$$

The finite element model dimensions of a weld specimen were 150 mm × 50 mm × 8 mm, with a 2 mm square gap was between them, as shown in Figure 1a. QT S690 and MC S690 steels were considered for simulations to be carried out. Convection was applied on all surfaces of the plate except the heat-affected area. Figure 1 shows the FE model of the butt welded joint. Equation (7) could be resolved numerically with ANSYS® (19.2, ANSYS, Inc., Canonsburg, PA, USA) to carry out the sequential thermal distribution from the melting line to the base material. The geometry was divided into two parts with the characteristics described below.

The weld plate was made of two materials (QT S690 and TMCP S690), with a total of 148,147 and 30,300 nodes and elements, respectively. The weld bead was composed of 41,055 and 7800 knots and elements, respectively, which had a total of 189,202 and 38,100 individual nodes and elements, respectively. Figures 3 and 4 show the thermal conductivity and the specific heat as a function of the temperature of the high-strength steel QT S690/TMCP S690, respectively, and these values were obtained using the JMat software. This software was used to obtain the remaining thermo-mechanical material properties.

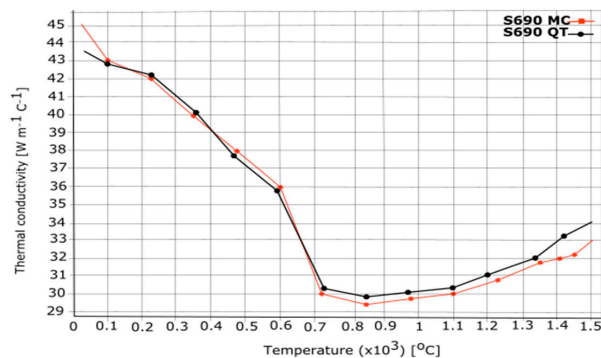


Figure 3. Thermal conductivity.

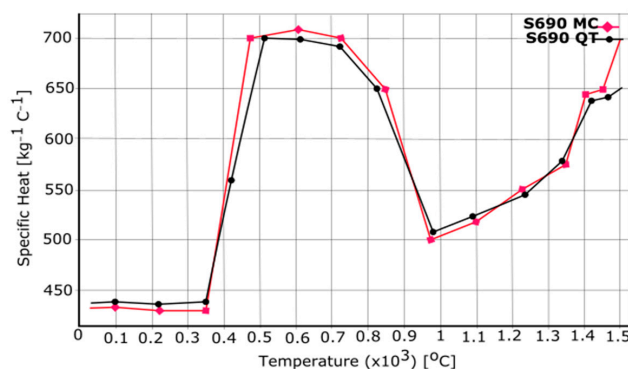


Figure 4. Specific heat.

4. Results and Discussion

A heat input value was assigned step by step for the duration of the welding procedure at speeds of 27.18, 27.12, and 22.26 cm/min. Afterward, the different positions of the welding procedure were recorded. Figure 5a shows the beginning of the welding process, where the melting zone is shown in red, while Figure 5b shows the welding position after 15 s (one-third of the travel direction); we observed thermal diffusion from all sides of the materials and noted that this repair network was not uniform for both bodies of material. Figure 5c shows the welding position after 45 s (two-thirds of the travel direction), and Figure 5d illustrates the end of the weld after 60 s (the end of the travel direction). The total welding process lasted 46 s for the first welding process, 58 s for the second welding process, and 60 s for the third welding process.

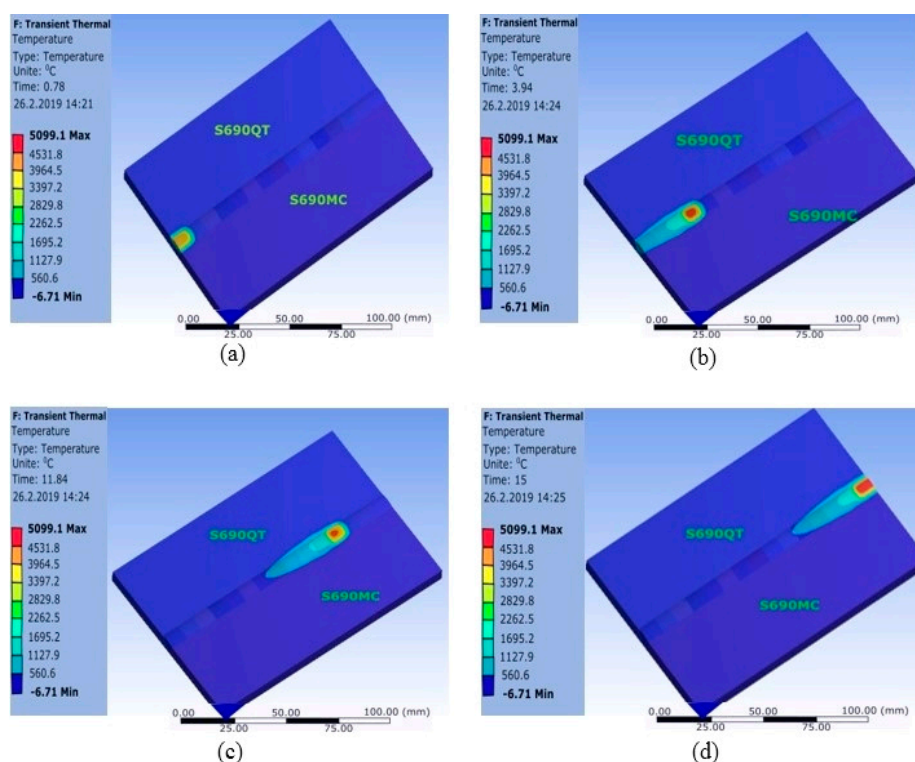


Figure 5. Thermal simulation process: (a) starting process; (b) simulation after 15 s; (c) simulation after 45 s; (d) the end of the process after 60 s.

4.1. Thermal Variations

Figure 6a–c shows the numerical results of the heat transfers in the weld seams of the two materials. The values of heat source applied to this program were 10, 14, and 17 kJ/cm. Subsequently, the same heat source values were experimentally applied using GMA welding as shown in Table 3. The analysis was carried out on the second welding pass. The first step was considered constant in all three samples. After welding the first pass, the weld joints underwent a slow cooling before applying the second-pass weld. Figures 6d and 7a,b represent the results of the temperature transfer from the melting point to the base material, allowing the evaluation of the required cooling time for the two base materials. On average, 1450 measurement points were recorded for each numerical and experimental analysis process. The analyses of the different behaviors of the heat sources led

to the ability to compare their behaviors. Figure 7c–e interpret the results of different heat sources (numerical and experimental) for each material. It was found that, when a heat source of 10 kJ/cm was applied, the numerical results indicated that the maximum measured temperatures in the QT steel and TMCP steel were approximately 1320 and 1200 °C, respectively, at a distance of 7 mm away from the centerline of the weld. The average cooling time of the two base materials was 14.5 s. During the experimental process, the average value of cooling time was 18.84 s. For the second test using heat input with a value of 14 kJ/cm, the numerical results indicated that the maximum temperatures in the QT steel and TMCP steel were approximately 1400 and 1300 °C, respectively, at a distance of 7 mm away from the centerline of the weld. The respective numerical and experimental cooling time results gave 24.85 and 30.45 s. For the last analysis using heat input with a value of 17 kJ/cm, the numerical results indicated that the maximum measured temperatures in the QT steel and TMCP steel were about 1600 and 1450 °C, with average values of the respective numerical and experimental cooling times of 29.45 and 36 s.

This difference in cooling time had an impact on the mechanical characteristics of the applied weld joint. An analysis of the samples in terms of the hardness and microstructure behavior allows us to understand in detail the implications of these cooling times.

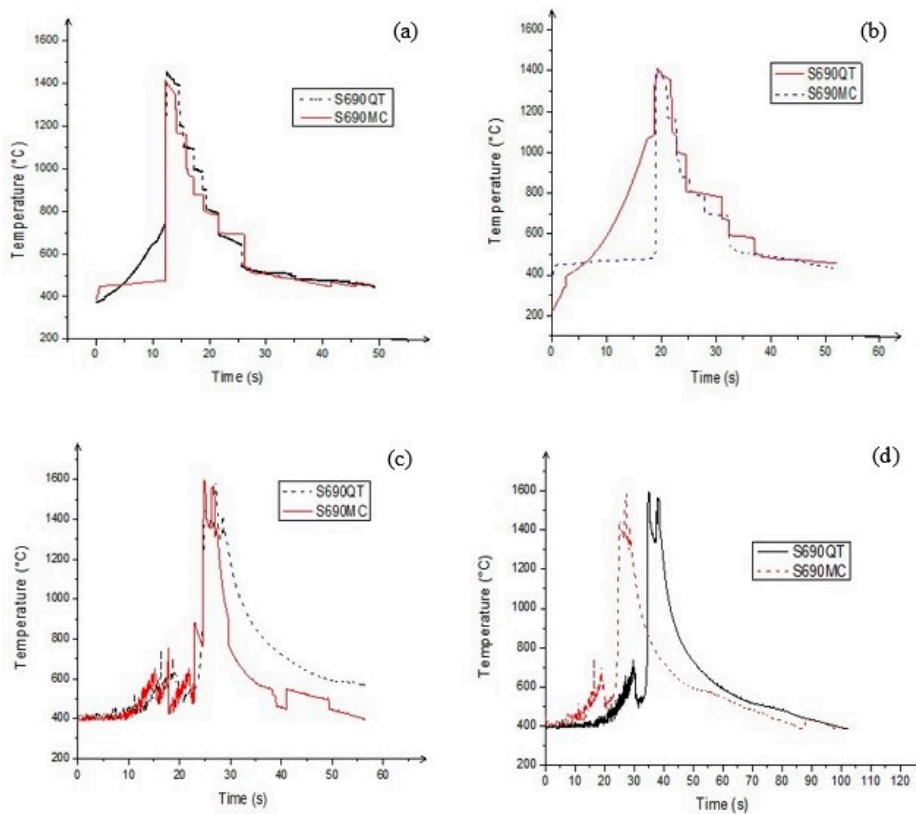


Figure 6. Cooling time results in the weld joint: numerical values using (a) 10 kJ/cm of heat input, (b) 14 kJ/cm of heat input, and (c) 17 kJ/cm of heat input; (d) experimental values using 10 kJ/cm of heat input.

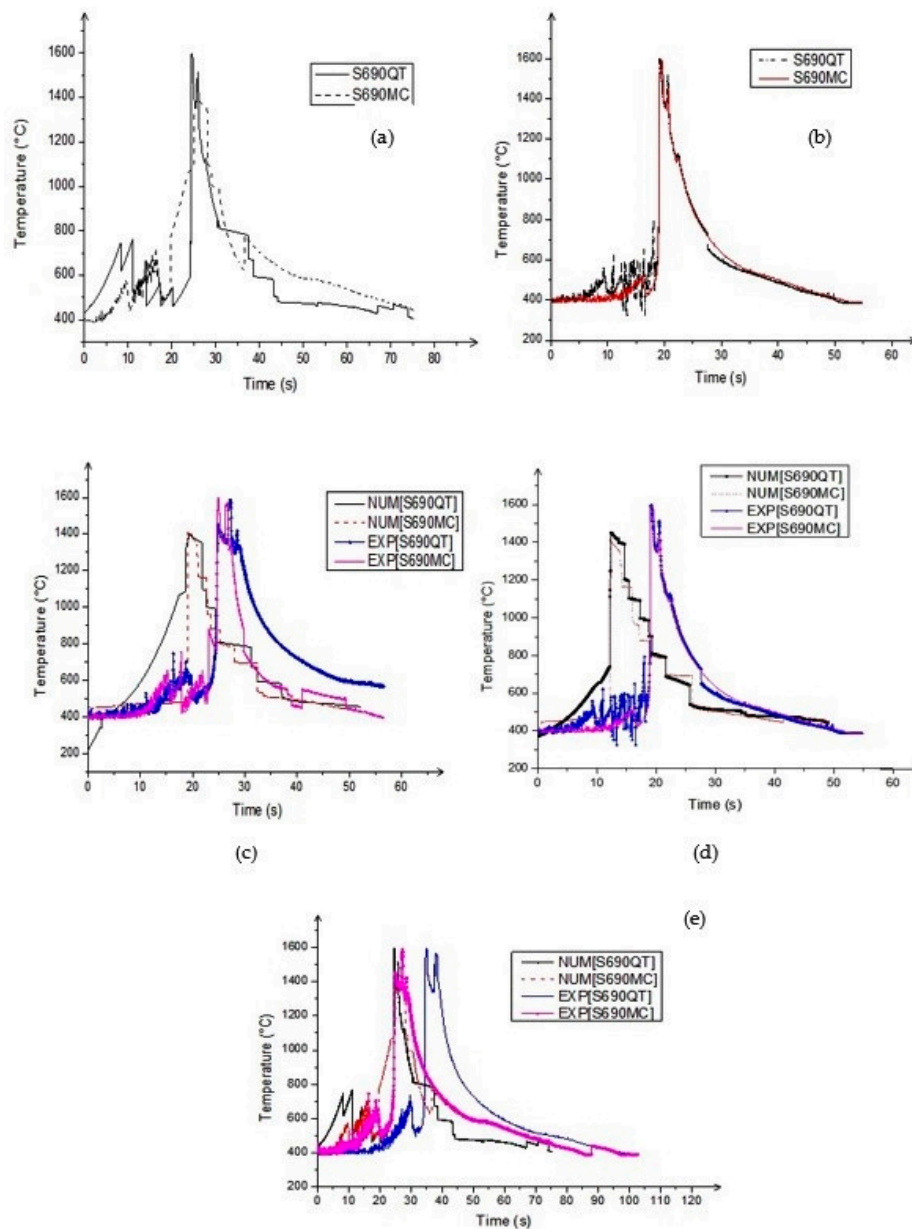


Figure 7. Cooling time results in the weld joint: experimental values using (a) 10 kJ/cm of heat input, and (b) 14 kJ/cm of heat input. Comparison between numerical and experimental values using (c) 10 kJ/cm of heat input, (d) 14 kJ/cm of heat input, and (e) 17 kJ/cm of heat input.

4.2. Microstructure Behavior of the QT Steel Welded Joint

In the QT steel, the CGHAZ, FGHAZ, inter-critical HAZ (ICHAZ), and subcritical HAZ (SCHAZ) were defined by optical microscopy (Figure 8). The microstructure varied continuously with a local peak temperature. The typical optical microstructure of QT steel, consisting mainly of tempered martensite

and bainite, is shown in Figure 8a. In this figure, the size of the initial austenite grain corresponds to grain size 12 (5.6 μm) according to ASTM E112-13. The microstructure of the base metal is homogeneous, and in-equigranularity is not observed. A limited carbon content of up to 0.15% in the base metal allowed lath martensite to be obtained and the formation of twinned martensite to be prevented.

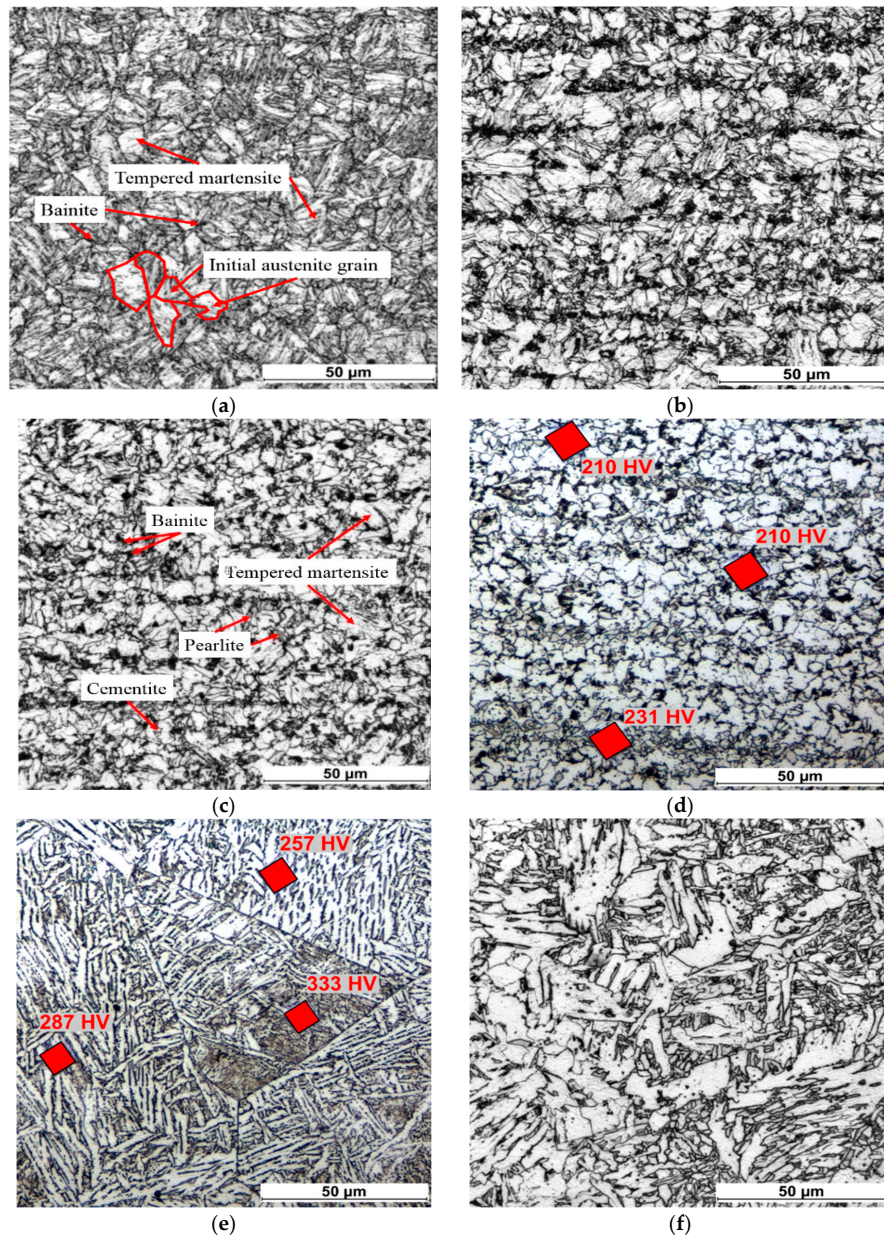


Figure 8. The optical microstructure of the quenched and tempered (QT) steel welded joint (second welding condition): (a) base metal; (b) subcritical heat-affected zone (SCHAZ); (c) inter-critical HAZ (ICHAZ); (d) fine-grain HAZ (FGHAZ); (e) coarse-grain HAZ (CGHAZ); (f) weld interface.

SCHAZ was the area most affected by the sudden changes in temperature, leading to the formation of cementite grains. In Figure 8b, we can identify some grain bainite grains of black cementite particles at this location, caused by carbide diffusion at low temperatures. The IGHZ corresponds to an area having a temperature range from the lower to upper critical point, and between the upper and lower critical point (cooling phase). During the heating phase, there was a temperature variation of about 720 to 910 °C in the HAZ. There was a transformation in grain austenite, which increased up to the peak temperature. During the cooling time, a transformation occurred in the first partial time of austenite grain (temperature ranging from 910 to 720 °C). At less than 720 °C, the solidification phase began with a transformation of small grain into a microstructure with a mixture of bainite, martensite (tempered), pearlite, and some cementite.

The FGHAZ refers to the HAZ which was subjected to peak temperatures between the upper critical point AC_3 and the austenite grain coarsening temperature, typically between about 910 and 1300 °C (Figure 8d). The CGHAZ and FGHAZ are both zones that became fully austenitic due to the thermal weld cycle. After a $\gamma \rightarrow \alpha$ transformation, the microstructure of these zones changed progressively depending on the previous austenite grain size. To identify and locate the CGHAZ and FGHAZ regions, it was necessary to rely on the different temperature ranges, or on the grain sizes in micrograph picture. During the heating phase (ferrite grain α to austenite grain γ), the grain surfaces grew (austenite grain increases). This development was possible due to the dissolution of the cementite, increasing the temperature. If the peak temperature decreased in this phase, there would have been a reduction in the growth of the original grain, which may have resulted in increased nitride and carbide formation. The microstructure of the CGHAZ of the QT steel in this work was composed of bainite and lath martensite (Figure 8e). Austenite grains grew during welding heating from 5.6 μm (grain size 12 according to ASTM E112-13) (base metal) to 75 μm (grain size 4–5). During the cooling phase (austenite γ to ferrite α transformation), the large transforming grains broke down to form fine grains at temperatures around 720 °C. In the analysis of this microstructure, we can clearly identify two main grains: bainite and martensite (with low carbon). Bainite is identified at a higher temperature compared to martensite. This grain may have the appearance of a trace of ferrite grain and cementite (Fe_3O), due to the high temperature of the upper bainite. The same traces of ferrite can be identified inside martensite grain at low temperatures.

The FGHAZ had the most reasonable grain structure. For the QT steel in this study, quantifying microstructural grain in the FGHAZ could help predict the possibility of brittle formations inside the microstructure. ImageJ 1.52p 22 software was used to define the different grain sizes in the microstructure. The measurement was made automatically with the aid of the ImageJ color threshold (Figure 9a,b). In total, 143 grains were counted from a surface sample with dimensions of 262 $\mu\text{m} \times 284 \mu\text{m}$. The surfaces of each grain were measured, which gave the following results: with QT 690 steel, the smallest size evaluated was 1.3 μm^2 , and the maximum size was equal to 62 μm^2 . The general average value of the area was evaluated by applying the relationship where \bar{X} represents the general average, X_i is the measurement of grain size, and n is the number of grain sizes. The general average grain size value gave results of $\bar{X} = 12.72 \mu\text{m}^2$. The standard deviation (SD) of individual measurements was calculated using the relationship below; after all calculations, the value of SD was determined as 13.5 μm^2 .

The characterization of samples using the software makes it possible to compare the sizes of the grain sizes according to ASTM E112-13. At the FGHAZ, the average found was 12.72 μm^2 .

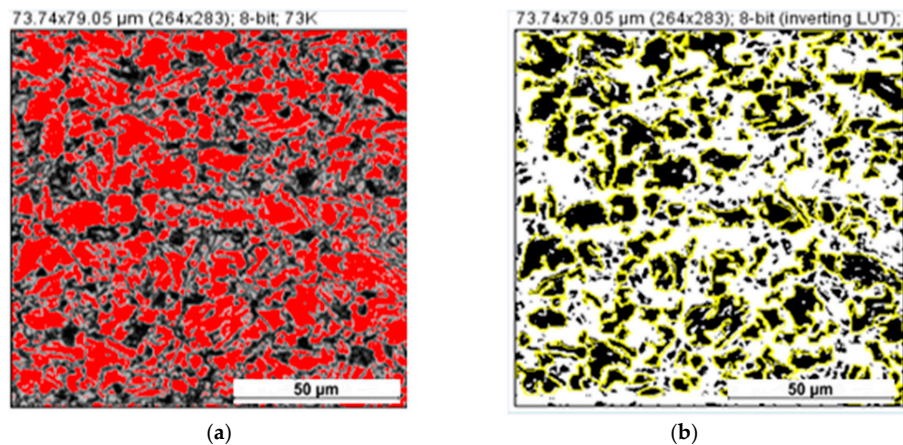


Figure 9. The microstructure of the FGHAZ region of QT steel for the second welded condition: (a) calibration using Threshold ImageJ; (b) measurement of grain area using ImageJ 1.52p 22.

4.3. Microstructure Behavior of the TMCP Steel Welded Joint

The TMCP steel in this study was a high-strength low-alloy structural steel manufactured by thermo-mechanically controlled processing. The TMCP steel contained about 0.05% less carbon than the QT-steel (Table 1). The reduction in carbon content allowed considerable improvement in the low-temperature toughness of the base metal. The 690 TMCP steel was mainly composed of 70% bainite and 30% ferrite (Figure 10a). The size of the grains corresponded to ASTM 112-13 grain size 14 (3.0 μm). During the thermal transformation process, the CGHAZ was transformed in its first phase according to the bainite–ferrite morphology (B–F), with a small amount of martensite–austenite (M–A). During the cooling phase, the austenite grain was transformed into ferrite at a high temperature of 720 $^{\circ}\text{C}$, and then into bainite. The internal composition of bainite may have retained some ferrite and carbide due to the elevation of temperature in this area. In the micrographs, most prior austenite grain boundaries are visible, allowing the mean austenite grain size to be measured. The ICHAZ and SCHAZ regions of the TMCP steel can hardly be distinguished (Figure 10d,e). The reason for this view was the low carbon content in the TMCP steel, which meant that heating to temperatures around the critical point AC_1 did not produce large-scale nucleation of cementite and its coagulation.

The same measurement procedure as with the QT steel was also followed with the TMCP steel (Figure 11a,b), with a total grain number count of 143 grains. It was observed that the smallest grain size evaluated was 1 μm^2 , and the maximum grain size was equal to 37 μm^2 . Based on these values, the overall value of the size was evaluated at $\bar{X} = 7.6 \mu\text{m}^2$. The standard value of grain deviation was calculated as 5.8 μm^2 (ASTM E112-13).

The average austenite grain size was 89.0 μm^2 (ASTM E112-13 grain size 4). Within the prior austenite grain, several crystallographic packets could be identified, with high misorientation angles between them, which slightly refined the effective grain size. The ratio of grain size number to grain size area of the TMCP steel, which was done to evaluate the surface concentration in the FGHAZ, is presented in Figure 12a. The result shows that, for the total of 143 grains, a higher grain concentration in the interval from 1–10 μm^2 was occupied by 112 grains. The remainder of the grains (31) occupied the surface area in the range from 10–25 μm^2 . In Figure 12b, the statistical data present the results of QT steel grain size by sample; 80 grains were identified occupying an area of 1–10 μm^2 , while the second zone included 35 grains occupying an area of 10–30 μm^2 , and the last zone included 28 grains occupying an area of 30–62 μm^2 .

Comparative analysis indicates a high concentration of grains in the upper surfaces of the QT 690 compared to the TMCP 690 steel. The average difference was $12.7 \mu\text{m}^2$ for QT 690 and $7.6 \mu\text{m}^2$ for TMCP 690 steel.

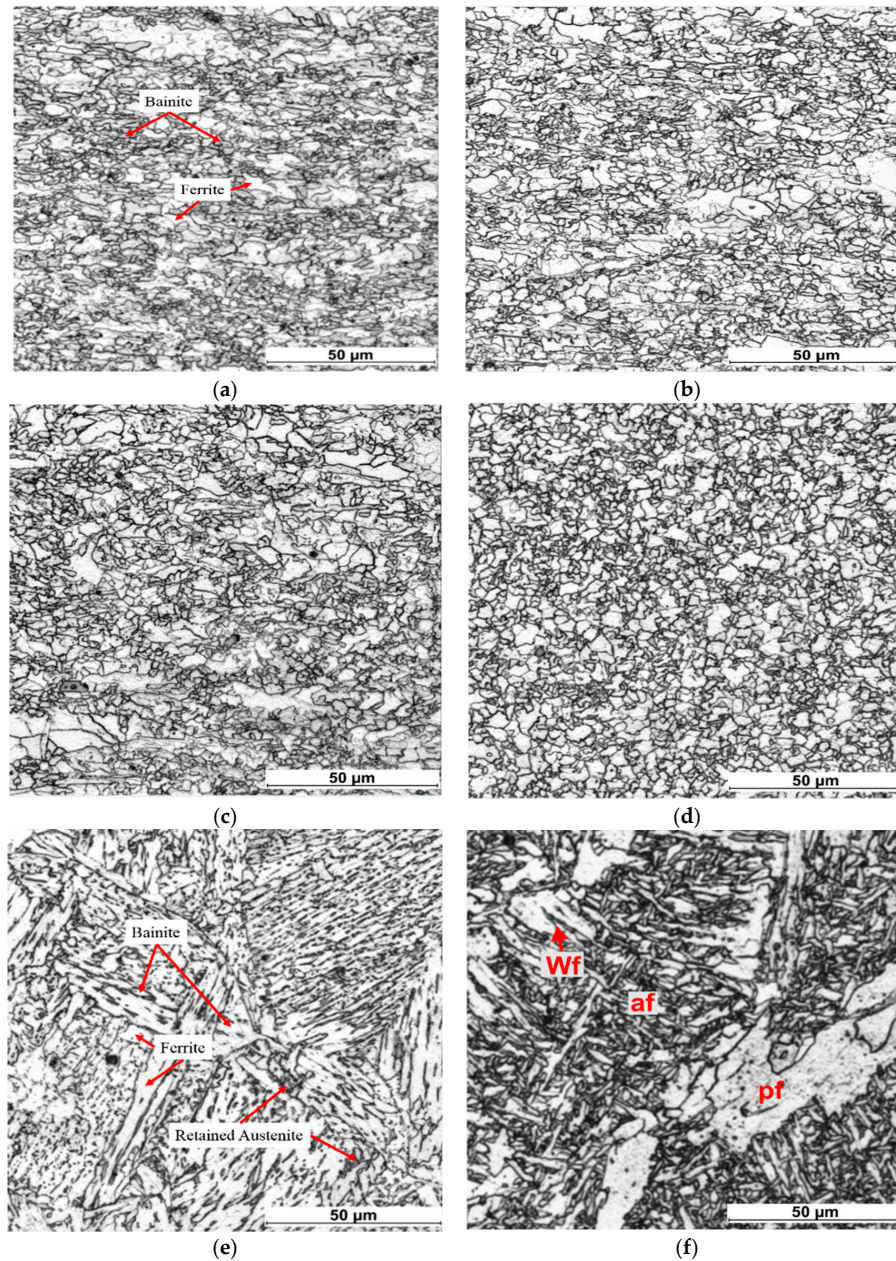


Figure 10. The microstructure of the thermo-mechanically controlled process (TMCP) steel welded joint with the second welding condition: (a) base metal; (b) SCHAZ; (c) ICHAZ; (d) FGHAZ; (e) CGHAZ; (f) weld metal (Wf—Widmanstätten ferrite; af—acicular ferrite; pf—polygonal ferrite).

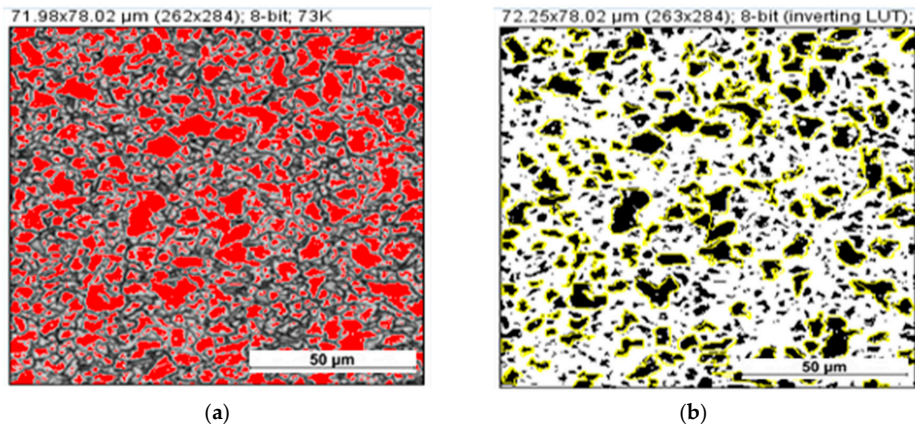


Figure 11. The microstructure of the FGHAZ region of TMCP steel for the second welding condition: (a) calibration using Threshold Image; (b) measurement of grain area using ImageJ 1.52p 22.

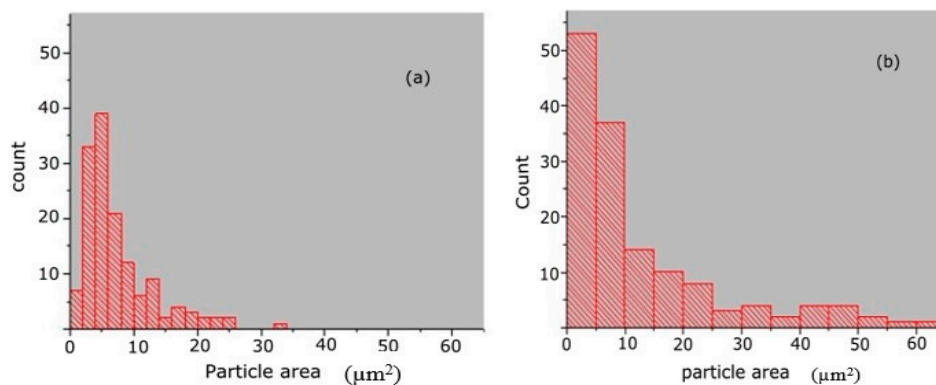


Figure 12. Ratio of grain number (count) to particle area: (a) for TMCP steel; (b) for QT steel.

4.4. The Microstructure of the Weld Metal

During the welding process of the different samples, the zone in which the filler metal is applied is generally subjected to the highest temperatures. In the analysis of the different samples, a formation was observed as a function of the temperature phases: Widmanstätten, polygonal, and acicular ferrite. It should be noted here that these forms of ferrite differ in their internal displacement, and at the boundary of the austenite grains. During the cooling process (from γ to ferrite α transformation), polygonal ferrite was formed. A longer cooling time led to the formation of Widmanstätten ferrite. Its development can be seen at the boundary of austenite grain during the carbon diffusion. When the temperature decreased, there was the formation of an acicular ferrite transformation. It should be noted that acicular ferrite occurs within small grains during carbon diffusion and during equilibrium nucleation. The difference is that, with acicular ferrite, there is no diffusion during growth.

4.5. Comparison of Dissimilar Weld Joint Hardness Profiles

The experimental data show that the HAZ of the same grade steels with different chemical composition and initial microstructure was significantly different for the same welding conditions. Naturally, the local mechanical properties of the HAZ and, consequently, the mechanical properties of the weld joints would also be substantially different. The hardness measurements made in this

analysis were for one line per sample. Three samples were measured (for 10 kJ/cm, 14 kJ/cm, and 17 kJ/cm). Figure 13 shows the heterogeneity of the welded joints. The hardness of the weld metal was also virtually identical (220 vs. 230 HV0.1). The weld metal was undermatched, and the yield stress of the filler metal was 72% of that of the base metal. When the heat source value was applied at 10 kJ/cm, the hardness value on the CGHAZ increased by 15% to 310 HV0.1 vs. 270 HV0.1 of the hardness of the base material, and decreased by 10% to 260 vs. 290 HV0.1 for the TMCP steel. Upon increasing heat input from 1 to 10 to 17 kJ/cm, the cooling time increased, and the hardness of the CGHAZ in the QT steel decreased from 310 to 260 HV0.1. In the FGHAZ, the hardness of the two steels underwent the greatest decrease—20% for the QT steel, and 30% for the TMCP steel. The hardness of the metal heated slightly below AC_3 decreased by 30% to 210 HV0.1 (ICHAZ). Upon heating between AC_1 and AC_3 (ICHAZ), the three heat source values resulted in an average hardness value of 210 HV0.1 for the QT steel and 230 HV0.1 for the TMCP steel. The cause of the austenite composition in the microstructure varying from 0 to 100% depended on the local peak temperature. As the austenite transforms into ferrite during cooling, its fraction determines the hardness at the inter-critical HAZ region. The SCHAZ area was much more impacted, with a meager hardness value of 180 HV0.1 when the heat source was high (17 kJ/cm). For the TMCP steel, the average value of 260 HV0.1 was reasonable.

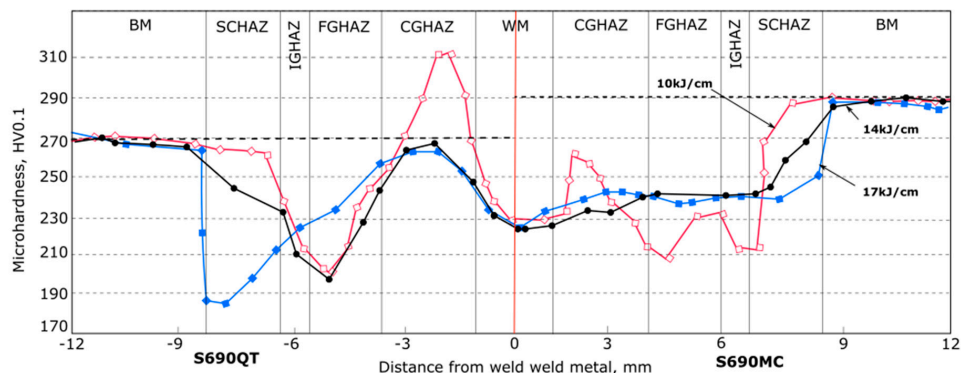


Figure 13. Effect of heat input on the microhardness profile of the welded joints: (left) QT steel; (right) TMCP steel. The dotted line shows the base metal hardness.

The width of the soft (unhardened) zone was different in both plates of steel; in the QT steel, it was mainly determined by the width of the fine-grain region, and, in the TMCP steel, it was determined by the total width of the coarse- and fine-grain regions. In the latter case, the width of the soft zone was equal to 5 mm, which is large relative to the thickness of the welded joint. The sharp increase in hardness can be explained by the formation of a bainitic–martensitic microstructure (due to the high carbon content) and grain growth. In the second case, the hardness drop was caused by primary recrystallization of the microstructure and the formation of more equilibrium products of austenite decomposition during cooling. Both plates of steel showed the lowest hardness in the fine-grain region due to the creation of predominantly polygonal ferrite.

5. Conclusions

This numerical and experimental investigation focused on the analysis of the effect of heat input on the microstructure and mechanical properties of weld joints of 690-MPa QT and TMCP steel. Based on the results of this study, the analysis of these heat inputs focused on two HAZ regions: the CGHAZ and FGHAZ. The key findings can be summarized as follows:

1. For developing the numerical analysis, a three-dimensional (3D) nonlinear thermal analysis finite element model was used to predict the thermal fields during the welding. The results showed

an acceptable confirmation between the experimental and numerical thermal fields of the three samples within a range of 7–19% in predicting the temperature.

2. The maximum respective values of the temperature measured in QT steel and TMCP steel were about 1300 and 1200 °C for a heat input of 10 kJ/cm, 1400 and 1300 °C for a heat input of 14 kJ/cm, and 1600 and 1450 °C for a heat input of 17 kJ/cm.
3. A heat input of 10 kJ/cm resulted in the maximum rapid cooling time (numerical $t_{8/5}$, 14.5 s, and experimental, 18.84 s), which increased hardness by 15% to 310 HV0.1 in the CGHAZ region of the QT steel and decreased the hardness value by 10% to 260 vs. 290 HV0.1 for the TMCP steel. In the QT steel, local brittle zone formations in the martensite–bainite microstructure in the CGHAZ were observed.
4. In the TMCP steel, the hardness drop was caused by a reconstructive transformation in the primary recrystallization of the microstructure and the formation of more equilibrium products of austenite decomposition (CGHAZ), with lowest hardness seen in the fine-grain heat-affected zone (FGHAZ) region due to the creation of polygonal ferrite.
5. Upon increasing heat input from 14 to 17 kJ/cm, the cooling time of the welding process was increased (numerical $t_{8/5}$, 29 s, and experimental, 36 s), leading to a decrease in the hardness of the CGHAZ in the QT steel by 16% from 310 to 260 HV0.1 due to the full austenite (thermal weld cycle), while maintaining the hardness value of the TMCP steel. This helped avoid the brittle formation in the inter-critical coarse-grain HAZ (ICCGHAZ) of TMCP steel and also to avoid defects in the weld zone.
6. In the FGHAZ, the hardness of the two steels underwent the greatest decrease—20% for the QT steel, and 30% for the TMCP steel.
7. The SCHAZ area was greatly impacted with a very low hardness value of 180 HV0.1 when the heat source was high (17 kJ/cm). The main reason for that softening was a high heat input; thus, heat input should be controlled and limited, especially for a thick plate, because the softening effect of the welded joint is proportional to the plate thickness.
8. The coarse-grain heat-affected zone (CGHAZ) showed relatively high hardness and large-size grains, and the tempering zone had comparable hardness and grain size to the base metal.
9. The analyzed grain samples showed an increased surface on the 690 QT steel (12.6 μm^2) compared to the 690 TMCP steel (4.43 μm^2). A probable reason is that the carbon content in QT steel, higher compared to 690 TMCP steel, caused carbon diffusion during para-equilibrium nucleation and growth in the austenite grain size.

The results obtained in this analysis may help predict the heat source values expected to have a favorable yield of material properties in the heat-affected zone. Future studies could be conducted to simulate and analyze the effect of the heat input on the mechanical behavior (stress and distortions) of the weld joint.

Author Contributions: F.N.B. performed the numerical and experiment analysis, wrote the original draft, and contributed to review and editing. P.K. supervised the study, reviewed the results, and wrote the conclusion. P.L. and V.K. provided the resources.

Funding: The research was funded by Energy-efficient systems based on renewable energy of Arctic conditions “EFREA”, Grant number K51054 and Finnish cultural foundation for its financial support.

Acknowledgments: The authors would like to thank Esa Hiltunen, Anti Heikkinen and Antti Kähkönen for their support to the arrangement of experimental work.

Conflicts of Interest: The authors declare no conflicts of interest.

References

1. Haslberger, P.; Holly, S.; Ernst, W.; Schnitzer, R. Microstructure and mechanical properties of high-strength steel welding consumables with a minimum yield strength of 1100 MPa. *J. Mater. Sci.* **2018**, *53*, 6968–6979. [[CrossRef](#)]

2. Di, H.; Sun, Q.; Wang, X.; Li, J. Microstructure and properties in dissimilar/similar weld joints between DP780 and DP980 steels processed by fiber laser welding. *J. Mater. Sci. Technol.* **2017**, *33*, 1561–1571. [[CrossRef](#)]
3. Pandey, C.; Mahapatra, M.; Kumar, P.; Thakre, G.; Saini, N. Role of evolving microstructure on the mechanical behavior of P92 steel welded joint in as-welded and post weld heat treated state. *J. Mater. Proc. Technol.* **2019**, *263*, 241–255. [[CrossRef](#)]
4. Mironov, S.; Sato, Y.; Yoneyama, S.; Kokawa, H.; Fujii, T.; Hirano, S. Microstructure and tensile behavior of friction-stir welded TRIP steel. *Mater. Sci. Eng. A* **2018**, *717*, 26–33. [[CrossRef](#)]
5. Hulka, K.; Gray, J.M. High-temperature processing of line-pipe steels/niobium science and technology. In Proceedings of the International Symposium Niobium, Orlando, FL, USA, 2–5 December 2001.
6. Nishioka, K.; Ichikawa, K. Progress in thermomechanical control of steel plates and their commercialization. *Sci. Technol. Adv. Mater.* **2012**, *13*, 203001.
7. Hochhauser, F.; Ernest, W.; Rauch, R.; Vallant, R.; Enzinger, N. Influence of the soft zone on the strength of welded modern HSLA steels. *Weld. World* **2006**, *56*, 77–85. [[CrossRef](#)]
8. Kim, B.; Lee, S.; Kim, J.; Lee, D. Microstructure and local brittle zone phenomena in high-strength low-alloy steel welds. *Metall. Trans. A* **1999**, *22*, 139–149. [[CrossRef](#)]
9. Loureiro, R. Effect of heat input on plastic deformation of undermatched weld. *J. Mater. Proc. Technol.* **2002**, *128*, 240–249. [[CrossRef](#)]
10. Hwang, R.; Lee, T.; Lee, G. Correlation of microstructure and mechanical properties of thermo-mechanically processed low-carbon steels containing boron and copper. *Metall. Mater. Trans. A* **2010**, *41*, 85–96. [[CrossRef](#)]
11. Chang, W.S. Microstructure and mechanical properties of 780 MPa high strength steel produced by direct quenching and tempering process. *J. Mater. Sci.* **2002**, *37*, 1973–1979. [[CrossRef](#)]
12. Schroter, F. Structural steel for the application in offshore, wind and hydro energy production. Comparison of application and welding properties of frequently used materials. *Int. J. Microstruct. Mater. Prop.* **2011**, *6*, 4–19. [[CrossRef](#)]
13. Lambert-Perlade, A.; Gourgues, A.F.; Pineau, A. Austenite to bainite transformation in the heat-affected zone of a heat strength low carbon steel. *Acta Mater.* **2004**, *52*, 2337–2348. [[CrossRef](#)]
14. Lanbert-Perlade, A.; Gourgues, A.F.; Besson, J.; Sturel, T.; Pineau, A. Mechanism and modeling of cleavage fracture in simulated heat-affected zone microstructures of high-strength low alloy steel. *Metall. Mater. Trans. A* **2004**, *35*, 1039–1053. [[CrossRef](#)]
15. Bhatti, A.; Barsoum, Z.; Hidekazu, M.; Barsoum, I. Influence of thermo-mechanical material properties of different steel grades on welding residual stresses and angular distortion. *Mater. Des.* **2015**, *65*, 878–889. [[CrossRef](#)]
16. Liu, D.; Li, T.; Emi, T. Microstructure and mechanical properties in hot-rolled extra high-yield-strength steel plates for offshore structure and shipbuilding. *Metall. Mater. Trans. A* **2011**, *42*, 1349–1361. [[CrossRef](#)]
17. Layus, P.; Kah, P.; Ryabov, V.; Martikainen, J. Evaluation of applicability of thick E500 TMCP and F500W QT-steel plates for Artic service. *Int. J. Mech. Mater. Eng.* **2016**, *11*, 1–15. [[CrossRef](#)]
18. Dusan, A.; Vukic, L.; Ruzica, R.; Srbislav, A.; Branislav, H.; Milan, D. Optimal welding technology of high strength steel S690QL. *Mater. Eng.* **2015**, *22*, 33–47.
19. Porter, D.; Laukkanen, A.; Nevasmaa, P.; Rahka, K.; Wallin, K. Performance of TMCP-steel with respect to mechanical properties after cold forming and post-forming heat treatment. *Int. J. Press. Vessel. Pip.* **2004**, *81*, 867–877. [[CrossRef](#)]
20. Sadeghian, M.; Shamanian, M.; Shafyei, A. Effect of heat on microstructure and mechanical properties of dissimilar joints between super duplex stainless steel and high strength low alloy steel. *Mater. Des.* **2014**, *60*, 678–684. [[CrossRef](#)]
21. Ito, R.; Hiraoka, K.; Shiga, C. Characteristics of the heat-affected zone in ultra-fine-grained steel during ultra-narrow gap GMA welding. *Weld. Int.* **2005**, *19*, 458–466. [[CrossRef](#)]
22. Hamada, M. Control of strength and toughness at the heat affected zone. *Weld. Int.* **2003**, *17*, 265–270. [[CrossRef](#)]
23. Pirinen, M.; Martikainen, J.; Layus, P.; Karhin, V.; Ivanov, Y.S. Effect of heat input on the mechanical properties of welded joints in high-strength steel. *Weld. Int.* **2015**, *2*, 14–17. [[CrossRef](#)]
24. Lan, L.; Qiu, C.; Zhao, D.; Gao, X.; Du, L. Microstructural characteristics and toughness of the simulated coarse-grained heat affected zone of high strength low carbon bainite steel. *Mater. Sci. Eng. A* **2011**, *529*, 192–200. [[CrossRef](#)]

25. Shi, Y.; Han, Z. Effect of thermal weld cycle on microstructure and fracture toughness of simulated heat-affected zone for an 800 MPa grade high strength low alloy steel. *J. Mater. Proc. Technol.* **2008**, *207*, 30–39. [[CrossRef](#)]
26. Goldack, J.; Chkravarti, A.; Bibby, M. A new finite element model for welding heat sources. *Metall. Trans. B* **1984**, *15*, 299–305. [[CrossRef](#)]



© 2019 by the authors. Licensee MDPI, Basel, Switzerland. This article is an open access article distributed under the terms and conditions of the Creative Commons Attribution (CC BY) license (<http://creativecommons.org/licenses/by/4.0/>).

Publication III

Bayock, F., Kah, P., Mvola, B., and Layus, P.

Effect of Heat Input and Undermatched Filler Wire on the Microstructure and Mechanical Properties of Dissimilar S700MC/S960QC High-Strength Steels

Reprinted with permission from

Metals

Vol. 9(8):883, pp. 1-20, 2019

© 2019, MDPI

Article

Effect of Heat Input and Undermatched Filler Wire on the Microstructure and Mechanical Properties of Dissimilar S700MC/S960QC High-Strength Steels

Francois Njock Bayock , Paul Kah , Belinga Mvola and Pavel Layus

Laboratory of Welding Technology, Lappeenranta-Lahti University of Technology, P.O. Box 20, 53851 Lappeenranta, Finland

* Correspondence: francois.njock.bayock@lut.fi; Tel.: +358-465876937

Received: 8 July 2019; Accepted: 8 August 2019; Published: 12 August 2019



Abstract: The effect of heat input on the microstructure and mechanical properties of dissimilar S700MC/S960QC high-strength steels (HSS) using undermatched filler material was evaluated. Experiments were performed using the gas metal arc welding process to weld three samples, which had three different heat input values (i.e., 15 kJ/cm, 7 kJ/cm, and 10 kJ/cm). The cooling continuous temperature (CCT) diagrams, macro-hardness values, microstructure formations, alloy element compositions, and tensile test analyses were performed with the aim of providing valuable information for improving the strength of the heat-affected zone (HAZ) of both materials. Micro-hardness measurement was conducted using the Vickers hardness test and microstructural evaluation by scanning electron microscopy and energy-dispersive X-ray spectroscopy. The mechanical properties were characterized by tensile testing. Dissimilar welded samples (S700MC/S960QC) with a cooling rate of 10 °C/s (15 kJ/cm) showed a lower than average hardness (210 HV5) in the HAZ of S700MC than S960QC. This hardness was 18% lower compared to the value of the base material (BM). The best microstructure formation was obtained using a heat input of 10 kJ/cm, which led to the formation of bainite (B, 60% volume fraction), ferrite (F, 25% volume fraction), and retained austenite (RA, 10%) in the final microstructure of S700MC, and B (55%), martensite (M, 45%), and RA (10%), which developed at the end of the transformation of S960QC. The results showed the presence of 1.3 Ni, 0.4 Mo, and 1.6 Mn in the fine-grain heat-affected zone of S700MC. The formation of a higher carbide content at a lower cooling rate reduced both the hardness and strength.

Keywords: GMA welding process; scanning electron microscopy; dissimilar welding; optical microscopy; energy-dispersive X-ray spectroscopy; S960QC; S700MC

1. Introduction

Emerging technologies in various manufacturing applications (e.g., construction of facilities, piping systems of nuclear power plants, and automotive power plants) now require and could significantly benefit from joining different steel grades. Welding dissimilar materials is not without its difficulties, and this challenge has caused researchers to explore new materials. The potential advantages of these new materials are that they could be environmentally beneficial, have lower manufacturing and maintenance costs, and their thermal properties may make them easier to use in hot or cold climates [1–3]. For instance, in the construction of many structures such as vehicles (i.e., automobiles), reducing the weight has a significant impact on durability, effectiveness, and operating costs. Improved characteristics in the weld joint can lead to the beneficial outcomes of lower weight and increased rigidity. In dissimilar welding of high-strength steels (HSS), knowledge of the correlation between heat input data and alloy elements formed in the heat-affected zone (HAZ) may enable

selection of welding material and welding parameters such that essential mechanical properties of the weld joint (i.e., hardness and strength) can be maintained. Structural steels with a yield strength greater than or equal to 900 MPa are classified as ultra-high-strength steels (UHSS). Those with an ultimate yield strength of less than 900 MPa and greater than or equal to 450 MPa are classified as high-strength advanced steels (AHSS), and those with an ultimate yield strength of less than 450 MPa are classified as HSS [4–6].

Gas metal arc (GMA) welding is a process in which an electric arc is formed continuously or discontinuously between the consumable electrode and the workpiece [7,8]. Karkhin et al. [9] indicated that the shielding of inert or active gases (Ar, He, CO₂, CO₂ + O₂) needs to be compatible with the chemical characteristics of the base materials and the geometry of the weld joint. Utilization of a thermomechanically controlled process to regulate the mechanical behavior of HSS, which have a relatively low carbon content, greatly reduces the duration of the welding process. The reduction in the welding process time is made possible by decreasing the preheating temperature, which has an impact on the relative stability of the alloy element in the HAZ.

The thermomechanically controlled welding process for HSS S700MC requires the consideration of several factors, such as mechanical properties, chemical composition, welding process, and choice of filler wire [10–15]. Guo et al. [16] used autogenous laser welding (ALW) and multi-pass ultra-narrow gap laser welding (NGLW) in the evaluation of the mechanical properties and microstructure of a welded joint of S700MC and S960QC HSS. The authors noted that the fast cooling rate of both welding processes resulted in hard martensite (M) formation in the fusion zone (FZ) and HAZ. This formation improves the strength of the weld joint but decreases the toughness of S700MC and S960QC. Much research has analyzed the effect of heat input and undermatched filler wire on the mechanical properties of S960MC steel. It has been noted that when using the GMA welding process with undermatched filler wire, softening will increase in the HAZ. This softening may be due to the heat input values, the dilution percentage or the mixture of alloy element compositions in the base material (BM), and filler wire. A number of authors have observed a lack of M formation at the end of transformation processes with low heat input values. An experiment was carried out to determine the usability of welded HSS S960QC in arctic regions (where the ambient temperature is approximately −25 °C to −30 °C during winter). The researchers found that using a heat input of 5 to 6.5 kJ/cm increased the hardness but caused a brittle fracture in the HAZ of the weld joints [17–19]. To avoid this undesirable phenomenon, preheating and post-weld heat treatment of the weld joint during the welding process are required. It is also recommended that a suitable choice of welding process be made. Further, the type of filler wire is of significance. By applying high heat input values when welding dissimilar HSS API X56 PSI and duplex stainless-steel UNS32750, the authors noted an increase in the strength in the HAZ of HSS API X65 PSI, which resulted in the formation of pearlite and ferrite within the austenite grain. A decrease in the heat input caused a decrease in the strength and the formation of ferrite (F) and bainite (B) in the microstructure [20–24]. The same behaviors were observed when Tasalloti et al. [25] used the GMA welding process to weld S960QC/S32205 HSS and duplex stainless steel. They demonstrated that there is a relationship between the welding parameters and the microstructure behavior, especially for HSS in the HAZ of the weld joint. Remarkably, this suggests that when welding high-strength low alloy steel (HSLA), an increase in the cooling rate leads to an increase in the formation of M. This increase in M has a negative effect on the mechanical properties of the welds. Yan et al. [26] confirmed this argument by analyzing the micro-alloying elements, such as carbon, manganese, and silicon, on the microstructure of quenching and partitioning (Q&P) steels. They noted that an increase in the yield strength of molybdenum (Mo)–niobium (Nb) micro-alloyed steel, treated by Q&P, was caused by the precipitation strengthening of NbC (niobium–carbon) and a refinement of the martensitic structure. Based on these results, it can be observed that improvement of the mechanical properties (i.e., strength, toughness, and elongation) in the HAZ of dissimilar HSS welded joints is a significant challenge. This improvement depends on parameters such as the chemical composition of the materials (base materials and filler wire), the welding parameters (heat input,

welding speed, current, voltage, and gas flow), geometry of the weld sample, and the mechanical properties of the base materials.

This study aimed to investigate the effect of heat input and undermatched filler wire on the microstructure composition and mechanical properties of the heat-affected zone of dissimilar high-strength steels S700MC/S960QC. The specimens were welded using GMA welding and the thermal profiles were defined to evaluate the cooling times when using different heat input values. The cooling time was added to the continuous cooling temperature (CCT) diagrams step-by-step, which enabled the determination of the start and end of the transformation in both materials. The CCT diagrams of the investigated steels were plotted using JMatPro software (JMatPro 2018, University of Leicester, Leicester, UK) which permitted identification of the different phase transformation stages during the cooling process. Based on the CCT diagram of S700MC and the CCT diagram of S960QC, the thermal profiles of both diagrams were used to evaluate the cooling time differences among them ($t_{8/5}$).

The HV5 macro-hardness measurements were made using a Wilson Wolpert 452SVD Vickers hardness tester with a load of 5 kgf [27]; the dwell time measurements were 20 s. At least 45 random measurements across the samples were used after polishing. The microstructure of the samples used for the hardness tests was characterized using optical microscopy (OM) and scanning electron microscopy (SEM) with a voltage of 15 kV and a resolution of 20 μm . The volume fraction of the microstructure formation was determined using ImageJ pro software (ImageJ 2013, NIH, Bethesda, MD, USA). To determine the chemical constituents in the austenite grain, energy-dispersive X-ray spectroscopy (EDS) using area scan analysis with a step size of 2.5 μm was conducted for samples cooled at 21 $^{\circ}\text{C/s}$. The sample for EDS was prepared by repolishing the microstructure of the sample and etching with picric acid of 4 vol %, followed by fresh Nital solution of 2 vol % for 20 s.

The tensile test was conducted using ZWICK/ROZ Z 330 RED equipment (Zwick Rowell, Ulm, Germany) with a maximum load capacity of 100 kN according to the EN ISO 6892-1:2016 standard [28].

2. Experimental Setup

2.1. Welding Procedure

The experiments were conducted using S700MC and S960QC dissimilar materials. Gas metal arc welding using a shielding gas of Ar + 18% CO_2 , with a flow rate of 17 L/min, and an automatic robotic system equipped with a digital laser sensor allowing for the intuitive reading and evaluation of the $t_{8/5}$ cooling time during the welding process were used. The equipment, illustrated in Figure 1, was integrated into the central unit and interconnected the interface programming system, the robot system, the thermal recorded laser sensor, and the power source. The parts to be welded were placed in a cabinet at both ends. Changes in the heat input automatically changed the speed of the welding torch. Table 1 shows the different parameters used for the heat input. As the welding processes were used on two passes, the first pass remained constant at a value of 7 kJ/cm for all samples. The second weld pass had three heat input values, which were applied to the three samples, and which allowed for the determination of the cooling curves during the welding process and for the calculation of cooling rates favorable to the different samples.

Table 1. Welding conditions.

Welded Samples	Pass 1				Pass 2			
	Current (A)	Voltage (V)	Welding Speed (cm/min)	Heat Input Q (kJ/cm)	Current (A)	Voltage (V)	Welding Speed (cm/min)	Q (kJ/cm)
WS1	215	25.3	37.3	7	211	26.7	18	15
WS2	215	25.3	37.3	7	203	26.6	37.5	7
WS3	215	25.3	37.3	7	208	26.7	24	10

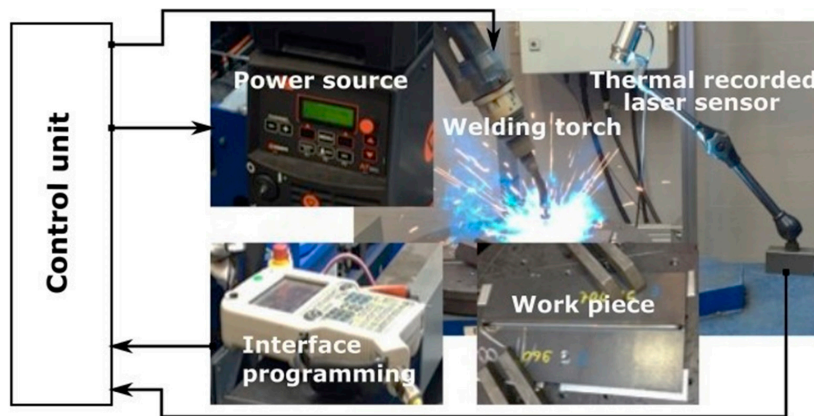


Figure 1. Automatic robot gas metal arc (GMA) welding process using a recorded laser thermal profile, ABB IRC 5 robot control unit.

The arc efficiency of the GMA welding process used for determination of the heat input values was 0.8. A laser sensor was used to measure and record the thermal profile at the different phases of welding. The measured thermal profile data were saved in the central unit of the welding equipment, where the captured weld seam data were stored for subsequent import to LabVIEW software (LabVIEW 2018, NI, Austin, TX, USA) for thermal profile distribution analysis.

Three specimens of dissimilar structural steels (S700MC/S960QC) with dimensions of $300 \times 200 \times 8 \text{ mm}^3$ and a V-groove butt joint with an angle of 60° and a 2 mm gap were produced (Figure 2a,b). Several welds were made with different heat input values. Figure 2b represents the configuration of the welded sample. The samples were made using a filler wire Union NiMoCr with a 1 mm diameter. Table 2 shows the chemical composition of the base materials and filler wire, obtained according to the weight % (wt %) and mechanical properties, and characterized by the yield strength (YS), ultimate yield strength (UTS), elongation ($A_5\%$), and Vickers hardness (HV5). The carbon equivalent (CE) of the investigated steels was calculated according to the following equation [17]:

$$CE = C + \frac{Mn}{6} + \frac{(Cr + Mo + V)}{5} + \frac{(Ni + Cu)}{15} \quad (1)$$

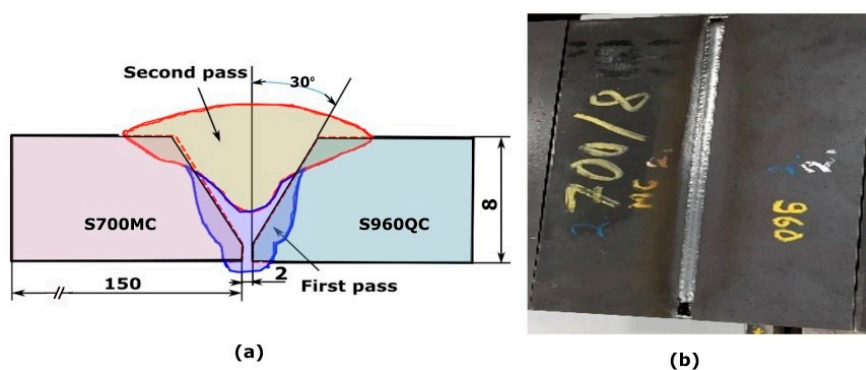


Figure 2. Weld geometry: (a) weld joint geometry, (b) welded appearance of one specimen.

Table 2. Chemical composition and mechanical properties of S700MC and S960QC steels and filler material NiCrMo700. Chemical composition, wt %.

Materials	Chemical Composition, wt %														
	C	Si	Mn	Al	B	Nb	Ti	V	Cu	Cr	Ni	Mo	N	P	S
S700MC	0.056	0.16	1.18	0.027	0.002	0.044	0.12	0.006	0.02	0.062	0.066	0.0150	0.005	0.01	0.005
S960QC	0.09	0.21	1.05	0.03	0.002	0.003	0.032	0.008	0.025	0.82	0.04	0.04	-	0.01	0.004
Filler wire	0.08	0.60	1.40	-	-	-	0.05	-	≤0.30	0.30	2.50	0.45	-	-	-

Mechanical Properties				
Materials	Yield Strength, MPa	Ultimate Tensile Strength, MPa	Elongation A ₅ , %	Hardness HV5
S700MC	768	822	12	280
S960QC	960	1000	18	320
Filler wire	780	830	17	270

2.2. Tests of Weld Joints

In this study, the specimens were tested using non-destructive and destructive methods. The welded samples were machined and polished such that they had smooth surfaces suitable for use in microscopic analysis. All samples used were prepared according to the ISO 17637-2017 standard [29].

2.2.1. Conducted Non-Destructive Tests

A hardness test was conducted for a line of measurement using a Wilson Wolpert 452SVD Vickers hardness tester (ITW, Chicago, IL, USA) according to ISO 6507-1:2018. These measurements were taken point-by-point over the entire length of the sample.

Optical microscopy (OM) was applied using different positions of the sample to determine the microstructure of the welded sample.

Scanning electron microscopy analysis using a Hitachi SU3500 (Hitachi High-Technologies America, Chicago, IL, USA) scanning electron microscope was conducted to analyze the specimens etched in a first etchant (4% solution of HNO₃ in ethanol).

The EDS analysis using the Hitachi SU3500 equipment (Hitachi High-Technologies America, Chicago, IL, USA) was used to identify the variation in the composition of the alloy elements in the specific areas of the HAZ of both materials.

2.2.2. Conducted Destructive Tests

The destructive test in this analysis was a tensile test using ZWICK/ROZ Z 330 RED equipment. Six specimens were prepared, i.e., two per weld sample.

3. Results

3.1. Thermal Profile

Figure 3 presents the thermal profile registered after welding dissimilar HSS of S700MC/S960QC. The cooling time ($t_{8/5}$) was obtained by evaluating the time during the interval between the temperatures of 800 °C and 500 °C. The first curve (in black) shows the thermal profile using the heat input of 15 kJ/cm (WS1). From this curve, the peak temperature observed was 1600 °C, and the cooling time registered was $t_{8/5} = 41$ s. The reason for this cooling time was the increase in the heat input rather than changes in other values. The second curve (in red) presents the thermal profile using the heat input of 7 kJ/cm (WS2). The peak temperature observed was 1200 °C, which was less than the value for the other experiments and the cooling time was $t_{8/5} = 13$ s. The only reason for this cooling time was the decrease in the heat input value. The last curve (in blue) presents the thermal profile using the heat input of 10 kJ/cm (WS3). The results here show the peak temperature at 1400 °C, which produced a cooling time of $t_{8/5} = 33$ s.

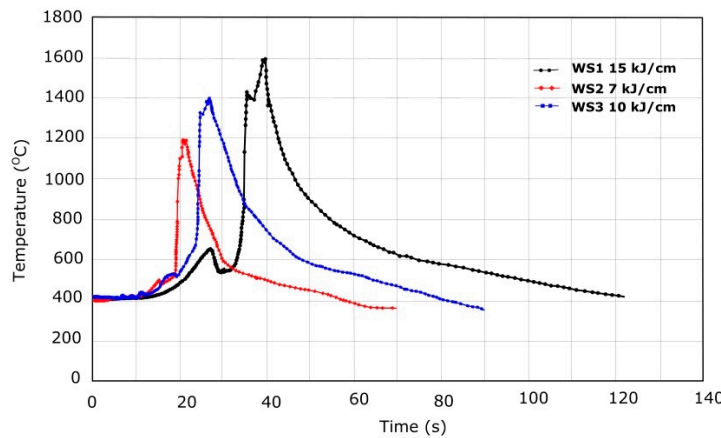


Figure 3. Thermal profile of the three weld samples.

The final microstructure, the HAZ behavior, and the mechanical properties depend greatly on the cooling rate and the peak temperature reached during the welding temperature cycle. For low-carbon steels, like S700MC and S960QC, the temperature that was used to calculate the cooling rate was 550 °C. In the experimental analysis, the cooling time ($t_{8/5}$) for the interval of 800 °C to 500 °C was measured during the welding process and is shown in Table 3. In the literature, researchers have presented an empirical relation, using low-alloy carbon steels, to evaluate the cooling time–temperature from 800 °C to 500 °C during a welding process [9,30]:

$$\Delta t_{8/5} = (0.67 - 0.0005T_0) \frac{q_{source}}{v} \left(\frac{1}{500 - T_0} - \frac{1}{800 - T_0} \right) \quad (2)$$

or

$$\Delta t_{8/5} = (0.043 - 4.3 \times 10^{-5}T_0) \left(\frac{q_{source}}{vh} \right)^2 \left(\frac{1}{(500 - T_0)^2} - \frac{1}{(800 - T_0)^2} \right) \quad (3)$$

where $\frac{q_{source}}{v}$ is the heat input per unit length, obtained by the heat source, and T_0 is the preheating temperature (initial temperature). Equation (1) is applied for three dimensions and Equation (2) for two dimensions. To evaluate the cooling rate (R_{500}), the initial temperature T_0 is assumed to be constant, with or without preheating. The peak temperature T_{max} can be defined as in Equation (3) [9,30]:

$$T_{max}(y) - T_0 = \frac{1}{\sqrt{2\pi e}} \frac{\frac{q}{vh}}{c\rho} \frac{1}{y} \quad (4)$$

where y is the distance from the weld line in the HAZ (mm), e is the thickness of the workpiece (mm), and $c\rho$ is the specific heat capacity per unit of volume (0.005 J/mm³K).

Knowing the mode of heat propagation of the preheating temperature T_0 and the expression of $\frac{q}{v}$, the cooling rate R_{500} can be defined by [9,30]:

$$R_{500} = \frac{\partial T(0, T)}{\partial t} = -2\pi\lambda c\rho \frac{(T_{max} - T_0)^3}{\left[\frac{q}{vh} \right]^2} \quad (5)$$

where R_{500} (°C/s) is the cooling rate at 500 °C, which can increase with the value of $(T_{max} - T_0)$ and decrease with the heat density ($\frac{q}{v}$). λ is the thermal conductivity (W·m⁻¹·K⁻¹), v is the welding speed (mm/s), and h (mm) is the thickness of the weld joint.

Table 3. Calculated cooling rates for the three heat inputs.

Weld Heat Input	Cooling Time ($t_{8/5}$)	Cooling Rate (R_{500})
WS1 (15 kJ/cm)	47 s	10 °C/s
WS2 (7 kJ/cm)	13 s	33 °C/s
WS3 (10 kJ/cm)	31 s	21 °C/s

Table 3 presents the results of the cooling rates obtained for the three heat inputs in the various welded joints. A slow cooling rate was observed for the first heat input, which was considered high compared to the others. The heat input of 15 kJ/cm, after measuring the cooling time $t_{8/5}$ (47 s), gave a cooling rate of approximately 10 °C/s at a temperature of 500 °C R_{500} , after calculation. A fast cooling rate was observed in welding sample 2 (WS2), which had a heat input of 7 kJ/cm.

3.2. CCT Diagram of S700MC Steel

The CCT diagram of S700MC was calculated based on the cooling time ($t_{8/5}$) for the three heat inputs obtained during the welding operation, and the cooling curves are represented by the heat inputs of WS1 $t_{8/5} = 47$ s, WS2 $t_{8/5} = 13$ s, and WS3 $t_{8/5} = 31$ s. From this CCT diagram, it can be observed that in WS1, the transformation starts at a temperature of between 700 °C and 520 °C. The cooling curves were recorded from the austenitization temperature A_{c3} (800 °C) to the temperature after the transformation (400 °C). Using the cooling time values and the formations, the cooling rate can be evaluated ($R_{500} = 10$ °C/s). The consequence of having a lower R_{500} is an increase of the transformation temperature and the favoring of a predominance of F, with some B at a higher temperature. It is also clear that this increase in the heat input leads to a much bigger HAZ [31]. The faster cooling rate ($R_{500} = 33$ °C/s), which was found in WS2, leads to a decrease in the temperature transformation from 550 °C to 450 °C. The temperature transformation favors the formation of a predominance of B and a little F. So far, with the cooling observed, there was no M formation because, according to the CCT diagram, this cooling rate was still a little slow compared to the results produced in Reference [32] using a laser welding process with a heat input of 1.7 kJ/cm. The cooling rate of 21 °C/s, which was applied for WS3, has a temperature transformation that starts at a temperature of between 650 and 500 °C. Due to the medium heat input of this sample, the microstructure was mainly comprised of B, with some F, as shown in Figure 4.

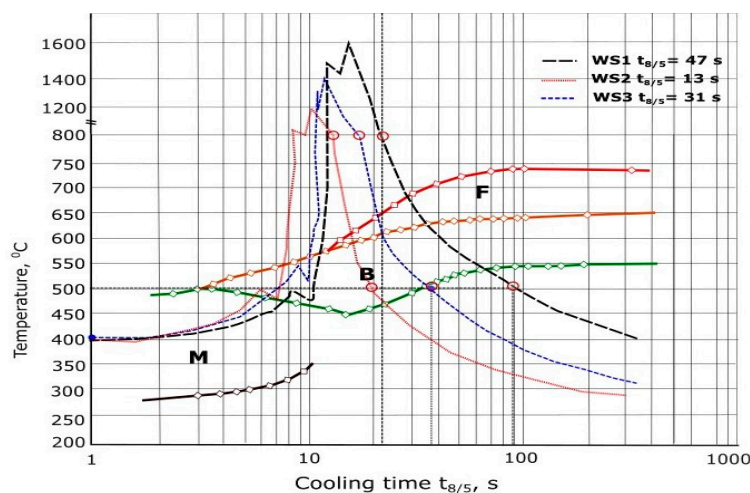


Figure 4. The cooling continuous temperature (CCT) diagram of S700MC (obtained using JMatPro software), including the cooling time curve values of the three heat input parameters.

3.3. CCT Diagram of S960QC Steel

Figure 5 presents a CCT diagram of S960QC showing the cooling time of the welded samples. The temperature was recorded from the austenite to the solidification. A slow cooling rate ($R_{500} = 10\text{ }^{\circ}\text{C/s}$), when the heat input of 15 kJ/cm was used, led to the formation of B in the microstructure. There was no observed formation of M. In WS2, which had a fast cooling rate ($R_{500} = 33\text{ }^{\circ}\text{C/s}$), a decrease in the temperature transformation in the CCT diagram (500 $^{\circ}\text{C}$ to 280 $^{\circ}\text{C}$) was observed. A predominance of M, with some B during the transformation, can be observed. The cooling rate $R_{500} = 21\text{ }^{\circ}\text{C/s}$, which is a medium cooling rate, has a formation of 50% of B and 50% of M (see Figure 5). The temperature transformations started at between 520 $^{\circ}\text{C}$ and 320 $^{\circ}\text{C}$.

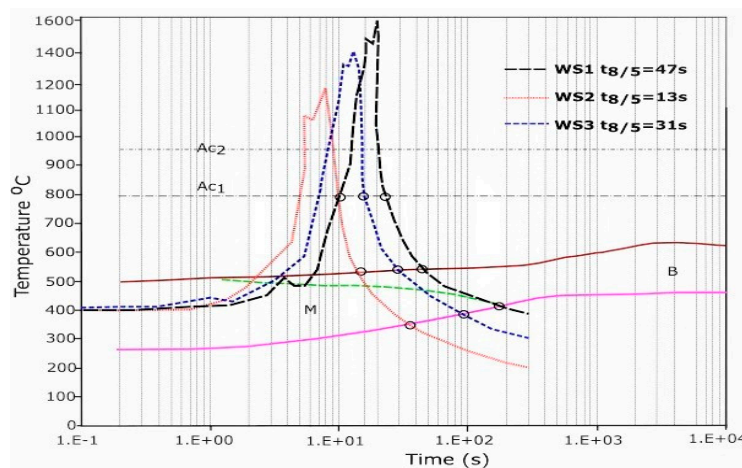


Figure 5. CCT diagram of S960QC steel (obtained using JMatPro software), including the cooling time curve values of the three heat input parameters.

3.4. Hardness Analysis of the Dissimilar Weld Joints

Figure 6 shows the hardness profile of the dissimilar welded samples after the samples were welded. It was measured using a Wilson Wolpert 452SVD Vickers hardness tester according to the ISO 6507-1:2018 standard [22]. The Vickers hardness mapping profiles across the welded joints were measured using a load of 5 kgf. The loading rate was 0.50 N/min, the unloading rate was 0.50 N/min, and the dwell time of measurements was 20 s. At least 45 random measurements across the samples were used to determine the characteristic average values. Figure 6a (left) presents the hardness profile, which had a different area of the HAZ for both the materials and the weld material. On the right side, the figure presents, in red, the measurement line, which provides a dotted representation of the different positions of the indents. The measurement line is 2 mm from the top of the weld joint.

For the first sample (WS1), the lowest hardness occurred in the fine-grain heat-affected zone (FGHAZ) of S700MC, with a value of 210 HV5. The average hardness in the HAZ of S700MC was 225 HV5. For S960QC, the lowest hardness occurred in the course-grain heat-affected zone (CGHAZ) (240 HV5) near the fusion line (between the CGHAZ and the WM). The hardness values in the weld metal of this sample were not significantly increased (260 HV5). When comparing the two base materials using WS1 (Figure 6a), the influence of the heat input value and the undermatching filler wire can be seen. The use of undermatching filler wire leads to a significant hardness drop in both sides of the welded joint [33]. This may be important as increasing the alloy content of the filler wire may enable the required hardness and strength of the weld metal to be obtained.

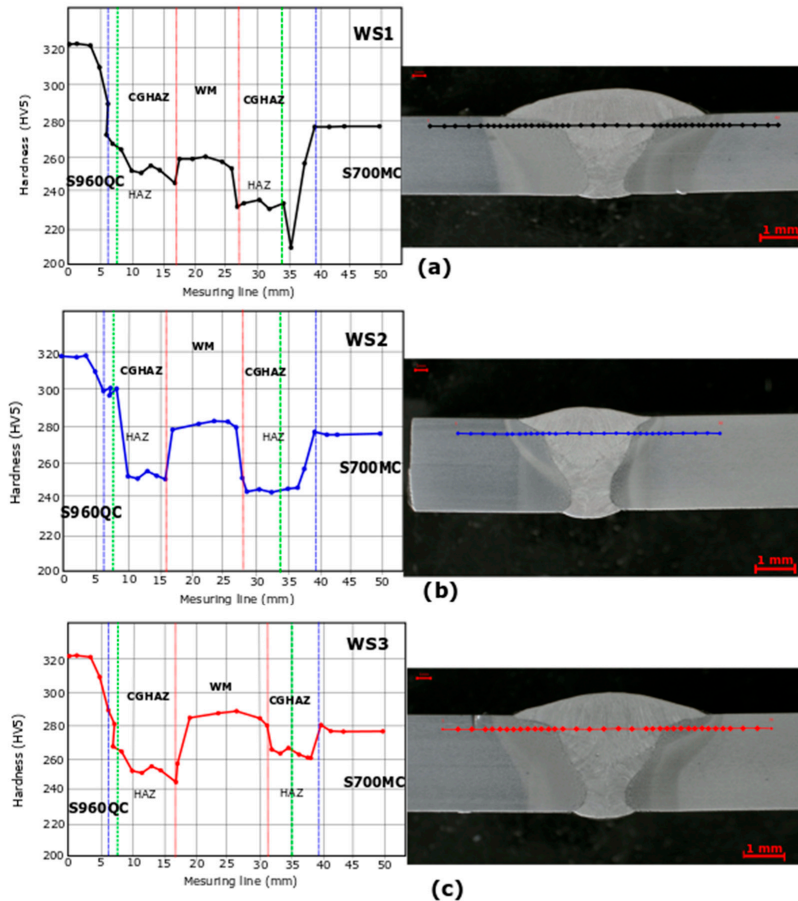


Figure 6. Hardness profile across the weld samples (WS): (a) hardness profile of WS1, (b) hardness profile of WS2, (c) hardness profile of WS3.

When the heat input was reduced, using 7 kJ/cm (Figure 6b), the average hardness value of the base S700MC steel as approximately 270–280 HV5. A decrease in the hardness value of 8% to 260 HV5 was observed near the CGHAZ. On the S960QC side, the average hardness measured was 300 HV5 lower compared to the BM (320 HV5). The average hardness of the weld metal was increased to 285 HV5. The reason for the hardness increase was the reduction of the heat input, which can lead to the formation of hard martensite (M) in the HAZ.

Figure 6c shows the hardness profile and a micrograph for the heat input of the WS3. A decrease in the average hardness of S700MC to 250 HV5 in the HAZ can be observed. The cause may be the increase in the heat input values, which favors a relatively faster cooling rate (21 °C/s). On the S960QC side, the peak hardness value was attributed to the FGHAZ, which was almost 300 HV5 and less than the BM. The reason was that the characteristic of the weld metal (mechanical and chemical composition) was less favorable to hardness than that of the BM (undermatched weld metal). The decrease in the heat input value in this sample also contributed to this result. One of the solutions to increase the hardness in this area is to increase the alloying content of the WM, which will increase the strength when using the GMA welding process and can lead to the desired hardness and strength in the weld metal [34].

3.5. Effect of the Welding Process on the Microstructure of the Dissimilar Joint

3.5.1. Base Materials

Figure 7 shows the microstructure corresponding to the thermomechanical-controlled process of S700MC steel and the quenched and tempered S960QC steel. The microstructure of S700MC was principally composed of approximately 70% B and 30% F (Figure 7a). The particularity of this steel is the microstructural control technique, which is a combination of controlled rolling and controlled cooling (accelerated cooling) during the production process. The microstructure of S700MC is subject to low alloy elements and may need almost no preheating, resulting in an improvement in the weldability using the GMA welding process. The typical SEM microstructure of 960QC steel is illustrated in Figure 7b, which shows a composition of fine M and B formed in the rolling direction. The appearance of M as a form of elongation prior to austenite grains in the rolling direction is also observed [35].

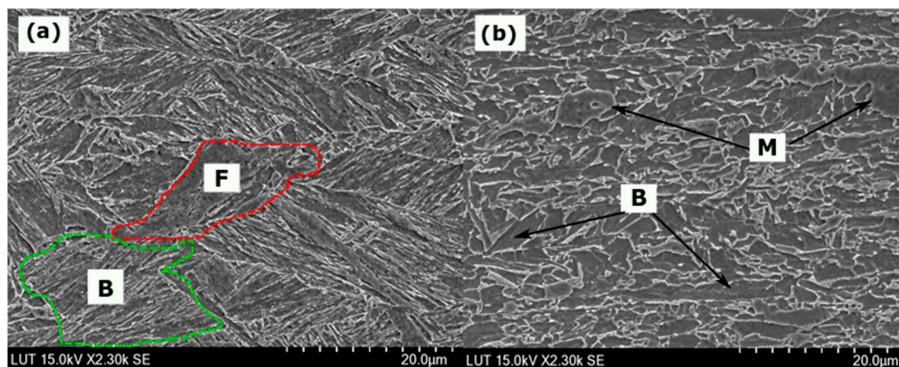


Figure 7. SEM micrographs of the base materials: (a) S700MC and (b) S960QC high-strength steels.

3.5.2. Microstructure Behavior of S700MC HAZ

The thermomechanically controlled HSS with a yield strength (YS) of 700 MPa had a low-carbon percentage (0.05%) and a composition of B and F in its base microstructure. The welding process (GMA welding) had a thermal impact on the microstructure of the HAZ, which was controlled by the peak temperature diffusion from the weld line to the base material. The weld sample used for the microstructure analysis was WS3 (10 kJ/cm). The microstructures have been described as sub-zones, which were identified in this analysis as the coarse-grain heat-affected zone (CGHAZ) and fine-grain heat-affected zone (FGHAZ) for both materials. The microstructures were examined using the OM and SEM images to investigate the austenite transformation from F to B for S700MC, and from B to M for S960QC. Figure 8a shows the examined sub-zone microstructure of S700MC, presenting the weld metal (WM), CGHAZ, FGHAZ, and BM. The WM and CGHAZ were subjected to the high peak temperature, which can lead to the development of a re-austenization of the grain structure. Figure 8b presents an OP image of CGHAZ of S700MC, which resulted from the highest temperature above the austenization temperature (800 °C) and during an extended period, achieved by increasing the grain size (Figure 8c,d). Figure 8e,f shows the microstructure of S700MC in the FGHAZ region of the HAZ. From this SEM image, a decrease in the austenite grain due to the increase in the distance from the fusion line to the BM can be seen.

Examination using SEM images with a resolution of 20 μm of the CGHAZ and FGHAZ allowed the different microstructural compositions in the sub-division zones of the HAZ of S700MC to be identified (see Figure 8c–f). Based on the examination, the CGHAZ austenite transformed to F, because of the higher peak temperature near the fusion line (800 °C), and B at 550 °C. The peak temperature in the FGHAZ was lower than in the CGHAZ (550 °C) and the austenite was transformed into B,

while the other austenite parts were transformed into RA. A larger amount of B and a mixture of RA and F were seen. Figure 8c indicates that B sheaves in the austenite grain accrue in the same direction and plate morphologies appear. This figure also shows an existing feature of B, which corresponds to its concentration volume fraction and which can be defined as bainite–ferrite (BF).

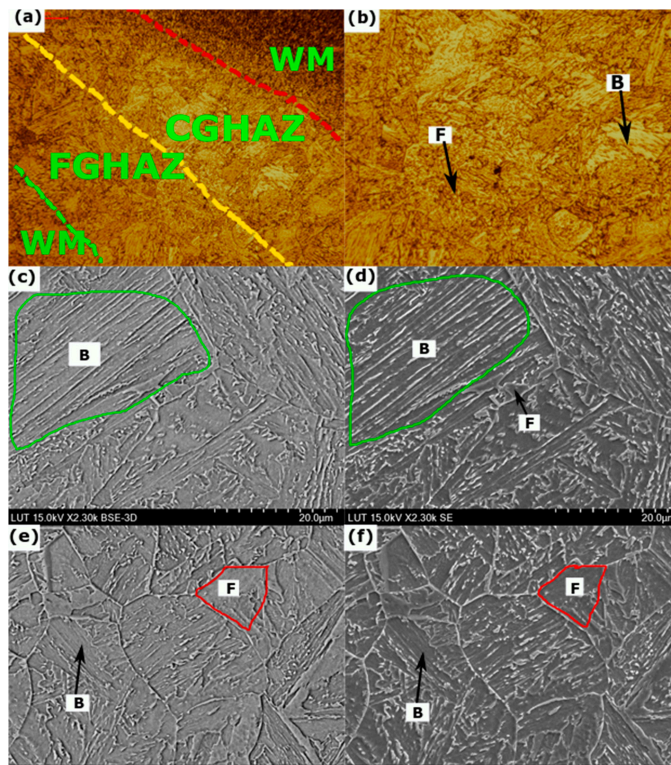


Figure 8. Optical microscopy (OM) and SEM micrographs showing the microstructures of S700MC steel in different sub-zones of the welded joint: (a) description of different sub-zones of the welded joint, (b) OM image of the coarse-grain heat-affected zone (CGHAZ) of S700MC, (c–d) SEM image of CGHAZ, and (e–f) SEM image of fine-grain heat-affected zone (FGHAZ).

In the FGHAZ (420 °C), the decrease in the temperature leads to austenite transformation to B and some of F to RA because of the incomplete transformation.

3.5.3. Microstructure Behavior of S960QC HAZ

The S960 QC steel was quenched and tempered at 960 MPa and had a composition of 60% B and 40% M in its BM. The sub-regions inspected in the HAZ were the WM, CGHAZ, and FGHAZ. The same phenomenon was observed in the heat diffusion from the melting point to the base material. The microstructure of the sub-zones (WM, CGHAZ, and FGHAZ) of S960QC were analyzed using OM images and SEM images. The EDS analysis was performed to evaluate the alloy element composition and its influence on the mechanical properties of the sub-zones of both materials. The CGHAZ was observed to have the lowest peak temperature, lower than that of S700MC, and remained at 500 °C, leading to a decrease in the grain size, compared to S700MC, when using the same resolution (20 µm). Compared to S700MC, S960QC had a smaller grain size, which continuously decreased with the distance from the melting zone.

The different phases identified by the SEM images using a resolution of 20 μm are shown in Figure 9c,d for the CGHAZ, Figure 9e,f for the FGHAZ, and Figure 9g,h for the WM. After the GMA welding process and based on the SEM images, the CGHAZ austenite transformed completely to B at a temperature of 450 $^{\circ}\text{C}$ and to M at 360 $^{\circ}\text{C}$. Some of this M then transformed to tempered martensite (TM) due to the tempering after the welding process. The WM is the part in which the peak temperature is accrued due to the heat input concentration. Figure 9g,h shows the microstructure of the WM in the dissimilar joint, where two types of ferrite can be observed: pro-eutectoid ferrite (PF) and acicular ferrite (AF) at a temperature of approximately 800 $^{\circ}\text{C}$, at which solidification starts.

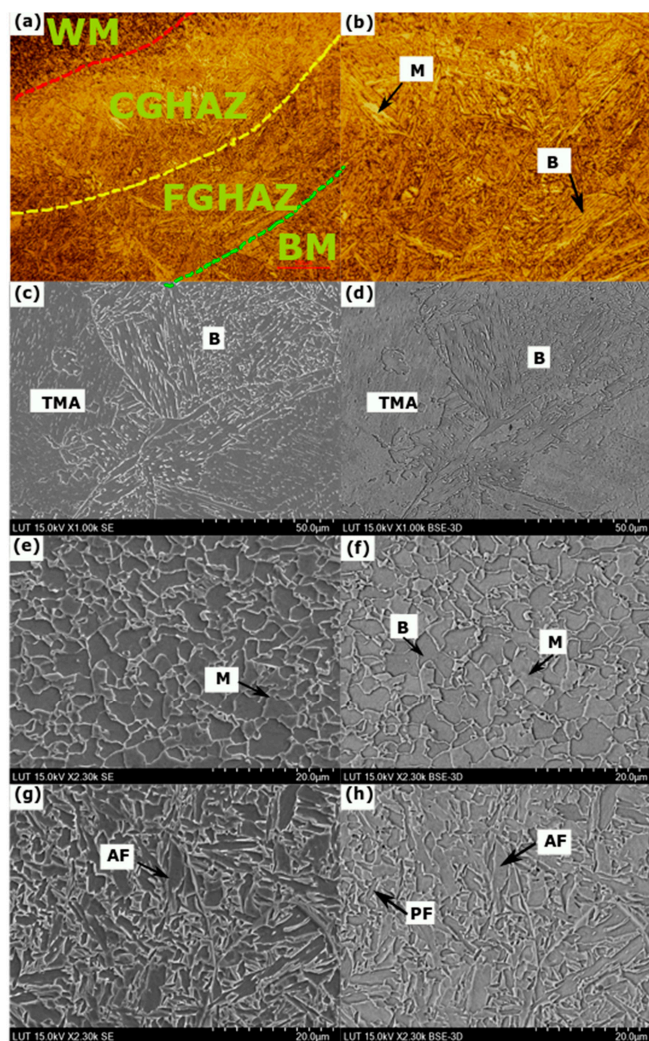


Figure 9. OM and SEM micrographs showing the microstructures of S960QC steel in the different sub-zones of the welded joint: (a) OM image showing the different sub-zones of the welded joint, (b) OM image of the CGHAZ of S960QC, (c–d) SEM image of CGHAZ using a resolution of 20 μm , (e–f) SEM image of the FGHAZ of S700MC, and (g–h) SEM image of the weld metal.

Based on the sampling of the SEM micrographs, measurements were carried out directly on the images of both materials focusing on the area of the CGHAZ and FGHAZ. The cooling temperatures used in the analysis were 615 °C and 420 °C for S700MC and 470 °C and 400 °C for S960QC. The images were uploaded to the image processing software (ImageJ Pro) for identification of the different grain surfaces in the image. Figure 10a–c shows the original picture, the representation of the block B (in grey), the surfaces formed by the deduction of the retained austenite (colored manually in yellow) and, finally, the infiltration ferrite + cementite (colored in red) for S700MC. The variable X_T is the total area mapped; X_1 is the surface area occupied by B (grey); X_2 is the surface area of the RA (colored manually in yellow); and X_3 is the space occupied by ferrite + cementite particles (in red). The ImageJ software (ImageJ 2013, NIH, Bethesda, MD, USA) first determined the overall surface of the sampled X_T , after which a measurement process was used to discover X_2 and X_3 . The following relationship determines the volume fraction (X_1) not occupied by B:

$$X_1 = X_T - (X_2 + X_3) \quad (6)$$

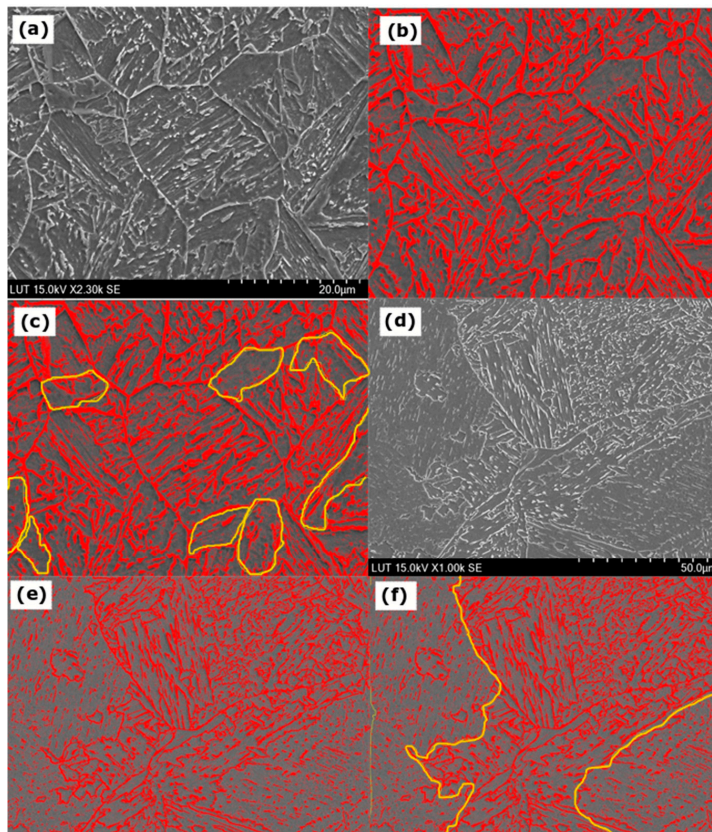


Figure 10. Evaluation of the volume fraction of bainite (B), martensite (M), retained austenite (RA), and ferrite using ImageJ Pro software: (a) original SEM image of S700MC, (b) darker area to measure B, red area to measure the volume fraction of ferrite, and cementite, (c) geometries of RA areas to measure the volume fraction of RA, shown in yellow, (d) original SEM image of S960QC, (e) darker area to measure the B volume fraction and red zone to measure the volume fraction of ferrite, and (f) geometries of the M areas to measure M, shown in yellow.

The same measurement method was applied for S960QC steel. The transformation was identified mainly as the cooling time of B, and M had temperatures of 470 °C and 400 °C. Figure 10a presents the original SEM image. The variable X_T is the total area of the sample resolution; X_1 is the part occupied by B (black), measured in Figure 10b; X_2 presents the ferrite particles and cementite (in red) obtained from the same figure as X_2 ; and X_3 is M, manually measured from the ImageJ Pro software (ImageJ 2013, NIH, Bethesda, MD, USA). The results of the analysis, providing the volume fraction as a function of the temperature points identified, are presented in Figure 11.

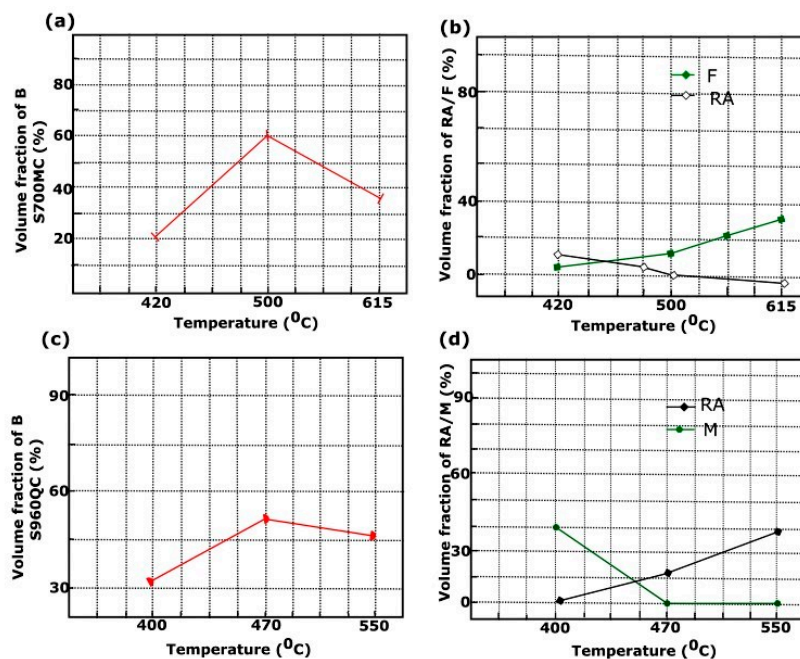


Figure 11. Volume fraction of B, F, and M for both materials: (a) volume fraction of B of S700MC, (b) volume fraction of RA and F of S700MC, (c) volume fraction of B of S960QC, and (d) volume fraction of M of S960QC.

Figure 11a shows that the maximum value of the volume fraction of B was approximately 60%, which was observed at a temperature of 500 °C. Figure 11b presents two results separately: (1) the volume fraction of the ferrite, which had a maximum value of 25% at a temperature of 615 °C, corresponding to the beginning of the solidification of the weld sample; and (2) the volume fraction of RA, with a maximum value of 10% at 420 °C. Figure 11c shows the volume fraction of B, produced in S960QC, which peaked at around 55% at a temperature of 470 °C. Figure 11d has two graphs which show the respective volume fractions of RA and M. As found in previous data, the volume fraction of M increases when the temperature slows down by 45%. During the transformation, incomplete processing of austenite grain is transformed into RA, which has a reduced temperature change to M, estimated to be 10% of its maximum value (less than 400 °C).

For analysis of the micro-alloy elements, EDS was applied to the two sides of the weld. Figure 12a shows the mapping and spectra records for the alloy elements in S700MC and Figure 12b shows the same information for S960QC. The EDS was calibrated at a voltage of up to 15 kV, with mapping at 20 kV, and the resolution of the image was 1024 by 768 for 2.5 μm . To perform EDS analysis, the specimens were polished and cleaned using an ultrasonic bath of hot $\text{C}_3\text{H}_6\text{O}$ and $\text{C}_2\text{H}_6\text{O}$ to ensure any impurities were removed. The data were recorded in weight %, which presents the percentages

of C transforms, Si, Cr, Mn, Fe, Ni, and Mo. Figure 12a,b shows the proportions of the weights of the micro-elements of the alloys obtained [36]. An absence of Ni and Mo in the microstructure of the S960QC (Figure 12a), a decrease in the weight % of Cr (0.1%), and an increase of Mn (1.8%) can be seen. These three alloy elements play a significant role in the relation between the microstructure behavior and mechanical properties of the weld joint, particularly regarding the HAZ.

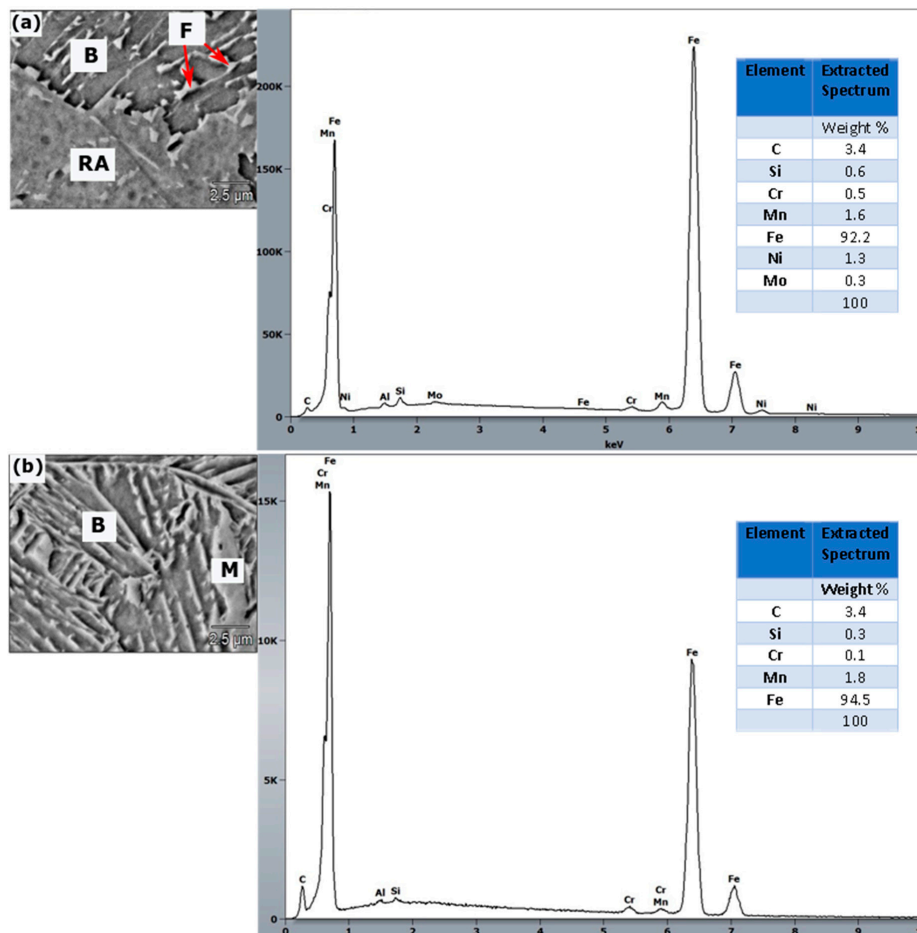


Figure 12. EDS analysis and elemental composition mapping: (a) S700MC and (b) S960QC.

The obtained weights of Mn, Ni, and Mo were 1.6, 1.3, and 0.4 for S700MC, and 1.8, 0, and 0 for S960QC, respectively. The absence of Ni in the CGHAZ of S960QC can cause softening in this area, even though there is a small increase in the weight % of Mn. As observed in the evaluation of the phase transformations, the rise in Mn promoted the appearance of M at the end of the transformation phase of S960QC. In the S700MC, the formation of the alloy elements of Mn, Ni, and Mo enabled the composition of B at 615 °C and M at 400 °C, as indicated in the previous results, showing a high-volume fraction of B (B = 60%). This high value of B, resulting from the appearance of the alloy elements, was the source of the softening in the CGHAZ, which was confirmed during the hardness analysis and showed the link between the microstructure behavior of the weld joint and the mechanical behavior of the weld.

Based on the estimation of the weight percentages of the alloy elements, it was possible to formulate a relationship to estimate the increase in the strain zones (σ_p) in both materials, which led to the reinforcement of precipitation in the areas analyzed using the EDS results:

$$\rho_p = \frac{0.538Gb f_B^{1/2}}{X} \ln\left(\frac{X}{2b}\right) \quad (7)$$

where G is the modulus of elasticity (in MPa), b (mm) is the vector of Burgers [24], f_B is the volume fraction of the particle bainite (B) of both materials, and X is the precipitation diameter of the B formation into austenite grain. After different evaluations, an increase in the yield strength, compared to the experimental values, which can be obtained by tensile test, was observed. For example, the precipitation strengthening (ρ_p) was 23.2 MPa for S700MC and 27 MPa for S960QC.

3.6. Tensile Test Analysis

Figure 13 shows all of the test specimens in which a fracture was visible. The tests were conducted according to EN ISO 6892-1:2010. The analysis was carried out using a ZWICK/ROZ Z 330 RED test machine. The dimensions of the samples and the results are summarized in Table 4. The samples in Figure 13a correspond to the heat input of WS1, the samples in Figure 13b correspond to the heat input of WS2, and the samples in Figure 13c correspond to the heat input of WS3. The elongation of S700MC (with an average of 7.8%) was lower than that of the BM (12%). The apparent elongation for S960QC may be the same or greater depending on the tensile strength applied to the different samples. It was difficult to evaluate the average elongation in the S960QC, because all fractures in the test samples were on the S700MC side (in the HAZ close to FGHAZ).



Figure 13. Tensile test results showing the fracture locations in different samples: (a) tensile test of WS1, (b) tensile test of WS2, and (c) tensile test of WS3.

Table 4. Results for six samples of the three specimens (WS1, WS2, and WS3).

Sample	Dimensions (mm)	So (mm ²)	Fe (kN)	YS (MPa)	TS Fm (kN)	UTS (MPa)	L _o (mm)	L _u (mm)	A ₅ %	Place of Rupture
1A	24.9 × 8	199.2	138	692.8	153.2	769.1	79	83.8	6.1	HAZ S700MC
1B	24.6 × 8	196.8	139	706.3	151.6	770.3	79.2	84.9	7.2	HAZ S700MC
Av.	-	-	-	699.5	-	769.7	-	-	6.6	-
2A	24.7 × 8	197.6	150	759.1	161.6	817.8	79.4	87.4	10	HAZ S700MC
2B	24.9 × 8	199.2	150	753.0	162	813.3	79.6	87.4	9.8	HAZ S700MC
Av.	-	-	-	756.1	-	815.5	-	-	9.9	-
3A	24.8 × 8	198.4	142	715.7	157.6	794.4	79.6	85.3	7.2	HAZ S700MC
3B	25 × 8	200	140	700	166.3	823	79.7	85	6.6	HAZ S700MC
Av.	-	-	-	707.9	-	808.7	-	-	6.9	-

Performing the measurements required some preliminary analysis. After preparation of the samples, calibration of the equipment for the study was needed. As a result, the parameters used in the table were required. First, the lengths of the different samples needed to be determined (L_0). An empirical relationship linked the initial length of a sample to the S_0 . Equation (6) presents the length L_0 function of S_0 :

$$L_0 = 5.65 \times \text{sqrt}(S_0) \quad (8)$$

With the final length (L_u), the calculations more easily determined the value of the elongation (A%) by applying the expression of Equation (7):

$$A\% = \frac{L_u - L_0}{L_0} \quad (9)$$

By applying the tensile strength (F_e) at both ends, it was possible to determine the yield strength by calculation based on the value of the area (S_0) stressed in the tension. Equation (8), as shown above, presents the relationship between the yield strength (R_e) and the section:

$$R_e = \frac{F_e}{S_0} \quad (10)$$

Subsequently, the relationship shown in Equation (9) was applied to determine the breakage limit. By imposing a force (F_m), causing shear of the sample and section (S_0) of the rupture zone, the following relation was established:

$$R_m = \frac{F_m}{S_0} \quad (11)$$

The tensile test results are summarized in Table 4, which lists the average values of the ultimate tensile strength (UTS), yield strength (YS), tensile strength (TS), elongation (A₅%), the rupture area, the initial length (L_0), total length (L_u), and the average of the whole results (Av.).

Based on these results, using the sample WS1 (15 kJ/cm), the average yield strength (R_e) after the two tests was 699.5 MPa, the ultimate yield strength (R_m) was 769.7 MPa, and the apparent average elongation for the welded joint was 6.6%. The YS, UTS, and elongation for this welded joint were observed to be lower than for the base materials. Using the welded sample WS2 (7 kJ/cm), the average YS, UTS, and elongation were found to be 756.1, 815.5, and 9.9%, respectively. For S960QC, YS, UTS, and apparent elongation were observed to be lower than the BM. For S700MC, YS, UTS, and apparent elongation were observed to be the same as the BM. When investigating the third specimen, WS3, the average YS, UTS, and elongation were found to be 707.9, 808.7, and 6.9%, respectively. The YS, UTS, and elongation of S700MC were found to be almost the same as those of the BM, which had a YS of 768 MPa and UTS of 822 MPa. However, the average elongation was found to be ≈36% lower than that of the BM. For S960QC, the YS and UTS were found to be lower than those of the BM, which had a YS of 960 MPa and UTS of 1000 MPa. All the tensile failures were in the HAZ on the S700MC side. The tensile tests of the samples confirmed the softening in the HAZ of S700MC observed in the macro-hardness tests. One reason for the softening was the choice of filler wire and heat input values, which had an impact on the chemical and mechanical characteristics of the weld joints. The hardness, YS, and UTS increased as the temperature dropped with the increasing cooling rate [37]. This phenomenon was due to the parameters, such as the alloy element compositions of both materials and the filler wire. Furthermore, the microstructure formations during the transformations also impacted the characteristics of the weld joint. The observations are supported by Yan et al. [25], who defined the micro-alloying elements (Ni, Cr, and Mo) as the key components that affect the mechanical and microstructure formation in the HAZ. Ali et al. [38] noted that the YS and UTS of low-carbon bainitic steel increase due to the refinement of prior austenite grain size. In addition, low hardness and strength in the S700MC steel result from the appearance of possible bainite with pro-eutectoid carbides at the boundary. The choice of heat input and filler wire (by increasing the

amount of alloys, such as Ni, Cr, and Mo) are the key solutions to improving the hardness and strength of the HAZ of the weld samples.

4. Conclusions

The effect of different heat input values (15, 7, and 10 kJ/cm) on weld joints of S700MC/S960QC steel were investigated using weld specimens of $300 \times 200 \times 8 \text{ mm}^3$ of the base material. Filler wire with a diameter of 1.0 mm and a composition NiCrMo700 was used in the experiment. Microstructure, hardness, and tensile test analyses were carried out to analyze the effect of heat input and undermatched filler wire on the strength of the weld joint. The following conclusions can be drawn:

1. Experimental analysis of the heat effects in welding dissimilar S700MC/S960QC using an undermatched filler wire enabled measurement of the hardness behavior of the weld joint and evaluation of the formation of B, F, M, and RA in the HAZ region of both BMs. The same reference samples were used to evaluate the volume fraction of microstructure formations at the end of the transformation and to evaluate the mechanical behavior in the HAZ.
2. Heat input of 7 kJ/cm resulted in a faster cooling rate (33 °C/s), which slightly decreased the average hardness in the HAZ of both materials. In the FGHAZ of S700MC, it was observed that there was a decrease in hardness of 11% to 245 HV5 versus 270 HV5 for the BM. In the S960QC steel, the lowest hardness was found in the FGHAZ, which decreased by 22% to 268 HV5 versus 320 HV5 for the BM. In the FGHAZ, using the whole sample, the hardness of both steels underwent a decrease of 15% for S700MC and 20% for S960QC.
3. When considering the microstructures obtained with a cooling rate of 21 °C/s, the B–F constituent formed at the interface of S700MC austenite grains and some lath B morphology was observed. For S960QC, the formation of B, M, and RA was observed during the transformation. In the microstructure with a carbon content of 0.09% (S960QC), the highest volume fractions of RA (18%), bainite (55%), and M (27%) were observed.
4. In the microstructure of S700MC with a carbon content of 0.056%, the highest volume fractions of B (60%), F (approximately 35%), and RA (5%) resulted in the composition of 1.3 Ni, 0.4 Mo, 1.6 Mn in the CGHAZ. Application of a heat input of 10 kJ/cm resulted in the best combination of alloy elements, which led to a slight increase in the hardness to 260 HV5 and a slight increase in the strength of the welded joint.
5. The tensile strength of GMA welded dissimilar S700MC and S960QC steel specimens had different values compared to the strength of the BM, and all the welded specimens failed in the HAZ of the S700MC side. The elongation of the specimens differed from that of the BM for all the studied cooling rates. The average elongation indicated a 17% decrease when compared to the BM.
6. The best combination of hardness and strength was achieved by choosing a cooling rate of 21 °C/s, which achieved an equilibrium of B, F, and M in the dissimilar S700MC/S960QC weld, reducing the formation of proeutectoid grain boundary carbide.
7. To improve the hardening ability and strength of the dissimilar S700MC/S960QC welded samples using GMA welding, an increase in the number of alloy elements in the filler wire, such as Ni, Cr, and Mo, is required.

Author Contributions: F.N.B. performed the experiment analysis, wrote the entire manuscript, and corrected the manuscript following discussion with the other authors. P.K. reviewed the draft for publication. B.M. created the design of the experiments and provided suggestions. P.L. provided critical feedback and additional input.

Funding: The research was funded by Energy-Efficient Systems Based on Renewable Energy of Arctic Conditions “EFREA” (Grant number K51054) and the Finnish Cultural Foundation (Grant number 190749).

Acknowledgments: The authors would like to thank Esa Hiltunen, Anti Heikkinen, Toni Väkiparta, and Antti Kähkönen for their support in the arrangement of the experimental work.

Conflicts of Interest: The authors declare no conflicts of interest.

References

1. Mvola, B.; Kah, P.; Martikainen, J.; Suoranta, R. Dissimilar high-strength steels: Fusion welded joints, mismatches, and challenges. *Rev. Adv. Mater. Sci.* **2016**, *44*, 146–159.
2. Monika, K.; Bala, M.; Nanda, K.; Prahalada, R. The Effect of Heat input on the Mechanical Properties of MIG welded Dissimilar Joint. *Inter. J. Eng. Res. Tech.* **2013**, *2*, 1406–1413.
3. Sarizam, M.; Yu-Ichi, K. Effect of cooling rate invariant selection during bainite transformation in heat affected zone of Cr-Mo steel. *J. Eng. Appl. Sci.* **2015**, *10*, 9481–9486.
4. Laitinen, R. Improvement of Weld HAZ toughness at Low Heat Input by Controlling the Distribution of M-A Constituents. Ph.D. Dissertation, Acta Universitatis Ouluensis, Oulu, Finland, 2006.
5. Tadashi, F.; Shin-ya, A.; Goro, M. Anisotropic Ferrite Growth and Substructure Formation du Bainite Transformation in Fe-9Ni-C alloys: In-Situ Measurement. *Mat. Trans.* **2018**, *59*, 214–223.
6. Njock Bayock, F.; Kah, P.; Mvola, B.; Pavel, L. Experimental review of the thermal analysis of dissimilar high-strength steel. *Rev. Adv. Mater. Sci.* **2019**, *58*, 38–49. [\[CrossRef\]](#)
7. Wei, G.; Lin, L.; Shiyun, D.; Dave, C.; Alan, T. Comparison of microstructure and mechanical properties of ultra-narrow gap laser and gas-metal-arc welded S960 high strength steel. *Opt. Lasers Eng.* **2017**, *91*, 1–15.
8. Gaspar, M.; Balogh, A. GMAW experiments for advanced (Q+T) high strength steels. *Prod. Pro. Syst.* **2013**, *6*, 9–24.
9. Karkhin, V.; Michailov, V.; Petrov, P. *Principles of Welding*; St.Petersburg Polytechnic University Publishing: St. Petersburg, Russia, 2016.
10. Porter, D.; Laukkanen, A.; Nevasmaa, P.; Rahka, K.; Wallin, K. Performance of TMCP steel for mechanical properties after cold forming and post-forming heat treatment. *Int. J. Press. Vessel Pip.* **2004**, *81*, 867–877. [\[CrossRef\]](#)
11. Siltanen, J.; Tihinen, S. Position welding of 960 MPa ultra-high-strength steel. *J. Laser Appl.* **2012**. [\[CrossRef\]](#)
12. Ndiwe, B.; Mvola, B.; Kah, P.; Njock Bayock, F. Effect of consumable filler wire composition to mismatches of high-Mn steels welded joints. In Proceedings of the International Ocean and Polar Engineering Conference, San Francisco, CA, USA, 25–30 June 2017.
13. Schneide, R.C.; Ernst, W.; Schnitzer, R.; Staufer, H.; Vallant, R.; Enzinger, N. Welding of S960MC with undermatching filler material. *Weld. World* **2018**, *62*, 801–809. [\[CrossRef\]](#)
14. Gorka, J. Assessment of Steel Subjected to the Thermomechanical Control Process with Respect to Weldability. *Metals* **2018**, *8*, 169. [\[CrossRef\]](#)
15. Gorka, J. Analysis of simulated welding thermal cycles S700MC using thermal imaging camera. *Adv. Mater. Res.* **2014**, *837*, 375–380. [\[CrossRef\]](#)
16. Gorka, J. Microstructure and properties of the high-temperature (HAZ) of thermo-mechanically treated S700MC high-yield-strength steel. *Mat. Tehnol.* **2016**, *50*, 617–621. [\[CrossRef\]](#)
17. Guo, W.; Crowther, D.; Francis, J.A.; Thompson, A.; Liu, Z.; Li, L. Microstructure and mechanical properties of laser welded S960 high strength steel. *Mat. Des.* **2015**, *85*, 534–548. [\[CrossRef\]](#)
18. Njock Bayock, F.; Kah, P.; Layus, P.; Karkhin, V. Numerical and experimental investigation of the heat input effect on the mechanical properties and microstructure of dissimilar weld joints of 690-MPa QT and TMCP steel. *Metals* **2019**, *9*, 355. [\[CrossRef\]](#)
19. Talas, S. The assessment of carbon equivalent formulas in predicting the properties of steel weld metals. *Mater. Des.* **2010**, *31*, 2649–2653. [\[CrossRef\]](#)
20. Changfei, W.; Zhaodong, W.; Xiangtao, D.; Guodong, W.; Raja, D. Effect of heat input on the microstructure and mechanical properties of low alloy ultra-high strength structural steel welded joint. *Steel Res. Int.* **2018**, *89*, 1–9.
21. Gyasi, E.; Kah, P. Structure integrity analysis of the usability of high strength steel (HSS). *Rev. Adv. Mater. Sci.* **2016**, *2*, 39–52.
22. Sadeghan, M.; Shamanian, M.; Shafyei, A. Effect of heat input on microstructure and mechanical properties of dissimilar joints between super duplex stainless steel and high strength steel. *Mat. Des.* **2014**, *60*, 678–684. [\[CrossRef\]](#)
23. Zhuangfei, W.; Minghao, S.; Shuai, T.; Guodong, W. Effect of heat input and M-A constituent on microstructure evolution and mechanical properties of heat affected zone in low carbon steel. *J. Wuhan Univ. Tech. Mat. Sci. Educ.* **2017**, *32*, 1163–1170.

24. Radaj, D. *Heat Effects of Welding*; Springer: Berlin, Germany, 1992.
25. Tasalloti, H.; Kah, P.; Martikainen, J. Effect of heat input on dissimilar welds of ultra-high-strength steel and duplex stainless steel: Microstructural and compositional analysis. *Mat. Charact.* **2017**, *123*, 29–41. [[CrossRef](#)]
26. Yan, S.; Liu, X.; Liang, T.; Chen, J.; Zhao, Y. Effect of micro-alloying elements on microstructure and mechanical properties in C-Mn-Si Quenching and Partitioning (Q&P) steels. *Steel Res. Int.* **2019**, *90*, 1–10.
27. ISO. *Standard Test Methods for Micro Indentation Hardness of Materials*; ISO 6507-1:2018; ISO: Geneva, Switzerland, 2018.
28. ISO. *International Standard Test Methods for Tensile Testing of Metallic Materials*; ISO 6892-1: 2016; ISO: Geneva, Switzerland, 2016.
29. ISO. *Non-Destructive Testing of Weld-Visual Testing of Fusion-Welded Joint*; ISO 17637-2017; ISO: Geneva, Switzerland, 2017.
30. Poorhaydari, K.; Patchett, B.; Ivey, D. Estimation of cooling rate in the welding of plates with intermediate thickness. *Weld. J.* **2005**, *84*, 149–155.
31. Xiuzhi, Y.; Lichao, Z.; Yusheng, S.; Shengfu, Y.; Chunfa, D. Effective microstructure unit in control of impact toughness in CGHAZ for high strength bridge steel. *J. Wuhan Univ. Tech. Mat. Sci. Educ.* **2018**, *33*, 177–184.
32. Hamada, M. Control of strength and toughness at the heat affected zone. *Weld. Inter.* **2003**, *17*, 265–270. [[CrossRef](#)]
33. Guo, W.; Li, L. Laser welding of high strength steels (S960 and S700) with medium thickness. *J. Laser Appl.* **2016**, *28*, 1–10. [[CrossRef](#)]
34. Hochhauser, F.; Ernest, W.; Rauch, R.; Vallant, R.; Enzinger, N. Influence of the soft zone on the strength of welded modern HSLA steels. *Weld. World* **2006**, *56*, 77–85. [[CrossRef](#)]
35. In, K.; Hyunbin, N.; Myungjin, L.; Daegeun, N.; Yeong-do, P.; Namhyun, K. Effect of Martensite-Austenite constituent on low-temperature toughness in YS 500 MPa Grade Steel Welds. *Metals* **2018**, *8*, 1–11.
36. ASTM. *Standard Practice for Radiographic Examination of Weldments Using X-Ray Film*; ASTM E1032-19; ASTM: West Conshohocken, PA, USA, 2019.
37. Tian, J.; Xu, G.; Zhou, M.; Hu, H. Refined bainite microstructure and mechanical properties of high-strength low-carbon bainitic steel treated by austempering below and above Ms. *Steel Res. Int.* **2018**, *89*, 1–10. [[CrossRef](#)]
38. Ali, M.; Porter, D.; Kömi, J.; Eissa, M.; El Faramawy, H.; Mattar, T. Effect of cooling rate and composition on microstructure and mechanical properties of ultrahigh-strength steels. *J. Iron Steel Res. Int.* **2019**. [[CrossRef](#)]



© 2019 by the authors. Licensee MDPI, Basel, Switzerland. This article is an open access article distributed under the terms and conditions of the Creative Commons Attribution (CC BY) license (<http://creativecommons.org/licenses/by/4.0/>).

Publication IV

Bayock, F., Kah, P., Mvola, B., Layus, P., and Cai, X.

Characterization of bainite-ferrite structures formed on the heat-affected zone of dissimilar welds of high-strength steel (S700MC/S960QC) and their dependency on the cooling time

Reprinted with permission from

72nd IIW Annual Assembly and International Conference. Conference Proceedings

Bratislava, Slovakia, 7-12 July

pp. 1-10, 2019

© 2019, IIW

Characterization of bainite-ferrite structures formed on the heat-affected zone of a dissimilar welds of high-strength steel (S700MC/S960QC) and their dependency on cooling time.

Francois Njock Bayock^{1,a}, Paul Kah^{1,b}, Belinga Mvola^{1,c}, Pavel Layus^{1,d}, Xiaoyu Cai^{2,e}

¹Mechanical Engineering, Welding Technology Laboratory, Lappeenranta-Lahti University of Technology, Lappeenranta, Finland

²State Key Laboratory of Welding and Joining, Harbin Institute of Technology, Harbin Shi, China

^afrancois.njock.bayock@lut.fi, ^bpaul.kah@lut.fi, ^ceric.mvola.belinga@lut.fi, ^dpavel.layus@lut.fi, ^exycai@hit.edu.cn

Abstract

Modern steel structures and joints must satisfy various increasingly demanding requirements such as high yield strength, improved cross section to mass ratio, and desirable ductile-to-brittle transition properties. Consequently, joining different types of high-strength steels has become an attractive option from the cost perspective and for weight and corrosion reduction. In dissimilar welding, however, there remains a need for better understanding of discrepancies in microstructure formation resulting from asymmetric heat distribution. In this study, a characterization of the transformation of bainite, ferrite, and martensite in the microstructure of the heat affected zone (HAZ) formed by a cooling time of 10 kJ/cm of heat input was carried out for dissimilar high-strength joint steels (S700MC/S960QC). The characterization was performed by scan electron microscopy (SEM) sampling, the images of which were analyzed by ImageJ Pro and evaluated by volume fraction of block – like granular bainite (GB). The alloy elements composition close to the fusion line of both materials was then assessed using energy-dispersive X-ray spectroscopy (EDS). The results showed a strong presence of GB, which had about 70% volume fraction in S700MC at 615 °C, and which comprised formations of lower bainite and retained austenite (RA) at 420 °C. The presence of 55% block GB was observed at 470 °C in S960QC, which was caused by the formation of tempered martensite (TMA) at 400 °C. Presence of 1.3Ni, 0.4Mo, and 1.6Mn in the coarse grain heat affected zone (CGHAZ) of S700MC confirmed the risk of brittle failure on the S700MC side due to the high presence of carbide and ferrite in the GB.

Keywords

dissimilar welding, S960QC, S700MC, granular bainite, tempered martensite

1. Introduction

The specifications of new steels, especially high strength, provide the desirable qualities of strength, hardness, and ductility at reduced weight, which significantly extends the range of possible applications. For example, in assembly of some parts of vehicle structures, there is the challenge of maintaining structural strength while simultaneously reducing the mass of the vehicle to improve fuel consumption and environmental sustainability. Dissimilar welds between high strength steels with a maximum yield strength of 700 MPa and yield strength of 960 MPa, would meet these aims of reducing mass while maintaining strength. However, joining two materials with different thermo-mechanical, chemical and manufacturing properties has an exceptional character, and requires thorough analysis of the welding processes used, and the effects of weld joint geometry and choice of filler material. Investigation of the feasibility of submitting such materials to pre and post weld heat treatment while maintaining their beneficial chemical and mechanical characteristics is a critical task [1-3].

Welding a material such as S700MC [4], which in its production has already undergone heat treatment, and maintaining its mechanical, and chemical characteristics even after having experienced a thermal shock with S960QC is a great challenge. S960QC, whose microstructure also has low alloy elements, exhibits thermal sensitive behavior and thus analysis of essential microstructure (phase transformation) change is required, particularly in the heat affected zone during the welding process. The microstructural composition of S700MC, consists mainly of bainite-ferrite (BF), and S960QC, is composed of bainite martensite (BM). During cooling process, displacement of phase transformations occurs around and even in the austenite grains. Transformation is observed from ferrite to bainite and, bainite to martensite, with some incomplete changes called retained austenite (RA) [7,8].

Much research has investigated characterization of the microstructure of steels with a low percentage of carbon. Most such research applies heat treatment to these steels and analyzes the behavior of the phase transformation of bainite, ferrite, and martensite. In most cases, the constituents of the austenite grains are identified and the volume fraction of the phase transformation then determined. These transformations have an important impact on the ductile to brittle factor of the weld joint.

In this study, welded samples are carefully prepared, and then analyzed by sampling using SEM images, to evaluate the composition of the microstructures of the weld joint (CGHAZ and FGHAZ). Determination of volume fractions

of the different grain surface was done using ImageJ Pro software. EDS analysis of the welded samples was used to determine the composition of alloy elements forming microstructures in the CGHAZ and for analysis of fusion line between the base metal and filler material. This analysis allowed the correlation between the cooling time ($t_{8/5}$), the microstructure behavior, and the mechanical properties of the weld joint to be determined.

2. Experimental Section

2.1 Materials

Dissimilar High-strength steels, namely S700MC and S960QC, and filler material X96, were welded as part of this investigation. The chemical composition of both steels and filler material is given in Table 1, which includes also the welding parameters of the welding process used. The GMAW welding was done using a robot system with protective shielding of Ar + 18% CO₂. The welded specimens had dimensions of 300 x 200 x 8 mm, and the weld was a V joint (60°) with 2 mm gap. Analysis of heat effects was carried out by varying the heat source parameters current (I), voltage (V), welding speed (s) and heat input (Q). The welding process was carried out according to the international standards ISO 1561-1-2017.

The automatic robotic welding process equipment comprising an ABB IRC robot control unit, MAG torch and data acquisition control unit used in this study is illustrated in **Fig. 1**. A laser sensor was installed in the welding equipment to record thermal transfer data for calculation of the cooling time ($t_{8/5}$) from 800 °C to 500 °C. In the laser thermal control process, the recorded cooling time was $t_{8/5}=31$ s. The prepared samples were placed in the SEM equipment for imaging of areas of the HAZ (WM, CGHAZ and FGHAZ) of the materials. 15.0 kV magnification was used and 50.0 μm definition to enable clear identification of microstructure growth in the austenite grain. ImageJ Pro software was used to determine the volume fraction of phase transformations (GB, TMA, and RA) inside the austenite grain. Energy-dispersive X-ray spectroscopy (EDS) was applied to evaluate the concentration of alloy elements close to the fusion line of both material. Analysis focused mainly on Mn, Ni, Mo, which have an impact on hardness in the HAZ of the weld joint.

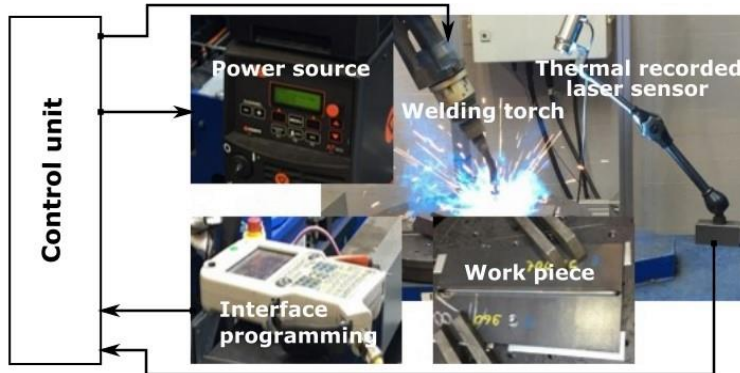


Fig. 1 Automatic GMAW process using an ABB IRC 5 Robot

Chemical composition of base and filler material. Wt. %.															
Materials	C	Si	Mn	Al	B	Nb	Ti	V	Cu	Cr	Ni	Mo	N	P	S
S700MC	0.056	0.16	1.18	0.027	0.002	0.04 4	0.12	0.0 06	0.0 2	0.0 62	0.0 66	0.01 5	0.00 5	0.01	0.005
S960QC	0.09	0.21	1.05	0.03	0.002	0.00 3	0.03 2	0.0 08	0.0 25	0.8 2	0.0 4	0.04	-	0.01	0.004
Filler material	0.12	0.8	1.9		-	-		-	≤0. 30	0.4 5	2.3 5	0.55		-	-
Welding parameters															
Welding current [A]				Arc voltage [V]		Welding speed[cm/mn]		Q [kJ/cm]		Torch angle		Shielding gas		Distance contact tube to work piece	
225				25.3		62.1		7 kJ/cm P1 10 kJ/cm P2		5°		Ar+ 18% CO ₂		18 mm	

Tab. 1 Chemical composition and mechanical properties of S700MC and S960QC steels and filler material X96

2.2 Experimental procedure

CCT diagrams drawn based on literature [13,14] and recorded thermal transfer data allowed identification of phase transformation in the microstructure of the WM, CGHAZ, and FGHAZ of both materials and filler material. Fig. 2a presents the CCT diagram for S960QC showing the cooling time of the welded sample which determines the phase transformations subsequently observed in the microstructure. The curve for S960QC indicates three transformation points: 550 °C, 470 °C and 400 °C. Following the liquefaction phase, cooling to 550 °C corresponds to the start of bainite transformation and 470 °C marks the end of the transformation. The end of bainite transformation

corresponds to beginning of the martensite transformation, which ends at a temperature estimated at 400 °C. Fig. 2b presents the CCT diagram for S700MC showing the cooling time curve of the weld. The following temperatures were defined as those triggering phase transformation in microstructures, particularly in the HAZ. The first phase transformation (ferrite) starts at 670 °C and ends at 615 °C, followed by the bainite transformation, which starts at 615 °C and ends at about 500 °C. Observation of the curves of the two CCT diagrams indicates that there may be incomplete transformations because differences in temperatures of the transformations in the different steels are very small.

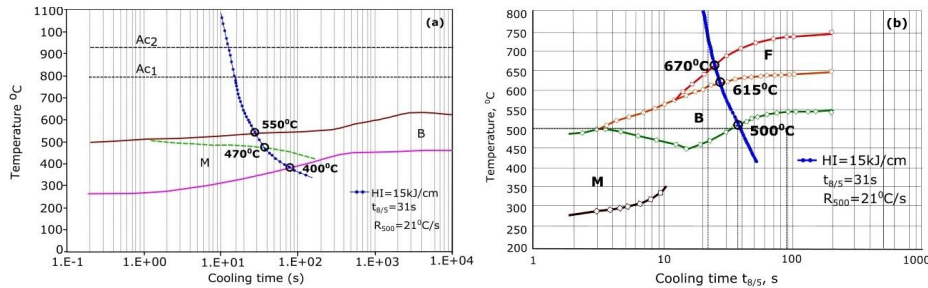


Fig. 2 CCT diagrams obtained by JMat Pro software: (a) CCT diagram for S960QC; (b) CCT diagram for S700MC

3. Results and Discussion

Fig. 3 shows SEM images of the CGHAZ and FGHAZ of S700MC, S960QC and WM of the weld joint of the dissimilar HSS S700MC/S960QC weld. Fig. 3(a) presents an SEM image of the CGHAZ of S700MC; Fig. 3(b) an SEM image of the CGHAZ of S960QC; Fig. 3(c) a macro image of the welded sample showing the mapping area; and Fig. 3(d) an SEM micrograph of the WM. Using mapping of Fig. 3(a), it can be seen that the cooling temperature of 615 °C corresponds to the ferrite-bainite phase transformation. From the image, it is difficult to draw clear conclusions in terms of the type of bainite or ferrite. Using mapping of Fig. 3(b), the micrograph of the CGHAZ of S960QC cooling temperature of 470 °C for the transformation of GB composed of ferrite cementite inside bainite transformations. The microstructure of the WM,

Fig.3(d), has a morphology of a fine line showing formation of Widmanstätten ferrite (WF) with some surfaces with isolated cylindrical and square shapes, which were identified as acicular ferrite (AF).

The same process was applied to the images on the right side of Fig. 3 with the difference that the mapping was performed on the FGHAZ, which allowed identification of the austenite grains and some phase transformations inside the grains. The different morphologies were characterized as bainite, ferrite, martensite and cementite, and retained austenite was observed in these grains. By observing austenite grains of S700MC at 500 °C Fig. 3(f), transformation of GB is detected with RA, which is identified as a dark area inside the austenite grain. transformation of bainite to RA is observed on austenite grains of S960QC at 400 °C, where RA is transformed to TMA.

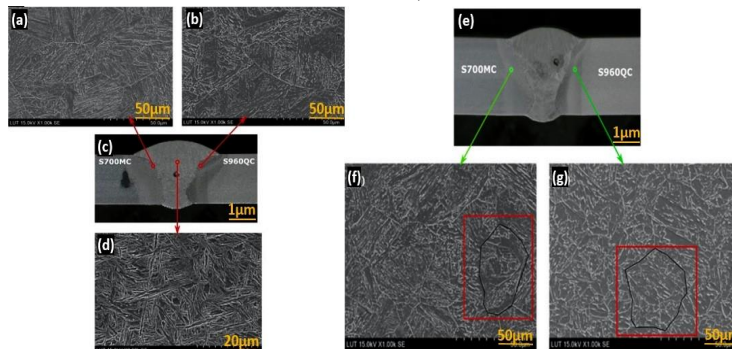


Fig. 3 Macro image of the sample and SEM images of the CGHAZ and FGHAZ of S700MC, S960QC and WM. (a) SEM image of CGHAZ of S700MC; (b) SEM image of CGHAZ of S960QC; (c) Macrograph of the sample; (d) SEM image of WM; (e) Macrograph of the sample; (f) SEM image of FGHAZ of S700MC; (g) SEM image of FGHAZ of S960QC

3.1 Microstructural features

The microstructure composition of austenite grains in the FGHZ of S700MC was characterized based on the geometry [15,16] illustrated in **Fig. 4(a)**. The yellow-colored block in a il in a black background is inferred as RA mixed with some amount of ferrite transformation (RA + F). The remainder of the austenite grain surface is recognized as GB. Inside the GB, the morphology of upper bainite is observed, as is some intergranular ferrite and carbide particles. The formation of intergranular ferrite is the result of a process of early phase transformation at high temperature, observed in the CCT diagram. This phase transformation is the cause of a displacive form of ferrite internally and around the austenite grain. On the S960QC side, austenite grains appear in

Fig.(4b), which displays different behavior at a temperature of around 400 °C. A grain boundary of ferrite develops along the austenite grain, and intergranular ferrite occupies a large part of the GB and RA, which can be identified here as TMA (in green) on the figure.

Tab. 2 presents features of some of the characterized microstructures of the studied materials. In S700MC, the shape of the bright dots inside the GB differs from that found in the GB of S960QC, which consists of bright lines. The structure of the GB of S960QC contains a lot of carbides (this can be justified by the lower cooling time) causing retained blocks of austenite in the grain.

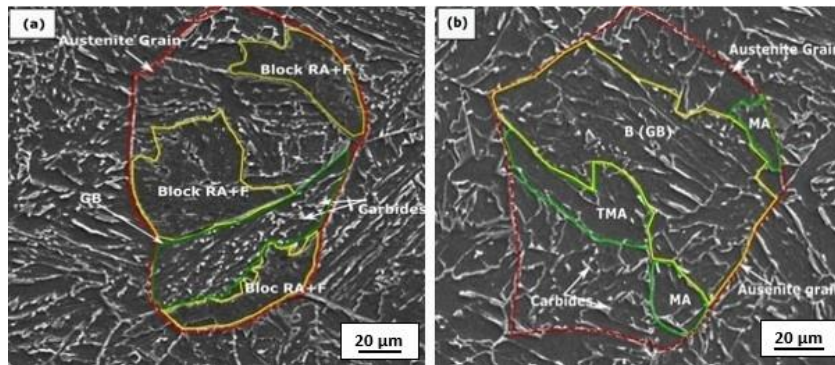
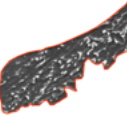


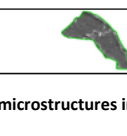


Fig. 4 SEM micro images showing the composition of structures formed in the austenite grains: (a) microstructure of S700MC austenite grains; (b) microstructure of S960QC austenite grains

Type of steel	Structural Feature	Characteristic	Cooling at 615 °C	Cooling at 420 °C	Phase transformation
S700MC		GBF	Bainite + Ferrite + Cementite		Bainitic Phase
		RA		Bainite+ RA	Bainitic phase
S960QC		Granular Bainite	470 °C Bainite transformation at 550 °C	400 °C	Bainitic Phase
		TMA		RA to TMA	Martensitic + Retained Austenitic

Tab. 2 Features of some microstructures in the CGHAZ of the studied materials (S700MC/S960QC)

3.2 Volume fraction of the phase

Based on sampling of the SEM micrographs, measurements were carried out directly on the images of both materials [16], focusing on the area of the CGHAZ and FGHAZ. The cooling temperatures using in the analysis were respectively 615 °C, 420 °C for S700MC and 470 °C, 400 °C for S960QC. The images were uploaded into the image processing software (ImageJ Pro) for identification of the different grain surfaces in the image. **Fig. 5(a), 5(b) and 5(c)** show for S700MC, respectively, the original picture, the representation of the block GB (in black color), the description of the surfaces formed by deduction of retained austenite, (colored manually in yellow), and finally the infiltration ferrite + cementite, (colored in red). XT is the

total area mapped, X_1 is the surface area occupied by GB (black color); X_2 is the surface area of the RA (colored manually in yellow); and X_3 is the space occupied by ferrite + cementite particles (in red). The ImageJ Pro software first determined the overall surface of the sampled X_T , after which a measurement process was used to discover X_2 and X_3 . The following relationship determines the volume fraction (X_i) not occupied by the GB:

$$X_1 = X_T - (X_2 + X_3) \quad (1)$$

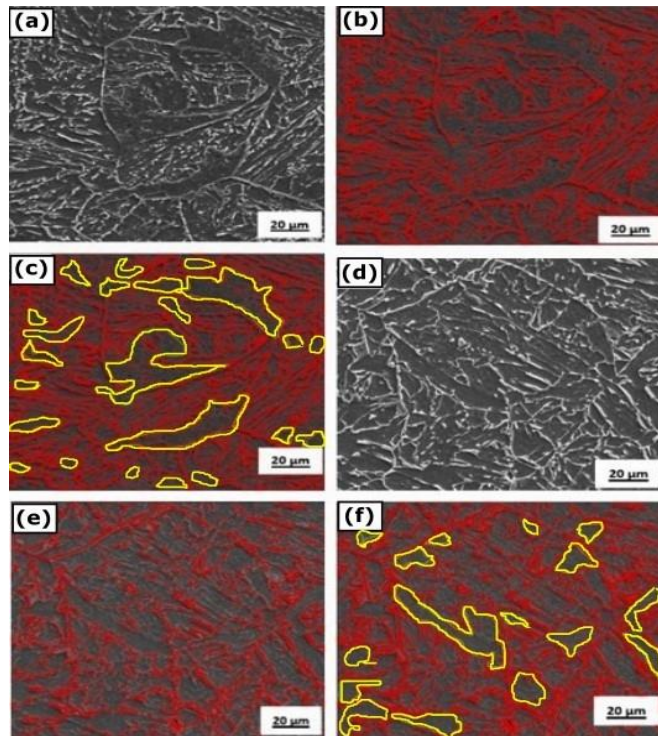


Fig. 5 Evaluation of volume fraction of GB, TMA, RA, and ferrite using ImageJ Pro software: (a) original micrograph of S700MC; (b) darker area to measure the GB, ferrite, and cementite, colored in red; (c) geometries to measure the volume fraction of RA, yellow; (d) original micrograph of S960QC; (e) darker area to measure the GB volume fraction, and red zone to measure the volume fraction of ferrite; and (f) geometries to measure the TMA, yellow

The same measurement method was applied for the S960QC steel. The phase transformation was identified mainly as cooling time GB and the TMA has temperatures of 470 °C and 400 °C respectively. **Fig. 4(a)** presents the original SEM image. X_T is the total area of the sample map; X_1 is the part occupied by the GB (Black) measured in **Fig. 4(b)**; X_2 represents the ferrite particles and cementite (in red) obtained on the same figure as X_2 ; and X_3 is TMA measured from ImageJ Pro software manually. The results of the analysis giving the fraction volumes as a function of the temperature points identified are presented in **Fig. 6**.

Fig. 6(a) shows the maximum value of the volume fraction of GB is about 70%, which is observed at a temperature of 500 °C. **Fig. (6b)** presents two results separately; the fraction volume of the ferrite, which has a maximum value of 60% at a temperature of 615 °C

corresponding to the start of solidification of the weld sample, and the fraction volume of RA with a maximum value at 25% at 420 °C. **Fig. 6(c)** shows volume fraction of GB produced in S960QC, which peaks at around 60% at a temperature of 470 °C. **Fig. 5(d)** has two graphs, which show the respective volume fractions of ferrite and TMA. As found in previous data, the volume fraction of ferrite increases when the temperature is still high, at 58%, and decreases as it decreases. During the transformation, incomplete processing inside the austenite grain will translate into RA, which has a reduced temperature change to TMA, which is estimated to be 34% to its maximum value (400 °C).

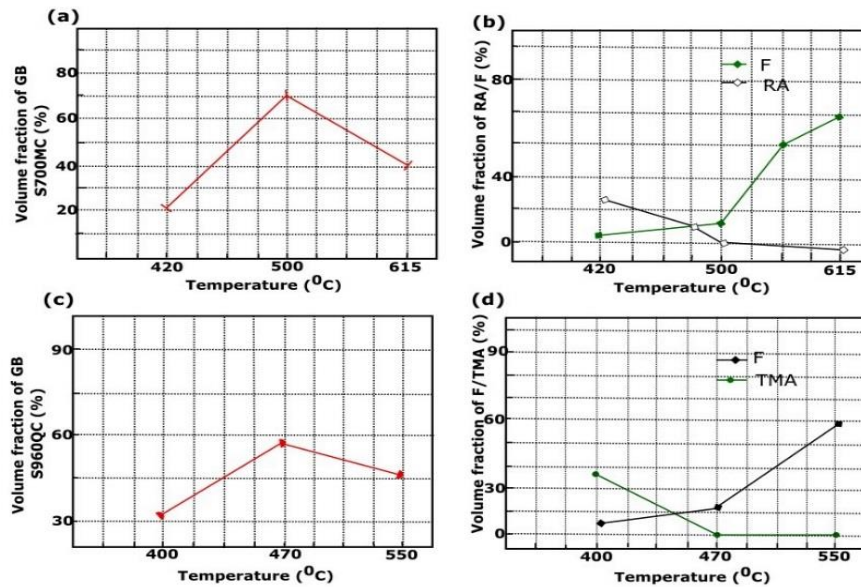


Fig. 6 Volume fraction of phase transformations in studied both materials: (a) volume fraction of GB of S700MC; (b) volume fraction of RA and F; (c) volume fraction of GB of S960QC; (d) volume fraction of TMA/F of S960QC

3.3 Precipitates in the welded sample using EDS Analysis

For analysis of the micro-alloy elements, EDS was applied to two sides of the weld. **Fig. 7** shows the mapping and spectra records for alloy elements in S700MC and **Fig. 8** the same information for S960QC. The EDS was calibrated at a voltage up to 15 kV with mapping at 20 kV, and the resolution of the image was 1024 by 768, with a

magnification of 2.5 μ m. The data was recorded in weight %, which presents the percentages of C transforms, Si, Cr, Mn, Fe, Ni, and Mo. **Tab. 3** shows the proportions of the weights of the micro-elements of alloys obtained. An absence of Ni, Mo in the microstructure of the S960QC can be seen, and an increase in the weight % of Mn. These three alloy elements play a significant role in the relation between the microstructure behavior and mechanical properties of the weld joint, particularly as regards the HAZ.

Element (%)	C	Si	Cr	Mn	Fe	Ni	Mo	%
S700MC (CGHAZ area)	3.3	0.6	0.5	1.6	92.2	1.3	0.4	100
S960QC (CGHAZ area)	3.4	0.3	0.1	1.8	94.2	-	-	

Tab. 3 Micro-alloy elements composition in both sides of the dissimilar welded joint (S700MC/S960QC)

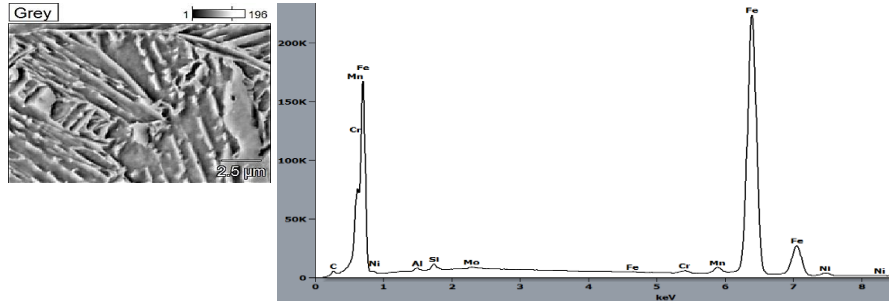


Fig. 7 EDS analysis of the composition of alloy elements in S700MC

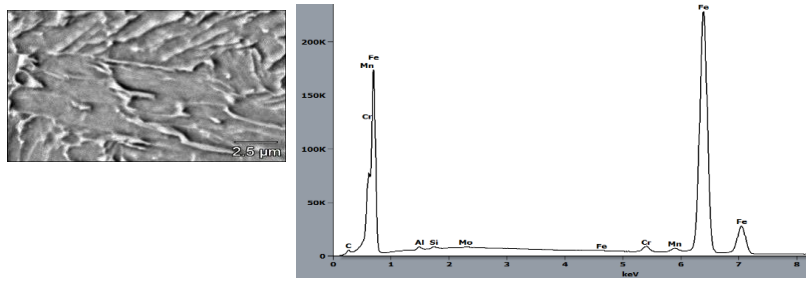


Fig. 8 EDS Analysis of the composition of alloy elements in S960QC

The respective weights of Mn, Ni, Mo obtained were 1.6, 1.3 and 0.4 for S700MC, and 1.8, 0, 0 for S960QC. The absence of Ni in the CGHAZ of S960QC can cause softening in this area even though there is a small increase in the weight % of Mn. As observed in the evaluation of the phase transformations, the rise in Mn promotes the appearance of martensite at the end of the transformation phase of S960QC. In the S700MC, the formation of alloy elements of Mn, Ni and Mo enable composition of upper bainite at 615 °C and TMA at 400 °C, as indicated in the previous results showing a high-volume fraction of GB (GB = 70%). This high value of GB resulting from the appearance of alloy elements is the source of softening in the CGHAZ, which was confirmed during the hardness analysis, and shows the link between the microstructure behavior of the weld joint and the mechanical behavior of the weld.

Equation 2 estimate the increasing of the strain zones of both materials, which lead to reinforced the precipitation strengthening (σ_p) in the area analyzed using EDS.

$$\rho_p = \frac{0.538Gb f_{GB}^{1/2}}{X} \ln\left(\frac{X}{2b}\right) \quad (2)$$

Where G indicates the modulus of elasticity (in MPa), b (mm) is the vector of **Jan burgers** [17], f_{GB} is the volume fraction of particle GB of both materials, and finally X is the precipitation diameter of the GB transformation into the austenite grain. After different evaluations, it is notice an increase in yield strength compared to the experimental values, which can be evaluated tensile test. The for example, the precipitation strengthening (ρ_p) obtained was 23.2 MPa for S700MC, and 27 MPa for S960QC respectively.

Conclusions

Phase evaluation of the transformation of bainite, ferrite, and martensite in the HAZ of a dissimilar weld joint of dissimilar high strength steels (S700MC/S960QC) welded with X96 filler material was carried out in this study. SEM and EDS analysis were used to identify the different phase transformations, quantify the volume fractions, and evaluate the composition of the alloy elements in the weld;

1. CCT diagrams indicated phase transformations in S700MC of ferrite from 670 °C to 615 °C and bainite from 615 °C to 500 °C.
2. In the case of S960QC steel, there is bainite transformation from 550 °C to 470 °C, and martensite from 470 °C to 400 °C.
3. SEM images confirmed the ascendancy of GB transformation for cooling time to 500 °C, allowing evaluation of the volume fraction of GB as 70% (500 °C), ferrite as 60% (615 °C) and RA of almost 23% at 420 °C.
4. In the austenite grain of the S960QC steel, there was development of GB with a high volume fraction of 70% at 470 °C, then some amount of ferrite cementite around and inside the austenite grain, evaluated as 40% at 550°C, which later transformed into TMA at 400 °C.
5. EDS analysis showed the absence of alloy elements such as Ni and Mo in the CGHAZ of S960QC, but their presence in the same area of the S700MC (1.3Ni, 0.4Mo). This finding confirms the correlation between the microstructural analyses suggesting softening in the HAZ and the mechanical behavior of the sample.
6. The noticeable presence of 1.3Ni, 0.4Mo, and 1.6Mn (S700MC) confirmed the temperature rise in the HAZ, as did the production of bainite with significant intrusion of ferrite and cementite.

The different compositions of alloy elements on different side of the dissimilar weld may produce different behaviors in the HAZ of the weld, for example, there may be an increase in toughness on the S960QC side caused by the absence of alloy elements such as Ni and Mo. It is essential to evaluate the amount of Mn found in the steel, in this case 1.8Mn, as increased strength can expose the weld to a higher risk of brittle fracture.

Acknowledgments

The authors gratefully acknowledge financial support from the Finnish Cultural Foundation (No. 190749), the EU project Energy-efficient systems based on Renewable Energy for Arctic Conditions (EFREA) (Grant number K51054).

Conflicts of Interest

The authors declare no conflicts of interest

References

- [1] Mvola B, Kah P, Martikainen Y, and Suoranta R **2015** *Reviews on Advanced Materials Science* **44**, pp. 146-159.
- [2] Njock B. F. Kah P, Mvola B. and Pavel L. **2019** *Review on Advanced Materials Science*, **58(1)**, pp. 38-49.
- [3] Pirinen M, Martikainen Y, Pavel L, Karkhin V. and Ivanov S **2015** *Welding International* **2**, pp. 14-17.
- [4] Gorka J. 2016 *Material and Technology* **50** pp. 617-621.
- [5] Yasar U. and Hamdullah C. **2015** *Advances in Structural Engineering and Mechanics (ASEM15)*, Incheon, Korea.
- [6] Lambert A, Drillet J, Gourgues F, Sturel T. and Pineau A. **2000** *Science and Technology of Welding and Joining* **5(3)**, pp. 168-173.
- [7] Siltanen J. and Tihinen S. **2012** *Journal. of Laser Applications*. doi.org/10.2351/1.5062489.
- [8] Kulakov M, Poole W. and Militzer M. **2014** *ISIJ International*, **54(11)** pp. 2627-2636.
- [9] Zajac S, Schwinn V. and Tacke H. **2005** *Materials Science Forum* 500-501 pp. 387-394.
- [10] Van Bohemen S.M.C, Sietsma J. **2010** *Materials Science and Engineering A* **527** pp. 6672-6676.
- [11] Mingxing Z, Guang X, Haijiang H, Qing Y. and Junyu T. **2017** *Steel Research International* **88(7)** pp. 1-7.
- [12] Seppälä O, Pohjonen A, Kaijalainen A, Larkiola J. and Porter D. **2018** *Procedia Manufacturing* **15**, pp. 1856-1863.
- [13] Gorka J. **2014** *Metals* **837** pp. 375-380.
- [14] Tasalloti H, Kah P, Martikainen J. **2017** *Material and Characterization* **123** pp. 29-41.
- [15] Navarro-Lopez A, Hidalgo J, Sietsma J. and Santofimia M. **2017** *Materials Characterization* **128** pp. 248-256.
- [16] Junyu T, Guang X, Mingxing Z. and Haijiang H. **2018** *Steel Research International* 1700469 pp. 1-10.
- [17] Shu Y, Xianghua L, Taosha L, Jingqi C. and Yang Z. **2019** *Steel Research International*, 1800257 pp. 1-10.

Publication V

Bayock, F., Kah, P., Salminen, A, Mvola, B., and Yang, X.
Feasibility study of welding dissimilar advanced and ultra-high strength steels

Reprinted with permission from
Rev. Adv. Mater. Sci.
Vol. 59(1), pp. 54-66, 2020
© 2020, DE GRUYTER

Research Article

Francois Njock Bayock*, Paul Kah, Antti Salminen, Mvola Belinga, and Xiaochen Yang

Feasibility study of welding dissimilar Advanced and Ultra High Strength Steels

<https://doi.org/10.1515/rams-2020-0006>

Received May 29, 2019; accepted Dec 11, 2019

Abstract: This study concerns the weldability of dissimilar Ultra high-strength steel (UHSS) and advanced high-strength steel (AHSS), which is used in the modern machine industry. The materials offered superior strength as well as relatively low weight, which reduces microstructure contamination during a live cycle. The choice of the welding process base of the base material (BM) and welding parameters is essential to improve the weld joint quality. S700MC/S960QC was welded using a gas metal arc welding (GMAW) process and overmatched filler wire, which was performed using three heat input (7, 10, and 15 kJ/cm). The weld samples were characterized by a Vickers-hardness test, scanning electron microscopy (SEM), and energy-dispersive X-ray spectroscopy (EDS). The test reveals a decrease of softening areas in the HAZ and the formation of the stable formation of Bainite-Ferrite for S700MC and Bainite-martensite for S960QC when the heat input of 10 kJ/cm is used. It is recommended to use the GMAW process and Laser welding (Laser beam-MIG), with an optimal welding parameter, which will be achieved a high quality of manufacturing products.

Keywords: UHSS, AHSS, welding processes, welding parameters, dissimilar weld joint, welding quality

1 Introduction

Nowadays, many industrial enterprises are starting to make greater use of high strength materials in the manufacturing of their products. A significant factor in driving the utilization of high strength materials is environmental concerns. The higher strength of such materials enables products of lower weight, for example, lighter automotive vehicle bodies and maritime vessel hulls. According to the energy conservation law, the lower body weight decreases the required kinetic energy transformed from the chemical energy of the burning of the fossil fuels used in the operation of such machines, therefore decreasing emissions of carbon dioxide [1–3]. Ultra-high strength steel is one of the groups of high strength materials suitable for machine manufacturing industries. Such steels are used in many different sectors like light cranes manufacturing, construction machines manufacturing, the automotive and vehicle industry, trucks, and vehicles, locomotive bodies, pipelines, ships, and other maritime vessels, aircraft, lightweight constructions, offshore constructions and highly loaded welded structures [4]. The global industry nowadays needs steel with low weight high-strength, which will increase their strength and their metallurgical properties. UHSS/AHSS was developed to be able to solve that problem and increase the quality of manufacturing products [5, 6].

In the literature, several different definitions have been presented for UHSS from the perspective of material strength:

1. The yield strength of the material is over 560 MPa;
2. The tensile strength of the material is over 700 MPa;
3. The yield strength of the material is 900 MPa and above;
4. The tensile strength of UHSS is up to 1700 MPa, especially for the martensitic steels [7–10].

Different definitions of UHSS exist, firstly, because of the novelty and rapid development of UHSS and, secondly, because of various researchers using different standards in different countries or industries. The term UHSS refers to the group of steel materials that have ultra-high-

***Corresponding Author: Francois Njock Bayock:** Laboratory of Welding Technology, Lappeenranta-Lahti University of Technology, P.O. Box 20, 53851, Lappeenranta, Finland; Email: Francois.Njock.Bayock@lut.fi

Paul Kah: Department of Engineering Science, University West, Gustava Melius gata 2 S-461 32 Trollhättan, Sweden

Antti Salminen: Department of Mechanical Engineering, University of Turku, FI-20014, Turku, Finland

Mvola Belinga, Xiaochen Yang: Laboratory of Welding Technology, Lappeenranta-Lahti University of Technology, P.O. Box 20, 53851, Lappeenranta, Finland

Open Access. © 2020 F. Njock Bayock et al., published by De Gruyter.



This work is licensed under the Creative Commons Attribution 4.0 License

strength, but the point at which material strength becomes ‘ultra-high’ is still under discussion in both industry and the research community. One standard definition defines steels with 210 to 550 MPa yield strength as “high strength steel” and other stronger types of steels as advanced high strength steel (AHSS). The term UHSS is then used for AHSS with tensile strengths exceeding 780 MPa. The AHSS is situated between HSS and UHSS, which differed with them by their alloy element composition and the production process.

The ultra-high-strength of UHSS is generated by the carefully defined chemical composition and the manufacturing methods used. The ultra-high-strength of the steels is achieved by employing precisely controlled amounts of common alloying elements like C, Mn, Si, Ni, Cr, and Mo and micro-alloying elements like Nb, Ti, V, B together with underlying metallurgical strengthening mechanisms. Such strengthening mechanisms are precipitation hardening, grain refinement, solid solution hardening, dislocation hardening, and transformation hardening. Usually, transformation hardening is the principal strengthening mechanism employed in manufacturing UHSS/AHSS in steel plant processes.

One area of interest is the so-called “third-generation steels” to link the gap of strength-elongation balance (both global and local) between conventional and UHS/AHS steels and austenitic-based steels. Other research concentrates on increasing processing methods for already-developed UHSS/AHSS materials. Many researchers see occasions for emerging new approaches to generate and form these brand-new steels, such as introduction heating procedures and advanced cooling techniques [6, 11–13]. In the research, some results were carried out in the prevention of carbide precipitation by investigated the optimal quenching temperature in the exceptional steel products such as sheet steel [14, 15]. On the product manufacturing side, stamping and cooling operations are being examined, as well as joining strategies and models for formability. The mechanical properties of base materials are also needed to well know, because of their implications in the formability and corrosion resistance.

The main problems encountered in the welding of UHSS/AHSS materials are softening and cracking. Figure 1 below shows the position of the UHSS and AHSS according to the ratio tensile strength and elongation. For the AHSS grade, the researchers evaluated the increase of the tensile strength, which reduced his elongation %. Idem for the UHSS that has an issue with the increase of the strength. The issues that those are faced now are to improve the mechanical properties of their weld joints, improve the weldability.

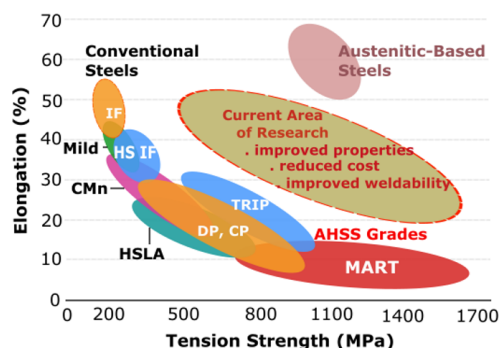


Figure 1: Strength distribution of different types of steels and the zone of the third generation of steels, an object of the current area of research [4, 7, 16].

The studies were conducted on the effect of welding parameters on the mechanical properties and microstructure formation of AHSS/UHSS steels. Their results were showing the implication of the welding parameters such as heat input, filler wire composition [16–18]. The research was also based on the effect of alloy element compositions, which has an effect on the strength of the weld joint [19–22]. The welding process, such as GMAW, Laser beam, Submerged arc welding, or Tungsten inert gas, has a standard parameter that influences the weld quality. The heat source data [12]. The weldability of UHSS/AHSS will depend on the welding parameter, which has an impact on their properties.

This paper aims to improve the weldability of dissimilar UHSS/AHSS. The study was evaluated the different UHSS/AHSS bases of the metallurgical production process and the chemical composition. The experimental method base of a Vickers-hardness test, the microstructure identification (SEM micrograph), and alloy element analysis (EDS X-ray mapping) on the HAZ were performed. The recommendation on the optimal welding process was set up to improve the strength and the microstructure formation on the weld joint.

2 Method and materials used to weld Category of UHSS/AHSS, Methods, and materials

The welding of UHSS and AHSS can be done base on many parameters such as the heat input parameters, the base material chemical characteristics and mechanical proper-

ties, filler wire characteristics for some welding process. By analyzing the differences between UHSS and AHSS will be set up according to their manufacturing, mechanical properties, and chemical composition. The improvement of the weld quality of UHSS/AHSS welded also depend on the mechanical properties and microstructure behavior were investigated. Knowing the mechanical properties of the base materials, the control of the welding process will lead to optimizing the strength of the weld joint by the reduction softening on the HAZ.

The classification of different UHSS/AHSS steels can be based on the Thermo metallurgical production process. The Transformation Induced Plasticity steel (TRIP), which is the formation of ferrite (F), Martensite (M), Bainite (B), and some retained of austenite (RA) at the end of the transformation. Figure 1a below shows the microstructure of TRIP- steel, which, when his temperature increases, the cooling process can be the result of more Ferrite causing at the end of the transformation, the formation of more carbide [20, 23]. The twinning induced plasticity steel (TWIP) is a steel that has a large amount of manganese (Mn) content. This alloy element has the particularity to increase the strength at the high temperature, causing a crack propagation in the HAZ of the weld joint. In TWIP-steel, the microstructure is based on his high amount of martensite and ferrite. The development of this amount causes some soft ferrite matrix (Figure 1b). It is also observed a hard bloc of martensite on the austenite grain. Figure 1c shows the microstructure of Dual phases (DP) steel. The composition of DP-steel is the base of ferrite and martensite formation.

The formation of hard martensite increases the strength of the material. The excellent ductility of the material is giving by the formation of the ferrite matrix. This type of UHSS can be hot or cold -formed and have a high hardening behavior, which should be carefully controlled to produce Ferritic-martensitic structure from the austenite grain.

Figure 1d below illustrates the microstructure of CP-steel. In the microstructure, the formation of granular bainite ferrite (GBF), and Martensite in the austenite grain are observed. His complexity is caused by the extreme refinement grain that created the retarded a precipitation of micro-alloy elements like Titanium (Ti) and Niobium (Nb). It has a high energy absorption, high residual stress, and excellent thermal expansion. Martensitic steel (MS) is illustrated in Figure 1e. The formation of tempered martensite gives the ultra-strength to the material. The composition of more tempered martensite is found in the austenite grain, which gave an ultra-strength in the material. Depending on the thermal process, it can be found some trace of ferrite and bainite in the microstructure. UHSS

and AHSS can exist as Ferrite-Bainite steel (FB), which can be described as fine ferrite matrix and fine second phase bainite. The bainite-ferrite (FB) steel is the composition of Bainite- ferrite formation in his microstructure.

Base on the description of the production of UHSS and AHSS, the welding dissimilar AHSS of S700MC with UHSS of S960QC was done. The welding was carried out using an overmatched filler wire in order to evaluate the influence of heat input in the softening area of the HAZ. The experiments were performed using the GMAW process, which followed by the microstructure formation at the starting Bainite and Martensite formation using SEM and EDS-X ray spectroscopy mapping. The mechanical tests were performed using Vickers-hardness tests and tensile tests. Table 1 below presents the chemical and mechanical properties of the materials used in this analysis. The welded specimens were welded with dimensions of $300 \times 200 \times 8 \text{ mm}^2$ using V-groove butt joint, 60° of angle, and 2 mm of a gap. The samples were welded using the overmatched filler wire with 1 mm of diameter. Table 2 below shows the welding parameters, which presents the shielding gas that was used in this analysis with a flow rate of 16 L/min. The welding process was conducted using a two-pass welds.

3 Results and discussions

3.1 Welding dissimilar UHSS/AHSS

In manufacturing, welding is the most important process, which allows having to finish products. Joining UHSS/AHSS using the GMAW process has one of the welding processes that can improve the strength in the HAZ area of the weld joint. Figure 2 below shows the macro picture showing the welded samples using GMAW with overmatched filler wire, which must increase the strength of the weld metal. Using the heat input of 7 kJ/cm, the geometry of the weld metal is small compared to those samples. Because of the low heat input, the temperature maximum in the melting zone is 1140°C . When it is applied, the respective heat input of 10 kJ/cm and 15 kJ/cm, and the maximum temperature reaches respectively 1400 and 1700°C . The mechanical properties and microstructures of the welded joints being strongly affected by the characteristics of the welding processes employed. The input behavior using a different form of welding process on the structure of the weld joint of UHSS/AHSS is a critical task. From the available investigations, the result of the temperature max has modified welding outcomes for specific UHSS/AHSS materials.

Table 1: AHSS/UHSS chemical composition and mechanical properties using overmatched filler wire.

Chemical composition, wt. %.																
Materials	C	Si	Mn	Al	B	Nb	Ti	V	Cu	Cr	Ni	Mo	N	P	S	CE
S700MC	0.056	0.16	1.18	0.027	0.002	0.044	0.12	0.006	0.02	0.062	0.066	0.0150	0.005	0.01	0.005	0.38
S960QC	0.09	0.21	1.05	0.03	0.002	0.003	0.032	0.008	0.025	0.82	0.04	0.04	-	0.01	0.004	0.49
Filler material	0.08	0.60	1.40	-	-	-	0.05	-	≤ 0.30	0.30	2.50	0.45	-	-	-	0.45

Mechanical properties			
Materials	Yield strength, MPa	Tensile strength, MPa	Elongation A ₅ , %
S700MC	768	822	12
S960QC	960	1000	18
Filler material	780	830	≥ 17

Hardness HV5	
	280
	320
	270

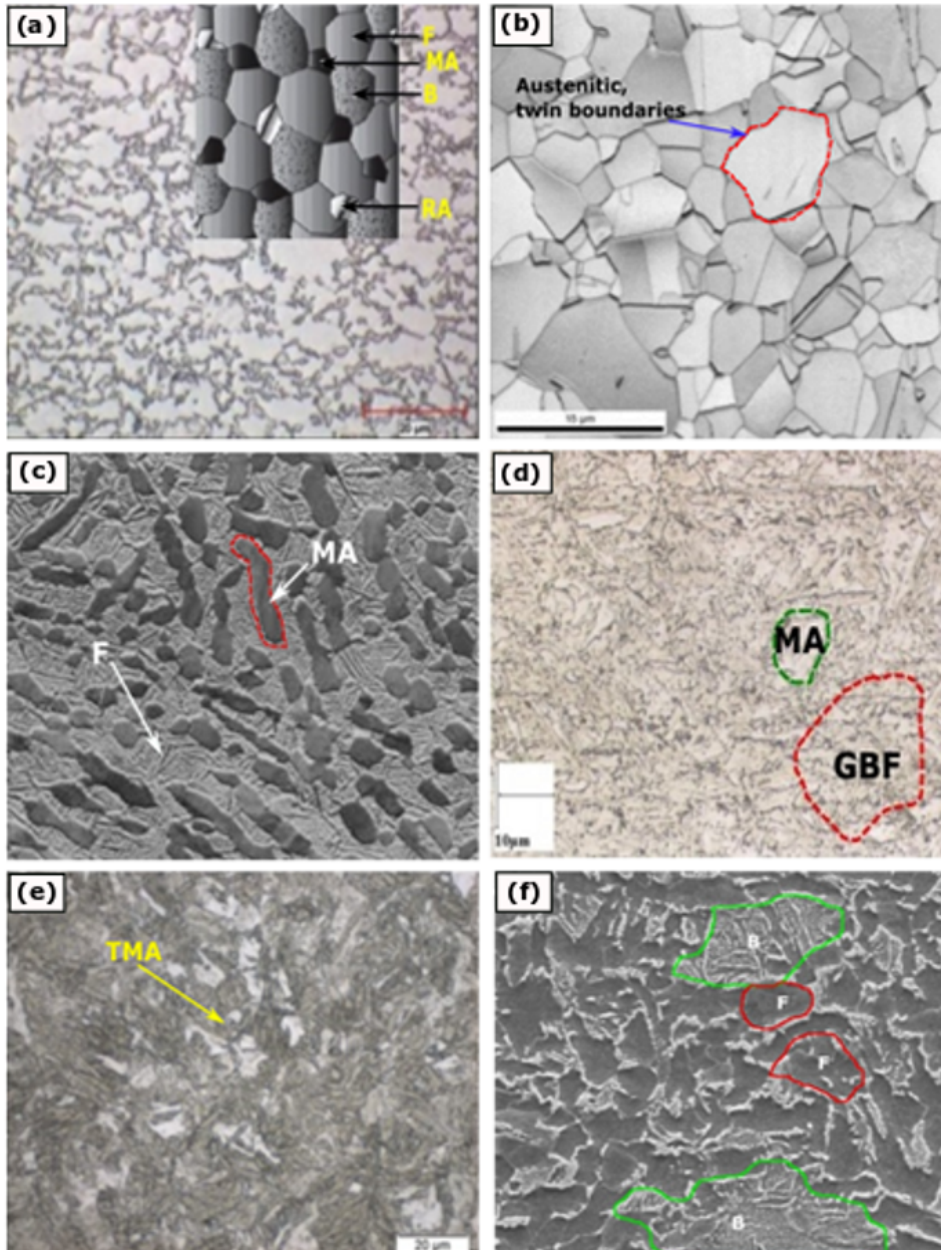


Figure 2: Microstructure UHSS and AHSS; (a) microstructure of TRIP 690 steel, (b) microstructure of TWIP steel, (c) microstructure of DP steel, (d) microstructure of CP 800/1000 steel, (e) microstructure of MS 950/1200 steel, and (f) The microstructure of FB 450/600 steel [16, 21].

Table 2: AHSS/UHSS Welding conditions

Welded samples	P1				P2			
	[A]	[V]	s [cm/min]	Q [kJ/cm]	[A]	[V]	s [cm/min]	Q [kJ/cm]
S1	215	25.3	60.2	7	208	26.7	60.2	7
S2	215	25.3	60.2	7	206	26.7	40	10
S3	211	25.3	60.2	7	211	26.7	30	15

The two significant factors that affect product quality in welded dissimilar UHSS/AHSS materials are softening and a tendency to crack propagations in the heat-affected zone (HAZ). The source of those issues is the heat input and the filler wire composition [24, 25]. Softening of the welded joint has undesirable effects such as:

- A decrease in strength compared to the base material, especially tensile strength;
- The hardness of the HAZ falling below that of the base material;
- A reduction in the fatigue strength of the material [26–28].

The experimental analysis made in this study showed the Vickers-hardness behavior of dissimilar joints of S700MC-S960QC- steels. Figure 2 below shows the results of tree samples using the different heat input parameters defined above. From Figure 2a, using the heat input of 7 kJ/cm, the most softening areas were in the FGHAZ of S960QC and S700MC. The weld metal area was the area that had a high average value of hardness (420 HV5). The lowest average hardness of the S960QC was 255 HV5, which was 19% lowest than the BM. In the S700MC side, the hardness average was evaluated at 210 HV5, which was 16% lowest than the BM. Using the heat input of 10 kJ/cm, Figure 2b below shows the hardness behavior in the weld joint, which was observed the decrease of its values in the CGHAZ of both sides of the HAZ and increased in the WM area. The lowest average value was observed in the SGHAZ of S700MC, which was 220 HV5 lowest than the BM. For the S960QC side, it was observed a relative change of the hardness values, which was increased a bit than the previous sample. The average value measured was 280 HV5, which was the reduction of 15% lowest than the BM. Figure 2c shows the hardness profile using the heat input of 15 kJ/cm. The results show the impact of the welding process in the HAZ and WM, which produced a softening area across the weld joint. The average hardness in the WM was 380 HV5, a bit highest than his initial value. The lowest average hardness was obtained in the FGHAZ of both sides of

the material, which was evaluated at 259 HV5 for S960QC and 220 HV5 for S700MC.

From this analysis, it is observed that the softening area at the edge of the HAZ area using the different heat input values. This experiment illustrates why the avoidance of material softening has become a significant area of study in welding research on dissimilar UHSS/AHSS. One of the reasons having to soften in the HAZ when weld UHSS/AHSS is the welding process, which links between the heat input parameters, the filler wire compositions (GMAW) [23, 29]. It can be added to the production process of the BM and the geometry of the weld joint. From the welding process, it is important to analyze the cooling process of the welded joint, which has an impact on the hardening behavior and the strength of the weld joint. The cooling process, which can be slow or rapid, can affect the strength of the weld joint. From the experimental analysis, when using the heat input of 7 kJ/cm, the cooling time results were 11.2 s. Using the heat input of 10 kJ/cm, the cooling time was 27.84 s and using the heat input of 15 kJ/cm, and the cooling time was 45.48 s. Having different cooling times, it is evident that the strength and the microstructure precipitation affect the welding process compare to the BM.

Figure 3 below shows the microstructure formation in the different areas of the HAZ of a dissimilar weld joint of S700MC/S960QC-steels. The images were performed using the SEM images with a resolution of 20 μm . The images were taken in the FGHAZ, CGHAZ of both parts of materials, and in the WM. The sample showing in this microstructure analysis was welded using the heat input of 10 kJ/cm, which had relatively good results when analyzed a hardness previously. The formation of martensite (M) and bainite (B) was observed in the FGHAZ of S700MC-steel (Figure 3a). From this microstructure formations, it was added some retained austenite (RA) formations due to incomplete transformations. In the S960QC side, the formation of tempered martensite (TMA) and bainite (B) were observed in his FGHAZ (Figure 3b). In the CGHAZ, the temperature can reach 900°C, and it was created some microstructure precipitation and micro strengthening ar-

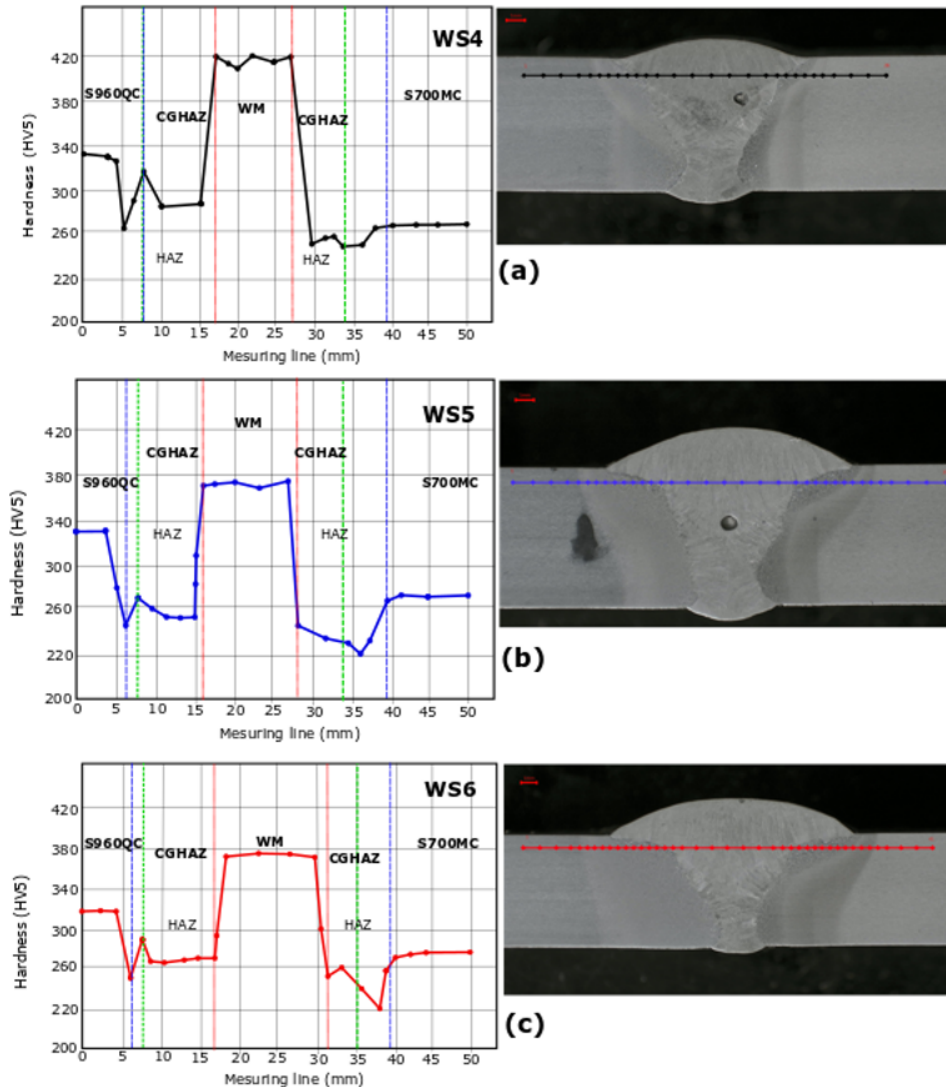


Figure 3: Vickers- hardness profile using overmatched filler wire in the weld joint: (a) hardness profile of weld sample using 7 kJ/cm of heat input, (b) hardness profile of weld sample using 10 kJ/cm of heat input, (c) hardness profile of weld sample using 15 kJ/cm of heat input.

eas. The micro strengthening formations in the microstructure was caused a formation of some Cementite across the grain boundaries of both materials. The Formation of B and RA were observed on the microstructure of S700MC steel (Figure 3c). From this microstructure was added some fine ferrite (F) formation due to the austenite temperature propagation in the austenite grain. Figure 3d below shows

the formation of B and some trace of F in the CGHAZ microstructure of S960QC-steel. The formation of F results by the most affected area by the thermal shock produced during the welding process. The microstructure was composed mostly of the filler wire chemical composition, in the melting zone. The microstructure formation was com-

posed of an Acicular ferrite (AF), and Widmanstätten ferrite (WF) (Figure 3e).

Applying welding operations to dissimilar UHSS/AHSS steels requires careful compliance with the welding procedure. The welding procedure is the procedure that includes the selection of welding parameters according to the mechanical characteristics. The chemical composition of a base material (carbon capacity in weight %, Mn, Ti, Ni, Al, B) has to be known when welding a sample. In this experiment, it was essential to evaluate the alloy element content in the HAZ of both materials, which participated in improving the strength of the weld joint. By applying the EDS X-ray spectrum mapping, the microstructure of the CGHAZ of both materials was analyzed. The results observed the proportion of weight % of micro-elements such as carbon (C), chromium (Cr), Manganese (Mn), Nickel (Ni), Molybdenum (Mo), Niobium (Nb), Silicon (Si), Vanadium (V). Figure 4a shows the EDS mapping, which observed the composition of 3.6C, 0.7Si, 0.5Cr, 1.7Mn, 1.6Ni, and Mo in the microstructure formation of the WM during the transformation. The increase of the carbon content, Mn, and Ni than their BM weight % content can be the reason that the increase of the hardness was observed above. The respective weights of Mn, Mo, Si, and Cr obtained were 1, 0.2, 0.2, and 1.2 for S700MC (Figure 4b) and 2, 0, 0.4, and 0 for S960QC (Figure 4c). The absence of Ni was observed, which has an impact on the strengthening of the weld joint.

3.2 Welding parameters on UHSS/AHSS for different processes

Welding dissimilar UHSS/AHSS is a big challenge that requires several methods to consider, which will lead to improving the microstructure and mechanical properties of the weld joint. It is essential to note that their microstructures change as a result of welding operations (welding parameters), which has an impact directly on the crack formation in the weld joint. To improve the quality of the weld joint when weld dissimilar UHSS/AHSS, the heat input values, welding geometry, filler wire composition, and the cooling rate are the most critical parameters to be controlled during the welding process. The cooling rate is reliant on many considerations: heat input value, cooling time itself, preheat temperature, a filler wire composition, process efficiency, material properties, and material geometric characteristics. Appropriate and effective control of multiple parameters and variables of the welding processes is required to control the heat input.

Power density is one crucial parameter closely linked to the heat input during the welding processes. In arc welding, the power density at the cross-section of the weldment normal to the welding direction for an arc moving at speed v is given by [14]:

$$q(x, t) = \frac{3IEf_1}{\pi\bar{r}^2} \exp\left\{-3\left(\frac{x}{\bar{r}}\right)^2\right\} \exp\left\{-3\left(\frac{vt_{8/5}}{\bar{r}}\right)^2\right\}$$

Where:

x – distance from the center of the heat source on the weldment surface in the cross-section;

$t_{8/5}$ – cooling time during the welding process;

I – welding current, (A);

E – welding arc voltage (V);

f_1 – arc efficiency (%);

\bar{r} – a characteristic radial dimensional distribution parameter that defines the region in which 95% of the heat-flux is deposited [21, 24].

From the equation, the current and voltage are proportional to the power density, and the traveling speed is inversely proportional to the power density. The two values x and t also meet the real situation, which is that the power density will decrease over time and with distance from the heat source to the weldment material. This equation can be applied to weld dissimilar UHSS/AHSS as well as conventional steel materials.

UHSS/AHSS steels require special attention when applying any welding procedure. The application of conventional or hybrid-electric arc welding can be used as in the case of mild steels, which combines MIG, MAG, TIG, or plasma. They are reputed to have good weldability better than for mild steel. The recurrent problem that recalls when welding this type of dissimilar steel is the application of the heat input parameters (current, voltage, heat input). The filler wire also needs to be analyzed when welding UHSS/AHSS for some welding process. The current polarity (AC and DC) will have to consider the ratios of lower or upper thickness to 2:1, which are considered very sensitive to welding operations. It is imperative to analyze the relationship that will have to exist in welding parameters and welding operations [20, 25, 27, 29]. The welding process using pulsion current recommends a specific filler wire resistance of 482 MPa. The use of this type of filler wire will optimize the current effect on the structure of the weld joint by effecting his strength and fatigue behavior. The electric resistance weld (ERW) can be used to weld dissimilar UHSS/AHSS. The only issue that has the ERW weld process his lowest input current compared to other welding processes. Depending on the chemical composition of the base materials, this current intensity can be even low-

Table 3: Comparison of different welding processes used with UHSS.

Process	SAW	MIG/MAG	Laser	ERW	TIG
Heat Input	easy	easy	Need accurate inspection, operation, and preparation	Need proper preparation	Need to be controlled
Cooling Rate	low	high	low	low	high
HAZ	controlled	controlled	controlled	/	controlled
Joint Preparation	Small HAZ, and low softening	Wide-ranging HAZ, and high softening	Slight HAZ, and little softening	/	Wide HAZ, and High softening
	/	Good strength and mechanical properties	Excellent strength and mechanical properties, bending properties may vary	/	Excellent strength and mechanical properties

Table 4: Different welding processes using different UHSS/AHSS materials.

SAW	MIG/MAG	Laser	ERW	TIG
TRIP	/	Weldability is good	Yttrium-aluminum-garnet laser for TRIP780 is good	+ electrode force, time, weld size, tip diameter, tightly controlled
TWIP	/	Weldability is good	/	+ electrode force, time, weld size, tip diameter
MS	/	Weldability is good	/	+ electrode force, time, weld size, tip diameter
DP	/	Good weldability for HAZ softening	MIG/MAG, Excellent weldability, low heat input	+ electrode force, time, weld size, tip diameter
CP	/	Weldability is good	/	+ electrode force, time, weld size, tip diameter
FB	Weldability is good	Weldability is good	Weldability is good	+ electrode force, time, weld size, tip diameter
QT	Weldability is good	Weldability is good	Weldability is good	+ electrode force, time, weld size, tip diameter
TMCP	Weldability is good	Weldability is good	Weldability is good	+ electrode force, time, weld size, tip diameter

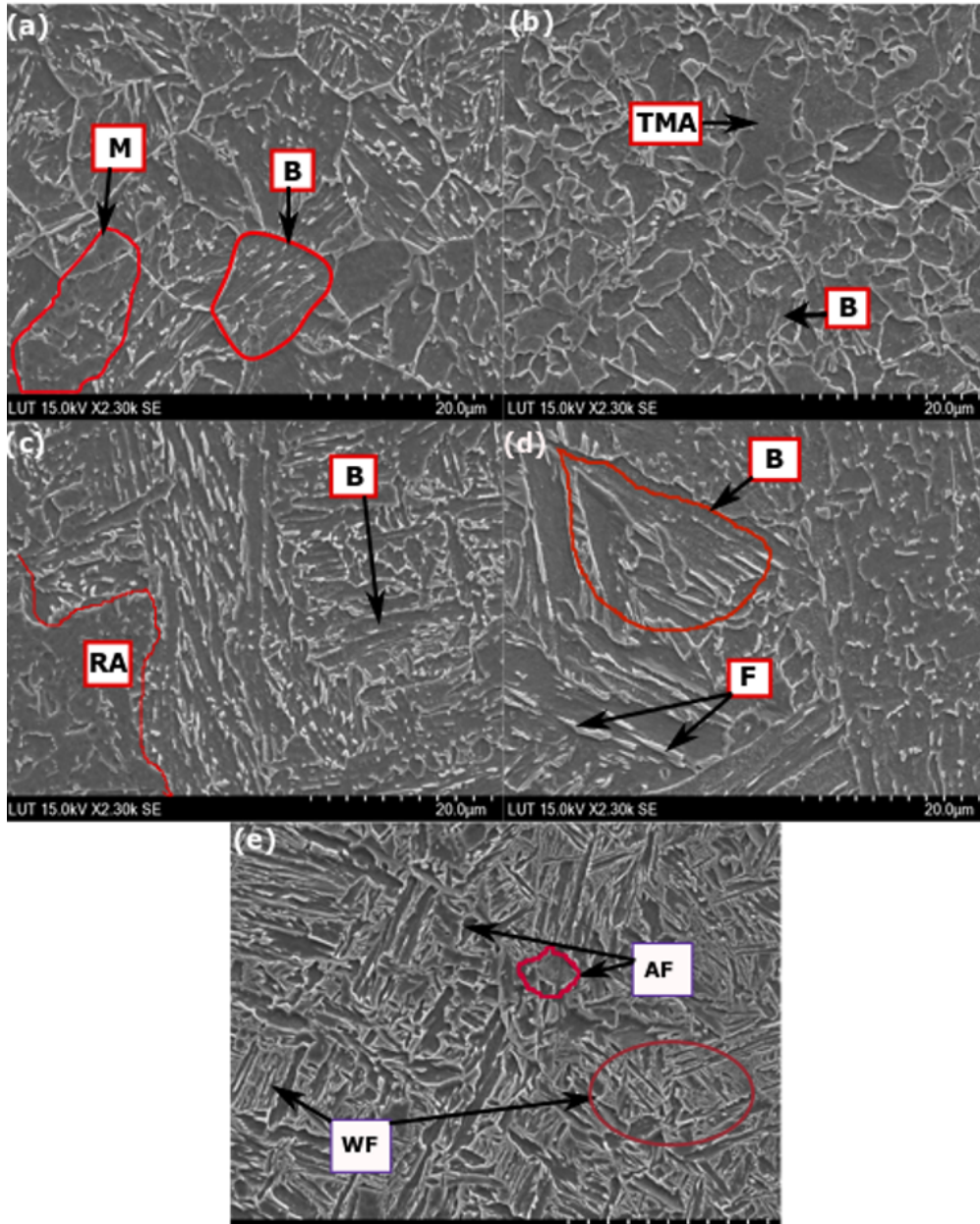


Figure 4: SEM micrograph, showing the microstructure of dissimilar S700MC/S960QC weld joint using overmatched filler wire: (a) FGHAZ of S700MC, (b) FGHAZ of S960QC, (c) CGHAZ of S700MC, (d) CGHAZ of S960QC, and WM.

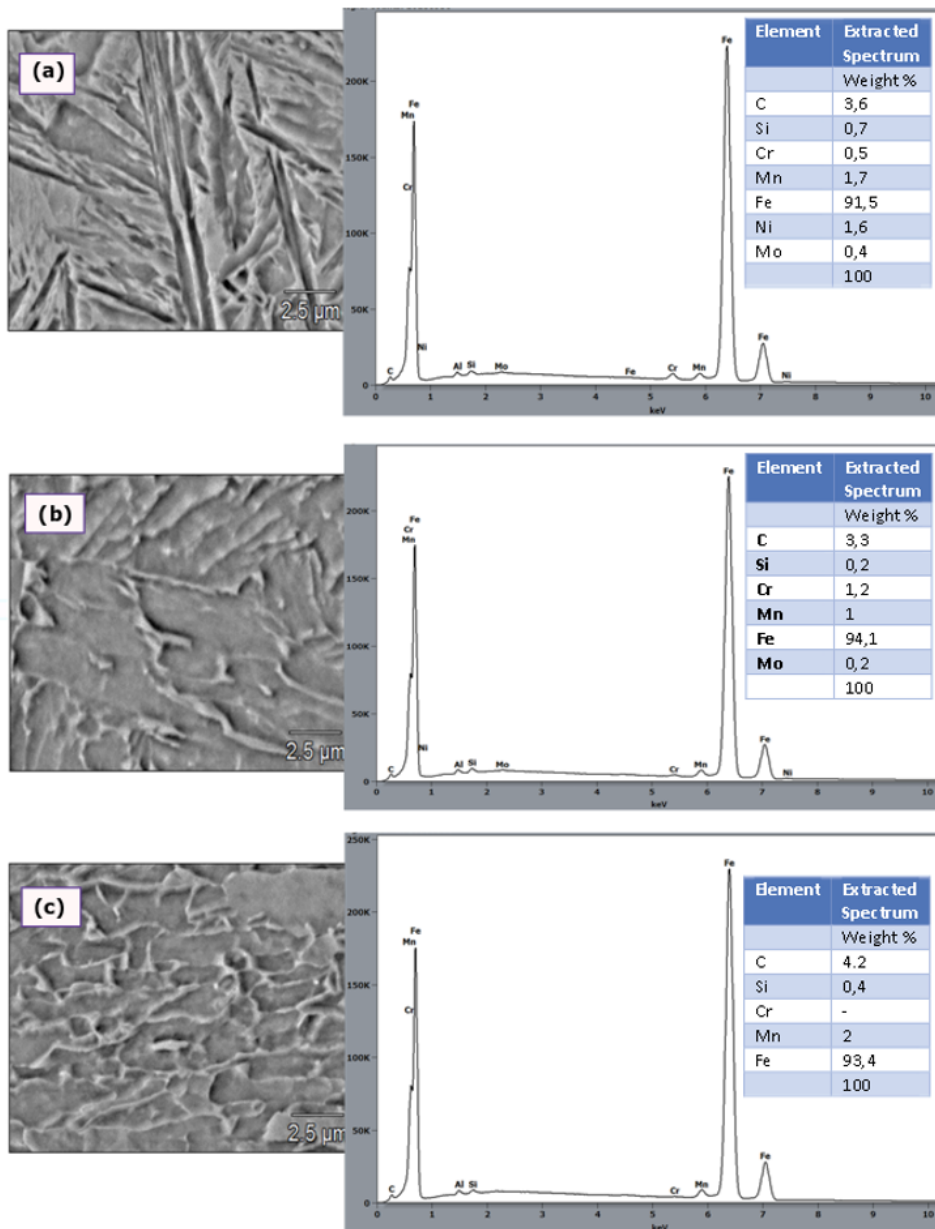


Figure 5: EDS X-ray mapping showing the alloy element composition: (a) WM mapping using overmatched filler wire, (b) CGHAZ of S700MC, (c) CGHAZ of S960QC.

ered. The following instructions shall be applied for welding of steels of type QT, TRIP, CP, FB, TWIP, and MS [19, 29]:

- Adjust the welding time according to the mechanical parameters and the chemical composition of the BM;
- Adjust weld size;
- The mechanical characteristics (yield strength, tensile yield strength) shall be in accord with the electrode forces;
- Adjust the electrode type with the largest possible diameter, as appropriate;
- Adjust the geometric characteristics of the weld joint with the welding time

Currently, there is a lack of systematic theoretical research and practical experimental work on welding methods for dissimilar UHSS/AHSS. The benefits from the use of such steels, a better understanding of their behavior is required. Moreover, the advantages of and complications involved with the welding dissimilar UHSS/AHSS are becoming more evident, listed in Table 1. Table 1 below shows a comparative analysis of the influence of the welding process on the weldability of dissimilar UHSS/AHSS. The results show a good behavior of dissimilar UHSS/AHSS when applied Laser welding process. It can be better to associate, for example, MIG welding with Laser welding, which will optimize the microstructure precipitation and the strength of the weld joint. Welding UHSS/AHSS using the Laser process will consider all those parameters that were cited above to produce an excellent strength minimizing softening in the HAZ. To preconize a welding process function of the type of material, Table 2 below presents the type of materials that can be welded using a different welding process. It is recommended to apply the MIG/MAG welding process to weld a material such as TRIP, TWIP, MS, DP, CP, FB, QT, and TMCP steel, which have a good result. From Table 2, it can be seen, based on current knowledge, that the most suitable welding process for UHSS/AHSS is resistance welding. However, data for some welding processes is lacking, indicated with the mark ‘/’ in the table. Robotic MIG welding of QT (S960QC) and TMCP (S700MC) materials were tested in the Welding Laboratory of Lappeenranta-Lahti University of Technology, and as was seen above, the evaluations from Hardness and microstructure (SEM, EDS). The analysis has shown excellent results when the excellent choice has operated in the welding parameters and filler wire composition.

4 Conclusions

In this study, the weldability of dissimilar UHSS/AHSS was analyzed, and experimental methods were performed using three heat input parameters and overmatched filler wire. The Hardness tests, SEM scanning test, and EDS X-ray spectrum mapping were carried out in order to observe the hardness behavior and the microstructure precipitations in the HAZ of the weld joints. The paper presents some recommendations that need to be considering, which found that;

- The increase of the heat input (15 kJ/cm) when welded dissimilar UHSS/AHSS results in the formation of more carbide in the austenite grain. The softening area will increase in the HSZ;
- The quantitative relationship was established between the heat input, the hardness, and the microstructure precipitation in the HAZ. Two significant problems have been recognized as regards welding processes the UHSS/AHSS materials: cold cracking and material softening near the HAZ. Precise and accurate control of heat input during the welding process is required;
- Welding dissimilar UHSS/AHSS using overmatched filler wire produces an increase of hardness in the WM area. His increase can optimize the strength of the weld joint when the ideal heat input is applied;
- The use of GMAW process with 10 kJ/cm as heat input value produces an equilibrium microstructure formation in the HAZ. This heat input develops a formation of Bainite-ferrite in the S700MC side and Bainite-Martensite in the S960QC side. This microstructure formation favorites to optimize the strength of the weld joint and avoid cracks propagation;
- Based on the equation of power density, welding parameters like arc voltage, welding current, and traveling speed affect the heat input of the welding joint. The power density equation illustrates that to ensure appropriate heat input, the welding parameters should be designed and tested before utilization of welding processes for UHSS/AHSS materials;
- As regards the different types of UHSS/AHSS materials used in production, it is noted that ferrite-bainite (FB) steel material has the best weldability. In industry, MIG/MAG and laser welding are the most common methods used, and UHSS/AHSS materials have shown good weldability with such processes;

Acknowledgement: The authors would like to thank the Finnish Cultural Foundation (Grant number 190749) for his financial support.

References

- [1] Mvola, B., P. Kah, J. Martikainen, and R. Suoranta. Dissimilar Weld joints operating in sub-zero Temperature environment. *Reviews on Advanced Materials Science*, Vol. 44, 2016, pp. 146–159.
- [2] Bayock, F. N., P. Kah, B. Mvola, and P. Layus. Experimental review of thermal analysis of dissimilar welds of High-Strength Steel. *Reviews on Advanced Materials Science*, Vol. 58, No. 1, 2019, pp. 38–49.
- [3] Hall, M. Introduction today's Ultra high-strength structural steels. *American Society for Testing and Materials*, Vol. 498, 1971.
- [4] SFS-EN ISO 5817, Welding-Fusion-weld joints in steel, nickel, titanium and their alloys. Brussels: *European Committee for Standardization (CEN)*, 2006, pp. 25.
- [5] Bjork, T., J. Toivonen, and T. Nykänen. Capacity of Fillet Welded Joints Made of Ultra High-Strength Steel. *Welding in the World*, Vol. 56, No. 3-4, 2012, pp. 71–84.
- [6] Larsson, J. K., J. Lundgren, E. Asbjörnsson, and H. Andersson. Extensive Introduction of Ultra High Strength Steels Sets New Standards for Welding in the Body Shop. *Welding in the World*, Vol. 53, No. 5-6, 2009, pp. 4–14.
- [7] Rodrigues, D. M., L. F. Menezes, and A. Loureiro. The influence of the HAZ softening on the mechanical behaviour of welded joints containing cracks in the weld metal. *Engineering Fracture Mechanics*, Vol. 71, No. 14, 2004, pp. 2053–2064.
- [8] Weber, G., H. Thommes, H. Gaul, O. Hahn, and M. Rethmeier. Resistance spot welding and weldbonding of advanced high strength steels. *Widerstandspunktschweißen und Punktschweißkleben von weiterentwickelten hochfesten Stählen. Materialwissenschaft und Werkstofftechnik*, Vol. 41, No. 11, 2010, pp. 931–939.
- [9] Mvola, B., P. Kah, J. Martikainen, and R. Suoranta. State of the art of advanced gas metal arc welding process: Dissimilar metal welding. *Journal of Engineering Manufacture*, Vol. 229, 2015, pp. 1694–1710.
- [10] Bayock, F. N., P. Kah, P. Layus, and V. Karkhin. Numerical and Experimental Investigation of the heat input effect on the mechanical properties and microstructure of dissimilar weld joint of 690-MPa QT and TMCP steel, *Metals*, Vol. 9, No 355, 2019, pp. 1–19.
- [11] Radjaj, D. Heat Effects of Welding, *Springer*, Berlin, Germany, 1992.
- [12] Fiedman, E. Thermo-mechanical analysis of the welding process using the finite element method. *Journal of Pressure Vessel Technology*, Vol. 97, No. 3, 1975, pp. 206–221.
- [13] Siltanen, J., S. Tihinen. Position welding of 960 MPa ultra-highstrength steel. *Journal of Laser Applications*, Vol. 464, 2018, pp. 1–13.
- [14] Liu, X., S. Lan, and J. Ni. Experimental Investigation on Joining Dissimilar Aluminum Alloy 6061 to TRIP 780/800 Steel Through Friction Stir Welding. *Journal of Engineering Materials and Technology*, Vol. 137, No. 4, 2015, pp. 11–21.
- [15] Kah, P., M. Pirinen, R. Suoranta, and J. Martikainen. Welding of Ultra High Strength Steels. *Advanced Materials Research*, Vol. 849, 2014, pp. 357–365.
- [16] Weber, G., and S. Goklu. Resistance Spot Welding of Uncoated and Zinc Coated Advanced High-Strength Steels (AHSS) - Weldability and Process Reliability-Influence of Welding Parameters. *Welding in the World*, Vol. 50, No. 3-4, 2006, pp. 23–32.
- [17] Smith, S., J. Uijl, T. Okada. The Effect of Ageing on the Spot Weld Strength of AHSS and the Consequences for Testing Procedures. *Welding in the World*, Vol. 54, No. 1-2, 2010, pp. 50–59.
- [18] Correard, G., G. P. Miranda, and F. Lima. Development of laser beam welding of advanced high-strength steels. *International Journal of Advanced Manufacturing Technology*, Vol. 83, No. 9-12, 2016, pp. 1967–1977.
- [19] Grajcar, A., M. Rozanski, S. Stano, and A. Kowalski. Microstructure Characterization of Laser-Welded Nb-Microalloyed Silicon-Aluminum TRIP Steel. *Journal of Materials Engineering and Performance*, Vol. 23, No. 9, 2014, pp. 3400–3406.
- [20] Bandyopadhyay, K., S. K. Panda, and P. Saha. Optimization of Fiber Laser Welding of DP980 Steels Using RSM to Improve Weld Properties for Formability. *Journal of Materials Engineering and Performance*, Vol. 25, No. 6, 2016, pp. 2462–2477.
- [21] Han, T., B. Park, and C. Kang. Hardening characteristics of CO₂ laser welds in advanced high strength steel. *Metals and Materials International*, Vol. 18, No. 3, 2012, pp. 473–479.
- [22] Saunders, N., Miles, M., Hartman, T., Hovanski, Y., Hong, S., and Steel, R. Joint strength in high speed friction stir spot welded DP 980 steel. *International Journal of Precision Engineering and Manufacturing*, Vol. 15, No. 5, 2014, pp. 841–848.
- [23] Bayock, F. N., P. Kah, B. Mvola, and P. Layus. Effect of heat input and undermatched filler wire on the microstructure and mechanical properties of dissimilar S700MC/S960QC highstrength Steels. *Metals*, Vol. 9, No 883, 2019, pp. 1–20.
- [24] Hamada, M. Control of strength and toughness at the heat affected zone. *Welding International*, Vol. 17, 2003, pp. 265–270.
- [25] Guo, W., L. Lin, D. Crowther, S. Dong, F. John, and A. Thompson. Laser welding of high strength steels (S960 and S700) with medium thickness. *Journal of Laser Applications*, Vol. 28, No. 2, 2016, pp. 022425-1, 022425-10.
- [26] Gorka, J. Assessment of Steel Subjected to the Thermomechanical Control Process with Respect to Weldability. *Metals*, Vol. 8, 2018, pp. 1–15.
- [27] Ito, R., K. Hiraoka, and C. Shiga. Characteristics of the heat-affected zone in ultra-fine grained steel during ultranarrow gap GMA welding. Softening zone and micro structures of the heat-affected zone in ultra-fine grained steels. *Welding International*, Vol. 19, No. 105, 2005, pp. 447–455.
- [28] Mazel, Yu. A., and Polishchuk, G. Increasing the wear resistance of components strengthened by surfacing. *Welding International*, Vol. 21, No. 5, 2007, pp. 387–390.
- [29] Fang, F., Q. Yong, C. Yang, and H. Su. Microstructure and precipitation behavior in HAZ of V and Ti microalloyed steel. *Journal of Iron and Steel Research International*, Vol. 16, No. 3, 2009, pp. 68–72.

ACTA UNIVERSITATIS LAPPEENRANTAENSIS

- 873. EGOROV, DMITRY. Ferrite permanent magnet hysteresis loss in rotating electrical machinery. 2019. Diss.
- 874. PALMER, CAROLIN. Psychological aspects of entrepreneurship – How personality and cognitive abilities influence leadership. 2019. Diss.
- 875. TALÁSEK, TOMÁS. The linguistic approximation of fuzzy models outputs. 2019. Diss.
- 876. LAHDENPERÄ, ESKO. Mass transfer modeling in slow-release dissolution and in reactive extraction using experimental verification. 2019. Diss.
- 877. GRÜNENWALD, STEFAN. High power fiber laser welding of thick section materials - Process performance and weld properties. 2019. Diss.
- 878. NARAYANAN, ARUN. Renewable-energy-based single and community microgrids integrated with electricity markets. 2019. Diss.
- 879. JAATINEN, PEKKO. Design and control of a permanent magnet bearingless machine. 2019. Diss.
- 880. HILTUNEN, JANI. Improving the DC-DC power conversion efficiency in a solid oxide fuel cell system. 2019. Diss.
- 881. RAHIKAINEN, JARKKO. On the dynamic simulation of coupled multibody and hydraulic systems for real-time applications. 2019. Diss.
- 882. ALAPERÄ, ILARI. Grid support by battery energy storage system secondary applications. 2019. Diss.
- 883. TYKKYLÄINEN, SAILA. Growth for the common good? Social enterprises' growth process. 2019. Diss.
- 884. TUOMISALO, TEEMU. Learning and entrepreneurial opportunity development within a Finnish telecommunication International Venture. 2019. Diss.
- 885. OYEDEJI, SHOLA. Software sustainability by design. 2019. Diss.
- 886. HUTTUNEN, MANU. Optimizing the specific energy consumption of vacuum filtration. 2019. Diss.
- 887. LIIKANEN, MIIA. Identifying the influence of an operational environment on environmental impacts of waste management. 2019. Diss.
- 888. RANTALA, TERO. Operational level performance measurement in university-industry collaboration. 2019. Diss.
- 889. LAUKKANEN, MINTTU. Sustainable business models for advancing system-level sustainability. 2019. Diss.
- 890. LOHRMANN, CHRISTOPH. Heuristic similarity- and distance-based supervised feature selection methods. 2019. Diss.
- 891. ABDULLAH, UMMI. Novel methods for assessing and improving usability of a remote-operated off-road vehicle interface. 2019. Diss.

892. PÖLLÄNEN, ILKKA. The efficiency and damage control of a recovery boiler. 2019. Diss.
893. HEKMATMANESH, AMIN. Investigation of EEG signal processing for rehabilitation robot control. 2019. Diss.
894. HARMOKIVI-SALORANTA, PAULA. Käyttäjät liikuntapalvelujen kehittäjinä - Käyttäjälähtöisessä palveluinnovaatioprosessissa käyttäjien tuottama tieto tutkimuksen kohteena. 2020. Diss.
895. BERGMAN, JUKKA-PEKKA. Managerial cognitive structures, strategy frames, collective strategy frame and their implications for the firms. 2020. Diss.
896. POLUEKTOV, ANTON. Application of software-defined radio for power-line-communication-based monitoring. 2020. Diss.
897. JÄRVISALO, HEIKKI. Applicability of GaN high electron mobility transistors in a high-speed drive system. 2020. Diss.
898. KOPONEN, JOONAS. Energy efficient hydrogen production by water electrolysis. 2020. Diss.
899. MAMELKINA, MARIA. Treatment of mining waters by electrocoagulation. 2020. Diss.
900. AMBAT, INDU. Application of diverse feedstocks for biodiesel production using catalytic technology. 2020. Diss.
901. LAPIO-RAPI, EMILIA. Sairaanhoidajien rajatun lääkkeenmääräämistoiminnan tuottavuuden, tehokkuuden ja kustannusvaikuttavuuden arviointi perusterveydenhuollon avohoidon palveluprosessissa. 2020. Diss.
902. DI, CHONG. Modeling and analysis of a high-speed solid-rotor induction machine. 2020. Diss.
903. AROLA, KIMMO. Enhanced micropollutant removal and nutrient recovery in municipal wastewater treatment. 2020. Diss.
904. RAHIMPOUR GOLROUDBARY, SAEED. Sustainable recycling of critical materials. 2020. Diss.
905. BURGOS CASTILLO, RUTELY CONCEPCION. Fenton chemistry beyond remediating wastewater and producing cleaner water. 2020. Diss.
906. JOHN, MIIA. Separation efficiencies of freeze crystallization in wastewater purification. 2020. Diss.
907. VUOJOLAINEN, JOUNI. Identification of magnetically levitated machines. 2020. Diss.
908. KC, RAGHU. The role of efficient forest biomass logistics on optimisation of environmental sustainability of bioenergy. 2020. Diss.
909. NEISI, NEDA. Dynamic and thermal modeling of touch-down bearings considering bearing non-idealities. 2020. Diss.
910. YAN, FANGPING. The deposition and light absorption property of carbonaceous matter in the Himalayas and Tibetan Plateau. 2020. Diss.



ISBN 978-952-335-527-9
ISBN 978-952-335-528-6 (PDF)
ISSN-L 1456-4491
ISSN 1456-4491
Lappeenranta 2020